# Synchronization and nonreciprocal interactions in quantum many-body systems

## Inauguraldissertation

zur

Erlangung der Würde eines Doktors der Philosophie vorgelegt der Philosophisch-Naturwissenschaftlichen Fakultät der Universität Basel

von

Tobias Nadolny

2025

Genehmigt von der Philosophisch-Naturwissenschaftlichen Fakultät auf Antrag von

Erstbetreuer: Prof. Dr. Christoph Bruder

Zweitbetreuer: Prof. Dr. Philipp Treutlein

Externe Expertin: Prof. Dr. Ana Maria Rey

Basel, den 16. September 2025

Prof. Dr. Heiko Schuldt, Dekan

# Summary

In nonequilibrium systems, individual constituents can self-organize, forming collective order without any external control. Self-organization offers a robust and scalable way to create complex structures; consequently, it is relevant in different contexts, including living systems, economics, and social dynamics. As a paradigmatic example of self-organization, synchronization describes how limit-cycle oscillators tend to lock their phases and, as a result, spontaneously form a phase-coherent state. Synchronization captures diverse phenomena like the simultaneous flashing of fireflies or phase locking in power grids. While synchronization usually arises through mutually attractive interactions, another class of self-organization occurs when interactions are nonreciprocal. In this case, the constituents may interact in an antagonistic way; for example, one constituent may repel another one, which in turn attracts the former, akin to the dynamics of predator and prey. Such interactions can result in a nonreciprocal phase transition, whereby individual constituents self-organize, forming a collective dynamical state similar to a chase-and-escape motion between predators and prey.

While synchronization and nonreciprocal phase transitions are extensively studied using classical models, nature is ultimately governed by the laws of quantum physics. This raises fundamental questions: Can physical systems, whose constituents are microscopically governed by quantum mechanics, exhibit synchronization and nonreciprocal phase transitions? If so, how does the quantum nature of the individual constituents affect the collective states and dynamics? These questions are particularly relevant given the experimental progress in controlling driven-dissipative quantum many-body systems, where interactions, driving, and dissipation can be engineered to a remarkable degree. Since these systems are inherently out of equilibrium, they are natural platforms for self-organization to occur.

Motivated by the rich phenomena of self-organization and the experimental progress in driven-dissipative quantum systems, this thesis explores how two paradigmatic selforganization transitions manifest in quantum systems. First, we discuss similarities and differences between classical and quantum synchronization, pointing out unique features in many-body quantum synchronization where the microscopic nature of individual quantum constituents qualitatively shapes the macroscopic synchronized state. Second, we offer a versatile framework for engineering antagonistic interactions among quantum constituents and establish that nonreciprocal phase transitions can occur in quantum systems. A central theme of this work is to provide intuition for the occurrence of self-organized, collective states based on a detailed understanding of the microscopic interactions. Furthermore, we emphasize the role of measurements, highlighting how dynamics and symmetry breaking become directly visible in individual quantum trajectories. Finally, we show that the fundamental insights gained about synchronization and nonreciprocal phase transitions have implications for the design of superradiant lasers relevant for precision applications. This thesis motivates future research to explore self-organization in quantum systems as a way of forming useful many-body states, such as squeezed states for enhanced metrology, where the order is not externally imposed but rather develops spontaneously through the interactions among the quantum constituents.

# **Publications**

Most results presented in this thesis, specifically in Chapters 5, 6, and 7, have been published in the following publications:

- Macroscopic Quantum Synchronization Effects
   T. Nadolny and C. Bruder
   Physical Review Letters, 131, 190402 (2023)
- Nonreciprocal Synchronization of Active Quantum Spins
   T. Nadolny, C. Bruder, M. Brunelli
   Physical Review X, 15, 011010 (2025)

   Featured in a press release by University of Basel.
- Nonreciprocal Interactions Induce Frequency Shifts in Superradiant Lasers
   T. Nadolny, M. Brunelli, C. Bruder
   Physical Review Letters, 134, 193603 (2025)

The following articles were also published during the making of this thesis. Their contents, however, are not covered in this thesis.

- Improving transmon qudit measurement on IBM Quantum hardware T. Kehrer, T. Nadolny, C. Bruder Physical Review Research 6, 013050 (2024)
- Quantum synchronization through the interference blockade T. Kehrer, T. Nadolny, C. Bruder Physical Review A 110, 042203 (2024)

# Contents

Sι	ımm	ary		iii
Pι	ublic	ations		v
1	Intr	Introduction		
2	Syn	chroni	zation	5
	2.1	Limit-	cycle oscillator	. 5
		2.1.1	Influence of fluctuations	. 7
	2.2	Two co	oupled oscillators	. 10
		2.2.1	Frequency detuning	. 10
		2.2.2	Influence of fluctuations	
	2.3	Kuran	noto model	. 15
		2.3.1	Frequency disorder	
		2.3.2	Influence of fluctuations	
	2.4		ciprocal interactions	
	2.5	Concl	asions	. 22
3	Оре	en qua	ntum systems	23
	3.1	Densit	y operator	. 23
	3.2	Lindb	lad master equation	. 25
	3.3	Contin	nuous measurements	. 25
	3.4	Casca	ded master equation and unidirectional interactions	. 27
4	Qua	antum	synchronization	31
	4.1		um van-der-Pol oscillator	. 31
		4.1.1	Quantum limit cycles	. 32
			Quantum limit cycles under heterodyne detection	. 34
		4.1.2	Two coupled oscillators	. 35
			Phase locking	. 36
			Frequency entrainment	. 37
			Quantum synchronization under heterodyne detection	. 38
		4.1.3	Large network of coupled oscillators	. 38
		4.1.4	Experimental implementation in trapped ions	. 41
	4.2	Quant	um spins	. 42
		4.2.1	Quantum limit cycles	. 42
			Quantum limit cycles under heterodyne detection	. 44
		4.2.2	Two coupled spins	. 44
	Phase locking			. 46
Frequency entrainment				
			Quantum synchronization under heterodyne detection	. 47
		4.2.3	Large network of coupled spins	. 48

		Finite-size systems	50
		Experimental implementation: superradiant laser	
	4.3		52
5	Mac	1 1 0	55
	5.1	v v	55
		5.1.1 Interference blockade	56
		5.1.2 Quantum synchronization blockade	58
	5.2	Many-body model	58
	5.3		60
	5.4		63
	5.5		66
		Appendix for Chapter 5	69
	5.A		69
	5.B	1	69
	5.C		72
6	Non	areciprocal synchronization of active quantum spins	75
	6.1	- · · ·	75
	6.2		79
	•		79
		•	80
	6.3	1	81
	6.4		82
	6.5	v v	84
	0.0		85
			85
		·	86
	6.6	• • • • • •	87
	6.7		88
	0.7		88
		<u> </u>	oc 91
	6.0	, <b>1</b> , 1	
	6.8	•	93
		6.8.1 Heterodyne measurement	
	<i>c</i> 0	6.8.2 Homodyne measurement	
	6.9	Implications for nonreciprocal quantum many-body systems	
	6.10	Conclusions	
	a 1	Appendix for Chapter 6	
	6.A	General complex coherent coupling	
	6.B	Transition between incoherent and synchronized states	
	6.C	Phase diagrams: amplitude and phase difference	
	6.D	Finite-size calculations of the steady state	
	6.E	Trajectory calculations	07
7	Free		09
	7.1	Introduction	
	7.2	Model	
	7.3	Nonreciprocal interactions	11
	7.4	Spontaneous emission and dephasing	15
	7.5	Conclusion	
		Appendix for Chapter 7	19

		Cumulant expansion and spectrum	
8	Con	nclusions and outlook	123
	8.1	Conclusions	123
	8.2	Outlook	124
A	cknov	wledgments	<b>128</b>
Bi	bliog	graphy	129

# Chapter 1

# Introduction

#### Self-organization

Complex structures can be formed through deliberate and precise control. To illustrate, artists transform marble into impressive sculptures; managers coordinate employees to achieve an efficient workflow; and programmers design algorithms for specific computational tasks. In each case, the resulting configuration – the artwork, the organized workflow, or the algorithm – is imposed externally.

Remarkably, similar forms of order can also arise spontaneously without any external control through the process of self-organization [Haken, 1983]. Beautiful patterns emerge in plants, teams can self-coordinate without hierarchical oversight, and neural networks spontaneously develop complex algorithms during training without a programmer setting parameters explicitly. Self-organization only occurs out of equilibrium, relying on a continuous energy exchange with the environment. The patterns and the complexity formed through self-organization appear on a wide range of scales from the distribution of matter in the Universe to intricate shapes of snowflakes and assemblies of cells [Cross and Greenside, 2009. Consequently, the importance of self-organization is appreciated in various fields, including chemistry [Prigogine, 1978], biology [Fang et al., 2019], economics [Farmer and Foley, 2009], and social dynamics [Castellano et al., 2009; Helbing, 2012. Self-organization offers advantages over externally controlled structure formation. First, it is inherently robust: Whereas an imperfection in the external control can result in a breakdown of the carefully crafted structure, self-organization is the result of distributed local interactions and thus often resilient to perturbations. Second, self-organization is more easily scalable since an increasing number of constituents does not require a more advanced external control.

A paradigmatic example of self-organization is synchronization. The Kuramoto model captures the essence of this phenomenon: Coupled oscillators tend to align their phases so that they will eventually share the same frequency despite differences in their natural frequencies [Kuramoto, 1984]. This demonstrates how pairwise interactions result in a collectively ordered state without external forcing. Many phenomena can be understood in terms of synchronization [Strogatz, 2003], including the simultaneous flashing of fireflies [Buck, 1938], phase locking in power grids [Witthaut et al., 2022], as well as collective emission in lasers [Zhu et al., 2015].

The interactions that lead to synchronization are usually reciprocal: Individual constituents share the same "goal" of aligning their phases. The concept of reciprocal interactions dates back to Newton's third law, which states that any action necessitates a symmetric reaction. For example, two equally charged particles symmetrically repel each other, and massive objects symmetrically attract each other. However, reciprocity of interactions is not always the rule; instead, interactions can be nonreciprocal, which significantly influences self-organization. This has recently been highlighted in the context of active matter, i.e., ensembles of active agents. Active agents are nonequilibrium entities that use energy to propel themselves or generate forces onto one another [Schweitzer,

2 1. Introduction

2003; Marchetti et al., 2013; Bechinger et al., 2016;  $te\ Vrugt\ and\ Wittkowski$ , 2025]. Each active agent is driven out of equilibrium locally, a characteristic that distinguishes active matter from other nonequilibrium systems such as boundary-driven systems. An exciting feature of active agents is that the forces exerted among them can be nonreciprocal so that the influence of agent A on agent B differs from B's influence on A.

A particularly interesting subclass of nonreciprocal interactions are antagonistic interactions, where A influences B in a way that is opposite to the way in which B influences A. In other words, A and B have competing goals with respect to each other. Antagonistic interactions occur, for example, in ecological systems where the population of predators grows at the expense of the number of prey [Lotka, 1925; Volterra, 1926], or in social dynamics as a competition between agreement and disagreement [Hong and Strogatz, 2011b]. Antagonistic interactions can cause a nonreciprocal phase transition where a dynamical pattern emerges in the form of a collectively ordered state that oscillates in time [You et al., 2020; Fruchart et al., 2021; Hanai, 2024].

#### Driven-dissipative quantum systems

Both synchronization and nonreciprocal phase transitions are extensively discussed in classical systems. Simple classical models are constructed to describe and understand these phenomena. Yet, our world is fundamentally governed by the laws of quantum mechanics. This raises a few key questions: Can physical systems, whose constituents are microscopically governed by quantum mechanics, exhibit synchronization and nonreciprocal phase transitions? If so, how can these self-organization transitions be formulated within the framework of quantum physics? These questions are partially addressed in the study of quantum synchronization [Walter et al., 2014; Lee and Sadeghpour, 2013], self-organization of cold atoms [Ritsch et al., 2013; Mivehvar et al., 2021], or collective effects like subradiance and superradiance [Dicke, 1954; Gross and Haroche, 1982]. However, many questions have remained unanswered: Does the quantum nature of the individual constituents influence the collective synchronization behavior? Are there nonreciprocal phase transitions in quantum systems, and how could the necessary antagonistic interactions occur among quantum constituents?

These questions become increasingly important due to the experimental progress in controlling quantum many-body systems. Some quantum systems can be described as isolated systems following the time evolution governed by a Hamiltonian. For instance, various quantum computing platforms are designed to achieve perfect isolation [Nielsen and Chuang, 2010]. However, the coupling to an environment and the resulting dissipation often cannot be neglected. Furthermore, control over the quantum system is enabled by various drives, e.g., through a microwave pulse or a laser beam. As a result, one often treats driven-dissipative quantum systems, which are inherently out of equilibrium since they can gain energy via the drive and lose energy to an environment. In recent years, nonequilibrium phenomena have been observed in a variety of experimental platforms, including solid materials in cavities [Hübener et al., 2021], cold atoms in cavities [Mivehvar et al., 2021] or in optical tweezers [Browaeys and Lahaye, 2020; Kaufman and Ni, 2021], chiral quantum optics [Suárez-Forero et al., 2025], trapped ions [Foss-Feig et al., 2025], and quantum fluids of light in nonlinear optical systems [Carusotto and Ciuti, 2013].

The high control of driven-dissipative quantum systems requires a precise theoretical understanding of nonequilibrium phenomena at the quantum level. Therefore, a considerable amount of research is performed towards this direction [Polkovnikov et al., 2011; Schaller, 2014; Eisert et al., 2015; Landi et al., 2022; Defenu et al., 2024; Sieberer et al., 2025]. The progress in understanding nonequilibrium quantum systems enables the design of quantum technologies that rely on drive and dissipation. Arguably, the laser is the most

1. Introduction 3

important technology of this class, relying on nonequilibrium gain and loss [Haken, 1983]. More recently, engineered dissipation is used for signal amplification [Clerk et al., 2010] and in quantum information platforms [Harrington et al., 2022]. It will be interesting to consider self-organization as a robust and scalable way to form useful structure among the quantum constituents, like phase-coherent, squeezed, or entangled states.

#### Overview of this thesis

This thesis is motivated by the rich phenomenology of spontaneous self-organization and the experimental progress in the control of driven-dissipative quantum systems. The main contribution of this thesis is to connect two paradigmatic classes of self-organization – synchronization and nonreciprocal phase transitions – to quantum physics. This connection is of fundamental interest, as it addresses the key questions regarding self-organization in quantum systems posed above. Also, it has practical implications allowing us to derive design principles for superradiant lasers, a promising type of laser relevant for precision applications. A central theme of this thesis is to intuitively explain why certain collective states arise through a comprehensive understanding of the pairwise interactions of any two constituents. Another recurring theme is the role of measurements. We highlight the backaction that the measurement imparts on the system, and use the resulting quantum trajectories to analyze dynamics and symmetry breaking beyond the ensemble description.

The thesis starts with a review of classical synchronization and nonreciprocal interactions in Chapter 2. To connect these concepts to quantum physics, we use the framework of open quantum systems, which allows us to efficiently describe the effects of an environment on the system. The notation and the concepts of open quantum systems that are relevant for this thesis are introduced in Chapter 3. We then review synchronization of driven-dissipative quantum oscillators with a novel emphasis on the role of measurements in Chapter 4. Chapters 2 to 4 build the basis for the presentation of our main results in the following three chapters.

In Chapter 5, we present a model of quantum oscillators whose synchronization behavior is qualitatively different from that of classical oscillators. Existing models of synchronizing quantum oscillators exhibit a self-organization transition that qualitatively resembles that of the Kuramoto model. Here, however, collective synchronization is shaped by the quantum nature of the individual oscillators. This is an example of self-organization where the microscopic details of the quantum constituents are visible in the macroscopic order.

In Chapter 6, we go beyond reciprocal interactions and analyze a quantum model that hosts a phase transition induced by nonreciprocal interactions. We offer a general framework to engineer antagonistic interactions, where two quantum systems influence each other in opposing ways. The key result is to show that a nonreciprocal phase transition can occur in a quantum many-body system. The transition is marked by the occurrence of a dynamical pattern oscillating in time. We will show how this pattern is made apparent and influenced through measurements.

The preceding chapters build a fundamental understanding of synchronization and nonreciprocal interactions in quantum systems. Chapter 7 connects these theoretical insights to the physics of a concrete physical system, the superradiant laser. This type of laser relies on synchronized atoms that emit coherent light with narrow linewidth, offering promising applications for precision technologies. We will show that nonreciprocal interactions can naturally occur among the atoms, altering their collective self-organization behavior. This causes a dynamical state, corresponding to a frequency shift, which limits the laser's optimal performance. We conclude and collect open questions for future studies in Chapter 8.

# Chapter 2

# Synchronization

Synchronization is a paradigmatic example of self-organization. It describes the phenomenon in which oscillating entities align their phases and entrain their frequencies even in the presence of noise and frequency disorder. Synchronization occurs in various ways throughout nature, as well as in engineered and social systems. Perhaps the most famous instance is that coupled clocks begin to tick in unison as originally discovered by Christiaan Huygens in 1673 [Pikovsky et al., 2001, Appendix A1]; his experiment is still revisited centuries later [Bennett et al., 2002; Goldsztein et al., 2021]. To give some more examples, synchronization can describe the simultaneous flashing of fireflies [Buck, 1938; McCrea et al., 2022], phase locking in power grids [Witthaut et al., 2022], crowds of people falling into step [Strogatz et al., 2005], and the coordinated firing of neurons in brains [Brown et al., 2004; Uhlhaas et al., 2009]. As such a widespread phenomenon, synchronization has been extensively studied in classical nonlinear dynamics [Pikovsky et al., 2001; Acebrón et al., 2005; Strogatz, 2019].

As we will discuss in this thesis, the concepts of synchronization also apply to quantum systems. To intuitively understand the dynamics of quantum systems that synchronize, it is helpful to be familiar with the basic concepts of synchronization in classical systems, which are presented in this chapter. In Section 2.1, we show how a single limit-cycle oscillator can be described in terms of its phase. Phase locking and frequency entrainment of two coupled oscillators are discussed in Section 2.2. In Section 2.3, we present the Kuramoto model that describes many coupled oscillators and features a self-organization transition from disorder to collective synchrony. The material presented in this chapter is largely based on the textbooks *Pikovsky* et al. [2001] and *Strogatz* [2019].

## 2.1 Limit-cycle oscillator

Our starting point is the harmonic oscillator. The time evolution of a harmonic oscillator with frequency  $\omega$  and unit mass,  $\ddot{x} = -\omega^2 x$ , can be expressed by the differential equation

$$\dot{\alpha} = -i\omega\alpha\,, (2.1)$$

where  $\alpha = x + ip$  and  $p = \dot{x}/\omega$ . There are different dynamical solutions to Eq. (2.1) that depend on the initial condition  $\alpha_0$ 

$$\alpha(t) = \alpha_0 \exp(-it\omega). \tag{2.2}$$

The energy  $|\alpha_0|^2$  determines the amplitude of the oscillation. Three possible evolutions are displayed in Fig. 2.1(a).

In contrast to the harmonic oscillator that has a constant energy, *limit-cycle oscillators* are driven-dissipative systems that continuously exchange energy with an environment. Importantly, the rate of energy exchange with the environment depends on the oscillator's state variables. This renders the differential equation governing the time evolution of the

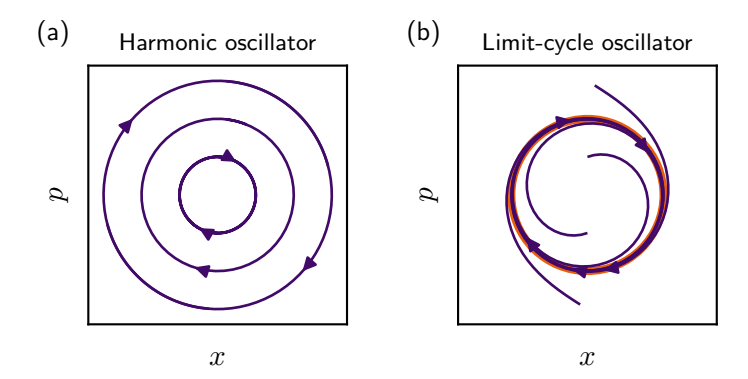


Figure 2.1: (a) Three trajectories of a harmonic oscillator in phase space. (b) Four trajectories of a van-der-Pol oscillator, Eq. (2.3), with  $\kappa_1 = \kappa_2 = \omega/2$ . The red circle shows the limit cycle to which all trajectories converge.

oscillator nonlinear, a necessary condition for the presence of limit cycles [Strogatz, 2019]. In the context of synchronization, we are interested in stable limit cycles where the gain and loss processes result in closed attracting trajectories in phase space. Independently of the initial condition, the oscillator's state approaches these periodic trajectories in the long-time limit. On the limit cycle, we can define a single variable to uniquely identify the oscillator's state. We call this the *phase* of the oscillator, which takes values between zero and  $2\pi$ ; it will be the central quantity in synchronization.

A paradigmatic model of a limit-cycle oscillator is the van-der-Pol (vdP) oscillator. In the regime of weak nonlinearity, the oscillator's amplitude  $\alpha$  follows the equation of motion [Pikovsky et al., 2001, Section 7.2]

$$\dot{\alpha} = -i\omega\alpha + \kappa_1 \alpha/2 - \kappa_2 |\alpha|^2 \alpha , \qquad (2.3)$$

with linear gain at rate  $\kappa_1 > 0$  and nonlinear loss at rate  $\kappa_2 > 0$ . The loss is nonlinear, since the effective loss rate depends on the amplitude squared. Figure 2.1(b) shows four trajectories with different initial conditions that approach the same limit cycle. The limit-cycle trajectory can be obtained by defining the amplitude  $r = |\alpha|$  and phase  $\phi = -\arg[\alpha]$  so that  $\alpha = r\exp(-i\phi)$ . The equations of motion for amplitude and phase of a vdP oscillator are

$$\dot{r} = (\kappa_1/2 - \kappa_2 r^2)r, \qquad (2.4)$$

$$\dot{\phi} = \omega \,. \tag{2.5}$$

Since  $\kappa_{1,2} > 0$ , the radius is attracted to the stable fixed point at  $r_0 = \sqrt{\kappa_1/2\kappa_2}$ . The phase increases linearly in time at rate  $\omega$ . We conclude that the vdP oscillator exhibits an attractive limit-cycle with constant amplitude  $r_0$  and frequency  $\omega$ .

The vdP oscillator as written in Eq. (2.3) represents the normal form of a Hopf bifurcation [Kuznetsov, 2023]. As such, it may represent the dynamics of a variety of dynamical systems, at least within a local parameter regime. To give an example, let us connect the model of a vdP oscillator to the laser. In a semiclassical description of the laser, the complex amplitude  $\alpha_l$  of the light field is coupled to a gain medium whose relaxation time is short compared to that of the light field. The gain medium can

consequently be adiabatically eliminated, which results in an effective description for the light-field amplitude [Scully and Zubairy, 1997, Chapter 5]

$$\dot{\alpha}_l = -i\omega\alpha_l + \frac{\kappa_+}{1 + \kappa_2|\alpha_l|^2/\kappa_+} \alpha_l - \kappa\alpha_l, \qquad (2.6)$$

with linear damping at rate  $\kappa$ , saturated gain at rate  $\kappa_+$ , and saturation coefficient  $\kappa_2$ . We can expand the right-hand side for small  $\kappa_2 |\alpha_l|^2 / \kappa_+$ , which is valid close to the lasing threshold, i.e., for  $\kappa \approx \kappa_+$ :

$$\dot{\alpha}_{l} \approx -i\omega\alpha_{l} + (\kappa_{+} - \kappa)\alpha_{l} - \kappa_{2}|\alpha_{l}|^{2}\alpha_{l} + \mathcal{O}\left(\frac{\kappa_{2}|\alpha_{l}|^{2}}{\kappa_{+}}\right). \tag{2.7}$$

We find the equation of the vdP oscillator, Eq. (2.3), with the effective linear gain  $\kappa_1 = \kappa_+ - \kappa$ . The lasing state, in which the light field assumes a nonzero value oscillating with the lasing frequency  $\omega$ , is obtained when the gain overcomes the damping,  $\kappa_+ - \kappa > 0$ . The lasing transition constitutes a self-organization transition, where the constituents of the gain medium, for example, individual atoms, emit light in phase [Haken, 1983]. In terms of the vdP oscillator, the lasing state corresponds to a limit cycle. The vdP oscillator discussed in this chapter can thus be thought of as a laser close to the lasing threshold. Our discussion of synchronization of vdP oscillators in the following sections therefore also captures the essentials of synchronization and injection locking of lasers [Siegman, 1986, Chapter 29].

#### 2.1.1 Influence of fluctuations

The dynamics of a physical system is generally not completely deterministic. Instead, fluctuations result in a stochastic time evolution. The fluctuations are usually the effect of an environment that influences the system dynamics. Even when the combined state of a system and its environment evolves deterministically, the system state by itself appears to fluctuate. For example, a Brownian particle can be described in a deterministic way, including the motion and interactions of all neighboring particles. It is simpler, however, to consider the influence of the environment on the particle as effective fluctuations that randomly change the state of the system [Zwanzig, 2001]. In equilibrium systems, the coupling to the environment and the strength of fluctuations are related by the dissipation-fluctuation theorem [Callen and Welton, 1951; Kubo, 1966]. However, the concept of fluctuations induced by the environment also extends to nonequilibrium systems like the vdP oscillator, where the energy exchange with the environment inevitably induces fluctuations in the system. In the example of the laser, the fluctuations may originate from thermal noise or from quantum fluctuations that persist at zero temperature.

Without specifying the details of the coupling to the environment, the fluctuations are usually modeled by a Langevin equation, i.e., an Itô stochastic differential equation [Zwanziq, 2001]; for a vdP oscillator, it reads

$$\dot{\alpha} = -i\omega\alpha + \kappa_1 \alpha/2 - \kappa_2 |\alpha|^2 \alpha + \sigma \xi_x(t) + i\sigma \xi_y(t). \tag{2.8}$$

The terms  $\xi_x(t)$  and  $\xi_y(t)$  are stationary Gaussian white-noise processes that induce independent fluctuations in the real and imaginary parts of the amplitude  $\alpha$ . The noise processes have zero mean,  $\mathbb{E}[\xi_x(t)] = \mathbb{E}[\xi_y(t)] = 0$ , and variance  $\mathbb{E}[\xi_x(t)\xi_x(t')] = \mathbb{E}[\xi_y(t)\xi_y(t')] = \delta(t-t')$ . The strength of the noise is  $\sigma^2$ .

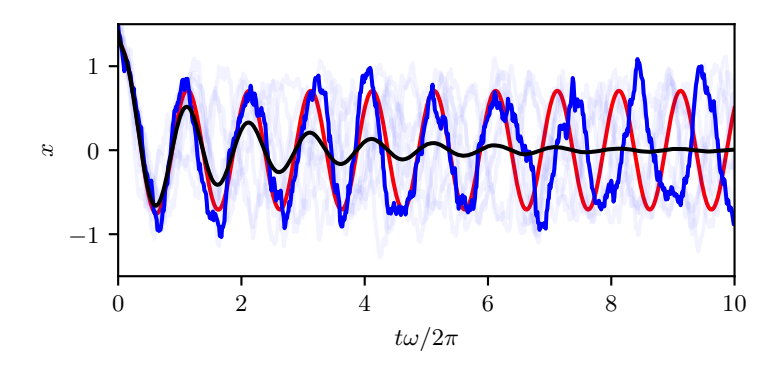


Figure 2.2: Limit-cycle oscillations in the presence of noise. The blue lines show  $x = \text{Re}[\alpha]$  for ten different trajectories, all starting with the same initial condition. One of them is highlighted in a darker blue. The black line displays the average evolution obtained by averaging over 16 000 trajectories. The red line shows a trajectory in the absence of noise. Parameters:  $\kappa_1 = \kappa_2 = \omega/2 = 10\sigma^2$ .

Integrating Eq. (2.8) results in a trajectory for  $\alpha$  that depends on the random realization of the noise. A few such trajectories are displayed in Fig. 2.2 (blue lines). They approximately follow the noiseless evolution (red line) with additional fluctuations.

Any Langevin equation can be converted to an equivalent Fokker-Planck equation [Risken, 1989; Zwanzig, 2001]. The Fokker-Planck equation describes the time evolution of the probability distribution for the system to be in a certain state. Here, we introduce the probability distribution P(x,p) for the vdP oscillator to be in the state  $\alpha = x + ip$  at time t (for ease of notation, we do not explicitly denote the time dependence). Equation (2.8) corresponds to the Fokker-Planck equation

$$\partial_t P(x,p) = -\nabla (\boldsymbol{\mu} P(x,p)) + \sigma^2 \nabla^2 P(x,p) ,$$

$$\nabla = \begin{pmatrix} \partial_x \\ \partial_p \end{pmatrix} , \quad \boldsymbol{\mu} = \begin{pmatrix} \omega p + \kappa_1 x/2 - \kappa_2 (x^2 + p^2) x \\ -\omega x + \kappa_1 p/2 - \kappa_2 (x^2 + p^2) p \end{pmatrix} ,$$
(2.9)

introducing partial differentials for t, x and p, e.g.,  $\partial_t = \partial/\partial t$ . The deterministic part of the time evolution enters via the term proportional to  $\mu$ , while the effect of the fluctuations is described by the term proportional to  $\sigma^2$ .

Fokker-Planck equations are partial differential equations whose analytical and numerical solutions are typically difficult to obtain. For a numerical solution, it is often easiest to integrate the corresponding Langevin equation for various initial conditions and realizations of the noise. Given sufficient realizations, the probability distribution P(x, p) is approximated by the relative number of occurrences of the values  $\alpha = x + ip$  at each time counted over all trajectories.

We take this approach to obtain the time evolution of the probability distribution shown in the upper panels of Fig. 2.3. We recognize the oscillation at frequency  $\omega$  and the attraction to the limit cycle since the probability distribution rotates and moves towards the limit-cycle amplitude  $r_0$ . Furthermore, note that the probability distribution spreads along the phase direction, indicating that the initial phase of the distribution is lost over time. This process is called *phase diffusion*. The initial distribution approaches a unique stationary distribution in the long-time limit, which is ring-shaped and phase-symmetric, i.e., invariant under rotations around the origin; see top right panel of Fig. 2.3. Similarly, the phase fluctuations are visible in the average of many trajectories in Fig. 2.2 (black line).

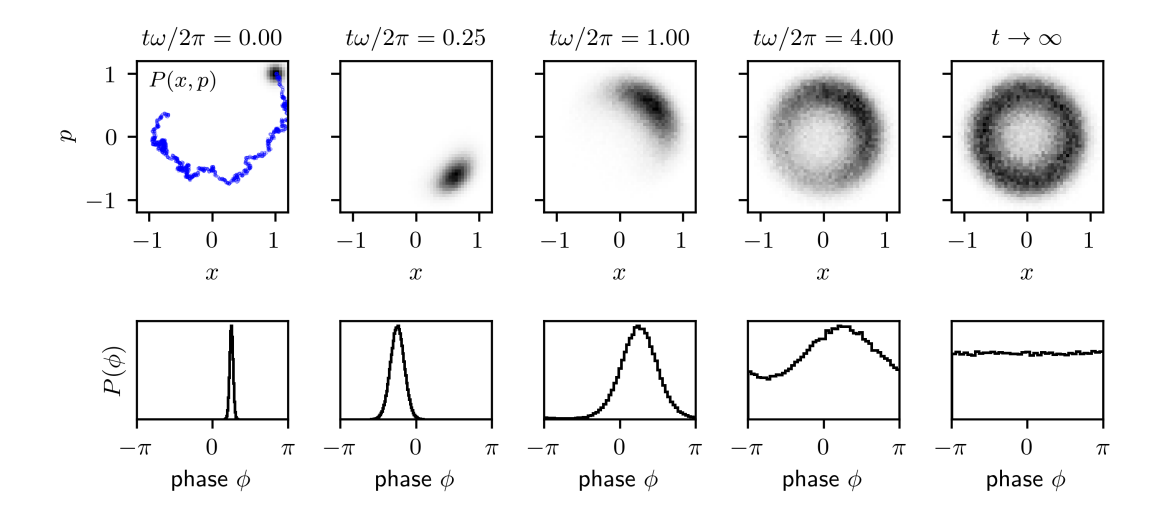


Figure 2.3: Time evolution of the classical vdP oscillator shown by the probability distributions P(x,p) (top row) and  $P(\phi)$  (bottom row). In the top row, the grayscale indicates the value of P(x,p). The distributions are obtained by sampling 16 000 trajectories and counting the occurrences per (x,p) or per  $\phi$ . One trajectory is shown by the blue line in the top left panel. Parameters:  $\kappa_1 = \kappa_2 = \omega/2 = 10\sigma^2$ .

In the long-time limit, the information about the initial phase is lost in all trajectories, so that their average gives zero.

The phase diffusion can be quantified by converting Eq. (2.8) to polar coordinates using Itô's formula. We obtain [Gardiner, 1997, Section 4.4.5]

$$\dot{r} = (\kappa_1/2 - \kappa_2 r^2)r + \frac{\sigma^2}{2r} + \sigma \xi_r,$$
 (2.10)

$$\dot{\phi} = \omega + \frac{\sigma}{r} \xi_{\phi} \,. \tag{2.11}$$

where  $\xi_r$  and  $\xi_{\phi}$  are independent Gaussian white-noise processes following the same statistics as  $\xi_x$  and  $\xi_y$ . In the equation for the phase, Eq. (2.11), the noise process enters with a factor of 1/r. Therefore, when the radius is large, the fluctuations in the phase are small.

Let us now assume that the rates  $\kappa_1$  and  $\kappa_2$  are large compared to  $\sigma^2$ . The radius then approximately takes the constant value  $r_0$ . This allows us to consider the Fokker-Planck equation for the phase distribution  $P(\phi)$ ,

$$\partial_t P(\phi) = -\omega \partial_\phi P(\phi) + \frac{\sigma^2}{2r_0^2} \partial_\phi^2 P(\phi) , \qquad (2.12)$$

corresponding to the Langevin equation  $\dot{\phi} = \omega + \sigma \xi_{\phi}/r_0$  [Pikovsky et al., 2001, Section 9.2]. The Fokker-Planck equation describes phase diffusion at rate

$$D \equiv \frac{\sigma^2}{2r_0^2} \,. \tag{2.13}$$

The time evolution of the phase distribution is shown in the bottom row of Fig. 2.3. Here, the phase diffusion becomes visible as a broadening of  $P(\phi)$ , which approaches a flat

curve in the long-time limit. Indeed, the steady state solution of Eq. (2.12) that satisfies  $\partial_t P(\phi) = 0$  is  $P(\phi) = 1/(2\pi)$ , i.e., completely flat.

In the example of the laser, the phase fluctuations result in a nonzero linewidth [Gardiner and Zoller, 2000; Scully and Zubairy, 1997]. The linewidth is an important characteristic of the laser, quantifying the quality of its coherence; it corresponds to the width of the spectrum of the laser's light. The spectrum is defined as the Fourier transform of the steady-state two-time correlations

$$g(\tau) \equiv \lim_{t \to \infty} \mathbb{E}[\alpha^*(t+\tau)\alpha(t)]. \tag{2.14}$$

The expectation value  $\mathbb{E}[\cdot]$  denotes an average over all possible noise realizations; in practice, it is approximated by a finite number of numerical simulations with different noise realizations. When the amplitude is large, amplitude fluctuations can be ignored, and phase fluctuations dominate the two-time correlation function. Furthermore, the phase evolution is stationary in the long-time limit, so that

$$g(\tau) = r_0^2 \mathbb{E}\left[\exp[i(\phi(\tau) - \phi(0))]\right].$$
 (2.15)

Inserting the solution of Eq. (2.11) with  $r = r_0$ , and using that the phase fluctuations are Gaussian, one obtains [Scully and Zubairy, 1997, Section 11.4]

$$g(\tau) = r_0^2 \exp(i\omega\tau - D|\tau|). \tag{2.16}$$

The spectrum is the Fourier transform of the autocorrelation function. Here, it evaluates to a Lorentzian distribution centered at frequency  $\omega$  with width 2D. This shows how the phase diffusion determines the laser linewidth.

## 2.2 Two coupled oscillators

In this section, we show that two limit-cycle oscillators that are coupled strongly enough can entrain their frequencies and lock their phases despite the presence of frequency detuning or noise.

#### 2.2.1 Frequency detuning

We start the discussion assuming zero fluctuations. The evolution of two detuned and coupled van-der-Pol oscillators is given by

$$\dot{\alpha} = -i\delta\alpha/2 + \kappa_1\alpha/2 - \kappa_2|\alpha|^2\alpha + V(\beta - \alpha)/2 \tag{2.17a}$$

$$\dot{\beta} = +i\delta\beta/2 + \kappa_1\beta/2 - \kappa_2|\beta|^2\beta + V(\alpha - \beta)/2$$
(2.17b)

with frequency detuning  $\delta$  and coupling strength  $V \geq 0$ . For simplicity, we consider only dissipative coupling; for an analysis of reactive coupling, see for example Pikovsky et al. [2001, Section 8.2.1]. In writing Eqs. (2.17), we have implicitly moved to a frame rotating at the average frequency of the two oscillators. In that frame, the frequencies of the oscillators are  $\pm \delta/2$ .

Similar to before, we define amplitudes and phases of the oscillators via  $\alpha = r_A \exp(-i\phi_A)$  and  $\beta = r_B \exp(-i\phi_B)$ . The equations of motion for the amplitudes  $r_{A,B}$  are

$$\dot{r}_A = (\kappa_1/2 - V/2 - \kappa_2 r_A^2) r_A + V r_B \cos(\phi)/2 \tag{2.18a}$$

$$\dot{r}_B = (\kappa_1/2 - V/2 - \kappa_2 r_B^2) r_B + V r_A \cos(\phi)/2, \qquad (2.18b)$$

and the equations for the phases are

$$\dot{\phi}_A = +\frac{\delta}{2} + \frac{V}{2} \frac{r_B}{r_A} \sin(\phi_B - \phi_A),$$
(2.19a)

$$\dot{\phi}_B = -\frac{\delta}{2} + \frac{V}{2} \frac{r_A}{r_B} \sin(\phi_A - \phi_B).$$
 (2.19b)

While the global phase  $\phi_A + \phi_B$  is irrelevant here, the phase difference  $\phi_{AB} = \phi_A - \phi_B$  plays a central role; its time evolution is

$$\dot{\phi}_{AB} = \delta - \frac{V}{2} \left( \frac{r_A}{r_B} + \frac{r_B}{r_A} \right) \sin(\phi_{AB}). \tag{2.20}$$

In the context of synchronization, the rates  $\kappa_1$  and  $\kappa_2$ , which stabilize the limit cycle, are considered large compared to the coupling strength V. In this case, Eqs. (2.18) are approximately fulfilled by the steady state  $\dot{r}_{A,B} = 0$  where  $r_{A,B} = r_0 = \sqrt{\kappa_1/2\kappa_2}$ . Equation (2.20) consequently becomes

$$\dot{\phi}_{AB} = \delta - V \sin(\phi_{AB}). \tag{2.21}$$

This equation is called the Adler equation [Adler, 1946; Pikovsky et al., 2001]. The Adler equation captures the essential dynamics of two coupled limit-cycle oscillators. It describes a competition between the detuning, which causes the phase difference to grow, and the coupling, which brings the phase difference closer to zero.

When the detuning is smaller than the coupling,  $|\delta| < V$ , the Adler equation exhibits a stable fixed point

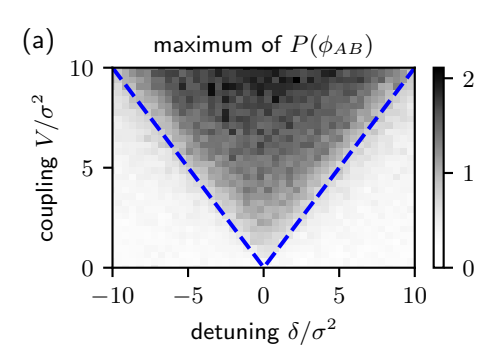
$$\phi_{AB}^{f} = \arcsin(\delta/V). \tag{2.22}$$

In this case, the two oscillators *synchronize*: They oscillate at the same frequency and their phase difference is locked to a constant value. The region in which synchronization occurs is called the Arnold tongue; the boundary between the synchronized and unsynchronized regimes,  $|\delta| = V$ , is shown in Fig. 2.4(a) by the blue dashed line.

When the detuning is larger than the coupling strength,  $|\delta| > V$ , the solution to the Adler equation is time dependent; the phase difference  $\phi_{AB}$  continuously increases or decreases. This corresponds to an unsynchronized state. The time period T during which  $\phi_{AB}$  increases by  $2\pi$  is

$$T = \int_0^{2\pi} d\phi_{AB} \frac{dt}{d\phi_{AB}} = \int_0^{2\pi} d\phi_{AB} \frac{1}{\delta - V \sin(\phi_{AB})} = \frac{2\pi}{\sqrt{\delta^2 - V^2}}, \quad \text{if } |\delta| > V. \quad (2.23)$$

The average observed frequency difference is thus  $2\pi/T = \sqrt{\delta^2 - V^2}$ . It is shown in Fig. 2.5(a) by the black line. For large values of the detuning  $|\delta| \gg V$ , the coupling has close to no influence; thus, the observed frequency difference approximately equals the bare frequency difference  $\delta$  shown by the gray dashed line. When the detuning decreases and approaches the coupling strength  $|\delta| \to V$ , the frequency difference decreases compared to the bare detuning, i.e., the frequencies of the two limit-cycle oscillators are pulled towards



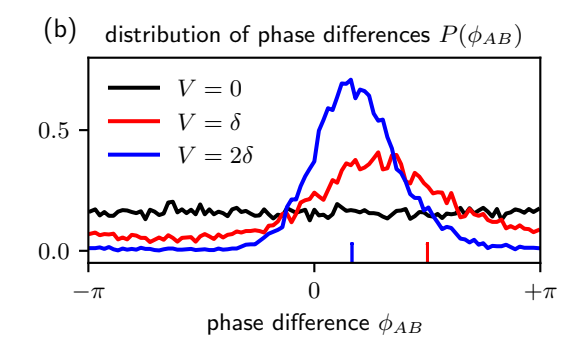


Figure 2.4: Phase locking of classical vdP oscillators. (a) Arnold tongue. The blue dashed line indicates the synchronization transition  $V=|\delta|$ . The grayscale shows the maximum of  $P(\phi_{AB})$ , a measure for synchronization in the presence of noise. (b) Distribution  $P(\phi_{AB})$  of the phase difference in the long-time limit in the presence of noise and detuning,  $\delta=\sigma^2$ . The blue and red ticks indicate the value of the phase  $\phi_{AB}^{\rm f}=\arcsin\delta/V$  in the absence of noise.

their average natural frequency. When the detuning is sufficiently small compared to the coupling,  $|\delta| < V$ , the two oscillators exactly entrain their frequencies as indicated by the plateau at zero frequency difference.

#### 2.2.2 Influence of fluctuations

In Section 2.1.1, we saw that noise causes fluctuations in the phase of a limit-cycle oscillator. As we show in this section, two coupled oscillators subject to fluctuations can nevertheless exhibit features of synchronization. However, in the presence of noise, phase locking and frequency entrainment are approximate rather than exact.

In the presence of phase fluctuations, the equations for the phases, Eqs. (2.19), (setting again  $r_A = r_B = \text{const.}$ ) become

$$\dot{\phi}_A = +\frac{\delta}{2} + \frac{V}{2}\sin(\phi_B - \phi_A) + \frac{\sigma}{\sqrt{2}}\xi_A,$$
 (2.24a)

$$\dot{\phi}_B = -\frac{\delta}{2} + \frac{V}{2}\sin(\phi_A - \phi_B) + \frac{\sigma}{\sqrt{2}}\xi_B. \qquad (2.24b)$$

The two independent Gaussian white-noise processes  $\xi_A$  and  $\xi_B$  both have zero mean and variance  $\mathbb{E}[\xi_{A,B}(t)\xi_{A,B}(t')] = \delta(t-t')$ . We have absorbed the dependence of the noise strength on the amplitudes  $r_{A,B}$  [see Eq. (2.11)] in the parameter  $\sigma$ . Introducing the noise process  $\xi$  – once more with zero mean and variance  $\delta(t-t')$  – that originates from the difference of the phase fluctuations of both oscillators, the Adler equation becomes

$$\dot{\phi}_{AB} = \delta - V \sin(\phi_{AB}) + \sigma \xi. \tag{2.25}$$

In the absence of noise, we identified a sharp transition between the unsynchronized and the synchronized states. Here, the fluctuations prevent exact phase locking. Nevertheless, we can quantify the amount of phase locking using the distribution  $P(\phi_{AB})$  of the phase difference in the long-time limit. Numerically, this distribution can be obtained by integrating the Adler equation in the presence of noise for various initial conditions and counting how often  $\phi_{AB}$  assumes a certain value in the long-time limit. The results are shown in Fig. 2.4(b) for different values of the coupling. When the coupling is absent, the

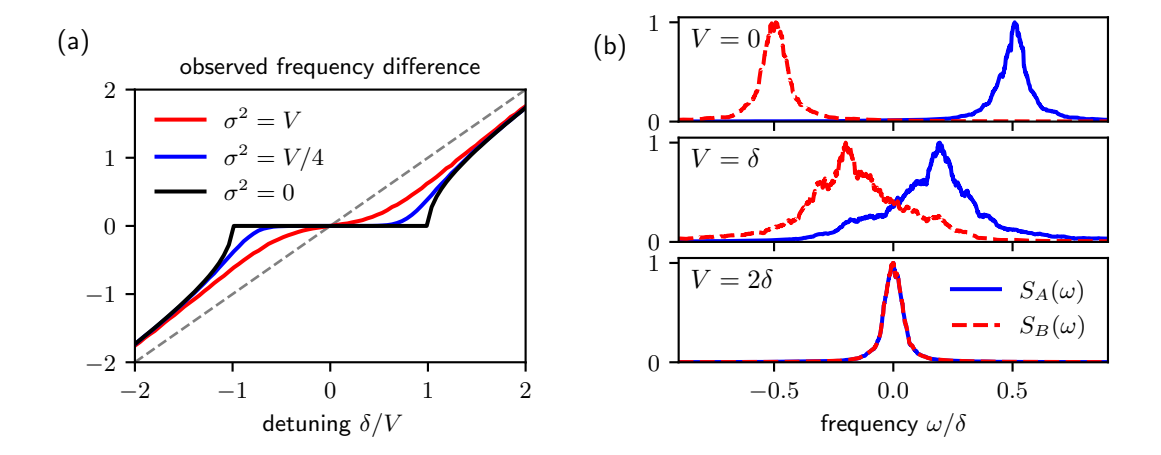


Figure 2.5: Frequency entrainment of classical vdP oscillators. (a) Observed frequency difference as a function of detuning. The dashed line shows the identity line for reference. The black line shows the noiseless case ( $\sqrt{\delta^2/V^2-1}$  as calculated in Eq. (2.23)). The blue and red lines show the observed frequency for two different noise strengths. Although difficult to see, the observed frequency is not exactly zero for any  $\sigma^2 > 0$  and  $|\delta| > 0$ . (b) Spectra of the two phase oscillators for  $\sigma^2 = \delta/5$ , as defined in Eq. (2.28). Each spectrum is averaged in bins of width  $\omega/\delta = 0.05$ .

phase distribution is flat, showing that all phase differences are equally likely. A nonzero coupling induces a phase preference indicated by a peak in the phase distribution. The phase is more likely to take values close to  $\phi_{AB}^{\rm f} = \arcsin(\delta/V)$ , the stable fixed point obtained in the noise-free analysis; see Eq. (2.22).

Figure 2.4(a) shows the maximum value of  $P(\phi_{AB})$  as a function of detuning and coupling strength. The maximum grows with increasing coupling and decreasing detuning, and displays a crossover at the synchronization transition  $V = |\delta|$  obtained in the noiseless case (blue dashed line). In conclusion, the phase distribution  $P(\phi_{AB})$  and its maximum value provide a quantitative measure of the amount of phase locking of two coupled oscillators.

For an intuitive understanding of synchronization in the presence of noise, we rewrite the dynamics as the overdamped motion of a particle in a potential following Pikovsky et al. [2001, Section 9.2]. Generally, the motion of a particle with position x and mass m subject to damping at rate  $\gamma$  in a potential U(x) is  $m\ddot{x} + \gamma \dot{x} = -\partial_x U(x)$ . In the limit of small mass or large damping,  $m\ddot{x} \ll \gamma \dot{x}$ , the inertial term can be neglected, which corresponds to the overdamped limit; see also Strogatz [2019, Sections 2.6 and 2.7]. In that case, the velocity of the particle is completely determined by the slope of the potential.

Here, the position of the particle corresponds to the phase difference  $\phi_{AB}$ . We recast the Adler equation (2.25) in the form

$$\dot{\phi}_{AB} = -\frac{\partial}{\partial \phi_{AB}} U(\phi_{AB}) + \sigma \xi \,, \quad U(\phi_{AB}) = -\phi_{AB} \delta - V \cos(\phi_{AB}) \,. \tag{2.26}$$

There are two qualitatively different cases for the shape of the potential  $U(\phi_{AB})$ ; they are depicted in Fig. 2.6. When the detuning is larger than the coupling,  $|\delta| > V$ , there are no local minima in the potential; see Fig. 2.6(a). The particle continually descends the slope, which translates to a continuously increasing phase difference (or decreasing if  $\delta < 0$ ). In contrast, when the coupling is larger than the detuning,  $V > |\delta|$ , the potential exhibits local minima; see Fig. 2.6(b). Without noise, the particle approaches a local minimum

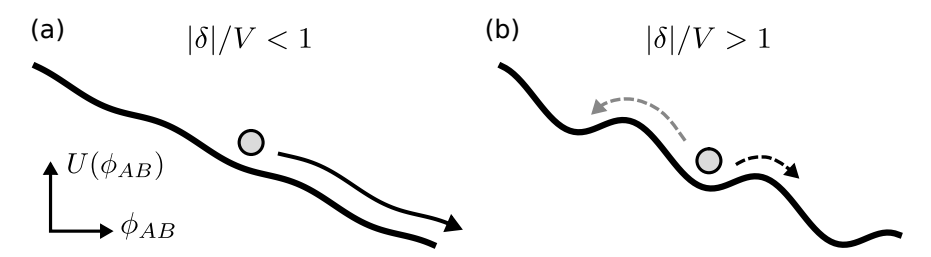


Figure 2.6: Dynamics of the Adler equation visualized by the potential  $U(\phi_{AB})$ . The phase  $\phi_{AB}$  is depicted as a gray circle in the potential landscape  $U(\phi_{AB})$ . (a) Unsynchronized case; the phase continuously falls down the slope. (b) Synchronized case; the phase is trapped in a local minimum. Phase fluctuations (dashed arrows) can cause the particle to move to a neighboring minimum. The process indicated by the black dashed arrow is more likely than the one indicated by the gray dashed arrow.

and remains there, corresponding to the synchronized state where the phase difference is locked and the frequency difference is zero. The noise at strength  $\sigma$ , however, disturbs the phase-locked state since fluctuations can cause the particle to slip to a neighboring local minimum. The phase slip occurs more likely in the direction of the slope, and thus the average frequency is nonzero for any nonzero  $\delta$ . This becomes evident in Fig. 2.5(a), which shows that exact frequency locking only occurs in the noiseless case. Nevertheless, we observe frequency pulling in the regime of small  $\delta$ , indicating approximate frequency entrainment.

To further analyze the approximate frequency entrainment in the presence of noise, we consider the spectrum of the oscillators. The spectrum allows us to analyze the properties of the trajectories in the frequency domain. We introduced it at the end of Section 2.1.1 for a single oscillator, see Eqs. (2.14) to (2.16). The steady-state two-time correlations are

$$g_a(\tau) = \lim_{t \to \infty} \mathbb{E}[\exp[i\phi_a(t+\tau) - i\phi_a(t)]], \qquad (2.27)$$

where  $a \in \{A, B\}$ . The spectra, which depend on frequency  $\omega$ , are obtained via Fourier transformation,

$$S_a(\omega) = \int_{-\infty}^{\infty} d\tau e^{-i\omega\tau} g_a(\tau). \qquad (2.28)$$

We numerically calculate the spectra by averaging over multiple trajectories obtained from integrating Eqs. (2.24). The spectra are shown in Fig. 2.5(b) for different values of the coupling strength. They are characterized by a peak whose position indicates the typical frequency and whose width originates from the phase diffusion. For zero coupling, the spectra both peak at the natural frequencies  $\pm \delta/2$ . With increasing coupling, they peak at frequencies closer to zero until they nearly overlap. This behavior is consistent with the average frequency difference shown in Fig. 2.5(a).

The frequency spectra and the phase distribution  $P(\phi_{AB})$  allow for quantifying frequency entrainment and phase locking even though noise prohibits exact synchronization. In Chapter 4, when discussing synchronization of quantum oscillators, we will encounter analogous measures of quantum synchronization.

2.3. Kuramoto model 15

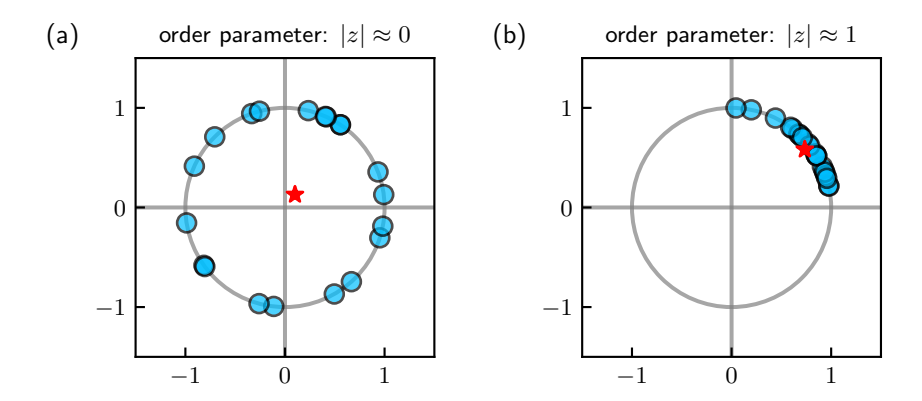


Figure 2.7: Order parameter of the Kuramoto model. Each oscillator is depicted as a blue disk on the unit circle. The position on the circle represents the phase  $\phi_i$ . The order parameter z is shown in the complex plane by the red star. (a) The phases take different values, corresponding to an unsynchronized state, and z is close to zero. (b) The phases take similar values, indicating a synchronized state, and |z| is close to one.

#### 2.3 Kuramoto model

Next, we extend the analysis to a large ensemble of coupled limit-cycle oscillators. As before, the oscillators' amplitudes are assumed constant. The phase dynamics are described by the Kuramoto model [Kuramoto, 1975]

$$\dot{\phi}_i = \omega_i + \frac{V}{N} \sum_{j=1}^N \sin(\phi_j - \phi_i) + \sigma \xi_i$$
(2.29)

for N oscillators with phases  $\phi_i$  and natural frequencies  $\omega_i$ . Each oscillator is subject to an independent noise process  $\xi_i$  (with zero mean and variance  $\delta(t-t')$  as before). All pairs of oscillators are coupled in the same way as discussed in the previous section. We have normalized the coupling strength V by 1/N to allow for a well-defined thermodynamic limit  $N \to \infty$ , where each oscillator is influenced by an infinite number of other oscillators; the coupling to each one, however, is infinitesimally small. For N = 2, the model is equivalent to the one of two coupled oscillators presented in Eqs. (2.24).

An important property of the Kuramoto model is that the set of equations (2.29) is invariant under a translation of all phases by a constant value  $\phi_i \to \phi_i + \phi_0$ . This corresponds to a U(1) symmetry. Physically, it means that no phase is preferred. As we will later see, the synchronized state spontaneously breaks the U(1) symmetry.

To quantify the degree of synchronization among all oscillators, we introduce the order parameter

$$z = \frac{1}{N} \sum_{j=1}^{N} \exp(i\phi_j) \equiv |z| \exp(i\psi). \qquad (2.30)$$

It is schematically depicted in Fig. 2.7. When the phases of the oscillators take different values, the order parameter takes a value close to zero. When the oscillators have similar phases, the order parameter takes a nonzero value with phase  $\psi$ . The order parameter allows us to rewrite Eq. (2.29) as

$$\dot{\phi}_i = \omega_i + V|z|\sin(\psi - \phi_i) + \sigma\xi_i. \tag{2.31}$$

This form makes it explicit that each oscillator is attracted to the phase  $\psi$  with an effective coupling strength V|z|.

In the limit  $N \to \infty$ , the continuum limit is helpful; therefore, we introduce the distribution  $f(\phi, \omega)$  of oscillators with phase  $\phi$  and natural frequency  $\omega$  at time t. In the continuum limit, the order parameter takes the form

$$z = \int_0^{2\pi} d\phi \int_{-\infty}^{\infty} d\omega e^{i\phi} f(\phi, \omega), \qquad (2.32)$$

and the Kuramoto model can be written as the Fokker-Planck equation [Strogatz, 2019]

$$\frac{\partial f(\phi,\omega)}{\partial t} = -\frac{\partial}{\partial \phi} \left[ (\omega + V|z|\sin(\psi - \phi))f(\phi,\omega) \right] + \frac{\sigma^2}{2} \frac{\partial^2 f(\phi,\omega)}{\partial \phi^2} \,. \tag{2.33}$$

#### 2.3.1 Frequency disorder

We first focus on the effect of frequency disorder and set the noise strength  $\sigma = 0$ . For simplicity, we consider the natural frequencies  $\omega_i$  to be sampled from a Lorentz distribution

$$g(\omega_i) = \frac{G}{\pi(\omega_i^2 + G^2)} \tag{2.34}$$

with width G. Without loss of generality, the average frequency is set to zero.

For small coupling strengths, the disorder in frequencies results in a uniform distribution of phases with vanishing order parameter, z=0. When increasing the coupling strength, we expect a transition to a synchronized state in which the oscillators assume similar phases and the order parameter is nonzero, |z| > 0.

In the limit  $N \to \infty$ , the transition point can be found by presuming that there is a solution with constant z (in the case of nonzero average frequency, we would assume a solution rotating with this frequency) [Strogatz, 2019]. If there is a constant solution, then we conclude from Eq. (2.31) and our analysis of the Adler equation that the oscillators with frequencies  $|\omega_i| < |z|V$  are phase locked. The phase of each locked oscillator with respect to the average phase  $\psi$  is determined by its natural frequency:  $\phi_i - \psi = \arcsin \frac{\omega_i}{V|z|}$ ; see Eq. (2.22). The density of locked oscillators is thus

$$f(\phi, \omega) = \delta \left( \phi - \psi - \arcsin \frac{\omega}{V|z|} \right) g(\omega).$$
 (2.35)

Inserting this density into (2.32) and evaluating the frequency integral, we find

$$z = Vz \int_{-\pi/2}^{\pi/2} d\phi \, e^{i\phi} \cos(\phi) g\left(V|z|\sin\phi\right) \,. \tag{2.36}$$

Here, we employed the fact that the unlocked oscillators do not contribute to the order parameter; the reason is that for any unlocked oscillator with frequency  $\omega_i$  and phase  $\phi_i$  there is an oscillator with frequency  $-\omega_i$  and phase  $\phi_i + \pi$ , and their combined contribution to the order parameter vanishes. For our presumed solution to be correct, the integral equation (2.36) must be fulfilled self-consistently. One solution is the unsynchronized state z = 0. For the case of a Lorentz distribution, a second solution to the self-consistency equation (2.36) can be obtained for V > 2G. It corresponds to a partially synchronized solution with

$$|z| = \sqrt{1 - \frac{2G}{V}} \,. \tag{2.37}$$

2.3. Kuramoto model 17

In this state, the oscillators have self-organized, forming a state of collective coherence indicated by the nonzero value of the order parameter.

Regarding the phase  $\psi$  of the order parameter, any value of  $\psi$  satisfies the self-consistency equation. While the Kuramoto model is phase symmetric, the synchronized solutions in the limit  $N \to \infty$  are not phase symmetric; in each solution, the order parameter assumes a particular phase  $\psi$  that depends on the initial condition. This is an instance of spontaneous symmetry breaking: Each solution spontaneously breaks the U(1) symmetry.

While the approach outlined above gives exact solutions for the synchronization threshold and the value of the order parameter, it does not inform about the stability of the unsynchronized and the partially synchronized solutions. In the following, we derive an equation of motion for the order parameter z employing the Ott-Antonsen Ansatz following  $Ott\ and\ Antonsen\ [2008]$  and  $Strogatz\ [2019]$ . This approach not only reproduces the solution of Eq. (2.37) but also guarantees its stability. In the absence of noise,  $\sigma=0$ , the Fokker-Planck equation (2.33) becomes the continuity equation

$$\frac{\partial f(\phi, \omega)}{\partial t} = -\frac{\partial}{\partial \phi} \left[ \left( \omega + V|z| \sin(\psi - \phi) f(\phi, \omega) \right) \right]. \tag{2.38}$$

To solve it, we introduce a Fourier decomposition of  $f(\phi, \omega)$  (after factoring out  $g(\omega)$ )

$$f(\phi,\omega) = \frac{g(\omega)}{2\pi} \sum_{n} f_n(\omega) e^{in\phi} = \frac{g(\omega)}{2\pi} \left[ 1 + \sum_{n=1}^{\infty} \left( f_n(\omega) e^{in\phi} + \text{c.c.} \right) \right], \qquad (2.39)$$

where c.c. abbreviates complex conjugation. Note that  $f_0(\omega) = 1$  since  $f(\phi, \omega)$  is normalized to one and  $f_n(\omega) = f_{-n}^*(\omega)$  since  $f(\phi, \omega)$  is real valued. Inserting the Fourier decomposition into Eq. (2.38), we can collect the terms proportional to  $\exp(in\phi)$  for each n to find

$$\frac{\partial}{\partial t} f_n(\omega) = n \left[ \frac{V}{2} (z^* f_{n-1}(\omega) - z f_{n+1}(\omega)) - i \omega f_n(\omega) \right]. \tag{2.40}$$

At first, it may seem that no progress was made; instead of describing infinitely many coupled phases, we now describe infinitely many coupled Fourier modes. Remarkably, however, the equations can be solved by the Ansatz  $f_n(\omega) = (\zeta(\omega))^n$ , if

$$\frac{\partial \zeta(\omega)}{\partial t} = \frac{V}{2} (z^* - z\zeta(\omega)^2) - i\omega\zeta(\omega). \tag{2.41}$$

While this is still an infinite-dimensional set of equations, we can make further progress when the frequencies follow a Lorentzian distribution. In this case, the integral expression for the order parameter, Eq. (2.32), can be evaluated via a contour integration. This yields  $z = \zeta^*(-iG)$ , which connects the  $f_n(\omega)$  evaluated at  $\omega = -iG$  to the order parameter z:

$$f_n^*(-iG) = z^n$$
 (2.42)

Finally, inserting  $z = \zeta^*(-iG)$  into Eq. (2.41) evaluated at  $\omega = -iG$  and n = 1, we find a dynamical equation for the order parameter

$$\dot{z} = \left(\frac{V}{2} - G\right)z - \frac{V}{2}|z|^2z. \tag{2.43}$$

We recognize the same equation that describes a van-der-Pol oscillator, see Eq. (2.3) with effective gain  $\kappa_1 = V - 2G$  and nonlinear loss rate  $\kappa_2 = V/2$ . For negative effective gain,

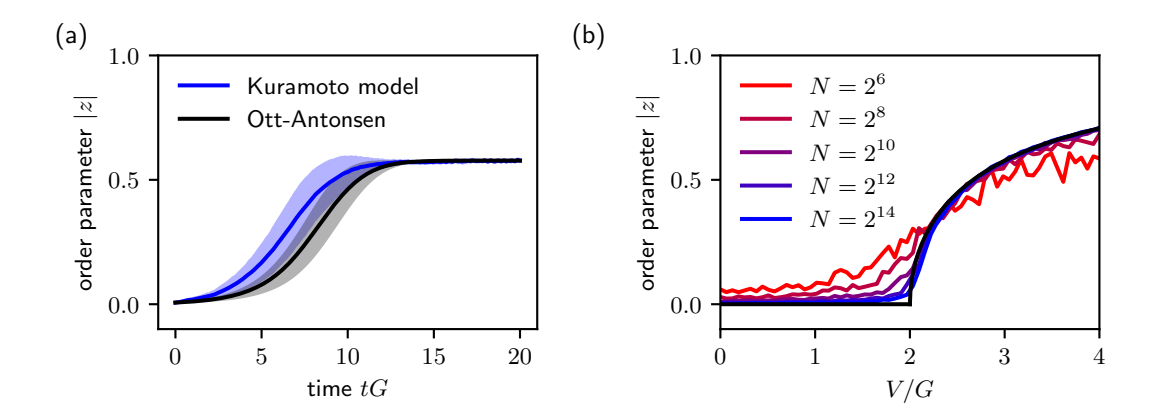


Figure 2.8: Order parameter in the Kuramoto model (noise free but frequency disordered). (a) Time evolution of the order parameter |z| for V=3G. Black is obtained from integration of Eq. (2.29) with  $\xi_i=0$  and  $N=2^{14}$ . Blue shows the Ott-Antonsen result of Eq. (2.43). In both cases, the line (shaded area) shows the mean (standard deviation) of 16 realizations. (b) Order parameter in the long-time limit. Red to blue lines show the results from the numerical integration of the Kuramoto model for increasing  $N=\{2^6,2^8,2^{10},2^{12},2^{14}\}$ . The analytical result expected for  $N\to\infty$  is shown by the black line.

i.e., when the coupling does not overcome the frequency disorder, V < 2G, the incoherent solution z = 0 is a stable fixed point. When the gain is positive,

$$V > 2G, (2.44)$$

there is a stable fixed point with  $|z| = \sqrt{1 - 2G/V}$ , consistent with Eq. (2.37). Having obtained a dynamical equation for the time evolution of the order parameter implies the stability of the unsynchronized and partially synchronized solutions. Here, the frequency is zero, since we have set the average value of the natural frequencies to zero; see Eq. (2.34). When the frequency distribution  $g(\omega)$  has a mean  $\overline{\omega} = \int d\omega g(\omega)$  different from zero, one would obtain an additional term  $+i\overline{\omega}z$  on the right side of Eq. (2.43).

The analytical result obtained by the Ott-Antonsen ansatz, Eq. (2.43), is compared with numerical simulations of the Kuramoto model for large numbers N in Fig. 2.8. Panel Fig. 2.8(a) displays the time evolution of the order parameter. The analytical result and the numerical solution converge onto the same value in the long-time limit, but do not exactly agree at all times. The reason for the discrepancy is that we have restricted the dynamics on the Ott-Antonsen manifold when making the Ansatz  $f_n(\omega) = (\zeta(\omega))^n$ . The initial conditions for the numerical simulation of Fig. 2.8(a), which are random phases, however, do not necessarily belong to this manifold. Nevertheless, the Ott-Antonsen manifold is shown to be attracting in certain cases [Ott and Antonsen, 2009; Pikovsky and Rosenblum, 2011, 2015]; consistently, the numerical simulations converge onto the same value as the analytical solution after a transient time. Figure 2.8(b) displays the order parameter as a function of the coupling strength. For an increasing number of oscillators, the results from the numerical simulation of the Kuramoto model converge to the analytical result of Eq. (2.37).

2.3. Kuramoto model 19

#### 2.3.2 Influence of fluctuations

Let us now consider the effect of fluctuations on the Kuramoto model, Eq. (2.29). First, we assume identical oscillators setting  $\omega_i = 0$ . We will identify a synchronization transition in the Kuramoto model despite the presence of fluctuations closely following Pikovsky et al. [2001, Section 12.2]. As in the previous section, we analyze the system in the limit of infinitely many oscillators and introduce the density  $f(\phi)$  of oscillators with phase  $\phi$  at time t. Here, the density does not depend on the frequency  $\omega$  since all oscillators are identical. The Fokker-Planck equation (2.33) now reads

$$\frac{\partial f(\phi)}{\partial t} = -\frac{\partial}{\partial \phi} \left[ V|z| \sin(\psi - \phi) f(\phi) \right] + \frac{\sigma^2}{2} \frac{\partial^2 f(\phi)}{\partial \phi^2}. \tag{2.45}$$

We expand  $f(\phi)$  in a Fourier series,  $f(\phi) = \frac{1}{2\pi} \sum_n f_n \exp(in\phi)$ , where  $f_1 = z^*$  and  $f_0 = 1$ . We obtain an equation similar to Eq. (2.40) with an additional diffusion term proportional to  $\sigma^2$ ,

$$\dot{f}_n = \frac{nV}{2} (f_{n-1}z^* - f_{n+1}z) - \frac{n^2\sigma^2}{2} f_n.$$
 (2.46)

The Ott-Antonsen Ansatz, which was used to solve Eq. (2.40), does not help here because of the diffusion term. To make further progress, let us instead consider Eq. (2.46) for n = 1, 2, and 3,

$$\dot{z} = \frac{V}{2}(z - f_2^* z^*) - \frac{\sigma^2}{2} z, \tag{2.47}$$

$$\dot{f}_2 = V[(z^*)^2 - f_3 z] - 2\sigma^2 f_2,$$
 (2.48)

$$\dot{f}_3 = \frac{3V}{2}(f_2 z^* - f_4 z) - \frac{9\sigma^2}{2} f_3. \tag{2.49}$$

First, we note that the incoherent state  $z = f_n = 0$  for  $n \ge 2$  is a fixed point. A stability analysis reveals that this solution is stable for small coupling strengths and unstable for

$$V > \sigma^2. \tag{2.50}$$

In this case, the incoherent state is unstable due to the attraction of the phases. The coupling results in a synchronized state with a finite order parameter |z| > 0.

The value of the order parameter can be approximately obtained near the threshold  $V \approx \sigma^2$ , as we now show. The linear terms in Eqs. (2.47) to (2.49) indicate that the modes  $f_n$  for  $n \geq 2$  decay faster  $(\sim \sigma^2)$  compared to the rate of change of  $z (\sim V - \sigma^2)$ . We therefore eliminate their time evolution setting  $\dot{f}_2 \approx 0$  and  $\dot{f}_3 \approx 0$ . From Eqs. (2.48) and (2.49), we then find that  $f_2$  is of order  $z^2$  and  $f_3$  is of order  $z^3$ . Near the threshold, |z| is expected to be small; so we use the further approximation  $f_3 \approx 0$  to find from Eq. (2.48):  $f_2 = V(z^*)^2/(2\sigma^2)$ . This expression is inserted in Eq. (2.47) resulting in

$$\dot{z} = \left(\frac{V}{2} - \frac{\sigma^2}{2}\right) z - \frac{V^2}{4\sigma^2} |z|^2 z.$$
 (2.51)

This equation is similar to Eq. (2.43). Instead of the frequency disorder parametrized by G, here, the noise at strength  $\sigma^2$  determines the damping rate of the order parameter. From Eq. (2.51), we see that the synchronization condition is  $V > \sigma^2$ , consistent with Eq. (2.50). We can now additionally calculate the steady-state solution of the order parameter

$$|z| = \sqrt{2\sigma^2 (V - \sigma^2)/V^2}$$
. (2.52)

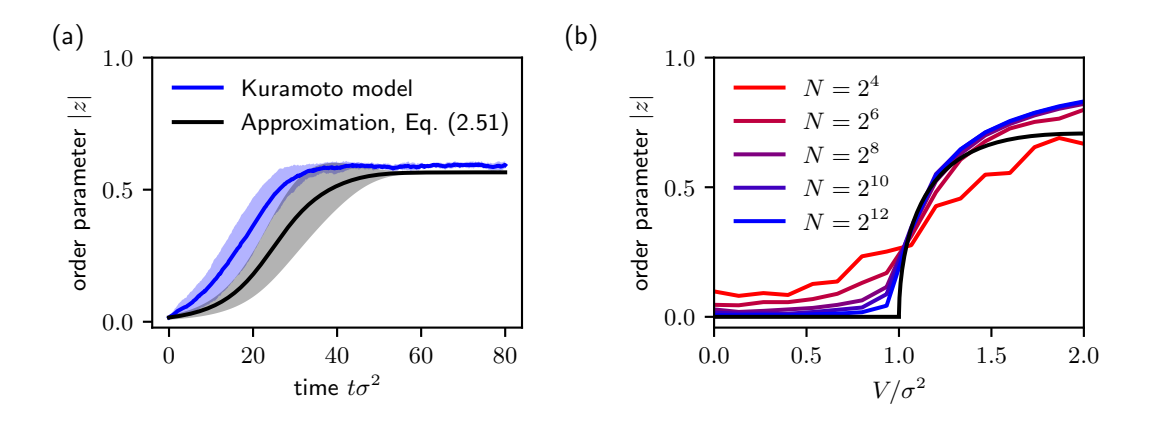


Figure 2.9: Order parameter in the Kuramoto model (disorder free but noisy). (a) Time evolution of the order parameter |z| for V=2.5 and  $N=2^{12}$ . Black shows the result of Eq. (2.51). Blue is obtained from integration of the Kuramoto model, Eq. (2.29), with  $\omega_i=0$ . In both cases, the line (shaded area) shows the mean (standard deviation) of 16 realizations. (b) Order parameter in the long-time limit. Red to blue lines show the result from the numerical integration of the Kuramoto model for increasing  $N=\{2^4,2^6,2^8,2^{10},2^{12}\}$ . The black line is the approximate result of Eq. (2.52).

The time evolution of Eq. (2.51) is compared to a direct simulation of the Kuramoto model of Eq. (2.29) in Fig. 2.9(a). While the approximation of the time evolution does not perfectly agree with the numerical simulation, the steady-state solution shown by the black line in Fig. 2.9(b) agrees very well with the numerical solution for large N in the vicinity of the transition. For larger coupling strengths, the approximation  $f_3 \approx 0$  becomes worse, and as a result, the solutions deviate. Improved approximations have been described, for example, by Tyulkina et al. [2018].

Finally, we state the critical coupling when both frequency disorder (a Lorentzian distribution with width G) and phase noise (fluctuations with variance  $\sigma^2$ ) are present. A stability analysis reveals that the incoherent state becomes unstable when [Strogatz and Mirollo, 1991]

$$V > \sigma^2 + 2G. \tag{2.53}$$

This result may be expected when combining Eqs. (2.44) and (2.50). It implies that the coupling needs to overcome both the disorder due to fluctuations and the frequency disorder.

In Chapters 4 to 5, we will describe models of coupled quantum oscillators that can be described by equations of motion for an order parameter similar to Eq. (2.51). As we will show, these models also feature a transition to a synchronized state similar to the Kuramoto model.

## 2.4 Nonreciprocal interactions

All the interactions among phases discussed so far are reciprocal: The phases of two coupled oscillators symmetrically tend to approach each other. The concept of reciprocal interactions is very general and dates back to *Newton* [1687] who stated that any action necessitates a symmetric reaction. For example, two equally charged particles symmetrically repel each other, and massive objects symmetrically attract each other. Reciprocal interactions generally occur in equilibrium systems where dynamics are governed by a

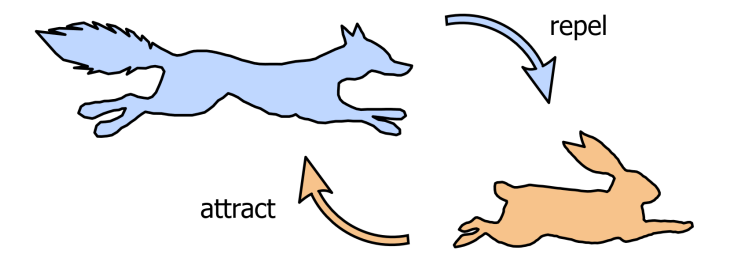


Figure 2.10: Sketch of nonreciprocal interactions.

potential landscape [*Ivlev* et al., 2015; *Fruchart* et al., 2021]. In nonequilibrium systems that are provided with energy from an environment, interactions can also be nonreciprocal, i.e., asymmetric.

A specific nonequilibrium system that can feature nonreciprocal interactions is *active* matter, which has attracted much interest in recent years [te Vrugt and Wittkowski, 2025]. An active system is composed of active agents. Each active agent has access to a source of energy that it can use to propel itself and exert forces on other agents. These forces do not necessarily conserve momentum and can be nonreciprocal.

Nonreciprocal interactions can be exemplified by a predator-prey model; see Fig. 2.10. Living animals can be considered active agents that convert food into motion and that exert influences on other animals. While prey attracts predators, predators clearly do not attract prey; instead, predators repel prey. These antagonistic interactions result in the onset of chase-and-run-away dynamics. One key result of this thesis is to show that such dynamics can occur among active quantum agents, which will be explained in Chapter 6.

Limit-cycle oscillators can feature nonreciprocal interactions as we now show. The state of two coupled limit-cycle oscillators is well described by their phases  $\phi_A$  and  $\phi_B$ . The equations of motion (in the absence of detuning and in the frame rotating at their common frequency) are

$$\frac{\mathrm{d}}{\mathrm{d}t}\phi_A = V\sin(\phi_B - \phi_A)/2,$$

$$\frac{\mathrm{d}}{\mathrm{d}t}\phi_B = V\sin(\phi_A - \phi_B)/2.$$
(2.54)

These equations describe attractive or repulsive phase interactions: When V > 0, phases  $\phi_A$  and  $\phi_B$  are mutually attracted to each other; when V < 0, both phases mutually repel each other. The interactions are *reciprocal*, and as such, they can be derived from a potential

$$U(\phi_A, \phi_B) = -\frac{V}{2}\cos(\phi_A - \phi_B)$$
 (2.55)

via  $\dot{\phi}_i = -\partial U/\partial \phi_i$ .

Consider now the modified equations

$$\frac{\mathrm{d}}{\mathrm{d}t}\phi_A = V_{BA}\sin(\phi_B - \phi_A)/2,$$

$$\frac{\mathrm{d}}{\mathrm{d}t}\phi_B = V_{AB}\sin(\phi_A - \phi_B)/2,$$
(2.56)

where the directional coupling strengths  $V_{BA}$  and  $V_{AB}$  determine how  $\phi_B$  influences  $\phi_A$  and how  $\phi_A$  influences  $\phi_B$ , respectively. When  $V_{BA} \neq V_{AB}$ , we refer to the interactions as nonreciprocal (or asymmetric). It is impossible to construct a potential that generates nonreciprocal interactions, like we did for reciprocal interactions in Eq. (2.55).

The most interesting case occurs when  $V_{BA}$  and  $V_{AB}$  have opposite sign, i.e.,  $\operatorname{sign}(V_{BA}) = -\operatorname{sign}(V_{AB})$ . We call these interactions antagonistic (adapting the terminology from, e.g., You et al. [2020] or Brauns and Marchetti [2024]). In this case, the two phases have opposite influences on each other. For example, when  $V_{AB} > 0$  and  $V_{BA} < 0$ ,  $\phi_A$  attracts  $\phi_B$ , while  $\phi_B$  repels  $\phi_A$ .

To solve Eqs. (2.56), let us rewrite them as the sum  $\bar{\phi}_{AB} = \phi_A + \phi_B$  and difference  $\phi_{AB} = \phi_A - \phi_B$  of the phases,

$$\frac{\mathrm{d}}{\mathrm{d}t}\bar{\phi}_{AB} = \frac{V_{AB} - V_{BA}}{2}\sin(\phi),$$

$$\frac{\mathrm{d}}{\mathrm{d}t}\phi_{AB} = -\frac{V_{AB} + V_{BA}}{2}\sin(\phi)$$
(2.57)

When  $V_{AB} + V_{BA} > 0$  (< 0), the phase difference will approach zero ( $\pi$ ) in the long-time limit, and the average phase approaches a constant value. The dynamics become more interesting when adding noise or disorder to the system, which perturbs the equilibrium synchronized state. This can result in a dynamical state, where the phases continuously change over time. Furthermore, the dynamical state can be stabilized against the effects of fluctuations through many-body interactions, resulting in a novel class of nonreciprocal phase transitions [Fruchart et al., 2021]. This idea will be discussed in a system of synchronizing quantum spins in Chapter 6.

#### 2.5 Conclusions

In this chapter, we reviewed important aspects of synchronization. We showed how a limit-cycle oscillator can be described in terms of its phase. Next, we analyzed the synchronization dynamics between two such oscillators. Building on this, we described synchronization in an ensemble of limit-cycle oscillators. This constitutes a self-organization transition, where pairwise phase alignment results in a phase-coherent collective state. Throughout, we emphasized the role of fluctuations that result in phase diffusion and prohibit exact synchronization. Finally, we introduced the basic ideas and notations of nonreciprocal interactions.

This chapter provides the necessary intuition to understand the dynamics of the quantum models that are presented in the following chapters. Several concepts of synchronization and nonreciprocity will be encountered again later. They include the idea of a limit cycle that relies on energy exchange with an environment; the role of phase fluctuations and phase diffusion; measures to quantify phase locking and frequency entrainment; synchronization transitions between two oscillators as well as in ensembles of many oscillators; and nonreciprocal phase interactions.

# Chapter 3

# Open quantum systems

As discussed in the previous chapter, limit-cycle oscillators rely on gain and loss of energy from and to an environment. When extending classical synchronization to quantum synchronization, we will analogously consider quantum systems that are in contact with an environment, allowing for an exchange of energy. The effect of the environment on the quantum system can be described within the framework of open quantum systems.

This chapter concisely reviews the key concepts and the notation of the theory of open quantum systems that are relevant for the remainder of this thesis; it is based on the textbooks *Breuer and Petruccione* [2002], *Wiseman and Milburn* [2010, Appendix A], and *Gardiner and Zoller* [2000]. We refer to these textbooks for a more detailed and comprehensive introduction to open quantum systems. We will introduce the density operator in Section 3.1 and its time evolution in Section 3.2. Furthermore, continuous measurements and cascaded interactions are presented in Sections 3.3 and 3.4.

## 3.1 Density operator

In quantum mechanics, a system is described by a state vector  $|\psi\rangle$ , which evolves under a Hamiltonian  $H_{\text{tot}}$  following Schrödinger's equation (throughout this work, we work with units where  $\hbar = 1$ )

$$\frac{\mathrm{d}}{\mathrm{d}t} |\psi\rangle = -iH_{\text{tot}} |\psi\rangle . \tag{3.1}$$

We now consider the case where the state vector  $|\psi\rangle$  naturally decomposes into a *system* and an *environment*. The total Hamiltonian can be written as

$$H_{\text{tot}} = H_{\text{s}} \otimes \mathbb{1}_{\text{e}} + \mathbb{1}_{\text{s}} \otimes H_{\text{e}} + H_{\text{se}}, \qquad (3.2)$$

where  $H_{\rm s}$  and  $H_{\rm e}$  are the system and environment Hamiltonians, which describe the coherent evolutions within system and environment, respectively. The interactions between system and environment are described by the Hamiltonian  $H_{\rm se}$ . The identity operators for system and environment are  $\mathbb{1}_{\rm s}$  and  $\mathbb{1}_{\rm e}$ .

Typically, the environment contains many more degrees of freedom than the system. For instance, the system may be a single qubit or oscillator, while the relevant environment is a measurement device or a vacuum chamber. When the quantum system is perfectly isolated from the environment,  $H_{\rm se}=0$ , the system evolves in a unitary way and is referred to as a *closed* quantum system.

Due to interactions between system and environment ( $H_{se} \neq 0$ ), however, the degrees of freedom of the system will in general become correlated with those of the environment. The total quantum state can be expressed as

$$|\psi\rangle = \sum_{i,j} c_{ij} |s_i\rangle \otimes |e_j\rangle ,$$
 (3.3)

where  $|s_i\rangle$  and  $|e_j\rangle$  span the basis of system and environment, respectively. The complex numbers  $c_{ij}$  are arbitrary but must fulfill the normalization condition  $\sum_{i,j} |c_{ij}|^2 = 1$ . We now consider the common case, where only observables of the system are relevant. This motivates the introduction of the *density operator* as follows. Using the trace operation  $\text{Tr}[\cdot] = \sum_{i,j} \langle s_i | \otimes \langle e_j | \cdot | s_i \rangle \otimes |e_j \rangle$ , the expectation value of any system operator  $O_s$  is

$$\langle \psi | O_{\mathbf{s}} | \psi \rangle = \text{Tr}[O_{\mathbf{s}} | \psi \rangle \langle \psi |] = \sum_{i,j} (\langle s_i | \otimes \langle e_j |) O_{\mathbf{s}} | \psi \rangle \langle \psi | (|s_i \rangle \otimes |e_j \rangle) . \tag{3.4}$$

We can split the trace into two parts, a trace over the system,  $\operatorname{Tr}_{s}[\cdot] = \sum_{i} \langle s_{i} | \cdot | s_{i} \rangle$ , and a trace over the environment,  $\operatorname{Tr}_{e}[\cdot] = \sum_{i} \langle e_{i} | \cdot | e_{i} \rangle$ , so that

$$\langle \psi | O_{\rm s} | \psi \rangle = \sum_{i} \langle s_{i} | O_{\rm s} \left( \sum_{j} \langle e_{j} | \psi \rangle \langle \psi | e_{j} \rangle \right) | s_{i} \rangle = \operatorname{Tr}_{\rm s} \left[ O_{\rm s} \operatorname{Tr}_{\rm e}[|\psi \rangle \langle \psi|] \right].$$
 (3.5)

The last expression motivates the definition of the density operator  $\rho \equiv \text{Tr}_{e}[|\psi\rangle\langle\psi|]$ , which allows us to calculate any expectation value of system operators through

$$\langle \psi | O_{\rm s} | \psi \rangle = \text{Tr}_{\rm s}[O_{\rm s}\rho],$$
 (3.6)

Consequently, system observables can be described using the density operator  $\rho$  of the system rather than the state vector  $|\psi\rangle$  for system and environment.

The density operator can be decomposed into a weighted sum of pure system states  $|s_i\rangle$ ,

$$\rho = \sum_{i} p_i |s_i\rangle\langle s_i| , \qquad (3.7)$$

where the sum of weights  $p_i$  is normalized,  $\sum_i p_i = 1$ . Whenever the density operator cannot be expressed as a single pure state, it describes a mixed state with purity  $\text{Tr}\left[\rho^2\right] < 1$ . Consider, for example, the simple case of a single system qubit (i.e., a two-level system with states  $|0\rangle$  and  $|1\rangle$ ) and a single environment qubit that are maximally entangled,  $|\psi\rangle = (|0_s\rangle \otimes |0_e\rangle + |1_s\rangle \otimes |1_e\rangle)/\sqrt{2}$ . After tracing out the environment qubit, the density operator of the system is  $\rho = (|0_s\rangle\langle 0_s| + |1_s\rangle\langle 1_s|)/2$ , which cannot be written as a pure state; it is a maximally mixed state with purity  $\text{Tr}\left[\rho^2\right] = 1/2$ .

From now on, and throughout this thesis, we drop the subscript 's' for system as all states and operators will refer to the system.

Let us now gain some more intuition about density operators and the associated mixed states. A mixed state represents a quantum state of incomplete knowledge. The system could be in any of multiple pure states, but it is not known which one. To illustrate this, consider an imperfect experiment that prepares the desired state, say, a qubit in the ground state  $|0\rangle$ , with probability  $p_0 < 1$ . There is, however, a probability  $p_1 = 1 - p_0$  that the qubit ends up in the excited state  $|1\rangle$ . Without any further information, the best one can do is to assert the state of the qubit after the preparation as the mixed state  $\rho = p_0 |0\rangle\langle 0| + p_1 |1\rangle\langle 1|$ .

Note that the decomposition of a density operator  $\rho$  into pure states is not unique. Consider a second experiment that prepares one of the two superposition states  $\sqrt{p_0} |0\rangle \pm \sqrt{p_1} |1\rangle$  with probability 1/2 each. The experiment produces the same mixed state as in the first experiment,  $\rho = p_0 |0\rangle\langle 0| + p_1 |1\rangle\langle 1|$ . Thus, the two distinct ensembles of pure states,  $\{|0\rangle, |1\rangle\}$  with probabilities  $\{p_0, p_1\}$  and  $\{\sqrt{p_0} |0\rangle \pm \sqrt{p_1} |1\rangle\}$  with probabilities  $\{1/2, 1/2\}$  yield the same density operator. Furthermore, the expectation value  $\langle O\rangle = \text{Tr}[O\rho]$  of any operator O is also independent of the underlying ensemble distribution. We will come back to ensembles of states in the context of measurements in Section 3.3.

## 3.2 Lindblad master equation

We have identified the density operator  $\rho$  as the key quantity of interest. It completely characterizes the state of the system and allows for the computation of all expectation values. Furthermore, the dynamics of the density operator completely describe the dynamics of the system. The time evolution of the density operator can be derived from Schrödinger's equation of system and environment, Eq. (3.1), using the Born approximation (weak system-environment coupling), the Markov approximation (memoryless environment), and a rotating-wave approximation (neglecting rapidly oscillating terms); the detailed derivation can be found in *Breuer and Petruccione* [2002] or *Manzano* [2020].

Within these approximations, the time evolution of the density operator is governed by the Lindblad master equation, or Gorini–Kossakowski–Sudarshan–Lindblad equation,

$$\frac{\mathrm{d}}{\mathrm{d}t}\rho = -i[H,\rho] + \sum_{i=1}^{N_J} \mathcal{D}[J_i]\rho \equiv \mathcal{L}\rho \,, \quad \mathcal{D}[J]\rho \equiv J\rho J^{\dagger} - \frac{1}{2} \left(J^{\dagger}J\rho + \rho J^{\dagger}J\right) \,. \tag{3.8}$$

with Hamiltonian H and  $N_J$  jump operators  $J_i$ . The interactions with the environment can change the coherent, i.e., Hamiltonian, evolution of the system, and thus H is generally not equal to  $H_s$  from Eq. (3.2). All the effects of the environment on the system are described by the jump operators  $J_i$  and the change in the Hamiltonian  $H - H_s$ . The jump operators describe dissipative dynamics and the Hamiltonian coherent dynamics. The Lindblad equation represents the most general equation for the time evolution of a density operator that preserves its properties (positive semi-definiteness and unit trace); see Breuer and Petruccione [2002] or Manzano [2020] for a proof. In Eq. (3.8), we also introduced the generator  $\mathcal{L}$  called the Liouvillian or Lindbladian, a shorthand notation for the right-hand side of the master equation.

To compute the equations of motions for any operator o and its expected value  $\langle o \rangle$ , the adjoint master equation is useful:

$$\frac{\mathrm{d}}{\mathrm{d}t}o = +i[H, o] + \sum_{i=1}^{N_J} \tilde{\mathcal{D}}[J_i]o, \quad \tilde{\mathcal{D}}[J]o \equiv J^{\dagger}oJ - \frac{1}{2}\left(J^{\dagger}Jo + oJ^{\dagger}J\right) 
= \frac{1}{2}\left([J^{\dagger}, o]J + J^{\dagger}[o, J]\right).$$
(3.9)

It describes the time evolution of the operator o in the Heisenberg picture.

The Lindblad master equation (3.8) (or its Heisenberg-picture equivalent Eq. (3.9)) has proven to be a versatile tool in numerous theoretical studies and accurately describes a variety of experiments relevant to this thesis; see for example *Karg* et al. [2020]; *Laskar* et al. [2020]; *Krithika* et al. [2022]; or *Behrle* et al. [2023]. We therefore adopt the Lindblad master equation as the starting point to describe the dynamics of the quantum systems studied in this thesis.

#### 3.3 Continuous measurements

In Section 3.1, we have established that open quantum systems are generally in a mixed state, i.e., a state of incomplete knowledge. More information about the system's state can be obtained through measurements. Different types of measurement yield different kinds and amounts of information [Wiseman and Milburn, 2010]. In this thesis, we are often interested in the dynamics of the system over an extended period of time. To measure the time evolution of the system for a single realization, continuous measurements are useful.

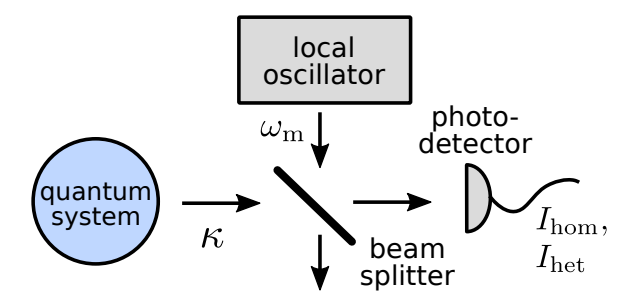


Figure 3.1: Sketch of the homodyne or heterodyne detection setup. The quantum system loses excitations at rate  $\kappa$ . Using a beam splitter, the signal from the quantum system is mixed with a local oscillator whose frequency is detuned from the signal by the frequency  $\omega_{\rm m}$ . A photodetector gives the homodyne or heterodyne current,  $I_{\rm hom}$  or  $I_{\rm het}$ .

In this section, we introduce continuous homodyne and heterodyne measurements following Wiseman and Milburn [2010, Chapter 4]. Homodyne detection measures a single quadrature of the system. Heterodyne detection measures two quadratures simultaneously, such as the x and y quadratures of a harmonic oscillator. While there are several other types of measurements, such as direct photodetection, we focus on heterodyne detection because it allows for obtaining information about the phase  $\arctan(x/y)$ , which is the central quantity in synchronization. As we will show in Chapter 4, heterodyne detection can be used to experimentally quantify the degree of synchronization in quantum systems.

We consider a general quantum system described by the master equation

$$\frac{\mathrm{d}}{\mathrm{d}t}\rho = \mathcal{L}\rho \equiv -i[H,\rho] + \sum_{i=1}^{N_J} \mathcal{D}[J_i]\rho \tag{3.10}$$

with arbitrary Hamiltonian H and  $N_J$  jump operators  $J_i$ . For example, the system could be a cavity that leaks photons, which are tracked by the detector; see Fig. 3.1.

By monitoring the effects of the system on the environment, one can extract information about the system state. In the example of the lossy cavity, monitoring the photons that leak from the cavity reveals information about the state of the cavity field. In heterodyne or homodyne detection, the leaking excitations are mixed with a local oscillator with frequency  $\omega_{\rm m}$ . For simplicity, we consider the case where only one jump operator,  $J_1 \equiv \sqrt{\kappa} J_1$ , is measured.

The master equation in the presence of homodyne or heterodyne detection is

$$\frac{\mathrm{d}}{\mathrm{d}t}\rho_{\mathrm{m}} = \mathcal{L}\rho_{\mathrm{m}} + \sqrt{\kappa} \frac{\mathrm{d}W}{\mathrm{d}t} \mathcal{H}[e^{i\omega_{\mathrm{m}}t}J]\rho_{\mathrm{m}}, \qquad (3.11)$$

$$\mathcal{H}[e^{i\omega_{\rm m}t}J]\rho_{\rm m} \equiv e^{i\omega_{\rm m}t}(J - \text{Tr}[J\rho_{\rm m}])\rho_{\rm m} + \text{H.c.}.$$
(3.12)

For a derivation, we refer to Wiseman and Milburn [2010, Chapter 4]. The density operator  $\rho_{\rm m}$  denotes the conditional state of the system under measurement. Its time evolution is governed by the Lindbladian  $\mathcal{L}$  of Eq. (3.10) and an additional stochastic term. The stochastic term contains the Wiener increment dW corresponding to an integrated Gaussian white-noise process. Its mean is zero,  $\mathbb{E}[dW] = 0$ , and its variance is  $\mathbb{E}[dW^2] = dt$ . The stochastic term describes the measurement backaction that results in fluctuations in the state of the system and renders the master equation a stochastic master equation.

Performing a continuous measurement on a system inevitably influences its time evolution. The system's time evolution conditioned on a measurement outcome is called a *quantum trajectory*. Each quantum trajectory will be different because it depends on the measurement backaction, i.e., the random fluctuations induced in the system due to the measurement. Different types of measurement (such as heterodyne, homodyne, or photodetection measurements) result in different types of measurement backaction. We will see an example of this in Section 6.8.

When the frequency  $\omega_{\rm m}$  matches the system frequency, the master equation loses the time dependence of the measurement operator. In that case, a single quadrature is continuously measured. The phase of the local oscillator determines along which quadrature the measurement is performed. For a large frequency  $\omega_{\rm m}$ , the quadrature that is measured changes rapidly. Effectively, two quadratures (call them x and y) are thereby measured simultaneously and the master equation becomes [Wiseman and Milburn, 2010, Eq. (4.108)]

$$\frac{\mathrm{d}}{\mathrm{d}t}\rho_{\mathrm{m}} = \mathcal{L}\rho_{\mathrm{m}} + \sqrt{\kappa/2} \left( \frac{\mathrm{d}W_x}{\mathrm{d}t} \mathcal{H}[J] + \frac{\mathrm{d}W_y}{\mathrm{d}t} \mathcal{H}[-iJ] \right) \rho_{\mathrm{m}}. \tag{3.13}$$

The two quadratures are measured with half the efficiency compared to the efficiency of homodyne detection. For each quadrature, there is an independent Wiener process  $dW_{x,y}$  (with the same statistical properties as dW above).

Averaging over the ensemble of possible quantum trajectories reproduces the unconditional evolution of the density operator governed by Eq. (3.10). This can be seen straightforwardly from Eq. (3.11): Averaging over the ensemble of possible trajectories implies averaging over the possible noise realizations; in this case, the additional term that describes the measurement backaction vanishes, since  $\mathbb{E}[\mathrm{d}W_{x,y}]=0$ . The density operator may thus be viewed as describing the ensemble of all quantum trajectories averaged over all possible measurement outcomes. As pointed out in Section 3.1, different ensembles can correspond to the same density operator. In the context of measurements, different ways to observe the system result in different ensembles of quantum trajectories that correspond to the same time evolution of the density operator.

In an experiment, the observed quantity is the output of the photodetector depicted in Fig. 3.1, i.e., the current  $I_{\rm hom}$ , which is related to the state of the system through

$$I_{\text{hom}} = 2\sqrt{\kappa} \operatorname{Re} \left[ \operatorname{Tr} \left[ e^{i\omega_{\text{m}}t} J \rho_{\text{m}} \right] \right] + dW/dt, \qquad (3.14)$$

By mixing this signal with  $\cos(\phi_{\rm m}(t))$  and  $\sin(\phi_{\rm m}(t))$  and time averaging, one can obtain the complex heterodyne current Wiseman and Milburn [2010]

$$I_{\text{het}} = \sqrt{\kappa} \operatorname{Tr}[J\rho_{\text{m}}] + \sqrt{1/2} \left( \frac{dW_x}{dt} + i\frac{dW_y}{dt} \right), \qquad (3.15)$$

The heterodyne current directly gives insight into the conditional expected value  $\text{Tr}[J\rho_{\rm m}]$ . As we will see in Chapter 4, the current thereby allows us to quantify synchronization of quantum systems.

# 3.4 Cascaded master equation and unidirectional interactions

In Section 2.4, we discussed how classical particles can interact nonreciprocally. We now extend this concept to quantum physics by presenting a general framework for nonreciprocal interactions in quantum systems. This framework is based on *cascaded* 

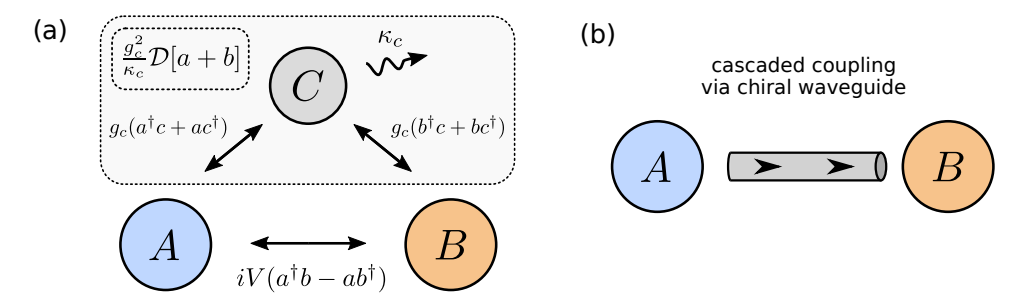


Figure 3.2: Unidirectional interactions. (a) Sketch of the coupling among the three modes A, B, and C. The mode C that is coupled to both A and B effectively mediates the dissipative coupling  $\frac{g_c^2}{\kappa_c} \mathcal{D}[a+b]$  (gray dotted box). (b) The effective cascaded coupling from A to B is schematically depicted by the chiral waveguide.

interactions [Gardiner, 1993; Carmichael, 1993]. Quantum nonreciprocal interactions may alternatively occur, for example, through optical binding forces of nanoparticles [Rudolph et al., 2024a,b], as a quadrature nonreciprocity [Wanjura et al., 2023], or via a dissipative gauge symmetry [Wang et al., 2023]. The advantage of cascaded interactions lies in their generality and broad applicability.

In the following, we follow Metelmann and Clerk [2015]. Consider the master equation for two systems, A and B, described by ladder operators  $a^{(\dagger)}$  and  $b^{(\dagger)}$ . They interact via the Hamiltonian  $iV(a^{\dagger}b-ab^{\dagger})$  where V is real-valued and sets the interaction strength. Additionally, both systems are coupled at strength  $g_c$  to a third subsystem, C, described by ladder operators  $c^{(\dagger)}$ . The third mode decays at rate  $\kappa_c$ . The system of three modes is depicted in Fig. 3.2(a); its master equation is

$$\frac{\mathrm{d}}{\mathrm{d}t}\rho = -i[iV(a^{\dagger}b - ab^{\dagger}), \rho] - ig_c[(a+b)c^{\dagger} + \mathrm{H.c.}, \rho] + \kappa_c \mathcal{D}[c]. \tag{3.16}$$

In the limit where  $\kappa_c$  is large compared to  $g_c$  and V, the third mode can be adiabatically eliminated: Setting  $\dot{c}=0$  yields  $c=g_c(a+b)/\kappa_c$ . Inserting this expression into the master equation (3.16) gives an effective description for modes A and B. For simplicity, let us consider the special case where the couplings to the third mode are such that  $V=g_c^2/\kappa_c$ . In this case, Eq. (3.16) becomes

$$\frac{\mathrm{d}}{\mathrm{d}t}\rho = -i[iV(a^{\dagger}b - ab^{\dagger}), \rho] + 2V\mathcal{D}[a+b]\rho. \tag{3.17}$$

As we will now show, the master equation (3.17) describes cascaded, i.e., unidirectional, interactions. The directionality is revealed by considering the time evolution in the Heisenberg picture; see Eq. (3.9). For an operator  $O_A$  that acts only on subsystem A, i.e.,  $[O_A, b^{(\dagger)}] = 0$ , we find

$$V^{-1}\frac{\mathrm{d}}{\mathrm{d}t}O_A = i[i(a^{\dagger}b - ab^{\dagger}), O_A] + 2\tilde{\mathcal{D}}[a + b]O_A = [a^{\dagger}, O_A]a + a^{\dagger}[O_A, a]. \tag{3.18}$$

This expression does not depend on any operator of subsystem B, implying that system A is not influenced at all by system B. In contrast, for operators  $O_B$  acting only on subsystem B, i.e.,  $[O_B, a^{(\dagger)}] = 0$ , we obtain

$$V^{-1}\frac{\mathrm{d}}{\mathrm{d}t}O_B = (2a^{\dagger} + b^{\dagger})[O_B, b] + [b^{\dagger}, O_B](2a + b), \qquad (3.19)$$

which depends on operators of both subsystems. We conclude that system B is influenced by system A but not vice versa, which constitutes *unidirectional*, or *cascaded*, interactions, schematically depicted in Fig. 3.2(b). We may recast Eq. (3.17) as

$$\frac{\mathrm{d}}{\mathrm{d}t}\rho = 2V(\mathcal{D}[a] + \mathcal{D}[b])\rho - V([b^{\dagger}, a\rho] + [\rho a^{\dagger}, b])$$
(3.20)

using the notation of Stannigel et al. [2012, Eq. (2)] to describe cascaded interactions. The first term of Eq. (3.20) describes the individual decay of each mode, while the second term describes the unidirectional interactions.

Experimentally, cascaded interactions can be mediated by nanophotonic waveguides [Petersen et al., 2014] or freely propagating laser beams [Karg et al., 2020]. Cascaded interactions have been demonstrated in various systems, such as superconducting qubits [Joshi et al., 2023], hybrid atomic-optomechanical systems [Karg et al., 2020], quantum dots [Söllner et al., 2015; Delteil et al., 2017], and atomic ensembles that emit unidirectionally into waveguides [Mitsch et al., 2014; Liedl et al., 2023, 2024].

While cascaded couplings are nonreciprocal, they do not allow for antagonistic interactions, where two subsystems can influence each other in opposing ways, as defined in Section 2.4. In Chapter 6, we will extend the concept of unidirectional interactions to antagonistic nonreciprocal interactions in quantum systems. This relies on the combination of two opposing cascaded couplings that include a phase shift.

# Chapter 4

# Quantum synchronization

In recent years, the understanding of synchronization in quantum systems has attracted a great deal of interest. Research topics include limit-cycle oscillations in quantum systems [Weiss et al., 2017; Roulet and Bruder, 2018b; Chia et al., 2020; Ben Arosh et al., 2021; Parra-López and Bergli, 2020; Es'haqi-Sani et al., 2020; Setoyama and Hasegawa, 2025; Dutta et al., 2025]; the relation between synchronization and entanglement or other quantum features [Lee et al., 2014; Roulet and Bruder, 2018a; Zhu et al., 2015; Witthaut et al., 2017; Lorenzo et al., 2022; Mari et al., 2013; Bandyopadhyay and Banerjee, 2023; synchronization behaviors unique to quantum systems [Lörch et al., 2016, 2017; Amitai et al., 2018; Dutta and Cooper, 2019; Shen et al., 2023a; and other questions [Zhirov and Shepelyansky, 2006; Giorgi et al., 2012; Ameri et al., 2015; Ishibashi and Kanamoto, 2017; Li et al., 2017; Buča et al., 2022; Bandyopadhyay and Banerjee, 2022; Wächtler and Moore, 2024. Experimentally, quantum synchronization has been observed in systems of cold atoms [Cox et al., 2014; Weiner et al., 2017; Laskar et al., 2020; Natale et al., 2025], nuclear spins [Krithika et al., 2022], as well as trapped ions [Zhang et al., 2023; Li et al., 2025, and it has been simulated on a quantum computer [Koppenhöfer et al., 2020. These experimental advances further motivate a detailed theoretical understanding of quantum synchronization.

This chapter offers a pedagogical introduction to synchronization of quantum systems. In Section 4.1, we will analyze the quantum analog of the classical van-der-Pol oscillator introduced in Section 2.1. We first present a single quantum van-der-Pol oscillator. Next, synchronization of two such oscillators is analyzed. Finally, we investigate self-organization via synchronization in a network of many coupled quantum van-der-Pol oscillators, similar to the Kuramoto model. An analogous analysis of synchronization among quantum spins is presented in Section 4.2, starting with a single spin and progressing to two coupled spins and finally a large ensemble of coupled spins. This will lead us to introduce the superradiant laser, which also shows a Kuramoto-like synchronization transition. Throughout this chapter, we will emphasize parallels between synchronization of quantum oscillators and of classical oscillators subject to fluctuations.

While this chapter mostly summarizes previous results of the literature, it also contains novel insights in quantum synchronization regarding the effects of measurement. We demonstrate that continuous heterodyne detection results in quantum trajectories that make the quantum limit cycle apparent. Furthermore, the measurement results in experimentally accessible quantities that approximate established theoretical measures of quantum synchronization.

# 4.1 Quantum van-der-Pol oscillator

We begin by presenting a quantum analog of the classical van-der-Pol (vdP) oscillator, which was introduced in Section 2.1. The quantum vdP oscillator is described by creation and annihilation operators  $a^{\dagger}$  and a that add or remove an excitation of a bosonic mode

and fulfill the commutation relation  $[a, a^{\dagger}] = 1$ . The bosonic mode can represent different physical systems, such as a light mode in a resonator or a trapped particle. Gain and loss of the oscillator are introduced through the coupling to an (unspecified) environment, whose effect on the system is described by a Lindblad master equation; see Chapter 3. The master equation of the quantum vdP oscillator is

$$\frac{\mathrm{d}}{\mathrm{d}t}\rho = -i[\omega a^{\dagger}a, \rho] + \kappa_1 \mathcal{D}[a^{\dagger}]\rho + \kappa_2 \mathcal{D}[a^2]\rho + \kappa \mathcal{D}[a]\rho. \tag{4.1}$$

The Lindblad dissipator is, as before,  $\mathcal{D}[o]\rho = o\rho o^{\dagger} - (o^{\dagger}o\rho + \rho o^{\dagger}o)/2$ . The oscillator's frequency is  $\omega$ , and  $\kappa_1$ ,  $\kappa_2$ , and  $\kappa$  are the rates of linear gain, nonlinear two-excitation loss, and linear loss, respectively. The master equation is invariant under a phase shift,  $a \to a \exp(i\phi_0)$ , which corresponds to a U(1) symmetry. The quantum vdP oscillator was first introduced by Lee and Sadeghpour [2013] and Walter et al. [2014], and has since become a paradigmatic model for studying quantum synchronization. It has recently been implemented in the motional mode of a trapped ion [Li et al., 2025]. Related models are presented by Chia et al. [2020], Ben Arosh et al. [2021], and Chia et al. [2025].

The connection between the quantum and classical vdP oscillators is evident in the time evolution of the oscillator's amplitude  $\langle a \rangle \equiv \text{Tr}[a\rho]$ . It can be computed using Eq. (3.9), resulting in

$$\frac{\mathrm{d}}{\mathrm{d}t} \langle a \rangle = -i\omega \langle a \rangle + \frac{\kappa_1 - \kappa}{2} \langle a \rangle - \kappa_2 \langle a^{\dagger} a^2 \rangle . \tag{4.2}$$

When the state is initialized as a coherent state  $|\alpha\rangle$   $(a |\alpha\rangle = \alpha |\alpha\rangle)$  and assuming that it remains a coherent state, one can approximate the last term in Eq. (4.2):  $\langle a^{\dagger}a^{2}\rangle \approx |\langle a\rangle|^{2}\langle a\rangle$ . The approximation is valid for short time scales compared to the strength of decoherence, where fluctuations play a negligible role. Within the approximation, one obtains

$$\frac{\mathrm{d}}{\mathrm{d}t} \langle a \rangle \approx -i\omega \langle a \rangle + \frac{\kappa_1 - \kappa}{2} \langle a \rangle - \kappa_2 |\langle a \rangle|^2 \langle a \rangle , \qquad (4.3)$$

which is the equation of motion for a vdP limit-cycle oscillator presented in Eq. (2.3) (there, we have set  $\kappa = 0$ ). In general, however, the fluctuations that stem from the coupling to the environment and that are inherently described by the master equation (4.1) cannot be neglected. They can be described by a classical approximation of the master equation (4.1) that is valid in the limit of large amplitudes, i.e.,  $\kappa_1 - \kappa \gg \kappa_2$  [Carmichael, 1999]. One finds the Langevin equation of the same form as Eq. (2.8) with noise strength  $\sigma^2 = 3(\kappa_1 + \kappa)/4 + 2\kappa_2$  [Lee and Sadeghpour, 2013]. In the following, we analyze the full master equation without any approximation to be able to also describe the regime of small excitation numbers quantitatively correctly.

#### 4.1.1 Quantum limit cycles

A numerical integration of the master equation (4.1) yields the time evolution of the density operator<sup>1</sup>. To display the time evolution in phase space, the density operator is projected onto coherent states, which gives the Husimi-Q distribution [Carmichael, 1999]

$$Q(\alpha) = \frac{1}{\pi} \langle \alpha | \rho | \alpha \rangle , \qquad (4.4)$$

<sup>&</sup>lt;sup>1</sup>Throughout this chapter, we use the Python package QuTiP [Johansson et al., 2012] to solve the master equations. The density operator is represented in the Fock basis using states  $|0\rangle$  to  $|N_{\text{fock}} - 1\rangle$ , where the number of states  $N_{\text{fock}}$  is chosen large enough so that the population in higher-level Fock states is negligible.

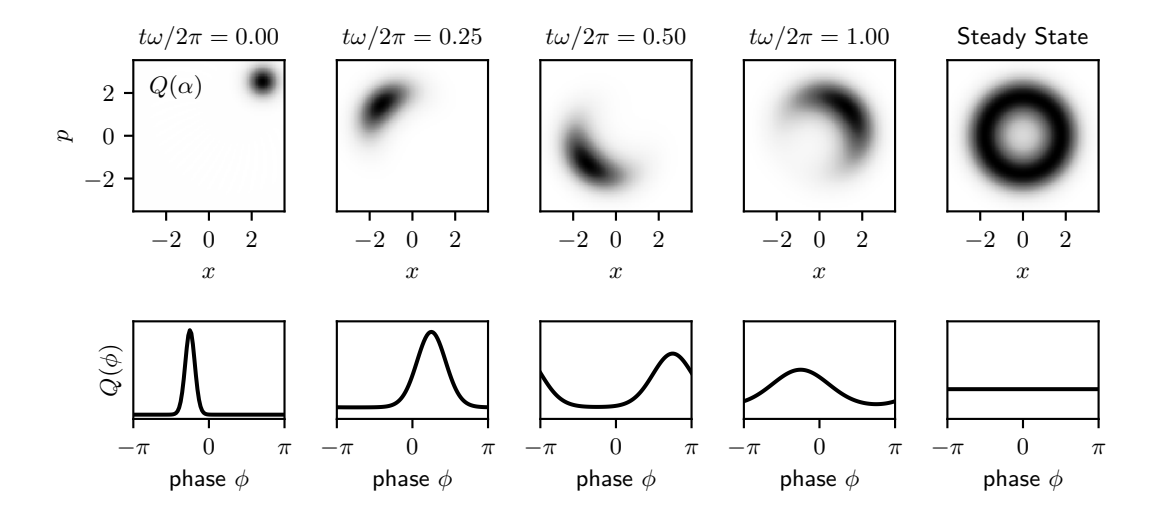


Figure 4.1: Time evolution of the quantum vdP oscillator shown by the Husimi-Q distribution  $Q(\alpha = x + ip)$  (top row) and the phase distribution  $Q(\phi)$  (bottom row). Parameters:  $\kappa_1 = \omega = 4\kappa$ ,  $\kappa_2 = \kappa/2$ .

a phase-space representation akin to classical probability distributions. The result is shown in Fig. 4.1. The dynamics can be understood as three simultaneous processes. First, the initial coherent state oscillates at frequency  $\omega$ , which can be seen in the Husimi-Q distribution as a rotation in time around the origin. Second, as a result of gain and nonlinear loss, the amplitude of the oscillation is attracted to the limit cycle, and the radial position of the state approximately approaches the value  $r_0 = \sqrt{\kappa_1/2\kappa_2}$ . Third, the state diffuses in phase due to the coupling to the environment. While the master equation is a deterministic differential equation that does not explicitly feature a noise process, it inherently captures the effect of fluctuations that stem from the coupling to the environment, as we will later discuss in more detail. The attraction towards the limit cycle and the phase diffusion together result in a stationary ring-shaped state in the long-time limit, see last panel of Fig. 4.1. The steady state is phase symmetric, which follows from the U(1) symmetry of the master equation.

Comparing Fig. 4.1 to Fig. 2.3, we find that for a vdP oscillator, the dynamics of  $Q(\alpha)$  are qualitatively the same as those of the probability distribution P(x,p). Similar to how P(x,p) describes the ensemble of trajectories, we will later see how  $\rho$  – and consequently  $Q(\alpha)$  – describes an ensemble of quantum trajectories.

The phase distribution  $Q(\phi)$  displayed in the bottom row in Fig. 4.1 is obtained by integrating out the radial degree of freedom

$$Q(\phi) = \int_0^\infty dr \, r \, Q(\alpha = re^{-i\phi}) \,. \tag{4.5}$$

It informs about the likelihood of the quantum vdP oscillator to assume a certain phase  $\phi$ . The phase distribution of the initial state is sharply peaked. Over time, it shifts due to the oscillation and flattens due to the phase diffusion approaching a flat distribution in the steady state. The phase distribution  $P(\phi)$  of the classical vdP oscillator qualitatively showed the same behavior; see Fig. 2.3.

#### Quantum limit cycles under heterodyne detection

While the steady state shown in the top right panel of Fig. 4.1 resembles the classical limit cycle in its circular shape, it is static and appears not to feature the dynamical oscillations of a classical limit cycle. The reason is that the density operator  $\rho$  describes the probability distribution of an ensemble of quantum trajectories. The probability distribution of an ensemble of classical trajectories in the presence of noise is also time-independent; see Section 2.1.1. We now show that individual trajectories display dynamical limit-cycle oscillations in the long-time limit. They can be made apparent through heterodyne detection.

The role of measurement and trajectories in the context of quantum synchronization has been explored in a few previous works. For one, homodyne detection has been proposed to enhance synchronization with or without feedback [Kato and Nakao, 2021; Shen et al., 2023b]. Moreover, an unraveling of the master equation into pure states has been employed to gain insights into synchronization along individual quantum trajectories [Zhirov and Shepelyansky, 2008, 2009; Weiss et al., 2016; Es'haqi-Sani et al., 2020] and to derive an effective phase equation [Setoyama and Hasegawa, 2024, 2025].

However, the full unraveling into pure states that is considered in previous studies is in general not experimentally feasible, as it requires perfect monitoring of all dissipative processes. Here, we take a realistic approach of unraveling only a single jump operator describing the loss of excitations. We consider a heterodyne detection introduced in Section 3.3 because it measures both quadratures and thus allows for obtaining information about the phase. Such an unraveling is possible in a variety of experimental setups, including microwave and optical resonators [Blais et al., 2004; Weiner et al., 2017] and, indirectly, two-level systems [Campagne-Ibarcq et al., 2016].

The stochastic master equation under heterodyne detection was introduced in Eq. (3.11); for the quantum vdP oscillator, it becomes

$$\frac{\mathrm{d}}{\mathrm{d}t}\rho_{\mathrm{m}} = -i[\omega a^{\dagger}a, \rho_{\mathrm{m}}] + \kappa_{1}\mathcal{D}[a^{\dagger}]\rho_{\mathrm{m}} + \kappa_{2}\mathcal{D}[a^{2}]\rho_{\mathrm{m}} + \kappa_{2}\mathcal{D}[a^{2}]\rho_{\mathrm{m}} + \kappa_{2}\mathcal{D}[a]\rho_{\mathrm{m}} + \frac{\mathrm{d}W}{\mathrm{d}t}\sqrt{\kappa} \left[e^{i\omega_{\mathrm{m}}t}(a - \mathrm{Tr}[a\rho_{\mathrm{m}}])\rho_{\mathrm{m}} + \mathrm{H.c.}\right].$$
(4.6)

It contains the measurement backaction term proportional to the noise process dW/dt.

We simulate the time evolution governed by Eq. (4.6) to obtain individual quantum trajectories; they are shown in Fig. 4.2. The state of the quantum vdP oscillator in each quantum trajectory shows a limit-cycle behavior: It is attracted to the limit cycle amplitude [see Fig. 4.2(a)] and displays persistent oscillations [see Fig. 4.2(b)]. While the steady-state density operator obeys the U(1) symmetry of the master equation, each trajectory breaks it since it displays a distinct phase at any point in time.

The measurement backaction also results in fluctuations of the state of the system. As a result, the oscillator's phase in each quantum trajectory fluctuates. Therefore, averaging over time or over several trajectories restores the U(1) symmetry of the master equation. Several trajectories starting with the same initial phase are shifted in their phases by a random amount at later times. The average of several trajectories decays to zero; see the black line in Fig. 4.2(b). It agrees well with the density matrix evolution shown by the gray dashed line in Fig. 4.2(b), which describes the average over all possible quantum trajectories. In the master equation (4.1), the effect of the fluctuations is captured as decoherence. It is contained in the term  $\kappa \mathcal{D}[a]\rho$  that not only describes the loss of excitations but also decoherence.

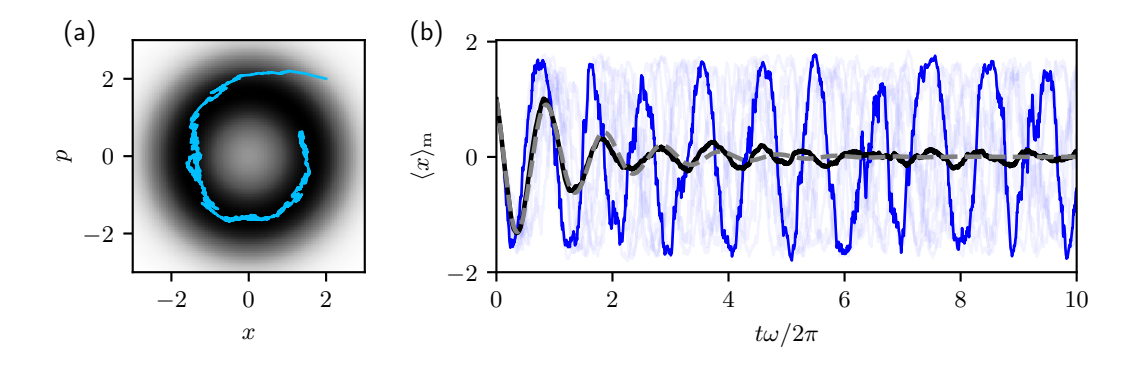


Figure 4.2: Quantum vdP oscillator: limit cycle under measurement. (a) The heatmap shows the steady-state Husimi-Q distribution from Fig. 4.1, top-right panel. The blue line shows the time evolution of  $\langle x \rangle_{\rm m}$  and  $\langle p \rangle_{\rm m}$  of one quantum trajectory. (b) The faint blue lines show the expectation value  $\langle x \rangle_{\rm m}$  of ten different quantum trajectories. The bright blue line highlights one of them. The black line shows the average of 100 such realizations. It overlaps well with the gray dashed line, which is the solution of  $\langle x \rangle$  of the master equation without measurement. Same parameters as in Fig. 4.1.

While expectation values of the conditional state are not directly observable in an experiment, the measured heterodyne current is accessible; see Eq. (3.15). For the quantum vdP oscillator, it is

$$I_{\text{het}} = \sqrt{\kappa} \operatorname{Tr}[a\rho_{\text{m}}] + \sqrt{1/2} \left( \frac{dW_x}{dt} + i\frac{dW_y}{dt} \right). \tag{4.7}$$

While it informs about the expected value of a, it contains additional detector noise that partially masks the signal.

The quantum trajectories obtained under heterodyne detection show qualitatively the same behavior as the trajectories of the classical vdP oscillator; see Fig. 2.2. Consequently, many aspects of quantum vdP oscillators can be qualitatively understood in terms of classical noisy oscillators. However, in the quantum limit, i.e., the limit of small numbers of excitations when  $\kappa_2/\kappa_1 \to \infty$ , the discretized level structure becomes relevant. While the limit-cycle of the classical vdP oscillator can have an arbitrarily small amplitude, the limit cycle of the quantum vdP oscillator with the smallest number of excitations is  $(2 |0\rangle\langle 0| + |1\rangle\langle 1|)/3$  [Lee and Sadeghpour, 2013]. Furthermore, other models of quantum limit cycles show a behavior different from classical synchronization; see for example Lörch et al. [2014].

#### 4.1.2 Two coupled oscillators

Having introduced the quantum vdP oscillator, we now examine how two such oscillators synchronize when coupled. The two quantum vdP oscillators are described by the master equation

$$\frac{\mathrm{d}}{\mathrm{d}t}\rho = \kappa_1(\mathcal{D}[a^{\dagger}] + \mathcal{D}[b^{\dagger}])\rho + \kappa(\mathcal{D}[a] + \mathcal{D}[b])\rho + \kappa_2(\mathcal{D}[a^2] + \mathcal{D}[b^2])\rho 
- i\frac{\delta}{2}[a^{\dagger}a - b^{\dagger}b, \rho] + V\mathcal{D}[a - b]\rho.$$
(4.8)

The density operator  $\rho$  describes the joint state of both oscillators represented by the operators  $a^{(\dagger)}$  and  $b^{(\dagger)}$ . The master equation describes the system in the frame rotating

at their average frequency and includes the gain and loss terms of Eq. (4.1) for both oscillators. For simplicity, we focus on oscillators with identical rates  $\kappa$  and  $\kappa_{1,2}$ . The frequency of each oscillator, however, can be different, which is parametrized by the detuning  $\delta$ . Finally, the coupling is described by the dissipative interaction term  $\mathcal{D}[a-b]\rho$  with interaction strength V.

Deriving the mean-field equation in the same way, in which Eq. (4.3) was derived, we find the same equations as those of the two coupled classical vdP oscillators, Eqs. (2.17) with  $\alpha = \langle a \rangle$ ,  $\beta = \langle b \rangle$ . We therefore expect phase locking and frequency entrainment as discussed for the classical case in Section 2.2. These expectations will be confirmed in the following by analyzing the master equation (4.8).

#### Phase locking

Various measures for phase locking of quantum oscillators have been suggested [Ludwig and Marquardt, 2013; Lee and Sadeghpour, 2013; Walter et al., 2014; Mari et al., 2013; Hush et al., 2015; Weiss et al., 2016; Jaseem et al., 2020a]. Here, we use the Husimi-Q distribution, extending the definition of Eq. (4.4) to two oscillators

$$Q(\alpha, \beta) = \frac{1}{\pi} \langle \alpha | \otimes \langle \beta | \rho | \alpha \rangle \otimes | \beta \rangle . \tag{4.9}$$

It is obtained by projecting the density operator on the coherent states  $|\alpha\rangle$  and  $|\beta\rangle$ . We chose the Husimi-Q distribution because it provides a natural analog to classical phase-space distributions and allows us to treat phase locking of classical and quantum vdP oscillators as well as spins (as we see in Section 4.2) in a parallel way. From  $Q(\alpha, \beta)$ , we derive the distribution  $Q(\phi_{AB})$  of the phase difference  $\phi_{AB} = \phi_A - \phi_B$ . It is obtained by integrating out the radial degree of freedom as well as the total phase,

$$Q(\phi_{AB}) = \int_0^{2\pi} d\phi_A \int_0^{2\pi} d\phi_B \int_0^{\infty} dr_A r_A \int_0^{\infty} dr_B r_B Q(\alpha = r_A e^{-i\phi_A}, \beta = r_B e^{-i\phi_B})$$
$$\times \delta(\phi_{AB} - \phi_A + \phi_B). \tag{4.10}$$

The integrals can be evaluated analytically, allowing for an efficient way to compute the phase distribution<sup>2</sup>. Figure 4.3(b) displays the phase distribution by the solid lines for different coupling strengths. In the absence of coupling, the phase distribution  $Q(\phi_{AB})$  is completely flat, i.e., all phase differences are equally likely, indicating the absence of phase locking. When increasing the coupling strength,  $Q(\phi_{AB})$  develops an increasingly large peak, indicating partial phase locking; it becomes more likely for the phase difference to take a value close to zero. To quantify the degree of synchronization by a single number, we use the maximum value of the phase distribution,  $\max Q(\phi_{AB})$ . It is shown in Fig. 4.3(a) as a function of coupling strength and detuning. The amount of phase locking increases with  $V/|\delta|$ . The white dashed lines indicate the synchronization threshold  $V = |\delta|$  for the classical analog without fluctuations. The phase locking behavior of two coupled quantum

$$Q(\phi_{AB}) = \sum_{\substack{n_{\alpha}, n_{\beta}, \\ m_{\alpha}, m_{\beta}}} e^{i\phi_{AB}(n_{\alpha} - m_{\alpha})} \frac{\Gamma(1 + (n_{\alpha} + m_{\alpha})/2)\Gamma(1 + (n_{\beta} + m_{\beta})/2)}{2\pi\sqrt{n_{\alpha}!n_{\beta}!m_{\alpha}!m_{\beta}!}} \times (4.11)$$

using the Gamma function  $\Gamma()$  and the Kronecker-Delta symbol  $\delta_{i,j}$ .

Expanding the coherent states in the Fock basis,  $|\alpha\rangle = \sum_{n=0}^{\infty} \alpha^n (n!)^{-1/2} \exp(-|\alpha|^2/2) |n\rangle$  (and similarly for  $|\beta\rangle$ ), the integrals of Eq. (4.10) can be evaluated, resulting in

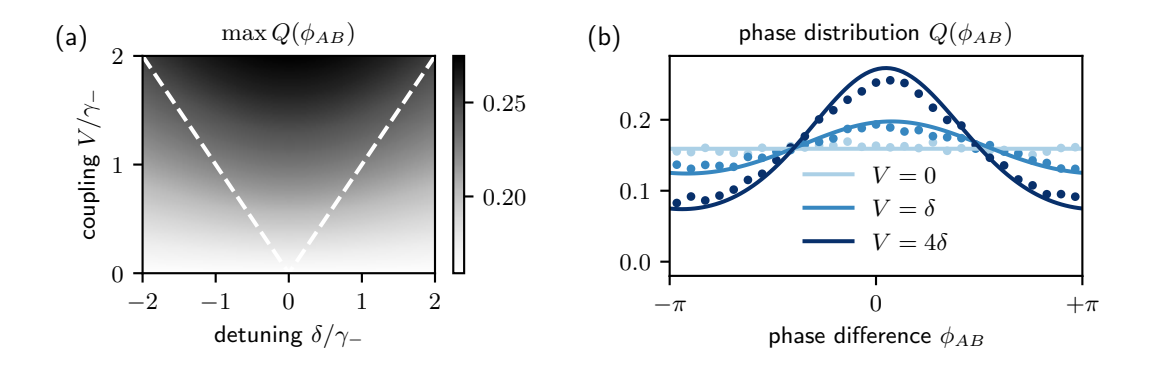


Figure 4.3: Phase locking of quantum vdP oscillators. (a) The grayscale shows the maximum of the phase distribution  $\max Q(\phi_{AB})$ , a measure of phase locking. The white dashed line indicates the synchronization transition  $V = |\delta|$  expected in classical noiseless oscillators. (b) The lines show the phase distribution  $Q(\phi_{AB})$  for different values of the coupling strength. The scatter points show the corresponding estimate of the phase distribution obtained via the heterodyne current; see Eq. (4.15). Parameters:  $\kappa = \kappa_2$ ,  $\kappa_1 = 3\kappa_2$ . (b)  $\delta = \kappa/2$ .

vdP oscillators is qualitatively the same as that of two classical oscillators in the presence of fluctuations; compare to Fig. 2.4.

#### Frequency entrainment

Frequency entrainment of the two oscillators can be analyzed via their spectra [Walter et al., 2015]. The spectra of classical oscillators were introduced in Section 2.2; see Eq. (2.28). For quantum oscillators, the steady-state spectra are defined as [Breuer and Petruccione, 2002]

$$S_{A}(\omega) = \lim_{t \to \infty} \int_{-\infty}^{\infty} d\tau \langle a^{\dagger}(t+\tau)a(t)\rangle e^{-i\omega\tau},$$

$$S_{B}(\omega) = \lim_{t \to \infty} \int_{-\infty}^{\infty} d\tau \langle b^{\dagger}(t+\tau)b(t)\rangle e^{-i\omega\tau},$$
(4.12)

i.e., the Fourier transforms of the two-time correlations  $\langle a^{\dagger}(t+\tau)a(t)\rangle$  and  $\langle b^{\dagger}(t+\tau)b(t)\rangle$ . They inform about the dynamics of oscillators A and B in the frequency domain. We show the spectra of the two coupled quantum vdP oscillators in Fig. 4.4 by the solid lines. We find a behavior similar to that of classical vdP oscillators; compare to Fig. 2.5(b): Each spectrum features a peak whose width stems from the phase diffusion and whose position represents the typical frequency. The frequency difference is  $\delta$  in the absence of a coupling and approaches zero when increasing the coupling. Due to phase fluctuations, there is no exact frequency entrainment.

In summary, we have shown that the synchronization behavior of two coupled quantum vdP oscillators is qualitatively the same as that of two classical oscillators in the presence of fluctuations. The quantum character can, however, result in a qualitatively different behavior, for example when the coupled oscillators are anharmonic [ $L\ddot{o}rch$  et al., 2017]. Further quantum effects in synchronization have been shown for a single oscillator subject to an external drive. They include multiple Arnold tongues due to the quantized level structure [ $L\ddot{o}rch$  et al., 2016] and a boost of synchronization via dissipation [Mok et al., 2020].

#### Quantum synchronization under heterodyne detection

Both phase locking and frequency entrainment can be observed via heterodyne detection. Consider the evolution of the two quantum vdP oscillators in Eq. (4.8) with an additional independent measurement for each oscillator,

$$\frac{\mathrm{d}}{\mathrm{d}t}\rho = -i\frac{\delta}{2}[a^{\dagger}a - b^{\dagger}b, \rho] + \kappa_{1}(\mathcal{D}[a^{\dagger}] + \mathcal{D}[b^{\dagger}])\rho + \kappa_{2}(\mathcal{D}[a^{2}] + \mathcal{D}[b^{2}])\rho + V\mathcal{D}[a - b]\rho + \\
+ \kappa\mathcal{D}[a]\rho_{\mathrm{m}} + \frac{\mathrm{d}W_{A}}{\mathrm{d}t}\sqrt{\kappa} \left[e^{i\omega_{\mathrm{m}}t}(a - \mathrm{Tr}[a\rho_{\mathrm{m}}])\rho_{\mathrm{m}} + \mathrm{H.c.}\right] + \\
+ \kappa\mathcal{D}[b]\rho_{\mathrm{m}} + \frac{\mathrm{d}W_{B}}{\mathrm{d}t}\sqrt{\kappa} \left[e^{i\omega_{\mathrm{m}}t}(b - \mathrm{Tr}[b\rho_{\mathrm{m}}])\rho_{\mathrm{m}} + \mathrm{H.c.}\right] .$$
(4.13)

The second and third lines describe the heterodyne detection of oscillators A and B, respectively. The two detectors produce the currents

$$I_{\text{het,A}} = \sqrt{\kappa} \operatorname{Tr}[a\rho_{\text{m}}] + \sqrt{1/2} \left( dW_{A,x}/dt + idW_{A,y}/dt \right) ,$$

$$I_{\text{het,B}} = \sqrt{\kappa} \operatorname{Tr}[b\rho_{\text{m}}] + \sqrt{1/2} \left( dW_{B,x}/dt + idW_{B,y}/dt \right) ;$$

$$(4.14)$$

see Eq. (3.15) The currents are determined by the expectation values of a and b and the detector noise.

The currents can be used to approximate the measures of phase locking and frequency entrainment, i.e., the phase distribution  $Q(\phi_{AB})$  and the spectra  $S_{A,B}(\omega)$ . The phase difference between the two oscillators is estimated by the phase relation of the currents

$$\phi_{AB}^{\mathrm{m}} = \arg[I_{\mathrm{het,B}}/I_{\mathrm{het,A}}]. \tag{4.15}$$

The phase distribution can be approximated by the normalized frequency of occurrence of  $\phi_{AB}^{\rm m}$  in the stationary state, which is shown in Fig. 4.3(b) by the scatter points. They approximate well the phase distribution  $Q(\phi_{AB})$ . Moreover, the heterodyne currents can be used to estimate the spectra via [Wiseman and Milburn, 2010, Section 4.5.1]

$$S_A^{\rm m}(\omega) = \lim_{t \to \infty} \int_{-\infty}^{\infty} d\tau e^{-i\omega\tau} \mathbb{E}[I_{\rm het,A}(t+\tau)^* I_{\rm het,A}(t)] = \kappa S_A(\omega) + 1 \tag{4.16}$$

and analogously for oscillator B. The constant term stems from the white noise of the detector partially masking the signal. The measured spectra are shown in Fig. 4.4 by the scatter points. They approximate well the spectra  $S_{A,B}(\omega)$  displayed by the solid lines despite the presence of the constant noise floor.

In summary, heterodyne detection presents a tool to approximately measure both phase locking and frequency entrainment of coupled quantum limit cycles. Thereby, it connects previously suggested theoretical measures of quantum synchronization with quantities accessible in experimental settings.

#### 4.1.3 Large network of coupled oscillators

Let us now extend our analysis to a large network of quantum vdP oscillators in analogy to the classical Kuramoto model. The density operator  $\rho$  now describes the collective state of N oscillators that are described by creation and annihilation operators  $a_i$  and  $a_i^{\dagger}$  for  $i \in \{1, ..., N\}$ , where each  $a_i$  acts on a subspace of the joint Hilbert space,

$$a_i \equiv \underbrace{\mathbb{1} \otimes \cdots \otimes \mathbb{1} \otimes a}_{i-1 \text{ times}} \underbrace{a \otimes \mathbb{1} \otimes \cdots \otimes \mathbb{1}}_{N-i \text{ times}}. \tag{4.17}$$

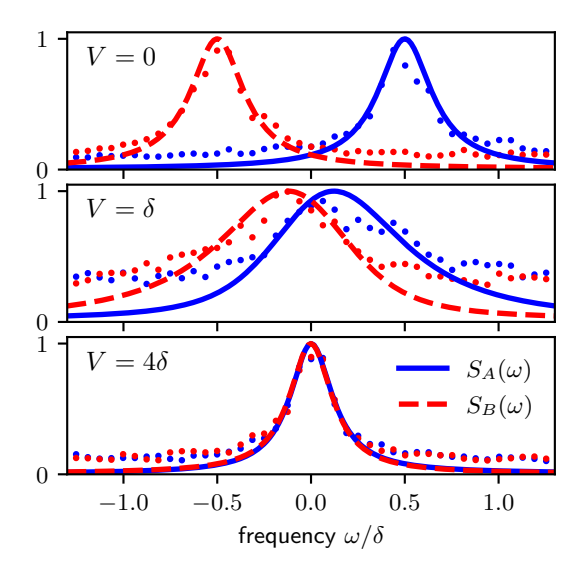


Figure 4.4: Frequency entrainment of quantum vdP oscillators. The lines show the spectra as calculated by Eq. (4.12) for oscillators A (blue solid) and B (red dashed). The scatter points show the spectra calculated from the heterodyne currents; see Eq. (4.16). The heterodyne spectra are averaged over a window of width  $\delta/10$ . Parameters:  $\kappa = \kappa_2$ ,  $\kappa_1 = 3\kappa_2$ ,  $\delta = 5\kappa_2$ .

The master equation describing the network is an extension of Eq. (4.8) to N coupled quantum vdP oscillators (we now set  $\kappa = 0$  for simplicity),

$$\frac{\mathrm{d}}{\mathrm{d}t}\rho = \sum_{i=1}^{N} \left( \kappa_1 \mathcal{D}[a_i^{\dagger}] + \kappa_2 \mathcal{D}[a_i^2] \right) \rho + \frac{V}{N} \sum_{i < j} \mathcal{D}[a_i - a_j] \rho. \tag{4.18}$$

All oscillators are assumed to have equal frequency, and we have moved to a frame rotating at this frequency. The case of different frequencies is discussed by Lee et al. [2014]. The master equation is invariant under a global rotation  $a_i \to a_i \exp(i\phi_0)$  by a constant angle  $\phi_0$ , which constitutes a U(1) symmetry – the same symmetry that we identified in the Kuramoto model. The last term of Eq. (4.18) describes an all-to-all coupling. The sum runs over all pairs of oscillators, which are coupled dissipatively and in the same form of Eq. (4.8). As established in the previous section, the terms  $\mathcal{D}[a_i - a_j]$  result in in-phase locking of oscillators i and j. Therefore, all oscillators pairwise attract each other in their phases, which will result in global phase locking. The case of reactive, i.e., Hamiltonian, all-to-all coupling is discussed by Lee and Sadeghpour [2013].

The size of the Hilbert space grows exponentially with the number N of oscillators, so that an exact solution of master equation (4.18) becomes infeasible for large N. Even for moderate N=4 and including only the first 4 Fock states, the density matrix has  $4^4 \times 4^4 - 1 \approx 6 \times 10^5$  independent real-valued entries. However, the master equation (4.18) can be solved in a simpler way in the limit of  $N \to \infty$ . In this case, a mean-field ansatz  $\rho = \bigotimes_{i=1}^{N} \rho_i$ , where the state of all oscillators factorizes, is exact [Spohn, 1980]. Since all oscillators are identical, it is sufficient to derive the equation of motion for one of the N oscillators, say  $\frac{\mathrm{d}}{\mathrm{d}t}\rho_1 = \mathrm{Tr}_{\neq 1}[\frac{\mathrm{d}}{\mathrm{d}t}\rho]$ , where the trace is performed over all oscillators

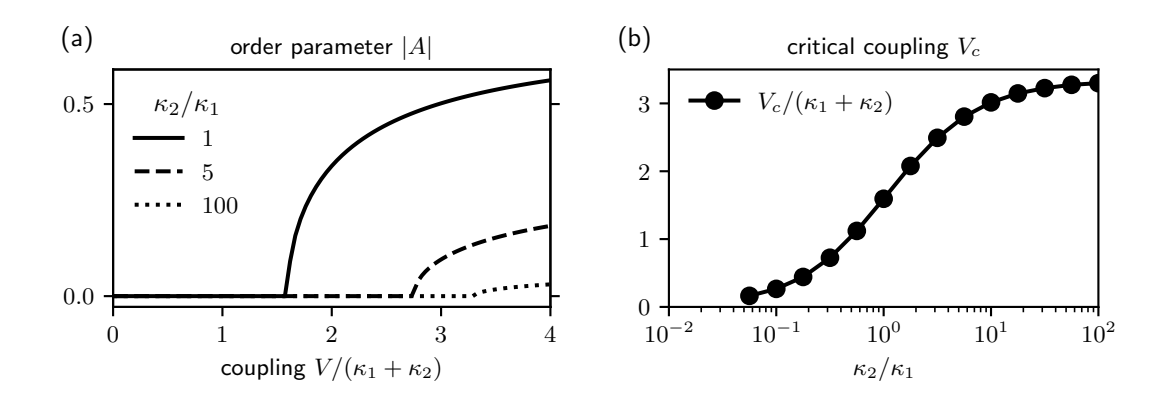


Figure 4.5: Kuramoto-like synchronization transition of quantum vdP oscillators. (a) Absolute value of the mean-field amplitude  $|A| = |\text{Tr}[a\rho_{\text{mf}}]|$  in the steady state as a function of the coupling strength for different ratios  $\kappa_2/\kappa_1$ . (b) Critical coupling  $V_c$  as a function of the ratio  $\kappa_2/\kappa_1$ .

except the first, and then to set all oscillators equal,  $\rho_i = \rho_{\rm mf}$ . In this way, we obtain the mean-field equation

$$\frac{\mathrm{d}}{\mathrm{d}t}\rho_{\mathrm{mf}} = \left(\kappa_1 \mathcal{D}[a^{\dagger}] + \kappa_2 \mathcal{D}[a^2] + V \mathcal{D}[a]\right)\rho_{\mathrm{mf}} - iV\left[H_{\mathrm{mf}}(\rho_{\mathrm{mf}}), \rho_{\mathrm{mf}}\right],\tag{4.19}$$

$$H_{\rm mf}(\rho_{\rm mf}) = i \operatorname{Tr}[a\rho_{\rm mf}]a^{\dagger} - i \operatorname{Tr}[a^{\dagger}\rho_{\rm mf}]a. \tag{4.20}$$

The mean-field equation is a nonlinear master equation: The time evolution of  $\rho_{\rm mf}$  depends on higher-order terms  $\rho_{\rm mf}^2$  due to the mean-field Hamiltonian  $H_{\rm mf}$ . It can be understood as a coherent drive of each oscillator with the mean amplitude  ${\rm Tr}[a\rho_{\rm mf}]$ . The complexity has substantially reduced from a linear equation describing N oscillators to a nonlinear equation of a single oscillator.

Let us define the mean-field amplitude as  $A \equiv \text{Tr}[a\rho_{\text{mf}}]$ . For increasing coupling, we expect a transition from a stable inhomogeneous state with vanishing coherence indicated by A=0 to a self-organized, synchronized state characterized by a nonzero value of the mean-field amplitude |A|>0. The parameter |A| is an order parameter of the transition, analogous to the order parameter |z| of the Kuramoto model defined in Eq. (2.30). To make the analogy explicit, we can introduce the phases  $\phi_j$  of the oscillators, and rewrite the mean-field amplitude as

$$A \equiv \text{Tr}[a\rho_{\text{mf}}] = \frac{1}{N} \sum_{j=1}^{N} \langle a_j \rangle = \frac{1}{N} \sum_{i=j}^{N} |\langle a_j \rangle| \exp(i\phi_j).$$
 (4.21)

The phase diffusion due to decoherence, which was discussed in Section 4.1.1, results in a spread of the phases  $\phi_j$  of the oscillators, which leads to a vanishing order parameter. The alignment of the phases due to the coupling term competes with the phase diffusion, and results in a state with a nonzero order parameter, where the oscillators approximately lock their phases.

We confirm this by integrating Eq. (4.19) to obtain the order parameter in the steady state. Figure 4.5(a) shows the steady-state value of the order parameter |A| as a function of coupling strength V. Indeed, there is a continuous transition to synchronization indicated by the order parameter, which assumes a nonzero value above a critical coupling strength  $V_c$ . We also see that  $V_c$  varies with the ratio  $\kappa_2/\kappa_1$ .

To obtain the critical coupling for small values of  $\kappa_2/\kappa_1$ , where the numerical integration of Eq. (4.19) is intractable, we have performed a stability analysis. We use the perturbation ansatz  $\rho_{\rm mf} = \rho_0 + \delta \rho$ , where  $\rho_0$  is the incoherent state that solves the mean-field equation for  $H_{\rm mf} = 0$ . Linearizing around small  $\delta \rho$ , we find

$$\frac{\mathrm{d}}{\mathrm{d}t}\delta\rho = \left(\kappa_1 \mathcal{D}[a^{\dagger}] + \kappa_2 \mathcal{D}[a^2] + V \mathcal{D}[a]\right)\delta\rho - iV\left[H_{\mathrm{mf}}(\delta\rho), \rho_0\right], \qquad (4.22)$$

which is of the form  $\frac{\mathrm{d}}{\mathrm{d}t}\delta\rho=M\delta\rho$ . We represent  $\delta\rho$  in the Fock basis with states  $|0\rangle$  to  $|N_{\mathrm{fock}}-1\rangle$ , to obtain an explicit expression for M, a matrix of dimension  $N_{\mathrm{fock}}^2\times N_{\mathrm{fock}}^2$ . The critical coupling  $V_c$  is obtained as the coupling strength above which at least one eigenvalue of M is positive, indicating the instability of  $\rho_0$ . In the range of Fig. 4.5(b),  $\kappa_2/\kappa_1 \geq 0.06$ , it is sufficient to include  $N_{\mathrm{fock}}=25$  states.

The value of the critical coupling as a function of the ratio of damping and gain is shown in Fig. 4.5(b). Lee et al. [2014] have analyzed the master equation (4.18) in the quantum limit  $\kappa_2/\kappa_1 \to \infty$ , finding the critical coupling  $V_c = 10\kappa_2/3$ . This is consistent with our result displayed in Fig. 4.5(b). Furthermore, the critical coupling in the classical limit is zero, as phase diffusion becomes negligible [Matthews et al., 1991]. Figure 4.5(b) additionally shows how the classical-to-quantum transition of the critical coupling from  $V_c = 0$  to  $V_c = 10\kappa_2/3$  takes place.

Through the above analysis, we have found that the synchronization transition of many dissipatively coupled quantum vdP oscillators resembles that of the Kuramoto model with quantitative differences [Lee et al., 2014]. Many-body systems of other types of quantum limit-cycle oscillators also behave qualitatively similarly to the Kuramoto model [Ludwig and Marquardt, 2013; Zhu et al., 2015; Davis-Tilley et al., 2018; Delmonte et al., 2023]. In Chapter 5, we will highlight qualitatively different behavior in a network of all-to-all coupled quantum limit-cycle oscillators. In that case, each oscillator only comprises three states, and the quantum nature of the oscillators will lead to a different synchronization behavior.

#### 4.1.4 Experimental implementation in trapped ions

One way to experimentally realize a quantum vdP oscillator is by employing sideband transitions either in trapped ions as proposed by *Lee and Sadeghpour* [2013] and refined by *Hush* et al. [2015], or in optomechanical systems [*Walter* et al., 2014]. For clarity, let us focus on the implementation in trapped ions.

The motion of an ion confined in a Paul trap can be approximately modeled as a harmonic oscillator with ladder operators  $a^{(\dagger)}$  that create or annihilate a motional phonon. The dissipative dynamics of a quantum vdP oscillator can be engineered using internal states of the ion: two excited states  $|e_1\rangle$  and  $|e_2\rangle$  that rapidly decay to a third state  $|g\rangle$ . Shining a laser that is blue detuned from the transition  $\sigma_{ge1} = |g\rangle\langle e_1|$  by the frequency corresponding to the energy of a single phonon results in the coupling  $H_b = g(\sigma_{ge1}a + \sigma_{ge1}^{\dagger}a^{\dagger})$ . This is called a blue sideband transition [Leibfried et al., 2003]. Since the state  $|e_1\rangle$  rapidly decays at rate  $\kappa_{e1}$ , we can adiabatically eliminate this internal degree of freedom to obtain

$$\frac{\mathrm{d}}{\mathrm{d}t}\rho = -i[g(\sigma_{ge1}a + \sigma_{ge1}^{\dagger}a^{\dagger}), \rho] + \kappa_{e1}\mathcal{D}[\sigma_{ge1}]\rho \to \frac{g^2}{\kappa_{e1}}\mathcal{D}[a^{\dagger}]\rho. \tag{4.23}$$

The two-photon loss can be engineered analogously with a sideband drive between states  $|g\rangle$  and  $|e_2\rangle$  that is red detuned by two phonon energies. Combining the two processes results in the dynamics of a quantum vdP oscillator.

A discretized version of this proposal has been implemented by Li et al. [2025]; instead of continuous sideband driving, the sidebands are sequentially applied for a short time. A similar system where there is no nonlinear loss, but saturated gain has been proposed by Hush et al. [2015] and realized by Behrle et al. [2023]. This system constitutes a phonon laser, i.e., a laser with phonons instead of photons. As we showed in Eq. (2.6), the quantum vdP oscillator approximates its dynamics close to the lasing threshold. Both Li et al. [2025] and Behrle et al. [2023] have studied phase diffusion and synchronization (or, equivalently, injection locking) to an external signal. In these systems, heterodyne detection is difficult since the loss of phonons is not directly detectable. Instead, the motional state of the ion is read out by employing once more the coupling to internal degrees of freedom. An extension to two (or more) coupled quantum vdP oscillators has so far not been realized but also proposed by Lee and Sadeghpour [2013], Lee et al. [2014], and Hush et al. [2015].

#### 4.2 Quantum spins

Quantum vdP oscillators have served as a good model to understand quantum synchronization due to their close relation to classical vdP oscillators. Building on this analysis, we now turn our attention to quantum spins, which only comprise a few states but nevertheless exhibit a similar synchronization behavior. Here, we focus on two-level systems, i.e., spins-1/2. In Chapter 5, three-level systems, i.e., spins-1, will be discussed to highlight quantum effects in synchronization. By studying the synchronization of quantum spins, one can understand the principal mechanism for superradiant lasing, which will be explained in Section 4.2.3. To arrive there, we first present a single spin-1/2 limit-cycle oscillator and the synchronization behavior of two coupled spins.

A quantum spin-1/2 (in the following referred to as spin) comprises two states  $|0\rangle$  and  $|1\rangle$ . Transformations of the state of the spin are described by Pauli matrices  $\sigma^{x,y,z}$  and ladder operators  $\sigma^{\pm}$ , defined as follows:

$$\sigma^{+} = |1\rangle\langle 0| , \quad \sigma^{-} = |0\rangle\langle 1| ,$$
  

$$\sigma^{x} = \sigma^{+} + \sigma^{-}, \quad \sigma^{y} = i(\sigma^{-} - \sigma^{+}), \quad \sigma^{z} = |1\rangle\langle 1| - |0\rangle\langle 0| .$$

$$(4.24)$$

If there are several spins, we add a subscript to distinguish which spin is being acted upon. Formally, when there are N spins and  $i \in \{1, ..., N\}$ ,

$$\sigma_i^{x,y,z,\pm} \equiv \underbrace{\mathbb{1}_2 \otimes \cdots \otimes \mathbb{1}_2 \otimes}_{i-1 \text{ times}} \sigma^{x,y,z,\pm} \underbrace{\otimes \mathbb{1}_2 \otimes \cdots \otimes \mathbb{1}_2}_{N-i \text{ times}}, \tag{4.25}$$

where  $\mathbb{1}_2$  is the  $2 \times 2$  identity operator. In the case of two spins, we will use subscripts A, B instead of 1, 2.

#### 4.2.1 Quantum limit cycles

The only gain and loss processes that are possible in a spin-1/2 system are linear; a nonlinear two-excitation loss that is key in the dynamics of a quantum vdP oscillator cannot exist in a two-level system. We will therefore consider the master equation

$$\dot{\rho} = -i\left[\frac{\omega}{2}\sigma^z, \rho\right] + \gamma_+ \mathcal{D}[\sigma^+]\rho + \gamma_- \mathcal{D}[\sigma^-]\rho \tag{4.26}$$

with frequency  $\omega$ , gain rate  $\gamma_+$ , and loss rate  $\gamma_-$ . A spin-1/2 has only three degrees of freedom  $s^{\pm,z} = \langle \sigma^{\pm,z} \rangle$ , and the master equation (4.26) can be rewritten as

$$\frac{\mathrm{d}}{\mathrm{d}t}s^{z} = (\gamma_{+} - \gamma_{-}) - (\gamma_{+} + \gamma_{-})s^{z}, \qquad (4.27)$$

$$\frac{\mathrm{d}}{\mathrm{d}t}s^{+} = i\omega s^{+} - (\gamma_{+} + \gamma_{-})s^{+}/2. \tag{4.28}$$

The first line describes the dynamics of the population  $s^z$ . In the steady state, the population is

$$s_{\rm ss}^z = \frac{\gamma_+ - \gamma_-}{\gamma_+ + \gamma_-} \,. \tag{4.29}$$

The second line describes the oscillation at frequency  $\omega$  and the decoherence at rate  $(\gamma_+ + \gamma_-)/2$ . We see that, as for the quantum vdP oscillator, gain and loss also result in decoherence. Due to the decoherence,  $s^+$  vanishes in the long-time limit.

In terms of the density operator, the steady state of the system is

$$\rho_{\rm ss} = \frac{1}{\gamma_+ + \gamma_-} \left( \gamma_- |0\rangle\langle 0| + \gamma_+ |1\rangle\langle 1| \right) . \tag{4.30}$$

This state is a mixture of the states  $|0\rangle$  and  $|1\rangle$ . Therefore, Roulet and Bruder [2018b] dismiss the possibility of synchronization in two-level systems. However, Parra-López and Bergli [2020] show that two-level systems can indeed exhibit features of synchronization, which have been observed in a trapped ion subject to an external drive [Zhang et al., 2023]. Our analysis of the dynamics of a spin-1/2 in the presence of heterodyne detection will support the idea that spins-1/2 can be considered as quantum limit-cycle oscillators.

First, we discuss the phase distribution of a spin-1/2, which is analogous to the phase distribution of the classical and quantum vdP oscillators. It is defined using spin-coherent states [Roulet and Bruder, 2018b; Parra-López and Bergli, 2020]

$$|\theta,\phi\rangle = \exp(-i\phi\sigma^z/2)\exp(-i\theta\sigma^y/2)|1\rangle$$
, (4.31)

and the Husimi-Q function

$$Q(\theta, \phi) = \frac{1}{2\pi} \langle \theta, \phi | \rho | \theta, \phi \rangle . \tag{4.32}$$

The phase  $\phi$  is the azimuthal phase, which is the relevant quantity to analyze synchronization. The parameter  $\theta$  determines the population difference, i.e., the number of excitations in state  $|1\rangle$  and  $|0\rangle$ :  $\langle \theta, \phi | \sigma^z | \theta, \phi \rangle = \cos(\theta)$ . The phase distribution of the phase  $\phi$  is obtained by integrating over  $\theta$ ,

$$Q(\phi) = \int_0^{\pi} d\theta \sin\theta Q(\theta, \phi) = \frac{1}{2\pi} + \frac{1}{4} \operatorname{Re}[\langle \sigma^+ \rangle e^{-i\phi}]. \tag{4.33}$$

Evaluating the integral reveals that the expectation value  $\langle \sigma^+ \rangle$  determines the shape of the phase distribution.

The dynamics of the master equation (4.26) are visualized by the distributions  $Q(\theta, \phi)$  and  $Q(\phi)$  in Fig. 4.6. Similar to the analyses of classical limit-cycle oscillators in the presence of fluctuations [see Fig. 2.3] and the quantum vdP oscillator [see Fig. 4.1], we identify three processes taking place: the rotation at frequency  $\omega$ , the attraction to the limit cycle, and the phase diffusion.

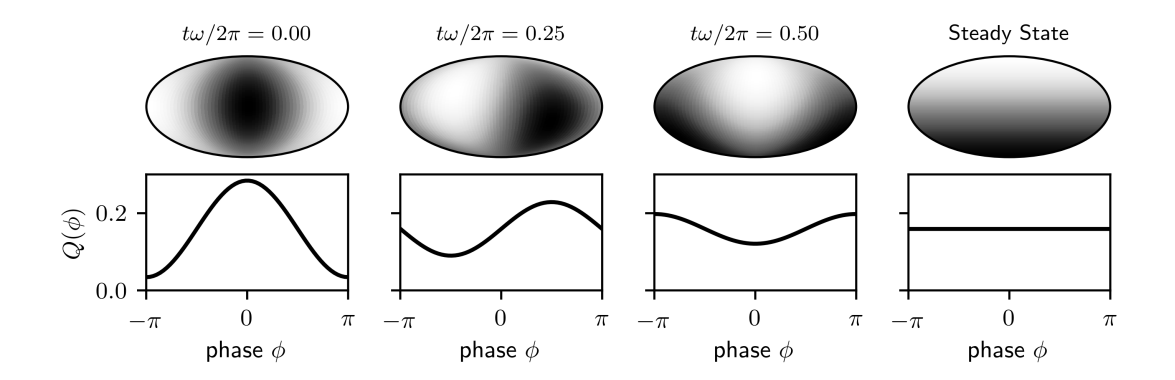


Figure 4.6: Time evolution of the spin-1/2 oscillator shown by the Husimi-Q distribution  $Q(\theta,\phi)$  (top row) and the phase distribution  $Q(\phi)$  (bottom row). The Husimi-Q distribution is shown by a Mollweide projection: Lines of constant  $\theta$  are horizontal; the top and bottom of the plot correspond to  $\theta=0$  and  $\theta=\pi$ , and  $\phi$  increases from left to right. Parameters:  $\gamma_+=\gamma_-/2,\omega=2\gamma_-$ .

#### Quantum limit cycles under heterodyne detection

As for the quantum vdP oscillator, the spin's limit-cycle structure becomes apparent through heterodyne detection. In the presence of a measurement of  $\sigma^-$ , the master equation is

$$\dot{\rho}_{\rm m} = -i\left[\frac{\omega}{2}\sigma^z, \rho_{\rm m}\right] + \gamma_{+}\mathcal{D}[\sigma^{+}]\rho_{\rm m} + \gamma_{-}\mathcal{D}[\sigma^{-}]\rho_{\rm m} + \frac{\mathrm{d}W}{\mathrm{d}t}\sqrt{\gamma_{-}}\left[e^{i\omega_{\rm m}t}(\sigma^{-} - \mathrm{Tr}[\sigma^{-}\rho_{\rm m}])\rho_{\rm m} + \mathrm{H.c.}\right].$$

$$(4.34)$$

Integrating this master equation, we obtain quantum trajectories for the spin-1/2 oscillator; several of them are shown in Fig. 4.7. Despite the presence of fluctuations, we see that the expectation value  $\langle \sigma^z \rangle_{\rm m}$  approaches a constant value, while the expectation value  $\langle \sigma^x \rangle_{\rm m}$  displays limit-cycle oscillations with frequency  $\omega$ . The ensemble average (black line) displays a damped oscillation that agrees well with the solution of the master equation (gray dashed line).

This behavior is equivalent to both the quantum vdP oscillator [see Fig. 4.2] and a classical noisy limit-cycle oscillator [see Fig. 2.2]. We conclude that the spin-1/2 system under measurement shows limit-cycle oscillations. The master equation (4.26) can be understood as describing the ensemble of all possible measurement outcomes. Certainly, under a different type of measurement, such as photodetection, the limit cycle would not be visible. One may take the point of view that a physical system described by a master equation does or does not display limit cycles depending on how the system is observed. This corresponds to considering quantum trajectories as "subjectively real" [Wiseman, 1996].

#### 4.2.2 Two coupled spins

Having described the limit cycle of a single spin-1/2, let us now discuss the synchronization behavior of two coupled spin-1/2 oscillators. Their time evolution is governed by

$$\dot{\rho} = -i\frac{\delta}{4}[\sigma_A^z - \sigma_B^z, \rho] + V\mathcal{D}[\sigma_A^- + \sigma_B^-]\rho + \gamma_+ \left(\mathcal{D}[\sigma_A^+] + \mathcal{D}[\sigma_B^+]\right)\rho + \gamma_- \left(\mathcal{D}[\sigma_A^-] + \mathcal{D}[\sigma_B^-]\right)\rho,$$
(4.35)

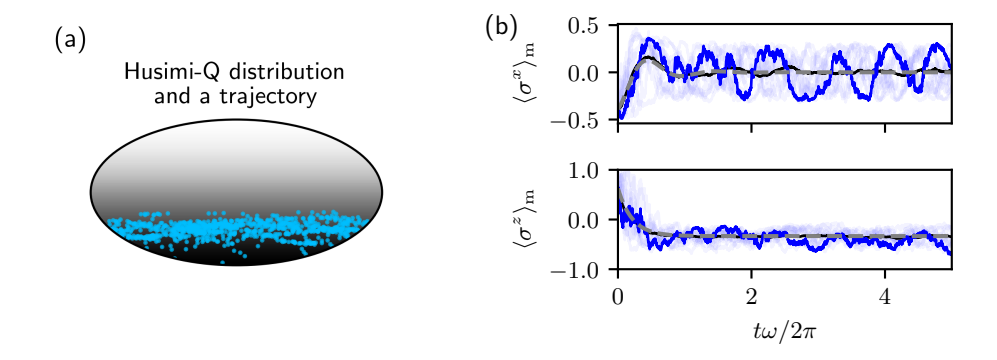


Figure 4.7: Spin-1/2 oscillator: Limit cycle under measurement. (a) The heatmap shows the steady-state Husimi-Q distribution from Fig. 4.6, top-right panel. The blue scatter points show the time evolution of one quantum trajectory. (b) The faint blue lines show the expectation values  $\langle \sigma^x \rangle_{\rm m}$  and  $\langle \sigma^z \rangle_{\rm m}$  of ten different quantum trajectories. The bright blue line highlights one of them. The black line shows the average of 100 such realizations. It overlaps well with the gray dashed line, which is the solution of  $\langle \sigma^x \rangle$  of the master equation without measurement. Same parameters as in Fig. 4.6:  $\gamma_+ = \gamma_-/2, \omega = 2\gamma_-$ .

The system is described in the rotating frame of the average frequency. The detuning between the two spins is  $\delta$  and the coupling strength is V. We can obtain intuition about the dynamics by considering the mean-field equations for the expectation values  $s_{A,B}^{+,z} = \langle \sigma_{A,B}^{+,z} \rangle$ 

$$\frac{\mathrm{d}}{\mathrm{d}t}s_{A}^{z} = (\gamma_{+} - \gamma_{-} - V) - (\gamma_{+} + \gamma_{-} + V)s_{A}^{z}, \qquad (4.36)$$

$$\frac{\mathrm{d}}{\mathrm{d}t}s_B^z = (\gamma_+ - \gamma_- - V) - (\gamma_+ + \gamma_- + V)s_B^z, \qquad (4.37)$$

$$\frac{\mathrm{d}}{\mathrm{d}t}s_A^+ = +i\delta s_A^+/2 - (\gamma_+ + \gamma_- + V)s_A^+/2 + Vs_A^z s_B^+/2, \qquad (4.38)$$

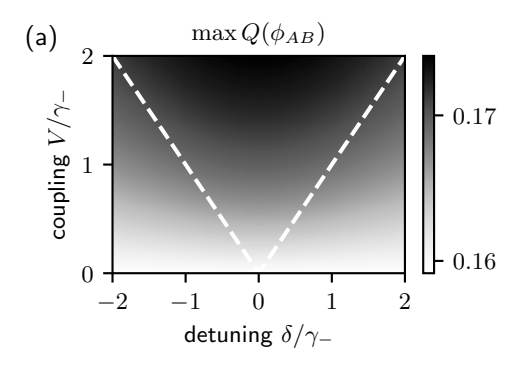
$$\frac{\mathrm{d}}{\mathrm{d}t}s_B^+ = -i\delta s_B^+/2 - (\gamma_+ + \gamma_- + V)s_B^+/2 + Vs_B^z s_A^+/2. \tag{4.39}$$

We have approximated  $\langle \sigma_A^z \sigma_B^+ \rangle = s_A^z s_B^+$  and the same for  $A \leftrightarrow B$ . Within this approximation, the phases  $\phi_{A,B} = \arg[s_{A,B}^+]$  evolve following

$$\frac{\mathrm{d}}{\mathrm{d}t}\phi_A = +\frac{\delta}{2} + s_A^z \frac{V}{2} \frac{|s_B^+|}{|s_A^+|} \sin(\phi_B - \phi_A), \qquad (4.40)$$

$$\frac{\mathrm{d}}{\mathrm{d}t}\phi_{B} = -\frac{\delta}{2} + s_{B}^{z} \frac{V}{2} \frac{|s_{A}^{+}|}{|s_{B}^{+}|} \sin(\phi_{A} - \phi_{B}). \tag{4.41}$$

The phase interactions are qualitatively the same as the phase interactions between two classical limit-cycle oscillators [see Eq. (2.19)] with an effective coupling strength that depends on the  $s_{A,B}^z$  as well as  $|s_{A,B}^+|$ . Therefore, we expect that a positive steady-state value of  $s_{A,B}^z$  results in in-phase locking, while negative  $s_{A,B}^z$  results in out-of-phase locking with phase difference  $\pi$ . To confirm this expectation, we now solve the full master equation (4.35) to analyze phase locking.



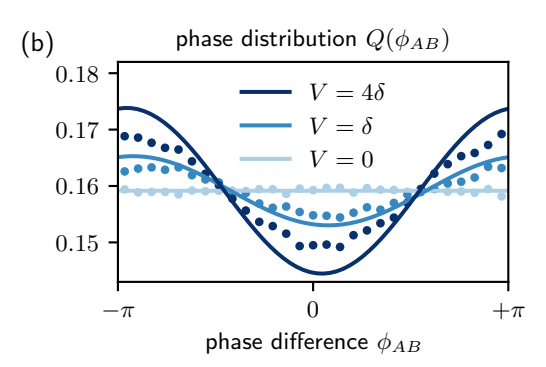


Figure 4.8: Phase locking of spin-1/2 oscillators. (a) The grayscale shows the maximum of the phase distribution  $\max Q(\phi_{AB})$ , a measure of phase locking. The white dashed line indicates the synchronization transition  $V = |\delta|$  expected in classical noiseless oscillators. (b) The lines show the phase distribution  $Q(\phi_{AB})$  for different values of the coupling strength. The scatter points show the corresponding estimate of the phase distribution obtained via the heterodyne current; see Eq. (4.49). Parameters:  $\gamma_+ = \gamma_-/2$ . (b)  $\delta = \gamma_-/2$ .

#### Phase locking

We use a distribution for the phase difference similar to the analyses of the classical and quantum vdP oscillators. It is obtained in analogy to Eq. (4.10) by first projecting the density matrix on spin-coherent states

$$Q(\theta_A, \phi_A, \theta_B, \phi_B) = \frac{1}{4\pi^2} \langle \theta_A, \phi_A | \otimes \langle \theta_B, \phi_B | \rho | \theta_A, \phi_A \rangle \otimes | \theta_B, \phi_B \rangle . \tag{4.42}$$

Then, we integrate over the polar angles  $\theta_{A,B}$  to obtain the combined phase distribution

$$Q(\phi_A, \phi_B) = \int_0^{\pi} d\theta_A \sin \theta_A \int_0^{\pi} d\theta_B \sin \theta_B Q(\theta_A, \phi_A, \theta_B, \phi_B), \qquad (4.43)$$

and we integrate over the global phase to obtain a distribution of the phase difference  $\phi_{AB} = \phi_A - \phi_B$ 

$$Q(\phi_{AB}) = \int_0^{2\pi} d\phi_A \int_0^{2\pi} d\phi_B Q(\phi_A, \phi_B) \delta(\phi_{AB} - \phi_A + \phi_B) =$$
(4.44)

$$= \frac{1}{2\pi} + \frac{\pi}{16} \operatorname{Re}\left[\left\langle \sigma_A^+ \sigma_B^- \right\rangle e^{i\phi_{AB}}\right]. \tag{4.45}$$

For the last step, the integrals have been carried out explicitly; see also Eqs. (A8) and (A13) of *Kehrer* et al. [2024] for a more general expression. Equation (4.45) explicitly shows the relation between the phase distribution and the presence of correlations as measured by  $\langle \sigma_A^+ \sigma_B^- \rangle$  between the two spins. If there are no correlations  $\langle \sigma_A^+ \sigma_B^- \rangle = 0$ , then the phase distribution is flat. As before, we use the maximum value,  $\max Q(\phi_{AB})$ , as a measure for synchronization.

The maximum value of  $Q(\phi_{AB})$  and the phase distribution are shown in Fig. 4.8. Qualitatively, we find the same behavior as for the quantum vdP oscillator and the classical noisy oscillator; see Fig. 4.3 and Fig. 2.4. Here, the spins phase lock with a phase difference of  $\pi$ , since we chose parameters where the gain is smaller than the loss, so that  $s^z$  assumes negative values. Later, we will also confirm that positive values of

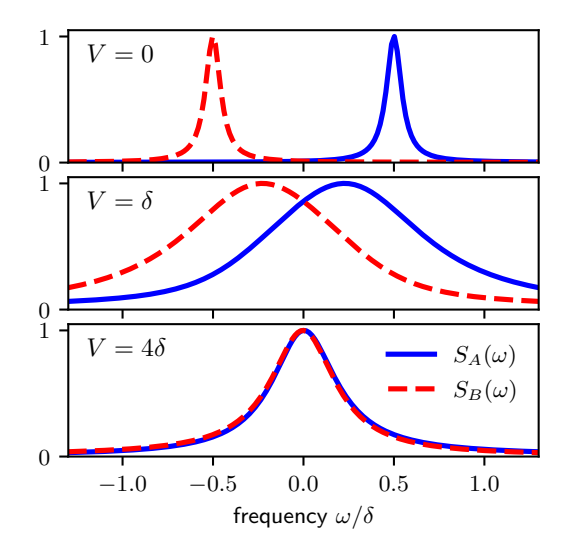


Figure 4.9: Frequency entrainment of spin-1/2 oscillators. The lines show the spectra as calculated by (4.46) for oscillators A (blue solid) and B (red dashed). Parameters:  $\gamma_+ = \gamma_-/2$ ,  $\delta = 5\gamma_-$ .

 $s^z$  correspond to in-phase locking. Quantitatively, the synchronization measure is in general smaller compared to the quantum vdP oscillators due to the smaller Hilbert space. For the spins, the maximum deviation of the phase distribution from  $1/(2\pi)$  is  $\pi/32$  where  $\langle \sigma_A^+ \sigma_B^- \rangle = 1/2$ . For the quantum and classical vdP oscillators, it is not bounded. Intuitively, this is because the phase diffusion is proportional to the inverse amplitude squared [see Eq. (2.13)] and can therefore be arbitrarily small for large amplitudes.

#### Frequency entrainment

To analyze frequency entrainment of two detuned spins, we calculate the spectra in analogy to Eq. (4.12)

$$S_{A,B}(\omega) = \lim_{t \to \infty} \int_{-\infty}^{\infty} d\tau \left\langle \sigma_{A,B}^{+}(t+\tau)\sigma_{A,B}^{-}(t) \right\rangle e^{-i\omega\tau}$$
(4.46)

i.e., the Fourier transforms of the two-time correlations  $\langle \sigma_{A,B}^+(t+\tau)\sigma_{A,B}^-(t)\rangle$ . The spectra are shown in Fig. 4.9 and display frequency entrainment in the same way as the quantum and noisy classical vdP oscillators; see Fig. 4.4 and Fig. 2.5.

#### Quantum synchronization under heterodyne detection

The analysis of synchronization of two spins under heterodyne detection is carried out in the same way as for the two quantum vdP oscillators. The conditional master equation is

$$\dot{\rho} = -i\frac{\delta}{4} [\sigma_A^z - \sigma_B^z, \rho] + V \mathcal{D}[\sigma_A^- + \sigma_B^-] \rho + \gamma_+ \left( \mathcal{D}[\sigma_A^+] + \mathcal{D}[\sigma_B^+] \right) \rho + \gamma_- \left( \mathcal{D}[\sigma_A^-] + \mathcal{D}[\sigma_B^-] \right) \rho + \frac{\mathrm{d}W_A}{\mathrm{d}t} \sqrt{\gamma_-} \left[ e^{i\omega_{\mathrm{m}}t} (\sigma_A^- - \mathrm{Tr} \left[ \sigma_A^- \rho_{\mathrm{m}} \right]) \rho_{\mathrm{m}} + \mathrm{H.c.} \right] + \frac{\mathrm{d}W_B}{\mathrm{d}t} \sqrt{\gamma_-} \left[ e^{i\omega_{\mathrm{m}}t} (\sigma_B^- - \mathrm{Tr} \left[ \sigma_B^- \rho_{\mathrm{m}} \right]) \rho_{\mathrm{m}} + \mathrm{H.c.} \right] ,$$

$$(4.47)$$

with the usual statistics of the noise processes  $dW_{A,B}$ ; see Section 3.3. The heterodyne currents,

$$I_{\text{het,A}} = \sqrt{\gamma_{-}} \operatorname{Tr} \left[ \sigma_{A}^{-} \rho_{\text{m}} \right] + \sqrt{1/2} \left( dW_{A,x} / dt + i dW_{A,y} / dt \right) ,$$

$$I_{\text{het,B}} = \sqrt{\gamma_{-}} \operatorname{Tr} \left[ \sigma_{B}^{-} \rho_{\text{m}} \right] + \sqrt{1/2} \left( dW_{B,x} / dt + i dW_{B,y} / dt \right) ,$$

$$(4.48)$$

can be used to measure phase locking. The phase difference  $\phi_{AB}$  between the two oscillators is estimated by the phase relation of the currents

$$\phi_{AB}^{\mathrm{m}} = \arg[I_{\mathrm{het,B}}/I_{\mathrm{het,A}}]. \tag{4.49}$$

The relative number of occurrences of the measured phase is shown by the scatter points in Fig. 4.8. They qualitatively follow the phase distribution  $Q(\phi_{AB})$ . While in principle, the spectra can be reconstructed from the heterodyne currents, in practice, the signal-to-noise ratio is small (therefore, the reconstructed spectra are not displayed in Fig. 4.9). The signal-to-noise ratio can be increased, however, by considering ensembles of two-level systems. We will see an example of this in Chapter 6; see Fig. 6.9(b).

#### 4.2.3 Large network of coupled spins

Let us now consider synchronization among N coupled quantum spins-1/2, which resembles the Kuramoto model. At the end of this section, we will highlight the connection to superradiant lasers.

We aim to extend the dissipative coupling between two spins of the previous section to all N oscillators. One approach is to include the jump operator from Eq. (4.35) that mediates the coupling for each pair of spins,

$$\frac{V}{N} \sum_{i \le j} \mathcal{D}[\sigma_i^- + \sigma_j^-] \rho. \tag{4.50}$$

We used this approach for the network of N coupled quantum vdP oscillators; see Eq. (4.18). An alternative approach is a single collective jump operator  $\mathcal{D}[S^-]\rho$ , where the collective spin operators are defined by  $S^{\pm} = \sum_{i=1}^{N} \sigma_i^{\pm}$ . This type of collective coupling can be efficiently implemented using a cavity, as we will see at the end of this section. One can show that

$$\mathcal{D}[S^{-}] = \sum_{i < j} \mathcal{D}[\sigma_{i}^{-} + \sigma_{j}^{-}] - (N - 2) \sum_{i=1}^{N} \mathcal{D}[\sigma_{i}^{-}], \qquad (4.51)$$

which implies that the spin-spin interactions are the same for both the pairwise and the collective coupling, but the collective coupling results in less damping for each spin. Hence, there is also less decoherence, and the tendency to synchronize is larger. Therefore, we will now study the collective coupling.

The quantum Lindblad master equation under consideration is

$$\dot{\rho} = \frac{V}{N} \mathcal{D}[S^-] \rho + \sum_{i=1}^{N} \left( \gamma_+ \mathcal{D}[\sigma_i^+] + \gamma_- \mathcal{D}[\sigma_i^-] \right) \rho. \tag{4.52}$$

To get an intuition for the dynamics, let us examine the mean-field equations for the phase  $\phi_i = \arg[\left\langle \sigma_i^+ \right\rangle]$  of each spin, where  $s_i^{\pm,z} \equiv \left\langle \sigma_i^{\pm,z} \right\rangle$ 

$$\frac{\mathrm{d}}{\mathrm{d}t}\phi_{i} = \frac{s_{i}^{z}V}{2N} \sum_{j=1}^{N} \left| s_{j}^{+}/s_{i}^{+} \right| \sin(\phi_{j} - \phi_{i}). \tag{4.53}$$

This set of equations is of the same form as the Kuramoto model [see Eq. (2.29)] with an effective coupling strength  $Vs_i^z|s_j^+/s_i^+|$ , which has been pointed out by Xu and Holland [2015] and Zhu et al. [2015]. When  $\gamma_+ > \gamma_-$ , the population of each spin is inverted and  $s_i^z$  assumes a positive value. In this case, the effective coupling is positive resulting in phase locking among all spins. This process competes with the decoherence, or more specifically, the phase fluctuations due to the coupling to the environment. We expect a Kuramoto-like transition as discussed in Section 2.3.2 from an incoherent to a synchronized state when increasing the collective coupling strength. The coupling strength, above which the spins synchronize, depends on the phase fluctuations, or decoherence, whose amplitude is dominated by  $\gamma_{\pm}$  as we will see below.

In the thermodynamic limit of infinitely many spins, the mean-field equations are exact [Spohn, 1980] and readily solvable when exploiting the permutational invariance by setting  $s^{\pm,z} \equiv s_i^{\pm,z}$  for all i. The mean-field equations are

$$\dot{s}^{+} = V s^{+} s^{z} / 2 - (\gamma_{+} + \gamma_{-}) s^{+} / 2,$$
  

$$\dot{s}^{z} = -2V |s^{+}|^{2} + (\gamma_{+} - \gamma_{-}) - (\gamma_{+} + \gamma_{-}) s^{z}.$$
(4.54)

The fixed point  $s^+=0$ ,  $s^z=(\gamma_+-\gamma_-)/(\gamma_++\gamma_-)\equiv s_0^z$  describes the incoherent state. One can think of this state as all spins possessing an independent random phase due to the large phase fluctuations, such that  $s^+=\sum_j |s_j^+| \exp(i\phi_j)$  averages to zero. This state is stable when the gain rate is smaller than the loss rate,  $\gamma_+<\gamma_-$ . When  $\gamma_+>\gamma_-$ , however, the population is inverted, allowing for phase locking. In this case, a stability analysis reveals that the incoherent state becomes unstable for a coupling V larger than the critical coupling

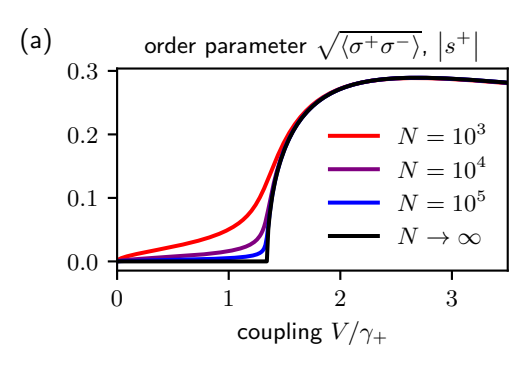
$$V_c = \frac{\gamma_+ + \gamma_-}{s_0^z} \,. \tag{4.55}$$

The critical coupling is proportional to the total decoherence  $\gamma_+ + \gamma_-$  (the decoherence from the collective coupling becomes negligible for  $N \to \infty$ ). For  $V > V_c$ , the attractive phase interactions overcome the decoherence, resulting in a synchronized state. The steady-state solution is

$$s^{z} = (\gamma_{+} + \gamma_{-})/V, \quad |s^{+}|^{2} = \frac{\gamma_{+} - \gamma_{-}}{2V^{2}}(V - V_{c}).$$
 (4.56)

Figure 4.10(a) displays the order parameter  $|s^+|$  by the black line, showing a Kuramotolike synchronization transition. The dependence of the critical coupling on the ratio  $\gamma_+/\gamma_$ is shown in Fig. 4.10(b) by the blue dashed line. For  $\gamma_+ < \gamma_-$ , there is no transition since there is no population inversion. For  $\gamma_+ \gg \gamma_-$ , the critical coupling approaches  $\gamma_+$ .

The effect of frequency disorder among the spins has been studied by Zhu et al. [2015], who found an exact expression for the order parameter in the presence of heterogeneous frequencies sampled from a Lorentzian distribution. As in the Kuramoto model, the coupling strength needs to overcome both frequency disorder and noise for synchronization to occur. A special case of frequency disorder is when there are two distinct frequencies. In this case, we can think of two species, or ensembles, of spins that are detuned from one another and that can synchronize in analogy to two synchronizing oscillators. This scenario



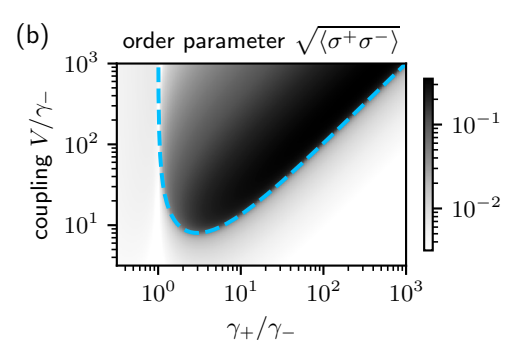


Figure 4.10: Kuramoto-like synchronization transition of spin-1/2 oscillators. (a) The black line shows the order parameter  $|s^+|$  in the long-time limit obtained from the mean-field analysis valid in the limit  $N \to \infty$ . The colored lines show the steady-state order parameter  $\sqrt{\langle \sigma^+ \sigma^- \rangle}$  in the finite-size system for various N. Parameters:  $\gamma_+ = 10\gamma_-$  (b) The heatmap shows the steady-state order parameter  $\sqrt{\langle \sigma^+ \sigma^- \rangle}$  for  $N = 10^4$ . The dashed line indicates the synchronization transition, Eq. (4.55), predicted by the mean-field equations. It agrees well with the boundary between small and large values of the order parameter.

has been proposed by Xu et al. [2014], who find a synchronization transition when the coupling is larger than the detuning. Later, Patra et al. [2019a,b, 2020] identified various dynamical behaviors in the same model, including chaos. Furthermore, an experimental implementation of synchronization between two spin ensembles has been carried out by Weiner et al. [2017]; see details on the experimental implementation below.

#### Finite-size systems

Next, we would like to understand how the synchronization transition depends on the number N of spins. Due to the exponential scaling of the degrees of freedom, we use a cumulant expansion [Kubo, 1962; Plankensteiner et al., 2022], which is a good approximation for large N. Within the cumulant expansion, we derive a set of Heisenberg equations from master equation (4.52) following Eq. (3.9). After taking the expectation value, all expectation values of a product of three operators are replaced following

$$\langle o_1 o_2 o_3 \rangle \to \langle o_1 o_2 \rangle \langle o_3 \rangle + \langle o_1 o_3 \rangle \langle o_2 \rangle + \langle o_1 \rangle \langle o_2 o_3 \rangle - 2 \langle o_1 \rangle \langle o_2 \rangle \langle o_3 \rangle. \tag{4.57}$$

Furthermore, the master equation (4.52) features a U(1) symmetry, which means that no global phase is preferred. Therefore, expectation values such as  $\langle \sigma_i^+ \rangle = 0$  or  $\langle \sigma_i^+ \sigma_j^z \rangle = 0$  will vanish in the long-time limit. We can exploit the U(1) symmetry to set these terms equal to zero, simplifying the equations. Finally, we invoke the permutational invariance among the spins to set all spins equal, e.g.,  $\langle \sigma_i^+ \sigma_j^- \rangle = \langle \sigma^+ \sigma^- \rangle$  for all  $i \neq j$ . This yields the closed set of differential equations

$$\frac{\mathrm{d}}{\mathrm{d}t}s^{z} = \left(\gamma_{+} - \gamma_{-} - \frac{V}{N}\right) - \left(\gamma_{+} + \gamma_{-} + \frac{V}{N}\right)s^{z} - 2V\frac{N-1}{N}\langle\sigma^{+}\sigma^{-}\rangle,$$

$$\frac{\mathrm{d}}{\mathrm{d}t}\langle\sigma^{+}\sigma^{-}\rangle = -\left(\gamma_{+} + \gamma_{-} + \frac{V}{N}\right)\langle\sigma^{+}\sigma^{-}\rangle + \frac{V}{2N}\left(\langle\sigma^{z}\sigma^{z}\rangle + s^{z}\right)$$

$$+ V\frac{N-2}{N}s^{z}\langle\sigma^{+}\sigma^{-}\rangle,$$
(4.58)

$$\frac{\mathrm{d}}{\mathrm{d}t} \langle \sigma^z \sigma^z \rangle = 2 \left( \gamma_+ - \gamma_- - \frac{V}{N} \right) s^z - 2 \left( \gamma_+ + \gamma_- + \frac{V}{N} \right) \langle \sigma^z \sigma^z \rangle$$

$$+ \frac{V}{N} \left( 4 \left\langle \sigma^+ \sigma^- \right\rangle - 4(N - 2) s^z \left\langle \sigma^+ \sigma^- \right\rangle \right) .$$

In the limit  $N \to \infty$ , they are equivalent to the mean-field equations (4.54).

We now use  $\sqrt{\langle \sigma^+ \sigma^- \rangle}$ , which measures the correlations among any two spins, (evaluated in the steady state) as an order parameter for synchronization. In Eq. (4.45), we already identified the relation between phase locking and the correlations between two spins. The order parameter thus quantifies the amount of phase locking between any two spins. Additionally,  $\sqrt{\langle \sigma^+ \sigma^- \rangle}$  becomes  $|s^+|$  for  $N \to \infty$ , further motivating its use as an order parameter.

The colored lines in Fig. 4.10(a) show the synchronization transition for finite N obtained within the cumulant expansion. Similarly to the transition in the Kuramoto model shown in Fig. 2.9, the sharp transition becomes a crossover for a finite number of oscillators. Figure 4.10(b) displays the spin correlations as a function of gain and collective coupling strength. There are close to zero correlations below the critical coupling (blue dashed line), while there is a significantly larger amount of correlations above it, consistent with the transition predicted by the mean-field analysis.

#### Experimental implementation: superradiant laser

The model of synchronization in a large ensemble of spins described above captures the essential physics of a superradiant laser. Superradiant lasers consist of a group of atoms coupled to a cavity; they are a promising source of coherent light due to their stable frequency and superior narrow linewidth [Chen, 2009; Meiser et al., 2009]. In contrast to a standard laser, the cavity decays rapidly, ensuring a small number of excitations in the cavity mode, which renders the laser robust against cavity fluctuations [Bohnet et al., 2012; Norcia and Thompson, 2016]. The laser light exhibits a stable frequency set by the atomic transition frequency. The incoherent drive of each atom (modeled by the term  $\gamma_+ \mathcal{D}[\sigma_i^+] \rho$ ) provides it with energy, allowing for continuous lasing [Norcia and Thompson, 2016; Laske et al., 2019; Kristensen et al., 2023]. In the following, we present a simple theoretical model of the superradiant laser based on Meiser et al. [2009].

The superradiant laser comprises N atoms, each modeled as a quantum spin-1/2 with two states out of the electronic level structure, simply labeled  $|0\rangle$  and  $|1\rangle$ . The atoms are placed in an optical cavity, resulting in a coherent coupling of all spins to the cavity mode at rate  $\Omega$ . The cavity is described by a bosonic mode with ladder operators  $a^{(\dagger)}$ ; it loses excitations at rate  $\kappa$ . The spins lose excitations due to spontaneous emission at rate  $\gamma_-$ , but they are repumped to the excited state at rate  $\gamma_+$ . The repumping can be engineered by a laser coherently driving the transition between state  $|0\rangle$  and a third excited level, which spontaneously decays to state  $|1\rangle$ . We note that realizing the incoherent drive presents an experimental challenge due to heating and atom loss; therefore, other mechanisms for repumping have been proposed [Liu et al., 2020; Reilly et al., 2025]. In the frame rotating with the spin frequency and the cavity frequency, which for simplicity are assumed equal, the master equation is

$$\frac{\mathrm{d}}{\mathrm{d}t}\rho = -i\Omega[a^{\dagger}S^{-} + aS^{+}, \rho] + \kappa \mathcal{D}[a]\rho + \sum_{i=1}^{N} \left(\gamma_{+}\mathcal{D}[\sigma_{i}^{+}] + \gamma_{-}\mathcal{D}[\sigma_{i}^{-}]\right)\rho, \qquad (4.59)$$

We will now connect this model to the master equation of the dissipatively coupled spins, Eq. (4.52). The Heisenberg equation for the cavity mode a reads

$$\frac{\mathrm{d}}{\mathrm{d}t}a = -\frac{\kappa}{2}a - iN\Omega S^{-}. \tag{4.60}$$

In the limit  $\kappa \gg \sqrt{N}\Omega$ , the cavity rapidly follows the spin degrees of freedom, and one can set  $\dot{a}=0$  to find  $a=-2i\Omega S^-/\kappa$ . After inserting this expression into the master equation (4.59), using  $\kappa \mathcal{D}[a] \to N^{-1}V\mathcal{D}[S^-]$  and  $(a^{\dagger}S^- + S^+a) \to 0$ , we obtain the effective model of a dissipatively coupled spin ensemble, Eq. (4.52) with  $V=4N\Omega^2/\kappa$ .

Having reduced the model of the superradiant laser to a model of synchronizing quantum spins makes it possible to understand the dynamics of the superradiant laser in terms of synchronization. The cavity-mediated coupling results in attractive phase locking among the atomic dipoles that counteracts phase diffusion due to decoherence. As we discussed in the context of the Kuramoto model in the presence of fluctuations [see Section 2.3.2], a collective phase-coherent state arises if the coupling is large enough, which intuitively explains the narrow linewidth of the laser. The minimal linewidth of a superradiant laser is  $\Delta\nu_{\rm min} = V/N$  [Meiser et al., 2009]. In terms of the cooperativity  $C = 4\Omega^2/(\kappa\gamma_-)$ , the expression becomes  $\Delta\nu_{\rm min} = C\gamma_-$ . Therefore, the cavity is designed such that the cooperativity C is small, and the states  $|0\rangle$  and  $|1\rangle$  are chosen such that the spontaneous emission rate  $\gamma_-$  is small. For typical experimental parameters,  $C \approx 0.15$  and  $\gamma_- \approx 10$  mHz, this evaluates to a minimal linewidth of  $\Delta\nu_{\rm min} \approx 1.5$  mHz. Superradiant lasers offer great technological promise as their exceptionally narrow linewidth is expected to improve the precision of optical atomic clocks [Ludlow et al., 2015].

Two experiments further highlight the connection between superradiant lasers and synchronization. Cox et al. [2014] investigated the response of a superradiant laser to external driving. Similarly to how two oscillators synchronize, the superradiant laser synchronizes to the external drive when the drive strength is sufficiently large compared to the detuning between the drive and laser frequencies. In the context of lasers, one also refers to this process as injection locking. Later, Weiner et al. [2017] experimentally studied synchronization between two detuned superradiant ensembles of atoms. Both phase locking and frequency entrainment were measured via heterodyne detection to characterize the synchronization of the two ensembles.

#### 4.3 Conclusions

In this chapter, we introduced the basic concepts of quantum synchronization, building on the previous chapter on synchronization in classical systems. We presented two models of quantum limit-cycle oscillators: quantum van-der-Pol oscillators and spins-1/2. We studied their synchronization behavior, moving from single limit-cycle oscillators to large networks of coupled oscillators. We have shown how these driven-dissipative quantum systems feature limit cycles, phase locking, frequency entrainment, and a collective Kuramoto-like synchronization transition. Finally, we connected synchronization in the spin ensemble to the superradiant laser. We will revisit this connection in Chapter 7.

Throughout, we have highlighted the qualitative similarity between synchronization of quantum oscillators and synchronization of classical oscillators subject to noise. We demonstrated that analogous measures of phase locking and frequency entrainment can be used to characterize synchronization of quantum and classical limit-cycle oscillators. The measures rely on phase-space distributions and emission spectra.

The qualitative similarity between quantum and classical synchronization becomes particularly evident through continuous measurement. Individual quantum trajectories

4.3. Conclusions 53

obtained through heterodyne detection exhibit persistent, coherent oscillations with additional noise similar to the trajectories of classical limit-cycle oscillators subject to noise. Viewing quantum limit cycles through the lens of a suitable measurement goes beyond the ensemble analysis using the density operator; this contributes to understanding what a quantum limit cycle is. Furthermore, the measurement perspective connects theoretical measures of quantum synchronization to an experimentally accessible quantity: the heterodyne current of the photodetector.

Having established the similarity between quantum and classical synchronization provides a solid intuition for the dynamics of the quantum systems that we will investigate in the remainder of this work. However, this similarity is not always present. Much research is devoted to understanding quantum, i.e., nonclassical, features of synchronization. For example, the relation between synchronization and entanglement is explored extensively [Lee et al., 2014; Roulet and Bruder, 2018a; Zhu et al., 2015; Witthaut et al., 2017; Lorenzo et al., 2022; Mari et al., 2013; Bandyopadhyay and Banerjee, 2023]. Furthermore, there are synchronization behaviors unique to quantum systems [Lörch et al., 2016, 2017; Amitai et al., 2018; Dutta and Cooper, 2019; Mok et al., 2020; Shen et al., 2023a]. In the following chapter, we will explore collective synchronization transitions that are unique to quantum many-body systems.

# Chapter 5

# Macroscopic quantum synchronization effects

The results of this chapter have been published in

Macroscopic Quantum Synchronization Effects, T. Nadolny and C. Bruder, Physical Review Letters, 131, 190402 (2023)

In Chapter 4, we extended the concept of synchronization to quantum systems. To a large extent, we found that the synchronization properties of both these models are qualitatively the same as those of classical systems with noise. This is not always the case; the present chapter shows that the quantum nature of oscillators can result in a qualitatively different synchronization behavior. In other words, we will present a self-organization transition to a collectively ordered state that inherits characteristic features of the individual quantum constituents.

It has been established in previous studies that quantum effects are relevant in the synchronization of a few quantum oscillators [Lörch et al., 2016, 2017; Dutta and Cooper, 2019; Shen et al., 2023a]; we present some of these effects in Section 5.1. For large networks of coupled oscillators, however, it remained unclear if these effects persist and if the microscopic details of each quantum oscillator matter for the macroscopic synchronization dynamics. While quantum features in large networks like the presence of entanglement and quantum discord are studied [Zhu et al., 2015; Witthaut et al., 2017; Lorenzo et al., 2022; Mari et al., 2013; Bandyopadhyay and Banerjee, 2023], the synchronization dynamics are mostly similar to the dynamics in classical synchronization. In Sections 5.2 to 5.4, we propose and discuss a model of a large network of coupled quantum oscillators in which the synchronization dynamics is qualitatively shaped by their quantum nature.

# 5.1 Quantum synchronization effects in one or two oscillators

We start by presenting a three-level (or spin-1) quantum limit-cycle oscillator and its synchronization behavior. Specifically, we present two blockades of synchronization marked by the absence of phase locking. Both originate from quantum properties. The interference blockade is related to coherences that interfere destructively [Koppenhöfer and Roulet, 2019]. The quantum synchronization blockade is due to off-resonances that stem from the quantized level structure [Lörch et al., 2017]. Understanding the synchronization behavior on the level of one or two oscillators allows us to explain the self-organization transition in a large network of coupled spin-1 oscillators in the following sections.

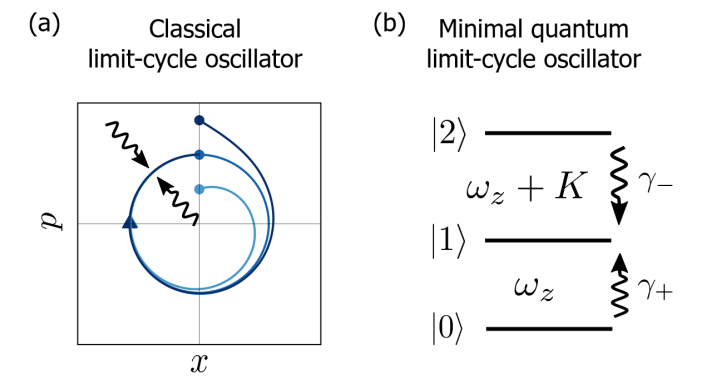


Figure 5.1: (a) Classical vdP limit cycle as presented in Chapter 2. Gain and loss stabilize a specific amplitude of the limit cycle. (b) Sketch of the spin-1 oscillator consisting of three levels. Gain and loss incoherently drive the population to state  $|1\rangle$ . The bare frequency is  $\omega_z$  and the asymmetry of the level structure is parameterized by K.

#### 5.1.1 Interference blockade

The individual oscillator under study is a quantum system with three states  $|0\rangle$ ,  $|1\rangle$ , and  $|2\rangle$ . It is described by spin-1 operators, which are defined as  $S^z = |2\rangle\langle 2| - |0\rangle\langle 0|$ ,  $S^+ = \sqrt{2}(|2\rangle\langle 1| + |1\rangle\langle 0|)$ , and  $S^- = (S^+)^{\dagger}$ . Two dissipative processes render the system a limit-cycle oscillator. They are  $\gamma_+ \mathcal{D}[|1\rangle\langle 0|] \rho$  and  $\gamma_- \mathcal{D}[|1\rangle\langle 2|] \rho$ , which pump the population from state  $|0\rangle$  to state  $|1\rangle$  at rate  $\gamma_+$  and from state  $|2\rangle$  to state  $|1\rangle$  at rate  $\gamma_-$ . Due to these gain and loss processes, each three-level oscillator forms a limit cycle [Roulet and Bruder, 2018b], whose population (measured by  $S^z$ ) is stabilized, while the phase of the amplitude (measured by  $S^+$ ) is free.

The analogy to a classical limit cycle is portrayed in Fig. 5.1. Panel (a) shows the limit-cycle of a classical van-der-Pol oscillator. Consider now decreasing its amplitude to the lowest few Fock states, specifically so that the limit-cycle amplitude matches the amplitude of the first Fock state  $|1\rangle$ . Restricting the dynamics to only the two neighboring Fock states,  $|0\rangle$  and  $|2\rangle$ , results in the minimal model for a quantum three-level, or spin-1, limit cycle as described above. It is sketched in Fig. 5.1(b). This system has been proposed by Roulet and Bruder [2018b] and studied in further works since [Koppenhöfer and Roulet, 2019; Solanki et al., 2023; Roulet and Bruder, 2018a; Kehrer et al., 2024]. We additionally allow for an asymmetric level structure, parameterized by K, which sets the asymmetry in energy differences between levels  $|2\rangle$  and  $|1\rangle$ , and the levels  $|1\rangle$  and  $|0\rangle$ .

The master equation for a three-level oscillator subject to an external drive is

$$\dot{\rho} = -i \left[ K |2\rangle\langle 2| + (\Omega S^{+} + \Omega^{*} S^{-}), \rho \right] + \gamma_{+} \mathcal{D} \left[ |1\rangle\langle 0| \right] \rho + \gamma_{-} \mathcal{D} \left[ |1\rangle\langle 2| \right] \rho. \tag{5.1}$$

We moved to a frame rotating with the frequency  $\omega_z$ . The first term describes the energy level asymmetry K. The second term represents an external drive with amplitude  $\Omega$  resonant with the bare frequency  $\omega_z$  (therefore, there is no time dependence in the rotating frame). Similar to phase locking between two oscillators, we will now discuss how the oscillator locks its phase to the external drive. Later, we use these results to understand the transition to a synchronized state in a large network.

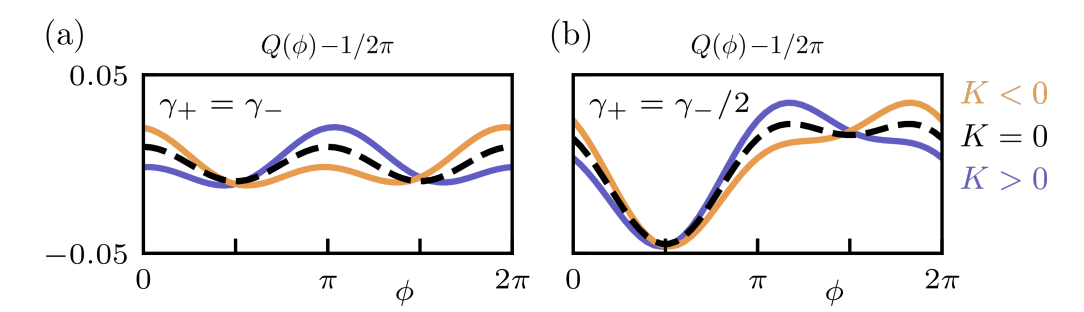


Figure 5.2: Phase distributions  $Q(\phi)$  (the mean  $1/2\pi$  is subtracted) of a single spin-1 oscillator subject to an external drive for K=0 (black dashed),  $K/(\gamma_- + \gamma_+) = -1/10$  (orange),  $K/(\gamma_- + \gamma_+) = +1/10$  (blue). (a) Equal rates  $\gamma_+ = \gamma_-$  result in the interference blockade when K=0, i.e., no unique phase is preferred. (b) Imbalanced rates  $\gamma_+ = \gamma_-/2$  lift the interference blockade. Parameters:  $\Omega/\gamma_- = 1/10$ .

In the same way that we analyzed the phase distribution of a spin-1/2 in Eq. (4.33), we assess the phase response of the spin-1 oscillator by the phase distribution [Lee and Sadeghpour, 2013; Roulet and Bruder, 2018b]

$$Q(\phi) = \int_0^{\pi} d\theta \sin \theta Q(\theta, \phi). \tag{5.2}$$

We use the Husimi-Q distribution

$$Q(\theta, \phi) = \frac{3}{4\pi} \langle \theta, \phi | \rho | \theta, \phi \rangle \tag{5.3}$$

and spin-coherent states

$$|\theta,\phi\rangle = \exp(-i\phi S^z) \exp(-i\theta S^y) |2\rangle$$
, (5.4)

with  $S^y = i(S^- - S^+)/2$ . This phase distribution was generalized to SU(3) coherent states including two free phases by Jaseem et al. [2020b] and Solanki et al. [2023]; for our purposes, it is sufficient to consider one phase.

To discuss phase locking in the long-time limit, we compute the steady state of the master equation (5.1) and show the resulting phase distributions  $Q(\phi)$  in Fig. 5.2. Figure 5.2(a) displays the case of equal gain and loss,  $\gamma_+ = \gamma_-$ . For K = 0, the coherences resulting from the external drive have opposite signs, such that their contributions to the phase distribution partially cancel, which is referred to as the *interference block-ade* [Koppenhöfer and Roulet, 2019]. It becomes apparent in the phase distribution (black dashed line), which shows two peaks of equal height at  $\phi = 0$  and  $\phi = \pi$  instead of a single maximum. This means that the oscillator does not uniquely lock its phase with respect to the external drive; rather, it shows a bistable behavior, locking equally likely in and out of phase. For other ratios of  $\gamma_+/\gamma_-$ , the interference blockade is lifted and the phase distribution indicates a unique phase preference. For example, in Fig. 5.2(b), where  $\gamma_+ = \gamma_-/2$ , the black-dashed line indicates a phase preference at around  $\phi = 3\pi/2$ .

The asymmetry parameter K also lifts the interference blockade, resulting in in-phase locking for K < 0 and anti-phase locking for K > 0. This behavior is exemplified by the colored lines of Fig. 5.2(a,b), where the orange line (negative K) peaks closer to 0 and  $2\pi$ , while the blue line (positive K) peaks closer to  $\pi$ . The fact that negative K corresponds to in-phase alignment while positive K implies anti-phase alignment will be relevant in our discussion of synchronization in a large ensemble in Section 5.3.

#### 5.1.2 Quantum synchronization blockade

Next, consider two coupled spin-1 oscillators, each of the form described in the previous subsection and displayed in Fig. 5.1(b). The two oscillators have frequency  $\omega_z \pm \delta/2$ . Their quantum master equation in the frame rotating with the average frequency  $\omega_z$  is

$$\dot{\rho} = -i\left[\frac{\delta}{2}(S_A^z - S_B^z) + K(|2\rangle\langle 2|_A + |2\rangle\langle 2|_B) + V_{AB}(S_A^+ S_B^- + S_B^+ S_A^-), \rho\right] + \left(\gamma_+ \mathcal{D}\left[|1\rangle\langle 0|_A\right] + \gamma_- \mathcal{D}\left[|1\rangle\langle 2|_A\right] + \gamma_+ \mathcal{D}\left[|1\rangle\langle 0|_B\right] + \gamma_- \mathcal{D}\left[|1\rangle\langle 2|_B\right]\right)\rho.$$

$$(5.5)$$

The two oscillators labeled A and B differ by the detuning  $\delta$  between them. The interaction among the oscillators is described by the Hamiltonian  $V_{AB}(S_A^+S_B^- + S_B^+S_A^-)$ . In contrast to the coupling discussed in the previous chapter [see Eq. (4.8) and Eq. (4.35)], the coupling is coherent and not dissipative.

As for the quantum van-der-Pol oscillators and the spins-1/2 [see Eq. (4.10) and Eq. (4.43)], we analyze phase locking using the phase distribution  $Q(\phi_{AB})$  for the relative phase  $\phi_{AB}$ ,

$$Q(\phi_{AB}) = \int d\theta_A d\theta_B d\phi_A d\phi_B \sin \theta_A \sin \theta_B \times Q(\theta_A, \theta_B, \phi_A, \phi_B) \times \delta(\phi_{AB} - \phi_A + \phi_B).$$
(5.6)

Here, we use the Husimi-Q function generalized to two oscillators

$$Q(\theta_A, \theta_B, \phi_A, \phi_B) = \frac{9}{16\pi^2} \langle \theta_A, \phi_A | \otimes \langle \theta_B, \phi_B | \rho | \theta_A, \phi_A \rangle \otimes | \theta_B, \phi_B \rangle . \tag{5.7}$$

We compute the steady state of the master equation (5.5) and the corresponding phase distribution  $Q(\phi_{AB})$ . The maximal value of the phase distribution, max  $Q(\phi_{AB})$ , serves as a measure for the strength of phase locking; it is shown in Fig. 5.3(a) for different values of  $\delta$  and K. Clearly, there is stronger phase locking in the region  $|K| \approx |\delta|$  and suppression of synchronization when |K| is different from  $|\delta|$ . This is the microscopic quantum synchronization blockade [Lörch et al., 2017]. To explain this finding, let us first consider  $\delta = -K$ . In this case, the energy difference between states  $|1\rangle$  and  $|2\rangle$  of oscillator A is equal to that between states  $|0\rangle$  and  $|1\rangle$  of oscillator B. Thus, the transition  $|1\rangle_A \otimes |1\rangle_B \leftrightarrow |2\rangle_A \otimes |0\rangle_B$  is resonant, which leads to a strong phase locking. We also find strong phase locking for  $\delta = +K$  where the energy difference between states  $|0\rangle$  and  $|1\rangle$  of oscillator A is equal to that between states  $|1\rangle$  and  $|2\rangle$  of oscillator B. Then, the transition  $|1\rangle_A \otimes |1\rangle_B \leftrightarrow |0\rangle_A \otimes |2\rangle_B$  is resonant. These two transitions are the most important ones, since they include the limit-cycle state  $|1\rangle_A \otimes |1\rangle_B$ , which is the most populated one. When  $|\delta|$  differs significantly from |K|, the influence of the coupling is suppressed since the dominant transitions are off-resonant. Figure 5.3(a) highlights the resonances as well as the suppression of synchronization.

The microscopic quantum synchronization blockade has been highlighted as a quantum effect of synchronization, where identical oscillators synchronize less strongly compared to detuned oscillators. We will later see how this blockade between two oscillators influences the macroscopic synchronization behavior in the many-body model of two ensembles of spin-1 oscillators. In that context, we will also come back to Panels (b) and (c) of Fig. 5.3.

# 5.2 Many-body model

So far, it has remained an open question whether quantum effects in synchronization survive when increasing the number of oscillators. Will the quantum nature of the

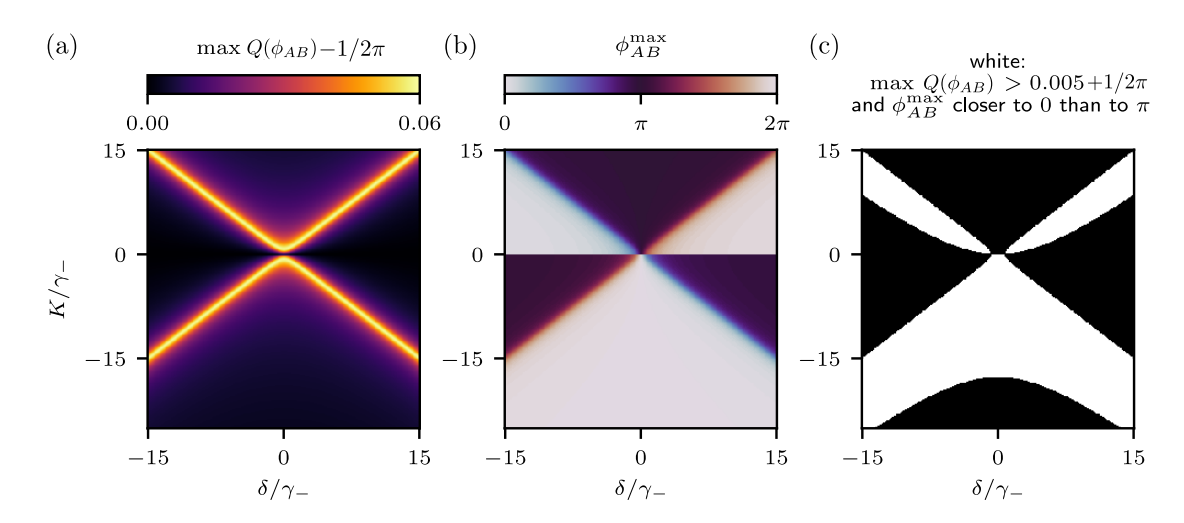


Figure 5.3: Analysis of phase locking of two spin-1 oscillators. (a) Maximum of the phase distribution (the mean  $1/2\pi$  is subtracted). (b) Argument  $\phi_{AB}^{\rm max}$  of the maximum shown in (a). The relative phase is approximately zero below the resonances and approximately  $\pi$  above them. At the resonances, they cross  $\pm \pi/2$  as indicated by the blue and red stripes. Furthermore, the phase shift between oscillators A and B below the resonances is closer to zero for  $K \lesssim -\delta$ , and closer to  $\pi$  for  $K \lesssim \delta$  as indicated by the white and black regions. (c) In this bitmap, white pixels indicate that the maximum of the phase distribution is larger than the threshold of  $5 \times 10^{-3}$ , and the maximum phase is closer to 0 than to  $\pi$ . Parameters:  $\gamma_- = 2\gamma_+$ ,  $V = \gamma_-/10$ .

oscillators be reflected in the macroscopic dynamics? Or does the detailed microscopic description of each oscillator become irrelevant, resulting in dynamics described by generic classical synchronization models? A third possibility is the emergence of behavior not visible at the level of a few coupled oscillators.

We will now answer these questions and show how in a macroscopic ensemble of interacting quantum oscillators, the synchronization behavior is qualitatively shaped by their quantum nature. This is explained through a comprehensive understanding of the behavior of individual oscillators presented in the previous section. Both the interference blockade and the quantum synchronization blockade remain influential in a large network. We also identify aspects of the dynamics that are understood as typical synchronization transitions independently of the microscopic quantum properties. Finally, we discuss phase frustration in the network: If the coupling causes each oscillator to favor antialignment of its phase with respect to the other oscillators, collective synchronization is suppressed. This results in emergent blockades of synchronization only present in the many-body system.

We first consider the model schematically shown in Fig. 5.4. It comprises a large group of N all-to-all coupled oscillators and thus resembles the Kuramoto model discussed in Section 2.3. Here, however, the group consists of quantum oscillators with three states  $|0\rangle$ ,  $|1\rangle$ , and  $|2\rangle$  each, as presented in the previous sections. In the frame rotating with the bare frequency  $\omega_z$ , the time evolution is governed by the quantum master equation  $\dot{\rho} = -i[H_0 + H_{\rm int}, \rho] + \mathcal{L}\rho$ , with

$$H_{0} = \sum_{i} K |2\rangle\langle 2|_{i} , \quad H_{\text{int}} = \frac{V}{N} \sum_{i < j} (S_{i}^{+} S_{j}^{-} + S_{i}^{-} S_{j}^{+}) ,$$

$$\mathcal{L} = \sum_{i} (\gamma_{+} \mathcal{D} [|1\rangle\langle 0|_{i}] + \gamma_{-} \mathcal{D} [|1\rangle\langle 2|_{i}]) .$$

$$(5.8)$$

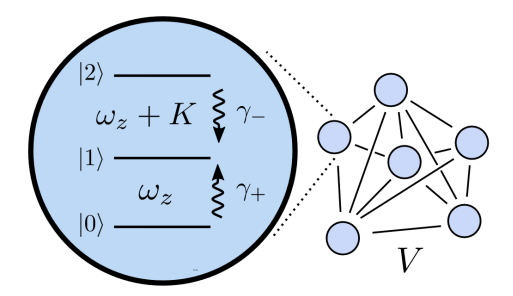


Figure 5.4: A group of N quantum oscillators that are all-to-all coupled through coherent interactions at strength V. Each oscillator consists of three levels ( $|0\rangle$ ,  $|1\rangle$ , and  $|2\rangle$ ) and is incoherently driven to state  $|1\rangle$  at rates  $\gamma_{\pm}$ . The bare frequency is  $\omega_z$  and the asymmetry of the level structure is parameterized by K.

In the sums, i and j take values from 1 to N. The spin-1 operators  $S_i^{z,\pm}$  are defined as before for each spin i. This master equation extends the model of two oscillators defined in Eq. (5.5) to a large ensemble of oscillators. It can be thought of as a Kuramoto model of spin-1 oscillators with coherent coupling. The bare Hamiltonian  $H_0$  describes the coherent dynamics in the absence of any coupling. For each oscillator, the parameter K sets the asymmetry in energy differences between levels  $|2\rangle$  and  $|1\rangle$ , and the levels  $|1\rangle$  and  $|0\rangle$ . The interaction among the oscillators is described by  $H_{\rm int}$ . All oscillators are coherently coupled to all others. The coupling strength within each group is V. Finally, as before, each three-level oscillator is incoherently driven to the level  $|1\rangle$ , with strength  $\gamma_+$  ( $\gamma_-$ ) from level  $|0\rangle$  ( $|2\rangle$ ).

Because of the exponential growth of the Hilbert space size, solving the master equation becomes intractable for large N. We employ a mean-field treatment, which for the case of an all-to-all coupling discussed here gives an exact solution for the macroscopic dynamics in the limit  $N \to \infty$  [Spohn, 1980]. This approach corresponds to neglecting correlations between oscillators, encoded in the product-state ansatz,  $\rho = \bigotimes_i \rho_i$  [Lee et al., 2014]. Since all oscillators are identical, their time evolution can be described in terms of a single three-level oscillator with density matrix  $\rho_{\rm mf}$  coupled to the mean amplitude  $\langle S^+ \rangle = {\rm Tr}[\rho_{\rm mf} S^+] = 1/N \sum_i \langle S_i^+ \rangle$ . Consequently, the dynamics of the group are described by the nonlinear master equations

$$\dot{\rho}_{\rm mf} = -i \left[ K |2\rangle\langle 2| + V \left( S^{+} \langle S^{-} \rangle + S^{-} \langle S^{+} \rangle \right), \rho_{\rm mf} \right] + \left( \gamma_{+} \mathcal{D} \left[ |1\rangle\langle 0| \right] + \gamma_{-} \mathcal{D} \left[ |1\rangle\langle 2| \right] \right) \rho_{\rm mf}.$$
(5.9)

This equation is the analog of the mean-field equations that we discussed for coupled quantum vdP oscillators and spins-1/2; see Eqs. (4.19) and (4.54). To obtain the results below, we numerically time-integrate the nonlinear master equation (5.9). Additionally, we perform a stability analysis of the unsynchronized state  $\rho_{\rm mf} = |1\rangle\langle 1|$ , which is a solution of  $\dot{\rho}_{\rm mf} = 0$ .

# 5.3 Synchronization transition

To investigate the state of the group, we utilize the mean amplitude  $\langle S^+ \rangle = 1/N \sum_i \langle S_i^+ \rangle$  as an order parameter. The phase  $\phi_i$  of each oscillator is defined through  $\langle S_i^+ \rangle = \exp(i\phi_i) |\langle S_i^+ \rangle|$ . Consequently, the order parameter  $\langle S^+ \rangle$  is analogous to the one defined for the Kuramoto model; see Eq. (2.30). Intuitively, in the absence of any coupling all oscillators exhibit random phases due to the noise that stems from the coupling to the environment. In this case, we expect the mean amplitude to vanish in the limit

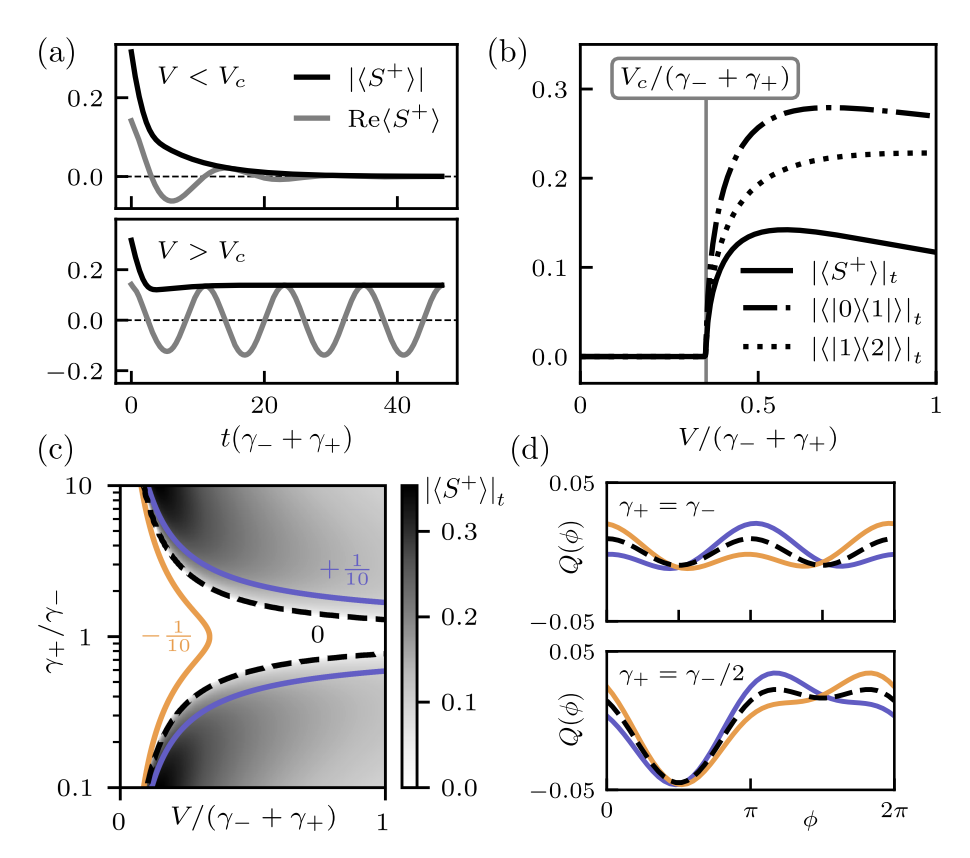


Figure 5.5: Synchronization of a single group. (a) Time evolution of the amplitude  $\langle S^+ \rangle$  below and above the critical coupling strength  $V_c$ , specifically  $V/(\gamma_- + \gamma_+) = 1/5$  and  $V/(\gamma_- + \gamma_+) = 3/5$ . (b) Time-averaged long-time limit amplitude  $|\langle S^+ \rangle|_t$  and coherences, showing a sharp transition at  $V_c$ . Parameters in (a) and (b):  $\gamma_+ = \gamma_-/2$  and K = 0. (c) Order parameter  $|\langle S^+ \rangle|_t$  as a function of the coupling strength V and  $\gamma_+/\gamma_-$  as a gray-scale image for asymmetry parameter K=0. The black dashed line displays the corresponding critical coupling strength obtained from a stability analysis. The orange and blue lines show the critical coupling strengths for  $K/(\gamma_- + \gamma_+) = -1/10$  and +1/10, respectively. In the region  $\gamma_+/\gamma_-$  around 1, synchronization is suppressed for  $K \geq 0$  due to the interference blockade; for negative values of K, the blockade vanishes and synchronization reappears, as indicated by the finite critical coupling strength for  $K/(\gamma_- + \gamma_+) = -1/10$  (orange line). (d) Phase distributions  $Q(\phi)$  (the mean  $1/2\pi$  is subtracted) for the same values of  $K/(\gamma_- + \gamma_+)$  as in (c) (same data as shown in Fig. 5.2).

of infinitely many oscillators  $N \to \infty$ . Indeed, numerical integration of the mean-field equations shows that for small coupling strengths, the group of oscillators converges to the steady state  $\rho_{\rm mf} = |1\rangle\langle 1|$  exhibiting no phase preference,  $\langle S^+ \rangle = 0$ .

The coupling among the oscillators, however, tends to align their phases. As in the Kuramoto model describing classical phase oscillators [see Section 2.3], there is a critical coupling strength  $V_c$  above which the group synchronizes. The critical coupling usually depends on both the noise and the frequency disorder inherent in the system. For a group of identical oscillators, there is no frequency disorder but only intrinsic noise whose strength depends on the rates  $\gamma_-$  and  $\gamma_+$  at which each oscillator couples to the environment.

Figure 5.5(a) displays the time evolution of the mean amplitude in both the unsynchronized and synchronized regimes. Below the critical coupling strength, the zero-amplitude state is stable. For  $V > V_c$ , in the synchronized regime, the alignment of phases leads to a finite amplitude in the long-time limit with persistent oscillations of  $\text{Re}[\langle S^+ \rangle]$ . The frequency of this oscillation will be further addressed when discussing the behavior of two coupled groups. Other quantities not shown in Fig. 5.5(a) also change when entering the synchronized phase: The states  $|0\rangle$  and  $|2\rangle$  become populated, and the coherence  $\langle |0\rangle\langle 2|\rangle$  exhibits oscillations at twice the frequency compared to those of  $\langle S^+ \rangle$ .

To analyze the presence of synchronization among the oscillators, we use the time-average of the (in general time-dependent) absolute value of the amplitude  $|\langle S^+ \rangle|_t$  in the steady state. Figure 5.5(b) depicts this order parameter as a function of the coupling strength, showing a sharp transition between the unsynchronized and synchronized states. This resembles the synchronization transition in the Kuramoto model; see Fig. 2.9(b).

So far, we set  $\gamma_+/\gamma_- = 1/2$  and observed a typical synchronization transition. We now present the order parameter as a function of both the coupling strength and the ratio  $\gamma_+/\gamma_$ in Fig. 5.5(c). Most notably, for equal gain and loss rates, the critical coupling diverges. i.e., the transition to synchronization disappears. This is a macroscopic manifestation of the interference blockade that we reviewed in Section 5.1.1. Synchronization of a single three-level quantum limit-cycle oscillator subject to an external drive is suppressed when gain and loss rates are equal due to destructive interference. As a result, there is no unique phase locking; see black dashed line in the top panel of Fig. 5.5(d) [Fig. 5.5(d) shows the same data as Fig. 5.2]. The divergence of the critical coupling strength in Fig. 5.5(c) reveals that the interference microscopic blockade also shapes the emergent collective order of the macroscopic ensemble. Let us explain this behavior. In the ensemble, each oscillator reacts as being driven by the mean field; compare Eq. (5.1) and Eq. (5.9) where the effective drive strength is  $\langle S^- \rangle$ . In the case  $\gamma_+ = \gamma_-$  and K = 0, the phase shifts  $\phi = 0$  and  $\phi = \pi$  between oscillator and drive are equally likely. For the ensemble of oscillators, this implies that each oscillator tends to align its phase either in or out of phase with the mean field. Hence, the response of each oscillator will on average not amplify the coherence of the group, which leads to the absence of synchronization, i.e., the macroscopic interference blockade.

For a single asymmetric three-level oscillator, the interference blockade is lifted for any non-zero value of the asymmetry parameter K [Solanki et al., 2023]. In contrast, we find that the blockade in the macroscopic ensemble is lifted only for K < 0, but persists for  $K \ge 0$ . This is indicated by the orange and blue lines in Fig. 5.5(c), which show the critical coupling for K < 0 and K > 0. In the case K < 0 (orange line), the critical coupling remains finite for  $\gamma_+ = \gamma_-$ . For K > 0 (blue line), however, the critical coupling diverges, indicating the interference blockade at equal gain and loss rates. To understand this behavior, let us once more revisit the microscopic quantum synchronization behavior. Figure 5.5(d) shows the phase distribution  $Q(\phi)$  of a single oscillator coupled to an external drive in the steady state for various values of K. The top panel concerns the

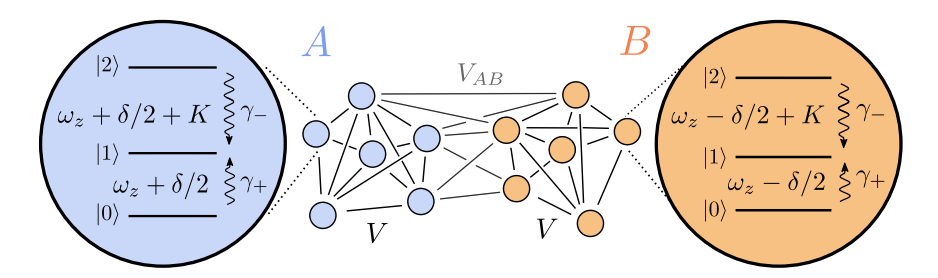


Figure 5.6: Two groups A and B of N quantum oscillators each. The oscillators in group A are detuned from the ones in group B by  $\delta$ . Otherwise, the oscillators are all-to-all coupled and of the same form as in Fig. 5.4 with bare frequency  $\omega_z$  and asymmetry parameter K. The coupling strength within each group is V, and the coupling strength between oscillators of different groups is  $V_{AB}$ .

critical case  $\gamma_+ = \gamma_-$ . For K < 0 (orange line), each oscillator preferably aligns its phase with the mean field, leading to synchronization of the group. On the other hand, for K > 0 (blue line), each oscillator favors a phase shift of  $\pi$  with respect to the mean field, resulting in phase frustration that hinders synchronization. Therefore, unlike the interference blockade of a single oscillator, the macroscopic interference blockade is only lifted for negative K. For  $\gamma_+ \neq \gamma_-$ , we similarly find that the phase distribution tends to peak closer to  $\phi = 0$  ( $\pi$ ) for negative (positive) values of K, which is reflected by the respective critical coupling strengths shown by the orange (blue) line in Fig. 5.5(c) being smaller (larger).

In summary, the ensemble of quantum oscillators may synchronize and form a phase-coherent collective state above a critical coupling strength, as expected from generic models of noisy classical oscillators. Importantly though, the quantum nature of the oscillators remains influential on the macroscopic scale: The interference blockade manifests itself as a blockade of global synchronization. Moreover, phase frustration, where each oscillator aims to antialign its phase with the mean field, causes an emergent additional blockade only present in the large network.

# 5.4 Synchronization in two groups

We now consider a model of two groups of quantum oscillators as depicted in Fig. 5.6. It comprises two groups of oscillators resembling models of two ensembles of classical phase oscillators [Okuda and Kuramoto, 1991; Montbrió et al., 2004]. The two groups, labeled A and B, differ by the detuning  $\delta$  between them. Each group is of the same form as in the previous section. The Hamiltonians and Lindblad dissipators of the quantum master equation  $\dot{\rho} = -i[H_0 + H_{\rm int}, \rho] + \mathcal{L}\rho$  are now

$$H_{0} = \sum_{i} \frac{\delta}{2} \left( S_{A,i}^{z} - S_{B,i}^{z} \right) + K \left( |2\rangle\langle 2|_{A,i} + |2\rangle\langle 2|_{B,i} \right) ,$$

$$H_{\text{int}} = \frac{V}{N} \sum_{\sigma} \sum_{i < j} \left( S_{\sigma,i}^{+} S_{\sigma,j}^{-} + S_{\sigma,i}^{-} S_{\sigma,j}^{+} \right) + \frac{V_{AB}}{N} \sum_{i,j} \left( S_{A,i}^{+} S_{B,j}^{-} + S_{A,i}^{-} S_{B,j}^{+} \right) ,$$

$$\mathcal{L} = \sum_{\sigma,i} \left( \gamma_{+} \mathcal{D} \left[ |1\rangle\langle 0|_{\sigma,i} \right] + \gamma_{-} \mathcal{D} \left[ |1\rangle\langle 2|_{\sigma,i} \right] \right) ,$$
(5.10)

where  $\sigma \in \{A, B\}$  is the group label. The coupling strength within each group is V, and the coupling strength between oscillators of different groups is  $V_{AB}$ .

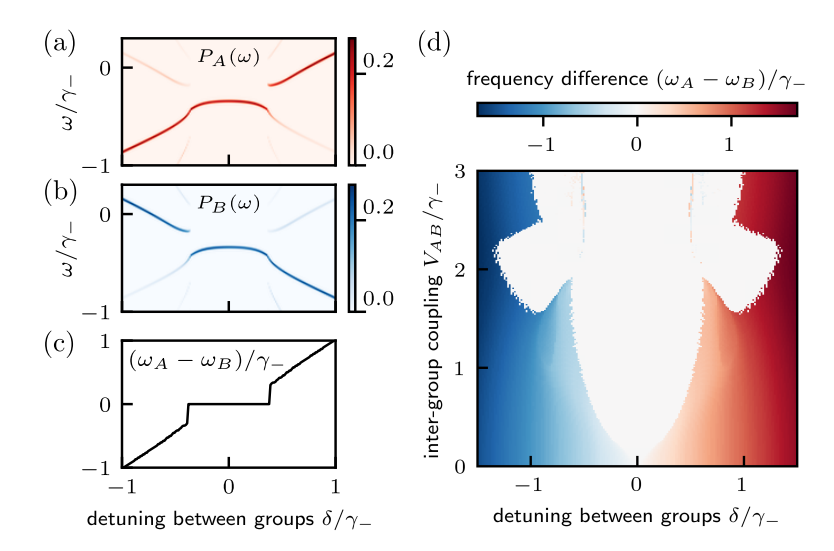


Figure 5.7: Synchronization of two groups. (a,b) Spectra  $P_{\sigma}(\omega)$  for  $\sigma=A,B$  obtained via Fourier transform of the time evolution of  $\langle S^{+}\rangle_{\sigma}$  as a function of detuning  $\delta$ . (c) Difference of the two dominant frequencies,  $\omega_{A}-\omega_{B}$ . (d) Frequency difference between the two groups as a function of detuning  $\delta$  and inter-group coupling  $V_{AB}$ . Parameters:  $K=0,V=2\gamma_{+}=\gamma_{-}$  (such that  $V>V_{c}$ ). (a–c):  $V_{AB}=V/2$ .

For the model of two distinct groups, we extend the product ansatz to  $\rho = \bigotimes_{\sigma,i} \rho_{\sigma,i}$ . Since all oscillators within each group are identical, their time evolution can be described in terms of two three-level oscillators with density matrices  $\rho_A$  and  $\rho_B$  coupled to the mean amplitudes  $\langle S^+ \rangle_{\sigma} = \text{Tr}[\rho_{\sigma} S^+] = 1/N \sum_i \langle S_{\sigma,i}^+ \rangle$  of each group. The dynamics of the two groups is governed by the two coupled nonlinear master equations

$$\dot{\rho}_{A} = -i[H_{A} + V_{AB}(S^{+} \langle S^{-} \rangle_{B} + S^{-} \langle S^{+} \rangle_{B}), \rho_{A}] + \tilde{\mathcal{L}}\rho_{A},$$

$$\dot{\rho}_{B} = -i[H_{B} + V_{AB}(S^{+} \langle S^{-} \rangle_{A} + S^{-} \langle S^{+} \rangle_{A}), \rho_{B}] + \tilde{\mathcal{L}}\rho_{B},$$
(5.11)

where  $H_{\sigma} = \pm \frac{\delta}{2} S^z + K |2\rangle\langle 2| + V (S^+ \langle S^- \rangle_{\sigma} + S^- \langle S^+ \rangle_{\sigma})$  and  $\tilde{\mathcal{L}} = \gamma_+ \mathcal{D}[|1\rangle\langle 0|] + \gamma_- \mathcal{D}[|1\rangle\langle 2|]$ . The sign in front of  $\delta/2$  is plus (minus) for group A (B). The following results are obtained through numerical integration of the nonlinear master equations (5.11) as well as a stability analysis of the unsynchronized state  $\rho_{\sigma} = |1\rangle\langle 1|$ .

We identify three different states in the long-time limit. The first is the absence of any synchronization, indicated by both amplitudes  $\langle S^+ \rangle_{\sigma}$  vanishing. Secondly, all oscillators of both groups can fully synchronize. Thirdly, there is a state of partial synchronization where all oscillators within each group synchronize internally but not with the oscillators of the other group.

To distinguish full and partial synchronization, we compare the oscillation frequencies of both groups. For this purpose, we compute the discrete Fourier transform (FT) of the amplitudes in the long-time limit to obtain the power spectra

$$P_{\sigma}(\omega) = \left| \text{FT}\{ \left\langle S^{+} \right\rangle_{\sigma}(t) \} \right|$$
 (5.12)

for each group. We have smoothed the time series with a Hann window [Oppenheim et al., 2013].

Figure 5.7(a,b) display the power spectra as a function of the detuning  $\delta$ . We have set V larger than the critical coupling such that the oscillators are synchronized within each group. For sufficiently small detuning compared to the inter-group coupling strength, we

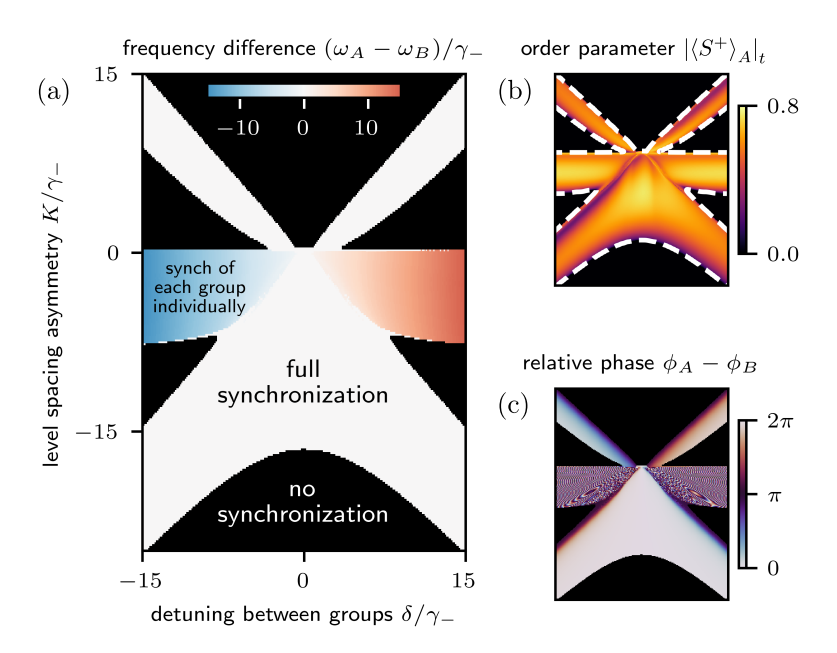


Figure 5.8: Macroscopic quantum synchronization blockade. Panels (a–c) show the frequency difference, the order parameter, and the relative phase, respectively, as a function of detuning  $\delta$  and asymmetry parameter K. The phase  $\phi_{\sigma}$  for  $\sigma=A,B$  is the argument of  $\langle S^{+}\rangle_{\sigma}$  in the long-time limit. In (b) and (c),  $\delta$  and K have the same range as in (a). In (b), the white dashed line indicates the transition between the incoherent state being stable and unstable. In (a) and (c), black color indicates regions where the order parameter vanishes, i.e., synchronization is absent. When each group synchronizes individually, i.e., in the blue and red regions in (a), the relative phase in (c) takes arbitrary values since there is no fixed phase relation between the two groups. Parameters:  $V_{AB} = V = 2\gamma_{+} = \gamma_{-}$ .

find a fully synchronized state as indicated by the identical spectra in this regime. Since each spectrum is dominated by one frequency, we continue the analysis using the two frequencies at which the spectra peak,  $\omega_{\sigma} = \operatorname{argmax}_{\omega} P_{\sigma}(\omega)$ . The frequency difference  $\omega_A - \omega_B$  between the two groups is displayed in Fig. 5.7(c). At small  $\delta$ , the frequencies are equal and the two groups are synchronized, while for large detunings,  $\omega_A$  and  $\omega_B$  differ by  $\delta$ . This corresponds to the dynamics described by the Adler equation for classical phase oscillators; see the black line in Fig. 2.5(a). To further demonstrate this correspondence, we show the frequency difference in Fig. 5.7(d) as a function of detuning  $\delta$  and inter-group coupling strength  $V_{AB}$ . For  $V_{AB} < V$ , both individually synchronized groups of oscillators can be regarded as two large oscillators that synchronize when their coupling is larger than their detuning. In this regime, the microscopic details are irrelevant and the behavior matches that of generic synchronization models. Specifically, we observe an Arnold tongue where the locking range grows with increasing coupling strength, the same behavior that we found in the context of the Adler equation. For  $V_{AB} > V$ , the inter-group coupling dominates, so that the analogy of two large coupled oscillators fails. As a result, the locking range does not increase monotonically with the coupling and the spectra show more than one relevant frequency component; see Appendix 5.A.

The previous analysis was done for a symmetric three-level structure, i.e., K=0. We now vary the asymmetry parameter K in addition to the detuning  $\delta$  and present the resulting phase diagram in Fig. 5.8. Remarkably, for large  $|K|/\gamma_-$ , we find synchronization only if  $|\delta| \sim |K|$ , while synchronization is absent for  $\delta$  around zero. This is a macroscopic manifestation of the quantum synchronization blockade [Lörch et al., 2017]: The two

groups synchronize when they are distinct, but not if they are similar. This is in contrast to the expected behavior that a greater similarity of oscillators increases their tendency to synchronize. As explained in Section 5.1.2, the absence of synchronization between two spin-1 oscillators is caused by their discrete energy spectrum. The effect of the coupling between two oscillators is suppressed when |K| significantly differs from  $|\delta|$  because the dominant transitions are off-resonant. Only close to the resonances  $K = \delta$  and  $K = -\delta$ , there is strong phase alignment of the two oscillators. This explains the microscopic synchronization blockade; however, it does not yet fully capture the macroscopic quantum synchronization blockade.

The macroscopic quantum synchronization blockade shows a feature that is not directly visible in the microscopic quantum synchronization blockade: In Fig. 5.8(a), we find synchronization only below the lines  $K = \delta$  and  $K = -\delta$  whereas in the case of two oscillators, Fig. 5.3(a), synchronization occurs close to these lines. To explain this, let us inspect more closely the microscopic synchronization blockade. Figure 5.3(b) shows that two coupled oscillators tend to align their phases below the lines  $K = \delta$  and  $K = -\delta$ , while above, they favor opposite phases. This is also visible on the level of the two ensembles; see Fig. 5.8(c). Since each oscillator reacts to the mean fields of both groups, their effect cancels when they have opposite phases. Altogether, for  $K \gtrsim \delta$ , both groups have opposite phases canceling their effect on each individual oscillator, resulting in the absence of synchronization. This constitutes another instance of phase frustration that results in an additional blockade of synchronization for  $K \gtrsim \delta$ .

The region where the two ensembles fully synchronize can be inferred from the microscopic properties under two reasonable assumptions. First, the two groups should lock onto a phase difference that is closer to zero than to  $\pi$  to avoid phase frustration. Second, the phase preference between any pair of oscillators induced by the coupling must be stronger than some critical value. Combining these two assumptions results in the white area shown in Fig. 5.3(c). It qualitatively agrees with the region where the macroscopic system fully synchronizes (white region in Fig. 5.8(a)). The value of the amplitude threshold is a free parameter that we chose to be  $5 \times 10^{-3}$ . Qualitative features such as the general X shape, whose bottom diagonals are broader than the top ones, are independent of this choice.

To summarize the analysis of two groups, parts of the collective states can be understood from a typical synchronization transition. In general, however, the quantum properties of each individual oscillator change the macroscopic states significantly. We demonstrated a blockade of global synchronization resulting from the quantized nature of the oscillators. Moreover, an extended blockade of synchronization emerges in the ensemble due to phase frustration, which is not present in the case of two coupled oscillators.

#### 5.5 Conclusions

While quantum effects in synchronization have been studied at the level of few coupled oscillators, it has remained an open question whether these effects persist when increasing the number of oscillators. To address this issue, we investigated the synchronization behavior of two macroscopically large groups of coherently coupled quantum limit-cycle oscillators. We demonstrated that quantum effects in synchronization persist on a macroscopic scale: For a single group, destructive interference manifests itself as a blockade of collective synchronization if gain and loss rates are comparable; for two detuned groups of oscillators with an asymmetric level structure, their quantized nature counterintuitively leads to synchronization of dissimilar groups. We also identified certain

5.5. Conclusions 67

aspects of the dynamics that can be understood from classical generic synchronization models: For a single group, the transition to synchronization necessitates a critical coupling strength to overcome decoherence; for two groups of oscillators with a symmetric level structure in the regime of small inter-group coupling strength, their dynamics can be understood as the synchronization of two classical phase oscillators. Finally, we uncovered emergent behavior only present in the macroscopic ensemble: Phase frustration, i.e., oscillators antialigning their phases, suppresses the global coherence and results in the absence of collective synchronization. We showed that phase frustration can prohibit synchronization in a single group and synchronization between two groups.

While we focused on a minimal model with three states, infinitely many oscillators, and an all-to-all coupling, we expect that the results apply more generally. The quantum synchronization blockade has been studied in the context of anharmonic oscillators [ $L\ddot{o}rch$  et al., 2017], and the interference blockade is present in systems with more than three states [Solanki et al., 2023]. Therefore, the effects described in this chapter may not only apply to three-level oscillators but also to other types of quantum limit-cycle oscillators. In finite-size systems, we have discussed in the context of the superradiant laser that the synchronization transition remains visible as a crossover; see Fig. 4.10(a). Therefore, it is to be expected that the effects presented here also remain in finite-size systems. In Appendix 5.B, we demonstrate that the coherence decays with a lifetime proportional to the number of oscillators. Finally, since global synchronization can persist for long-range interactions in networks of classical oscillators [ $Acebr\'{o}n$  et al., 2005] and quantum oscillators [Zhu et al., 2015], we expect that the all-to-all coupling that is assumed in this chapter is not essential. A detailed analysis of finite-size systems and long-range couplings is left for future work.

An experimental observation of quantum synchronization effects in many-body systems is challenging; even synchronization of a few interacting quantum oscillators remains to be experimentally demonstrated. Platforms for potential experimental realizations include superconducting circuits [Lörch et al., 2017; Nigg, 2018] and trapped ions [Lee and Sadeghpour, 2013; Hush et al., 2015; Lörch et al., 2017]. We elaborate on the experimental requirements and challenges in Appendix 5.C.

The results presented in this chapter can be regarded as self-organization of drivendissipative quantum constituents. Remarkably, the formation of a phase-coherent collective state depends on the microscopic quantum properties of the individual constituents. A comprehensive understanding of the individual constituents and their pairwise interactions allowed us to explain when self-organization occurs and why it breaks down in certain parameter regimes.

## Appendix for Chapter 5

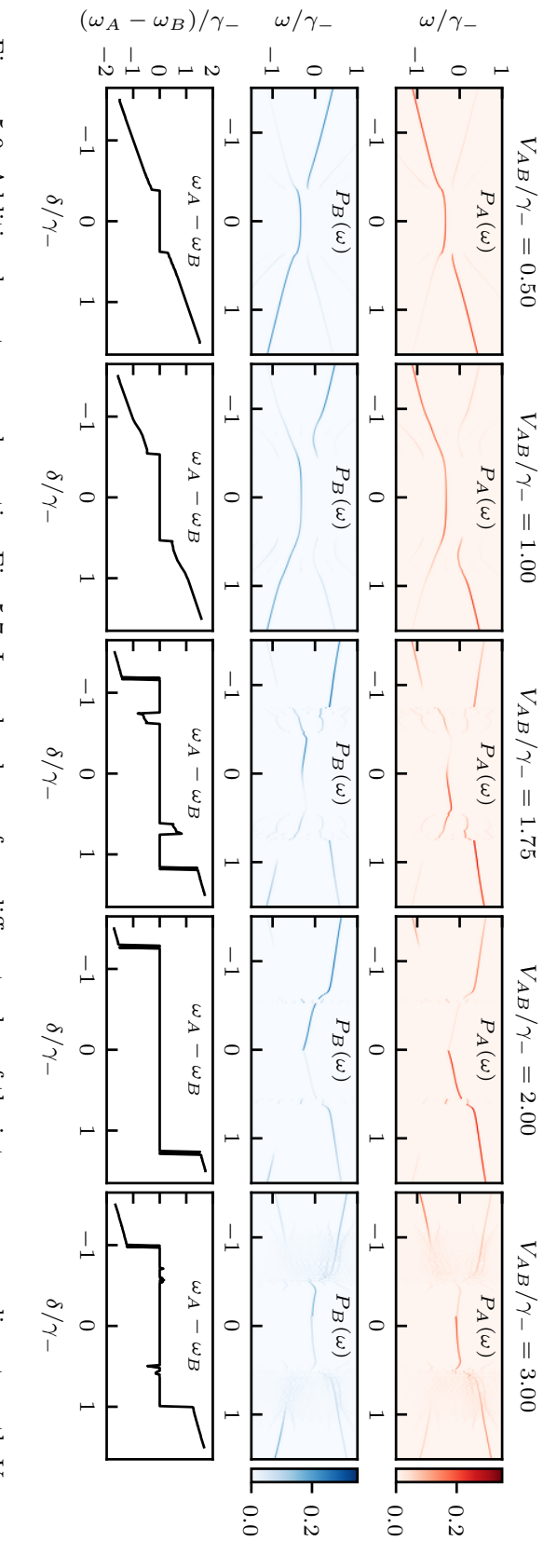
### 5.A Additional spectra

In Figs. 5.9 and 5.10 we show additional spectra complementing Figs. 5.7 and 5.8. In short, they demonstrate that for the results presented in this work, it is not necessary to consider the full spectra  $P_{\sigma}(\omega)$  to characterize the synchronization between two groups, but instead it is sufficient to use the difference of the dominant frequencies  $\omega_{\sigma} = \operatorname{argmax}_{\omega} P_{\sigma}(\omega)$ .

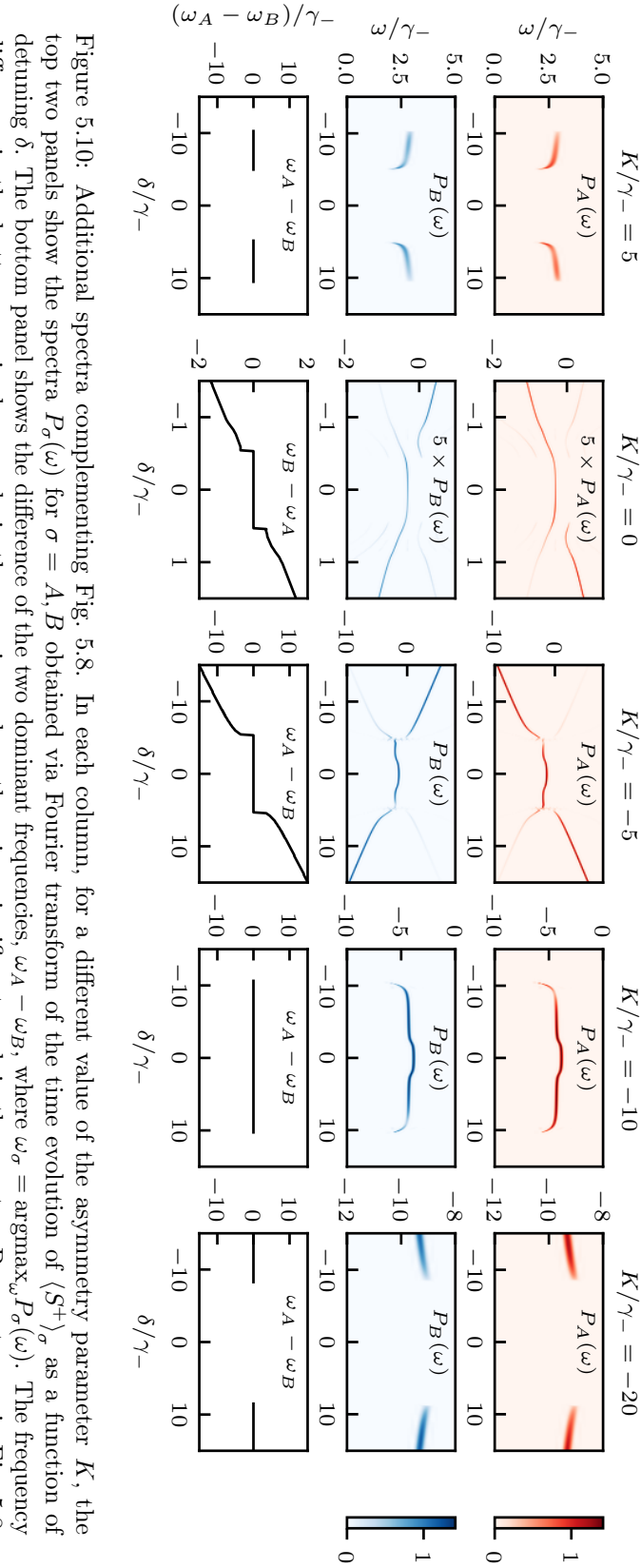
The full spectra displayed in Figs. 5.9 and 5.10 in general show more than one frequency component. For small inter-group coupling (see Fig. 5.9, two left columns, and Fig. 5.10, second and third columns), we observe a small additional frequency component that is picked up in each group from the other group. This additional peak, however, is clearly smaller than the dominant one, and therefore, we can safely focus on the main peak. The possibility of vanishing spectra (see first, fourth, and fifth columns in Fig. 5.10) is also captured by our analysis in Fig. 5.8, since in this case, the order parameter  $|\langle S^+ \rangle_{\sigma}|_t$  vanishes as well. However, in the regime, where the inter-group coupling is larger than the intra-group coupling,  $V_{AB} > V$  (see Fig. 5.9, middle to right columns), it is possible to find more than one dominant frequency component. In this regime, one can also observe the case where one group synchronizes more strongly than the other group. This is best visible in the fourth column of Fig. 5.9, where for negative (positive) detuning  $\delta$  group B (A) is more strongly synchronized, as indicated by the peak in the spectrum  $P_B$  ( $P_A$ ) being more pronounced. This regime ( $V_{AB} > V$ ) is not relevant for the results presented in this chapter, and its detailed analysis is left for future study.

## 5.B Finite-size analysis

To understand the influence of the group size, we go beyond the mean-field treatment and include some correlations between the observables. A systematic approach is to truncate higher-order cumulants [Kubo, 1962]. For this analysis, we truncate at the second-order correlations, i.e., neglect correlations between three and more observables. To do so, we use the Julia package QuantumCumulants.jl [Plankensteiner et al., 2022], which provides an automated way of deriving equations of motion including correlations up to a set order and converting them to Julia functions that can be integrated numerically. For the master equation of one group [see Eq. (5.8)], we obtain the results shown in Fig. 5.11. While it is interesting to consider correlations between spins that persist over time, here, we only investigate the behavior of the global coherence. Instead of a persistent non-vanishing value of  $|\langle S^+ \rangle|$  that is observed in the mean-field limit  $N \to \infty$ , the amplitude decays over time for finite N. We find that the lifetime (as measured by the time for the absolute value of the amplitude to decay to 1/e) increases linearly with the number of oscillators. The lifetime of the coherence in a group of 500 oscillators reaches  $T\gamma_- \approx 30$ , four times larger than the lifetime in the absence of any coupling.



detuning  $\delta$ . The bottom panel shows the difference of the two dominant frequencies,  $\omega_A - \omega_B$ , where  $\omega_\sigma = \operatorname{argmax}_\omega P_\sigma(\omega)$ . Parameters as in Fig. 5.7: K = 0,  $V = 2\gamma_+ = \gamma_-$  (such that  $V > V_c$ ). the top two panels show the spectra  $P_{\sigma}(\omega)$  for  $\sigma = A, B$  obtained via Fourier transform of the time evolution of  $\langle S^{+} \rangle_{\sigma}$  as a function of Figure 5.9: Additional spectra complementing Fig. 5.7. In each column, for a different value of the inter-group coupling strength  $V_{AB}$ ,



difference in the bottom row is shown only in those regions where there is a significant peak in the spectra. Parameters as in Fig. 5.8:  $V_{AB} = V = 2\gamma_+ = \gamma_-.$ 

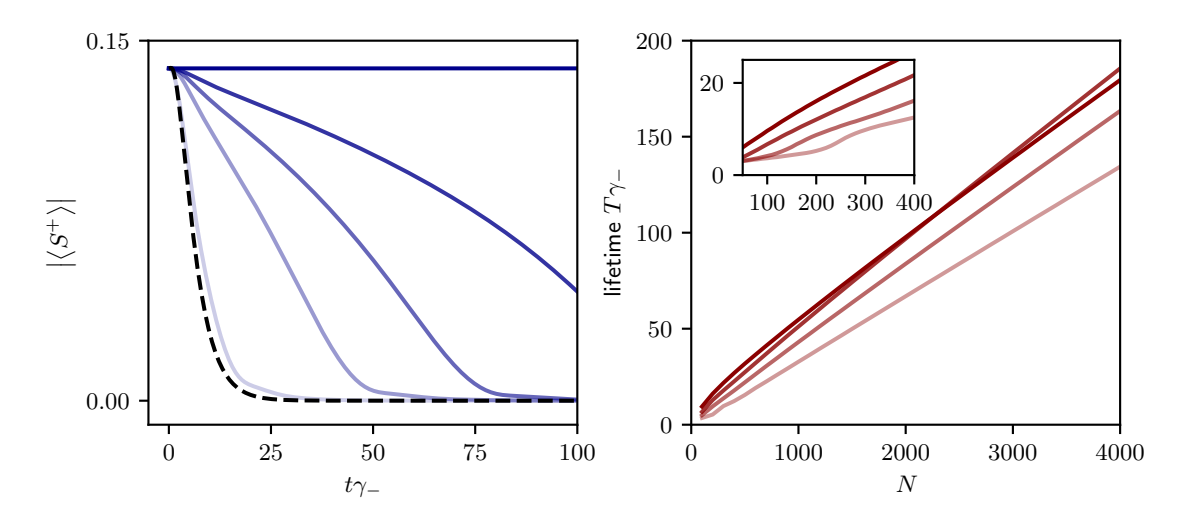


Figure 5.11: Finite-size analysis. Left: The time evolution of the absolute value of the amplitude  $|\langle S^+ \rangle|$  for different values of the number of oscillators N. From lighter to darker blue, N takes values 100, 500, 1000, 2000, and infinity, which corresponds to the mean-field result. The black dashed line shows the evolution in the absence of any coupling. Right: The lifetime  $T\gamma_-$  of the coherence as a function of N, for different values of the coupling strength, V. From darker to lighter red,  $V/\gamma_-$  takes values 0.75, 1, 1.25, 1.5. The inset shows the same data for smaller values of N.

#### 5.C Experimental requirements

We propose two possibilities to experimentally implement the models presented in this chapter. Clearly, an experimental implementation of a large network of coupled quantum oscillators will be extremely challenging since quantum synchronization effects have not even been observed between only two oscillators. The macroscopic interference blockade can be observed with a single group of identical oscillators, each possessing a symmetric level structure. The quantum synchronization blockade between two groups necessitates an asymmetric level structure and control of the detuning between the two groups. We briefly describe the implementation of the three levels of each oscillator, the gain and loss processes, and the coupling among the oscillators, for two versatile experimental platforms: superconducting circuits and trapped ions.

In superconducting circuits, following  $L\ddot{o}rch$  et al. [2017] and Nigg [2018], each oscillator is implemented in a transmon qubit. Gain and loss are engineered through coupling to ancillary modes; see Nigg [2018] for details. These incoherent processes result in a population narrowly distributed around one eigenstate  $|n\rangle$ , n>0, which allows for an effective approximate description of the dynamics using only three levels  $|n-1\rangle$ ,  $|n\rangle$ , and  $|n+1\rangle$ . These correspond to the levels  $|0\rangle$ ,  $|1\rangle$ , and  $|2\rangle$  with gain and loss stabilizing state  $|1\rangle$ , as considered in this chapter. Since each transmon qubit features an anharmonic spectrum, the three levels form an asymmetric three-level oscillator that is our building block. Control of the frequency of the transmon qubits allows for introducing two detuned groups of oscillators. For the coupling among the oscillators, in principle, each pair of oscillators can be capacitively coupled. Due to hardware constraints, however, it is difficult to couple all pairs of oscillators in this way. For collective synchronization, long-range coupling among the oscillators is required. While this is challenging, non-local couplings of transmon qubits have been described, for example, in [Majer et al., 2007; Onodera et al., 2020].

In trapped-ion setups, each oscillator can be implemented in a motional mode of an ion in an anharmonic potential [Lee and Sadeghpour, 2013; Hush et al., 2015; Lörch et al., 2017]. Gain and loss can be engineered by employing blue and red sideband transitions that incoherently drive transitions from one to another motional state [Leibfried et al., 2003]; see also Section 4.1.4. The anharmonicity of the energy spectrum allows for addressing individual transitions with varying strengths by tuning the sideband frequency. As described above in the case of transmon qubits, by engineering gain and loss to stabilize one motional eigenstate, the dynamics are reduced to this state and the two neighboring states. The anharmonic potential results in an asymmetry of the level structure of the three relevant states. By changing the harmonic part of the potential, the frequency of each oscillator, and hence the detuning between the two groups can be controlled. All oscillators are naturally coupled via the long-range Coulomb interaction. The coupling strength can be adjusted by varying the distance of the individual ions.

## Chapter 6

# Nonreciprocal synchronization of active quantum spins

The results of this chapter have been published in

Nonreciprocal Synchronization of Active Quantum Spins, T. Nadolny, C. Bruder, and M. Brunelli, Physical Review X, **15**, 011010 (2025)

In the previous two chapters, we presented synchronization of quantum many-body systems. All constituents of these systems – whether quantum van-der-Pol oscillators, spins-1/2 or spins-1 – shared the same "goal" of achieving a phase-locked coherent state. We now break this symmetry by considering two species of constituents with opposing goals, i.e., two species that interact in a nonreciprocal way.

Nonreciprocal interactions are extensively studied in classical systems in the context of active agents. Active agents are capable of exerting nonreciprocal forces upon one another. For instance, one agent, say A, may attract another agent B while B repels A. These antagonistic nonreciprocal interactions feature a wealth of exciting phenomena such as novel phase transitions and collective dynamical states called traveling-wave states. Whether these phenomena can originate in quantum many-body systems has remained an open issue, and proposals for their realization have been lacking.

In this chapter, we present a model of two species of quantum spins-1/2 that interact in an antagonistic nonreciprocal way of the attraction-repulsion type. We propose an implementation of the model based on two atomic ensembles coupled via chiral waveguides, which we introduced in Section 3.4. The spins are active due to the presence of local gain, which allows them to synchronize. In the thermodynamic limit, we show that nonreciprocal interactions result in a nonreciprocal phase transition to time-crystalline traveling-wave states, associated with spontaneous breaking of parity-time symmetry. We establish how this symmetry emerges from the microscopic quantum model. For a finite number of spins, signatures of the time-crystal phase can be identified by inspecting equal-time or two-time correlation functions. Continuous monitoring of the system, which we introduced in Section 3.3, has a remarkable effect: It induces a quantum traveling-wave state, i.e., a time-crystalline state of a finite-size quantum system, in which parity-time symmetry is spontaneously broken. The results of this chapter lay the foundation to explore nonreciprocal interactions in active quantum matter.

#### 6.1 Introduction

We briefly presented active matter and nonreciprocal interactions in classical systems in Section 2.4 as well as unidirectional, or cascaded, interactions between quantum systems

in Section 3.4. Let us nevertheless recapitulate the important points to give context for this chapter.

Active agents are nonequilibrium entities that convert energy into motion or nonconservative forces at the individual level [Bowick et al., 2022; Shankar et al., 2022; te Vruqt et al., 2025. A distinctive feature of active agents is that the forces exerted among them can be nonreciprocal. Nonreciprocity between two agents A and B occurs when the response of A to the action of B differs from that of B to A. Nonreciprocal interactions dramatically change the self-organization behavior in active matter, viz., ensembles of active agents, resulting in several universal manifestations. They include the transition from a static to a dynamical behavior [You et al., 2020], a new class of critical phenomena marked by exceptional points and spontaneous breaking of parity-time symmetry [Fruchart et al., 2021], as well as a dynamical analogue of geometrical frustration resulting in time-crystalline order [Hanai, 2024]. The consequences of nonreciprocal interactions are important in a variety of contexts, ranging from pattern formation [Brauns and Marchetti, 2024] to classical spin models [Avni et al., 2025; Loos et al., 2023]. They have been observed in metamaterials of various kinds [Brandenbourger et al., 2019; Librandi et al., 2021; Liu et al., 2024, nanoparticles [Reisenbauer et al., 2024], as well as in active forms of colloids, solids and plasmas [Meredith et al., 2020; Baconnier et al., 2022; Ivlev et al., 2015. Underlying all of these manifestations is a common type of nonreciprocal interactions, namely antagonistic interactions akin to predator-prey dynamics, where A is attracted by B while B is repelled by A. This effect is maximized in the limit of interactions with opposite strength but equal magnitude.

Nonreciprocity in quantum systems has also gathered a great deal of interest [Barzanjeh et al., 2025]. It is a resource for routing information in bosonic networks [Ranzani and Aumentado, 2015; Wanjura et al., 2023 and for quantum sensing [Lau and Clerk, 2018. Quantum emitters coupled to a chiral, i.e., unidirectional, waveguide have been proposed for the preparation of entangled states [Stanniqel et al., 2012; Pichler et al., 2015. In tight-binding models, nonreciprocity is responsible for anomalous localization properties [Hatano and Nelson, 1996, 1997; McDonald et al., 2022] and, supplemented with gain, gives rise to exotic non-Hermitian topological phases of bosonic systems [Wanjura et al., 2020; Porras and Fernández-Lorenzo, 2019; Brunelli et al., 2023; Okuma and Sato, 2023. Nonreciprocity is also of high practical relevance. Tunable and magnetic-free nonreciprocal quantum devices, implemented with optomechanics [Verhagen and Alù, 2017 or superconducting circuits [Lecocq et al., 2017], are advantageous for on-chip integration, scaling up superconducting quantum architectures, and improving quantum measurement readout. Recently, first steps toward understanding the role of nonreciprocal phase transitions [Hanai et al., 2019; Hanai and Littlewood, 2020; Chiacchio et al., 2023; Reisenbauer et al., 2024; Zhu et al., 2024; Zelle et al., 2024; Sieberer et al., 2025; Belyansky et al., 2025; Jachinowski and Littlewood, 2025 and nonreciprocal many-body interactions [Bright and Nunnenkamp, 2024; Begg and Hanai, 2024; Hanai et al., 2024] have been taken.

Current investigations of nonreciprocity in quantum systems are, however, more restrictive than those of nonreciprocal interactions in classical active matter, since only the magnitude, i.e., the absolute value, of the interaction strengths (or transmission coefficients) is typically considered [ $De\acute{a}k$  and  $F\ddot{u}l\ddot{o}p$ , 2012; Caloz et al., 2018]. This form of magnitude nonreciprocity is maximized for unidirectional interactions, i.e., when A exerts an influence on B while B is immune to A's influence, which corresponds to cascaded quantum dynamics [Gardiner, 1993; Carmichael, 1993]; see Section 3.4. In contrast, antagonistic interactions imply that A's influence on B and B's influence on A oppose each other, i.e., realize a stronger form of nonreciprocity than unidirectional interactions. Antagonistic attraction and repulsion are not accounted for by cascaded

6.1. Introduction 77

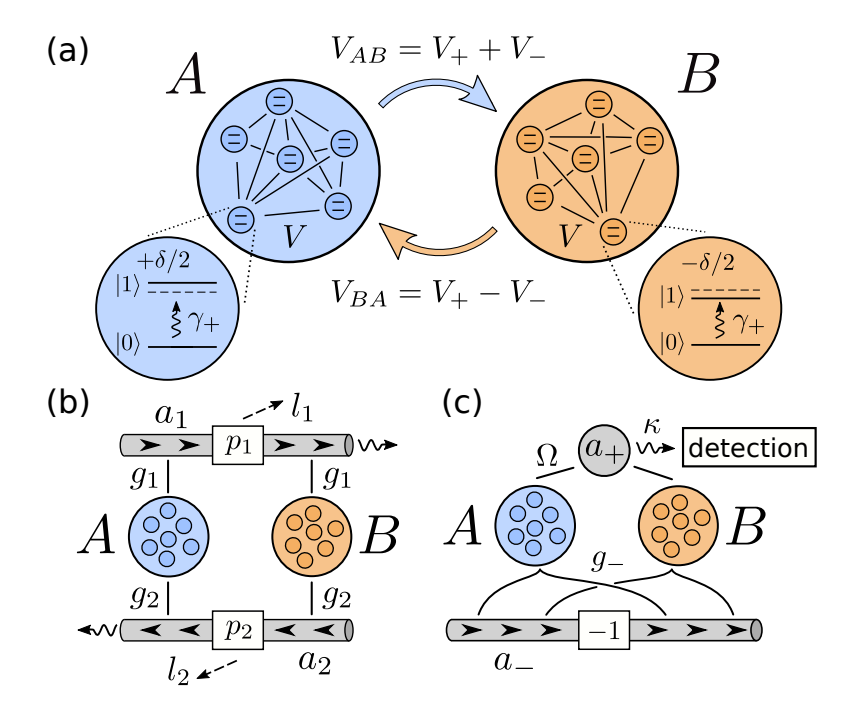


Figure 6.1: (a) The model comprises two groups A and B of N quantum spins-1/2 each. Each spin is incoherently driven from  $|0\rangle$  to  $|1\rangle$  at rate  $\gamma_+$  and the two spin species are detuned by  $\delta$ . Within each species, the spins are coupled with a strength V. Spins of species A (B) influence spins of species B (A) with a strength  $V_{AB}$  ( $V_{BA}$ ). If  $V_{AB} \neq V_{BA}$ , the interspecies coupling is nonreciprocal. (b) Physical implementation with doubly-cascaded interactions mediated by two independent chiral waveguides. The chiral modes  $a_{1,2}$  couple to the spins with strengths  $g_{1,2}$ . Between the two spin species, they pass a phase shifter which multiplies the modes by  $p_{1,2} \in \{\pm 1\}$ . Potential losses  $l_{1,2}$  are also accounted for. (c) Alternative implementation with braided interactions. The mode  $a_+$  is bidirectional and mediates reciprocal interactions between species A and B. The chiral mode  $a_-$  mediates purely coherent interspecies interactions.

interactions or other previously studied forms of nonreciprocity in quantum systems, e.g., based on reservoir engineering [Metelmann and Clerk, 2015] or dissipative gauge symmetry [Wang et al., 2023]. Despite their importance in classical active matter, antagonistic many-body interactions in the quantum regime have remained unexplored. Furthermore, it is not a priori clear how they can be realized.

In this chapter, we propose a model of synchronization of active quantum spins to explore the effects of antagonistic nonreciprocity in quantum many-body systems. As presented in Section 2.4, nonreciprocal couplings among limit-cycle oscillators can lead to attraction-repulsion interactions of their phases. For classical oscillators, such interactions have been shown to result in nonreciprocal phase transitions and traveling-wave states [Hong and Strogatz, 2011b; Sonnenschein et al., 2015; Hanai, 2024; Fruchart et al., 2021]. While synchronization in quantum systems is the subject of numerous works [see Chapter 4], the role of antagonistic interactions in quantum synchronization has not been explored prior to this work. Later, Kehrer and Bruder [2025] explored antagonistic interactions between two coupled quantum van-der-Pol oscillators.

The model at the center of this chapter comprises two species of quantum spins-1/2, as sketched in Fig. 6.1(a). Each spin is driven out of equilibrium via an incoherent gain that provides it with energy. Therefore, we refer to the spins as active spins in analogy to active matter, where each constituent is also individually provided with energy. The spins within

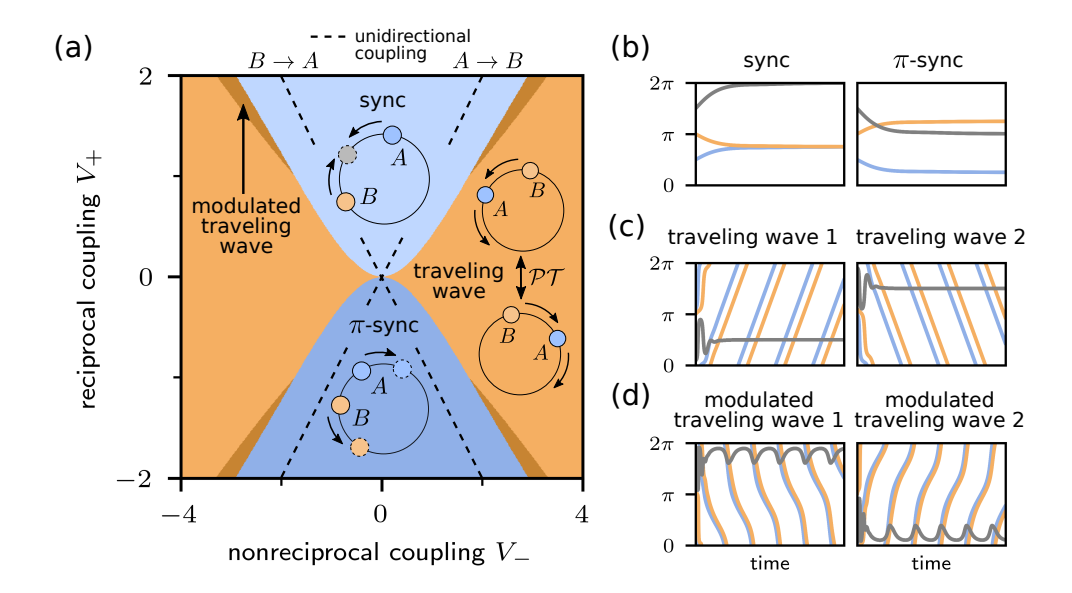


Figure 6.2: (a) Phase diagram in the thermodynamic limit. The insets sketch the dynamics in the respective phase. They depict species A and B as a colored disk whose position on a circle represents the phase of the spins; the arrows indicate the phase velocity. Stationary steady-state positions are indicated by disks with a dashed border. Parameters:  $\delta=0$ , V=2 (all coupling strengths in units of  $\gamma_+$ ). (b,c,d) Time evolution of the phases  $\phi_a=\arg[s_a^+]$  of species A (blue) and B (orange) in the thermodynamic limit. The phase difference is shown in gray. Parameters:  $\delta=0$ ,  $V=2\gamma_+$ , sync:  $V_-=0$ ,  $V_+=\gamma_+$ ;  $\pi$ -sync:  $V_-=0$ ,  $V_+=-\gamma_+$ ; traveling wave:  $V_-=\gamma_+$ ,  $V_+=0$ ; modulated traveling-wave:  $V_-=2.4\gamma_+$ ,  $V_+=1.5\gamma_+$ .

each species mutually synchronize due to a collective coupling to a common mode, similar to synchronization in superradiant lasers presented in Section 4.2.3. The interactions between the two species can be tuned from reciprocal couplings to unidirectional and antagonistic couplings. We find that, among active spins, antagonistic interactions are mediated by purely Hamiltonian couplings.

We propose an implementation of this model in a light-matter coupled system consisting of two atomic ensembles coupled by two chiral waveguides, which mediate unidirectional couplings each; see Fig. 6.1(b). Braided interactions reminiscent of the coupling of giant atoms [Kockum et al., 2018], as shown in Fig. 6.1(c), can be used to further enhance the antagonistic effects.

In the thermodynamic limit, the model features a nonreciprocal phase transition between static synchronized phases and a dynamical traveling-wave phase where the two species persistently oscillate; see Fig. 6.2(a). The transition is accompanied by spontaneous breaking of parity-time ( $\mathcal{PT}$ ) symmetry and is induced by antagonistic interactions, thus going beyond the scope of magnitude nonreciprocity. We show how the nonreciprocal phase transition emerges from an underlying open quantum system description. Guided by the physical implementation of Fig. 6.1(b), we define a suitable  $\mathcal{PT}$  symmetry for the Lindblad master equation for any system size that recovers the symmetry that is spontaneously broken in the thermodynamic limit.

In finite-size quantum systems, the  $\mathcal{PT}$  symmetry manifests itself in the spin correlations and the spectral density, where an exceptional point signals the nonreciprocal phase transition. While in classical systems full knowledge about the state is available, in a quantum system any measurement can only reveal a limited amount of information.

6.2. Model 79

Additionally, the choice of measurement alters the dynamical evolution. Quantum trajectories reveal that measurement backaction can spontaneously break  $\mathcal{PT}$  symmetry. These results show that traveling-wave states and nonreciprocal phase transitions are observable for finite-size quantum systems.

From the analysis of the proposed model of active quantum spins that synchronize, we are able to discuss in Section 6.9 general implications for a broader class of active quantum systems. They regard the engineering of antagonistic interactions, the importance of  $\mathcal{PT}$  symmetry on the level of the microscopic quantum master equation, the role of decoherence to stabilize a nonstationary state, and the influence of measurement backaction. We expect these to be relevant for other models of nonreciprocal phase transitions in active quantum systems.

#### 6.2 Model

#### 6.2.1 Quantum master equation

The agents of our model are two-level quantum systems, i.e., spins-1/2, grouped in two species A and B; see Fig. 6.1(a). As in Section 4.2, for each spin, we define the Pauli z-matrix  $\sigma_{a,i}^z = |1\rangle\langle 1|_{a,i} - |0\rangle\langle 0|_{a,i}$ , as well as raising and lowering operators  $\sigma_{a,i}^+ = |1\rangle\langle 0|_{a,i}$  and  $\sigma_{a,i}^- = |0\rangle\langle 1|_{a,i}$ . The indices run over the group label  $a \in \{A, B\}$  and the N spins per species  $i \in \{1, ..., N\}$ . All spins within each species are equal and they are described by the collective spin operators  $S_a^{\pm,z} = \sum_{i=1}^N \sigma_{a,i}^{\pm,z}$ .

We describe the spins within the framework of open quantum systems introduced in Chapter 3. The density matrix  $\rho$  describes the state of all spins, and its evolution is governed by the quantum master equation

$$\dot{\rho} = \mathcal{L}\rho = -i\left[H_0 + H_{\text{inter}}, \rho\right] + \left(\mathcal{L}_{\text{inter}} + \mathcal{L}_{\text{intra}} + \mathcal{L}_{\text{drive}}\right)\rho. \tag{6.1}$$

The Liouvillian operator  $\mathcal{L}$  is the short-hand notation for the generator of the dynamics. The dynamics comprises both Hamiltonian terms, which generate unitary evolutions, and dissipative terms, which arise from the system being in contact with an (unspecified) environment. The label 'inter' refers to *interspecies* coupling, i.e., coupling between spins of different species, while 'intra' refers to *intraspecies* coupling, i.e., coupling within the same species.

The Hamiltonian terms are

$$H_0 = \delta(S_A^z - S_B^z)/4$$
,  $H_{\text{inter}} = i\frac{V_-}{2N}S_A^+ S_B^- + \text{H.c.}$  (6.2)

The bare Hamiltonian  $H_0$  describes a frequency splitting  $\delta$  between the spins of species A and the spins of species B. The interaction Hamiltonian  $H_{\text{inter}}$  describes excitation exchanges with a purely imaginary amplitude, i.e.,  $V_-$  is real valued. We will later consider the more general case of complex  $V_-$  [see Fig. 6.3(c)]. As we will discuss in the following section,  $H_{\text{inter}}$  can be effectively implemented with chiral waveguides and results in antagonistic interactions. Besides Hamiltonian, i.e., coherent, coupling, we include a second type of interspecies coupling of dissipative nature with real-valued strength  $V_+$ ,

$$\mathcal{L}_{\text{inter}}\rho = \frac{V_{+}}{N} \left( \mathcal{D}[S_{A}^{-}, S_{B}^{-}] + \mathcal{D}[S_{B}^{-}, S_{A}^{-}] \right) \rho , \qquad (6.3)$$

where  $\mathcal{D}[o_1, o_2]\rho = o_1\rho o_2^{\dagger} - (o_2^{\dagger}o_1\rho + \rho o_2^{\dagger}o_1)/2$ . Importantly,  $V_+$  is allowed to take negative values. We also include dissipative intraspecies couplings with non-negative strength  $V \geq 0$ ,

$$\mathcal{L}_{\text{intra}}\rho = \frac{V}{N} \left( \mathcal{D}[S_A^-] + \mathcal{D}[S_B^-] \right) \rho , \qquad (6.4)$$

where  $\mathcal{D}[o] = \mathcal{D}[o, o]$  indicates the standard dissipator [Breuer and Petruccione, 2002], to which  $\mathcal{D}[o_1, o_2]$  reduces for equal jump operators. While the terms in Eq. (6.3) do not appear to be in standard Lindblad form, the full master equation (6.1) is, as can be seen by combining the two dissipative interactions into collective jump operators using  $\mathcal{D}[o_1 \pm o_2] = \mathcal{D}[o_1] + \mathcal{D}[o_2] \pm (\mathcal{D}[o_1, o_2] + \mathcal{D}[o_2, o_1])$ . The combined dissipative interaction terms are

$$\mathcal{L}_{inter} + \mathcal{L}_{intra} = \frac{|V_{+}|}{N} \mathcal{D}[S_{A}^{-} + \operatorname{sign}(V_{+})S_{B}^{-}] + \frac{V - |V_{+}|}{N} \left( \mathcal{D}[S_{A}^{-}] + \mathcal{D}[S_{B}^{-}] \right) .$$

$$(6.5)$$

The master equation describes a physical evolution when all rates of standard dissipators are non-negative. Therefore, we require  $V \ge |V_+|$ .

The collective jump operators  $S_{A,B}^-$  (and their sum or difference) arise from a collective coupling of all spins (of A, B) to a rapidly decaying mode. This process is known as superradiance and results in a buildup of coherence among the spins. It can also be understood as synchronization of the spins [Xu et al., 2014; Zhu et al., 2015] as we discussed when connecting superradiance to the Kuramoto model in Section 4.2.3. All three interaction terms contribute to the synchronization dynamics, as we will see in Section 6.4.

Finally, we consider an incoherent drive of each spin at rate  $\gamma_+$ , described by

$$\mathcal{L}_{\text{drive}}\rho = \gamma_{+} \sum_{i=1}^{N} \left( \mathcal{D}[\sigma_{A,i}^{+}] + \mathcal{D}[\sigma_{B,i}^{+}] \right) \rho. \tag{6.6}$$

Unlike the previous terms, this local gain acts individually on each spin. It provides energy at the microscopic level, a distinctive feature of active systems. In contrast to a thermal bath, the incoherent drive can result in population inversion, where the state  $|1\rangle$  is more populated than the state  $|0\rangle$ , an important feature as we will see in Section 6.4.

The proposed model possesses different symmetries. First, the master equation (6.1) is invariant under a global phase shift  $\sigma_{a,i} \to \exp(i\phi_0)\sigma_{a,i}$  for all spins  $\sigma_{a,i}$ ,  $i \in \{1, ..., N\}$  of both species  $a \in \{A, B\}$  where  $\phi_0 \in \mathbb{R}$ . This is a U(1) symmetry, which implies that no phase is preferred. We will see that phase locking spontaneously breaks the symmetry in the thermodynamic limit in Section 6.4. Second, there is no explicit time dependence of the master equation. The time-translation invariance can also be spontaneously broken in the thermodynamic limit, forming a continuous time crystal [Sacha and Zakrzewski, 2017; Iemini et al., 2018; Kongkhambut et al., 2022] in analogy to a standard crystal which breaks space-translation invariance; see Section 6.5. We will point out a third symmetry that can be broken simultaneously, parity-time  $(\mathcal{PT})$  symmetry, in Section 6.6.

#### 6.2.2 Cascaded quantum master equation

The model defined by Eq. (6.1) admits a simple interpretation in the framework of cascaded quantum systems [Gardiner, 1993; Carmichael, 1993], which we reviewed in Section 3.4. Cascaded interactions describe unidirectional couplings where one subsystem

influences another one but not vice versa. The Liouvillian  $\mathcal{L}$  defined in Eq. (6.1) can be rewritten in the equivalent form

$$\mathcal{L}\rho = -(V_{+} + V_{-})([S_{B}^{+}, S_{A}^{-}\rho] + [\rho S_{A}^{+}, S_{B}^{-}])/2N$$

$$-(V_{+} - V_{-})([S_{A}^{+}, S_{B}^{-}\rho] + [\rho S_{B}^{+}, S_{A}^{-}])/2N$$

$$-i[H_{0}, \rho] + \mathcal{L}_{intra}\rho + \mathcal{L}_{drive}\rho.$$
(6.7)

The first and second lines each describe cascaded quantum interactions from A to B and B to A, respectively, following the notation of Stannigel et al. [2012], which we introduced in Eq. (3.20). We conclude that the strength with which species A influences species B is  $V_{AB} = V_+ + V_-$  and the strength of B's influence on A is  $V_{BA} = V_+ - V_-$ , as depicted in Fig. 6.1(a). When the coupling strengths  $V_{AB}$  and  $V_{BA}$  differ, the interactions are nonreciprocal. We consequently refer to the parameter  $V_- = (V_{AB} - V_{BA})/2$  as nonreciprocal coupling strength and to  $V_+ = (V_{AB} + V_{BA})/2$  as reciprocal coupling strength. By rewriting the master equation (6.1) in the cascaded form of Eq. (6.7), we have found that the nonreciprocal coupling originates from the Hamiltonian term of Eq. (6.2), while the reciprocal coupling stems from dissipative coupling of Eq. (6.3).

In the absence of nonreciprocity,  $V_{-}=0$ , the model defined in Eq. (6.1) or (6.7) reduces to the model of two atomic ensembles that synchronize via purely dissipative, reciprocal interactions, proposed by Xu et al. [2014], realized by Weiner et al. [2017], and further analyzed by Patra et al. [2019a,b, 2020]. Unidirectional synchronization, studied by Roth and Hammerer [2016], is recovered when either  $V_{AB}$  or  $V_{BA}$  vanishes. This configuration maximizes magnitude nonreciprocity, i.e., an asymmetry in the magnitude of the directional couplings,  $|V_{AB}| \neq |V_{BA}|$ , which requires both dissipative and coherent interactions [Metelmann and Clerk, 2015. In contrast, our interest is in the even more nonreciprocal scenario in which  $V_{AB}$  and  $V_{BA}$  take opposite signs,  $\operatorname{sign}(V_{AB}) = -\operatorname{sign}(V_{BA})$ , which implies that nonreciprocal couplings dominate over reciprocal couplings,  $|V_-| > |V_+|$ . In this case, from Eq. (6.7) we see that the maximally nonreciprocal configuration  $V_{AB} = -V_{BA}$  is realized by purely coherent interspecies interactions, i.e.,  $V_{+}=0$ . This may seem surprising at first, since a purely Hamiltonian coupling between the two species has to be reciprocal. However, in our model, each spin is incoherently driven; see Eq. (6.6). We will see that this enables antagonistic quantum interactions of the phases of the spins, thus going beyond magnitude nonreciprocity.

## 6.3 Physical implementation

We now suggest a physical realization of the model defined in Eq. (6.1) that can be implemented in current experimental setups. It is based on the connection with cascaded interactions highlighted in Eq. (6.7) and allows us to gain more intuition about our model. We focus on the interacting part since the detuning and the incoherent drive of each spin have already been implemented, e.g., in atomic ensembles [Weiner et al., 2017].

The simplest configuration that implements our model is depicted in Fig. 6.1(b) and consists of the two spin ensembles A and B coupled by two independent chiral waveguides. Chiral waveguides mediate cascaded, i.e., unidirectional, interactions [Pichler et al., 2015], in our case between the two spin species. Experimentally, such interactions have been implemented between an atomic ensemble and a micromechanical membrane by freely propagating laser beams [Karg et al., 2020]. Cascaded interactions between single emitters and receivers have also been engineered in various other platforms [Petersen et al., 2014; Söllner et al., 2015; Delteil et al., 2017; Joshi et al., 2023].

The two chiral waveguides in Fig. 6.1(b) allow for two modes  $a_1$  and  $a_2$  to propagate in opposite directions and interact sequentially with the two spin ensembles A and B with

strengths  $g_1$  and  $g_2$ . Between the two ensembles, the modes pass a phase shifter which transforms  $a_{1,2}$  to  $p_{1,2}a_{1,2}$ . For simplicity, we focus on a change in sign only,  $p_{1,2} \in \{\pm 1\}$ . We also account for the losses  $l_{1,2}$  in the chiral waveguides between the two species via the transmission coefficients  $0 \le \eta_{1,2} = \sqrt{1 - l_{1,2}^2} \le 1$ .

Due to causality, the mode  $a_1$  can only result in species A influencing species B, and vice versa for mode  $a_2$ . They respectively mediate effective interspecies couplings with strengths

$$V_{AB}/N = p_1 2g_1^2 \eta_1$$
 and  $V_{BA}/N = p_2 2g_2^2 \eta_2$ . (6.8)

Thus, the setup shown in Fig. 6.1(b) is described by the effective master equation Eq. (6.1) or (6.7), with  $V_{\pm}/N = p_1 g_1^2 \eta_1 \pm p_2 g_2^2 \eta_2$  as well as  $V/N = g_1^2 + g_2^2$ . The presence of a phase shift is essential to achieve interspecies couplings with opposite signs, and thus allows for antagonistic interactions.

In this configuration, the interspecies coupling strengths cannot be arbitrarily large compared to the intraspecies coupling strength, since  $|V_{\pm}| \leq V$ . While the constraint  $|V_{+}| \leq V$  is unavoidable for the master equation to be physical, the coherent interactions between the two groups can be enhanced by considering looped or braided geometries known from giant atoms, which allow for  $|V_{-}| > V$  [Kockum et al., 2018; Karg et al., 2019]; a possible implementation is depicted in Fig. 6.1(c). It makes explicit the distinction between reciprocal and nonreciprocal couplings, mediated by the modes  $a_{+}$  and  $a_{-}$ , respectively. Braided couplings have been demonstrated in several physical systems, e.g., between atomic spins and a mechanical oscillator [Karg et al., 2020], superconducting qubits [Kannan et al., 2020], and magnetic spin ensembles [Wang et al., 2022].

The outputs of the waveguides provide a way to observe the spin dynamics using the input-output relation [Gardiner, 1993]. The output fields of the two chiral modes shown in Fig. 6.1(b) are

$$a_{1,\text{out}} = a_{1,\text{in}} + g_1(S_A^- + p_1 S_B^-),$$
  
 $a_{2,\text{out}} = a_{2,\text{in}} + g_2(S_B^- + p_2 S_A^-).$  (6.9)

They allow to observe correlations among the spins that we will discuss in Section 6.7.

## 6.4 Synchronization dynamics

To obtain intuition about the dynamics of the spins, we first employ a mean-field approach where any correlations between spins are neglected following the same approach as in Section 4.2.3 for a single species. Each spin (group label  $a \in \{A, B\}$  and index  $i \in \{1, ..., N\}$ ) has three degrees of freedom. They are the expectation values of spin operators  $\langle \sigma_{a,i}^{\pm,z} \rangle = \text{Tr}[\sigma_{a,i}^{\pm,z} \rho]$  taken with the density matrix at a given time. The coherence  $s_{a,i}^+ = \langle \sigma_{a,i}^+ \rangle = \langle |1\rangle\langle 1|_{a,i} - |0\rangle\langle 0|_{a,i}\rangle$  quantifies which of the states  $|0\rangle$  or  $|1\rangle$  is more populated. From the master equation (6.1), we derive the time evolution of the coherences and populations for each spin. Setting  $s_{a,i}^+ = s_{a,i} \exp(i\phi_{a,i})$ , with  $s_{a,i} \geq 0$ , introduces the real-valued phase of each spin  $\phi_{a,i}$ , which corresponds to the azimuthal phase on the Bloch sphere.

The time evolution of the phases is given by

$$\frac{\mathrm{d}}{\mathrm{d}t}\phi_{a,i} = \delta_a/2 + \frac{s_{a,i}^z}{2N} \sum_{b=A} \sum_{j=1}^N V_{ba} \frac{s_{b,j}}{s_{a,i}} \sin(\phi_{b,j} - \phi_{a,i}), \qquad (6.10)$$

where  $V_{AA} = V_{BB} = V$ , and  $\delta_A = -\delta_B = \delta$ . These equations establish a connection between the open quantum system in Eq. (6.1) and the nonreciprocal Kuramoto model, which describes the time evolution of all-to-all coupled phase oscillators with nonreciprocal interactions  $V_{AB} \neq V_{BA}$  [Fruchart et al., 2021; Hanai, 2024].

In the standard Kuramoto model, which we introduced in Section 2.3, the coupling strengths between the phases of oscillators are constant parameters. A positive coupling K>0 between two phase oscillators of the form  $\mathrm{d}\phi_1/\mathrm{d}t=K\sin(\phi_2-\phi_1)$  will lead oscillator 1 towards locking in phase with oscillator 2, i.e.,  $\phi_1$  is attracted by  $\phi_2$ . If K<0, however,  $\phi_1$  is repelled by  $\phi_2$ , i.e., oscillator 1 tends to align its phase diametrically opposite to the phase of oscillator 2. In contrast, in Eq. (6.10), the coupling strengths are not constant but depend instead on the instantaneous population  $s_{a,i}^z$  and amplitude  $s_{a,i}$  of the spins. The overall sign of the factors multiplying the sine terms determines whether the phases of the spins are attracted or repelled. The incoherent drive continuously pumps the population of each spin to the state  $|1\rangle$ , i.e., results in  $s_{a,i}^z>0$ . The dynamics are then determined by the effective interactions of the spins' phases.

The mean-field treatment is exact in the thermodynamic limit  $N \to \infty$  [Spohn, 1980]. Exploiting the permutational invariance and setting all spins within each group to be equal  $s_{a,i}^{\pm,z} \equiv s_a^{\pm,z}$ , we obtain the following dynamical evolution for the mean coherences and populations [for complex valued  $V_-$  we refer to Appendix 6.A],

$$\frac{\mathrm{d}}{\mathrm{d}t}s_A^+ = [(-\gamma_+ + i\delta)s_A^+ + Vs_A^+ s_A^z + V_{BA}s_B^+ s_A^z]/2, \qquad (6.11a)$$

$$\frac{\mathrm{d}}{\mathrm{d}t}s_B^+ = [(-\gamma_+ - i\delta)s_B^+ + Vs_B^+ s_B^z + V_{AB}s_A^+ s_B^z]/2, \qquad (6.11b)$$

$$\frac{\mathrm{d}}{\mathrm{d}t}s_A^z = \gamma_+ (1 - s_A^z) - 2V s_A^+ s_A^- - 2V_{BA} \operatorname{Re}[s_A^+ s_B^-], \qquad (6.11c)$$

$$\frac{\mathrm{d}}{\mathrm{d}t}s_B^z = \gamma_+ (1 - s_B^z) - 2V s_B^+ s_B^- - 2V_{AB} \operatorname{Re}[s_A^+ s_B^-]. \tag{6.11d}$$

For each species, the equations are the same as Eq. (4.54) with the additional interspecies interaction terms. As we saw in Section 4.2.3, the intraspecies couplings results in a transition to a synchronized state within each species. Let us recapitulate this process. Since  $V \geq 0$ , a positive value of the populations  $s_{a,i}^z > 0$  is required for synchronization. This is achieved by the incoherent drive, which allows for population inversion of the spins; see Eqs. (6.11)(c,d). At the same time, the incoherent drive also causes the decay of the coherences; see Eqs. (6.11)(a,b). This is the process of decoherence [Breuer and Petruccione, 2002, which diminishes phase locking and thus competes with the intraspecies interactions. When the rate of the incoherent drive dominates, the spins therefore converge to an unsynchronized state in which  $s_{A,B}^+=0$  due to the strong decoherence and  $s_{A,B}^z=1$ due to the strong driving. Above a critical value of the coupling strength  $V/\gamma_+$ , the unsynchronized solution becomes unstable. In this regime the spins of each species synchronize as indicated by a finite value of the coherences  $s_{A,B}^+$  [Xu et al., 2014; Zhu et al., 2015. This process spontaneously breaks the U(1) symmetry of our model: both the master equation (6.1) as well as the mean-field equations (6.11) are invariant under a global phase shift  $s_{A,B}^+ \to s_{A,B}^+ \exp(i\phi_0)$  for  $\phi_0 \in \mathbb{R}$ . Yet, in the thermodynamic limit the spins synchronize onto a phase that depends on the initial conditions, thus breaking the U(1) symmetry. Throughout this chapter, we consider values of  $V/\gamma_+$  large enough such that each species is independently synchronized. We refer to Appendix 6.B for further details on the transition to synchronization in this model.

Once synchronization within each species is achieved, the dynamics of the two species is determined by the interspecies couplings. The resulting phase diagram obtained by integrating Eqs. (6.11) is shown in Fig. 6.2(a). When  $V_{AB}$  and  $V_{BA}$  are both positive, the

phases attract each other and all spins of both species synchronize. When they are both negative, the phases of any two spins from different species repel each other, such that the two species lock with a phase shift of  $\pi$ . This results in two different synchronized regimes, which we call synchronized and  $\pi$ -synchronized, respectively. In Fig. 6.2(b) we show the time evolution of the phases of the two species for these two cases.

The most remarkable regime is that of antagonistic interactions, where  $V_{AB}$  and  $V_{BA}$  have opposite signs. In this case, Eq. (6.10) predicts that the spins of one species, say A, try to lock their phases with those of species B. The spins of species B, however, have the opposite inclination, namely, they tend to lock with a phase difference of  $\pi$  with respect to species A.

We stress that the incoherent drive plays a key role in enabling persistent nonreciprocal interactions among the phases of the spins, i.e., interactions whose effects extend beyond the transient. To illustrate this, we adopt a 'general notion of nonreciprocity' [Bowick et al., 2022; Fruchart et al., 2021], since the dynamics are not described in terms of forces. We say that two dynamical variables  $x_A, x_B$  interact in a nonreciprocal way whenever the coupling coefficients are asymmetric:  $\dot{x}_A = C_{BA}x_B$ ,  $\dot{x}_B = C_{AB}x_A$ , where  $C_{AB} \neq C_{BA}$ . In our model, this scenario is realized at the level of the phases [see Eq. (6.10) and the discussion below it], or equivalently at the level of the coherences, as we will now show. We recast Eq. (6.11) in matrix form (here setting  $\delta = 0$  for simplicity)

$$\frac{\mathrm{d}}{\mathrm{d}t} \begin{pmatrix} s_A^+ \\ s_B^+ \end{pmatrix} = \frac{1}{2} \begin{pmatrix} -\gamma_+ + V s_A^z & V_{BA} s_A^z \\ V_{AB} s_B^z & -\gamma_+ + V s_B^z \end{pmatrix} \begin{pmatrix} s_A^+ \\ s_B^+ \end{pmatrix} . \tag{6.12}$$

After some transient evolution, both  $s_A^z$  and  $s_B^z$  settle to a positive value due to the incoherent drive. Therefore, when  $V/\gamma_+$  is large enough, the coherences take a finite value due to the synchronization within each species. From the off-diagonal part of Eq. (6.12), we see that the sign of  $V_{AB}$  and  $V_{BA}$  determines the quality of the interactions. The interactions are nonreciprocal when  $V_{AB}s_A^z \neq V_{BA}s_B^z$ . Since the species are otherwise identical, this scenario occurs when  $V_{AB} \neq V_{BA}$ . Specifically, if sign  $V_{AB} = -\sin V_{BA}$ , they are of the antagonistic type. A similar argument can be made for any pair of two spins, one of species A and one of species B, concluding that the microscopic interactions are nonreciprocal. In the absence of the incoherent drive, the dynamics of the phases may still be nonreciprocal at special times; however, the incoherent drive allows for sustaining nonreciprocal interactions (and the resulting traveling-wave states) in the long-time limit.

## 6.5 Traveling-wave states

For large enough nonreciprocity, we find a regime of nonstationary states; see Fig. 6.2(a). They are characterized by stable oscillations of  $s_a^+$  in the long-time limit, i.e., the phases  $\arg[s_a^+]$  grow linearly in time; see Fig. 6.2(c). Figuratively, the spins of one species persistently chase after the spins of the other species, which in turn run away. The phase difference between the two species as well as  $|s_a^+|$  and  $s_a^z$  are constant. Such states are called traveling-wave states [Hong and Strogatz, 2011b; Fruchart et al., 2021; Brauns and Marchetti, 2024]. From Fig. 6.2(a), we also see that unidirectional interactions  $V_+ = \pm V_-$  highlighted by the diagonal dashed lines lie entirely inside the static regions, which confirms that traveling-wave states are beyond the reach of magnitude nonreciprocity. Moreover, between the  $(\pi)$ -synchronized and the traveling-wave regimes, we find a region of modulated traveling-wave states [Fruchart et al., 2021]. In these states, the relative phase difference as well as  $|s_a^+|$  and  $s_a^z$  also oscillate in time. Exemplary trajectories are shown in Fig. 6.2(d).

The traveling-wave state displays time-crystalline order [Hanai, 2024] and can be understood as an instance of a continuous time crystal [Sacha and Zakrzewski, 2017; Iemini et al., 2018; Kongkhambut et al., 2022]. As a time-dependent oscillatory state, it breaks the time-translation symmetry of the microscopic model (6.1), analogously to a standard crystal which breaks space-translation symmetry. In other words, the traveling-wave state is a dynamical pattern that emerges via self-organization due to the spin-spin interactions. The transition from a synchronized state to a traveling-wave state is a nonreciprocal phase transition. It is known to occur for ensembles of classical phase oscillators, where the phase diagram is similar to that of Fig. 6.2(a) [Fruchart et al., 2021, Extended Data Fig. 4(a)]. The emergence of a nonreciprocal phase transition and traveling-wave states from a microscopic quantum spin model is a key finding of this thesis.

#### 6.5.1 Order from decoherence

For classical phase oscillators, it has been shown that traveling-wave states require the presence of disorder in their frequencies or additional phase noise [Fruchart et al., 2021; Hanai, 2024]. In the absence of frequency disorder or noise, the oscillators will eventually reach either a synchronized or a  $\pi$ -synchronized state. Adding disorder or noise prevents relaxation towards these stationary states, stabilizing the dynamical states.

In our model, decoherence is responsible for the stabilization of the traveling-wave state, without the need to include any external source of noise or disorder. The decoherence stems from the coupling to the environment and implies a decay of the coherences  $s_{A,B}^+$ ; see Eqs. (6.11)(a,b). While the decoherence resulting from the dissipative interactions defined in Eqs. (6.3) and (6.4) is negligible for a large number N of spins, the incoherent drive at rate  $\gamma_+$  entails decoherence independently of N. The decoherence prevents a fully coherent, stationary state and thus takes the role of noise or disorder to perturb stationary states in classical systems. We conclude that the incoherent drive is essential for the emergence of traveling-wave states in two ways: It activates each spin by inverting the populations, which allows for nonreciprocal phase interactions; and it provides decoherence that stabilizes the dynamical state.

#### 6.5.2 Spontaneous PT-symmetry breaking

In the traveling-wave phase, we find two stable solutions that are shown in Fig. 6.2(c). They differ by the chirality of the emergent oscillation. Depending on the chirality, the observed frequency is either positive or negative, and the phase difference between the two species takes a constant value of approximately  $+\pi/2$  or  $-\pi/2$ ; see also Appendix 6.C. The two solutions are related by a symmetry transformation of the mean-field equations (6.11). This symmetry is referred to as a generalized  $\mathcal{PT}$  (parity-time) symmetry [Fruchart et al., 2021]. Introducing a shorthand notation for the mean-field equations (6.11),  $d\mathbf{s}/dt = \mathbf{L}(\mathbf{s})$ , where  $\mathbf{s} = (s_A^+, s_B^+, s_A^z, s_B^z)$  and  $\mathbf{L}(\mathbf{s})$  is the right-hand side of equations (6.11), we have

$$\mathbf{L}(\mathbf{s}) = \mathbf{L}^*(\mathbf{s}), \quad \text{if } \delta = 0. \tag{6.13}$$

The star denotes complex conjugation. The  $\mathcal{PT}$  symmetry implies that when  $\mathbf{s}(t)$  is a solution, then  $\mathbf{s}^*(t)$  is a solution as well:

for any solution 
$$\mathbf{s}(t) \Rightarrow \mathbf{s}^*(t)$$
 is solution. (6.14)

Each of the two stable solutions spontaneously breaks  $\mathcal{PT}$  symmetry, and the two solutions are related by the symmetry transformation, i.e., complex conjugation. The spontaneous

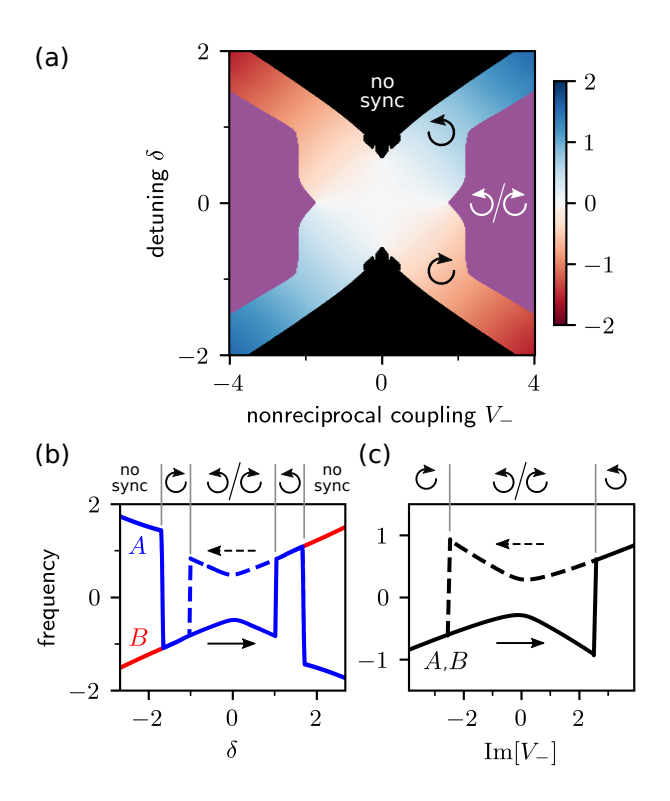
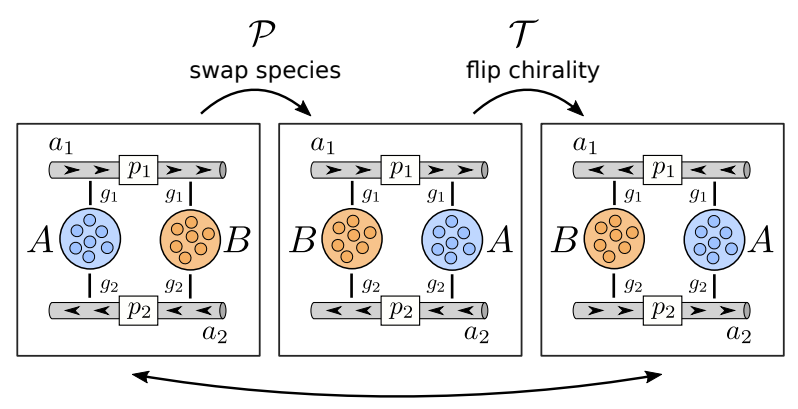


Figure 6.3: Explicit symmetry breaking. (a) The color bar indicates the frequency of the oscillation of the spins in the case of explicit symmetry breaking ( $\circlearrowleft$  or  $\circlearrowright$ ). Furthermore, the purple color indicates where the symmetry is spontaneously broken and either of two frequencies is obtained  $(\circlearrowleft/\circlearrowright)$ . Black shows the unsynchronized regime where the two spin species oscillate at different frequencies. (b) Cut through (a) at  $V_{-}=2.5$ . Shown are the frequencies of species A (red) and B (blue) when increasing (solid line) and decreasing (dashed line) the detuning. If the two species are synchronized, their common frequency is shown in blue. There are five regions from left to right: an unsynchronized state, a synchronized state in which the symmetry is explicitly broken ( $\circlearrowright$ ), two states that spontaneously break the symmetry  $(\circlearrowleft/\circlearrowright)$ , explicitly broken  $(\circlearrowleft)$  and unsynchronized. (c) Similar to (b) when the symmetry is explicitly broken by  $Im[V_{-}]$  at constant  $Re[V_{-}] = 1.5$ . There are no unsynchronized states in this case. Parameters:  $V_{+}=1$ , V=2. All frequencies and interaction strengths are given in units of  $\gamma_+$ .

breaking of  $\mathcal{PT}$  symmetry is a key feature of nonreciprocal phase transitions [Fruchart et al., 2021]. Time-translation invariance is concurrently broken: Each of the traveling-wave states forms one of two possible time-crystalline orders.

#### 6.5.3 Explicit PT-symmetry breaking

We illustrate the effect of explicitly breaking  $\mathcal{PT}$  symmetry in Fig. 6.3(a) by considering a finite detuning  $\delta$  between the species, which was set to zero in the analysis so far. For small values of  $\delta$ , spontaneous breaking still occurs as indicated by the purple regime. This shows that the traveling-wave phase possesses some degree of robustness to frequency imbalance, i.e., the spontaneous breaking of  $\mathcal{PT}$  symmetry occurs even when the  $\mathcal{PT}$  transformation is not a perfect symmetry of the model. For larger values of  $\delta$ , however, one of the two traveling-wave states becomes the only stable solution indicated by blue and red regions. For very large detuning, we find yet another regime (black) in which the two species are unsynchronized and oscillate at different frequencies. This is the expected



symmetric under combined  $\mathcal{PT}$ - transformation

Figure 6.4: Effect of parity  $(\mathcal{P})$  and time reversal  $(\mathcal{T})$  transformations in the implementation of our model using chiral waveguides. The model is  $\mathcal{PT}$  symmetric if  $\delta=0$ . A finite detuning distinguishes the left and right locations of the spins and thereby explicitly breaks the  $\mathcal{PT}$  symmetry.

behavior of two coupled limit-cycle oscillators that are strongly detuned as discussed in the context of the Adler equation; see Eq. (2.21).

In the traveling-wave regime, oscillations with opposite chiralities are stable. The bistability is associated with a hysteresis in the observed frequency of the oscillations. In Fig. 6.3(b), we show the hysteretic behavior by adiabatically increasing and decreasing the detuning. Starting from a large negative value of  $\delta$  where the spins are unsynchronized, the spins first enter a traveling-wave phase with unique chirality. Upon further increasing the detuning, the state maintains the same chirality throughout the coexistence phase, until it becomes unstable and the traveling-wave state with opposite chirality is attained. When reversing this parameter sweep, however, the spins remain in the state with opposite chirality in the coexistence regime. Similarly, including a nonzero imaginary part of  $V_-$  also breaks  $\mathcal{PT}$  symmetry explicitly, resulting in a hysteretic behavior, as shown in Fig. 6.3(c). Notice that the unsynchronized state only occurs for large  $\delta$ , while for large Im $[V_-]$ , the system remains in the explicitly broken regime.

## 6.6 Origin of PT symmetry

So far, we have discussed the generalized  $\mathcal{PT}$  symmetry as a property of the mean-field equations. We now show how the notion of  $\mathcal{PT}$  symmetry is grounded in physical terms and how it emerges from a microscopic theory. While  $\mathcal{PT}$  symmetry is typically discussed on the level of non-Hermitian Hamiltonians [Bender and Hook, 2024], here, an understanding of  $\mathcal{PT}$  symmetry on the level of the master equation is required. In open quantum systems, a distinction can be made between weak and strong symmetries [Buča and Prosen, 2012; Albert and Jiang, 2014]: For weak symmetries, the total Liouvillian commutes with the symmetry operation, while for strong symmetries, the Hamiltonian and all jump operators each commute with the symmetry operation individually.  $\mathcal{PT}$  symmetry of master equations has been defined both in a weak [Prosen, 2012; Huybrechts et al., 2020; Sá et al., 2023] and in a strong sense [Huber et al., 2020; Nakanishi and Sasamoto, 2022]. The notion we put forward corresponds to a weak symmetry. We will say that a Liouvillian  $\mathcal{L}$  is  $\mathcal{PT}$ -symmetric or invariant under  $\mathcal{PT}$  transformation when  $\mathcal{PT}\mathcal{L}(\mathcal{PT})^{-1} = \mathcal{L}$ . This choice of  $\mathcal{PT}$  symmetry is physically motivated by the proposed implementation of our model, as we now show.

The effects of  $\mathcal{PT}$  transformation in our model are depicted in Fig. 6.4. In the context of two interacting species, it is typical to define the parity transformation  $(\mathcal{P})$  as the exchange of the two species  $\mathcal{P}: A \leftrightarrow B$  [Huber et al., 2020; Nakanishi and Sasamoto, 2022; Bender and Hook, 2024. On the master equation level, this corresponds to the unitary swap  $\sigma_{A,i}^{\pm,z} \leftrightarrow \sigma_{B,i}^{\pm,z}$ . If a detuning is present, A and B change their frequency under  $\mathcal{P}$ . Therefore, in the implementation shown in Fig. 6.4, the detuning is a local property that distinguishes the left and right sides. For the definition of time reversal  $(\mathcal{T})$ , we inspect the effect of a time-reversed propagation of the two modes  $a_{1,2}$ , which is equivalent to flipping the chirality of the waveguides. Since  $V_-/N = p_1 g_1^2 \eta_1 - p_2 g_2^2 \eta_2$ , this effectively changes the sign of the coherent interactions between the two spin species. We therefore find  $\mathcal{T}: H_{\text{inter}} \to -H_{\text{inter}}$ . Combining the two transitions, we obtain that, if  $\delta = 0$ , our model defined by Eq. (6.1) is  $\mathcal{PT}$  symmetric, i.e., invariant under the combined  $\mathcal{PT}$  transformation  $(A \leftrightarrow B \text{ and } H_{\text{inter}} \rightarrow -H_{\text{inter}})$ . Otherwise, the  $\mathcal{PT}$  symmetry is explicitly broken. An imaginary part of  $V_{-}$  also explicitly breaks  $\mathcal{PT}$  symmetry. The same transformation is obtained when considering the implementation shown in Fig. 6.1(c), where the bidirectional waveguide is invariant under  $\mathcal{T}$ ; see Appendix 6.A.

Remarkably, the  $\mathcal{PT}$  transformation just introduced is equivalent to complex conjugation of the Liouvillian superoperator  $\mathcal{L}$  in Eq. (6.1), namely

$$\mathcal{PT}: (A \leftrightarrow B \text{ and } H_{\text{inter}} \to -H_{\text{inter}}) \iff \mathcal{L} \to \mathcal{L}^*.$$
 (6.15)

Complex conjugation of a generic Liouvillian, given a Hamiltonian H and a set of jump operators  $\{L_{\mu}\}$ , is defined as  $\mathcal{L}\rho = -i[H,\rho] + \sum_{\mu} \mathcal{D}[L_{\mu}]\rho \to \mathcal{L}^*\rho = +i[H^*,\rho] + \sum_{\mu} \mathcal{D}[L_{\mu}^*]\rho$ . A  $\mathcal{PT}$ -symmetric Liouvillian has several important consequences. First of all, in the thermodynamic limit, the  $\mathcal{PT}$  symmetry of the mean-field equations as defined in Eq. (6.14) follows:

$$\mathcal{L} = \mathcal{L}^* \Rightarrow \text{(for any solution } \mathbf{s}(t) \Rightarrow \mathbf{s}^*(t) \text{ is solution)}$$
 (6.16)

This can be shown in the following way. For any solution  $\rho_0(t)$ , i.e.,  $\dot{\rho}_0(t) = \mathcal{L}\rho_0(t)$ ,  $\rho_0^*(t)$  is a solution as well, since  $\dot{\rho}_0^*(t) = \mathcal{L}^*\rho_0^*(t) = \mathcal{L}\rho_0^*(t)$ . The mean-field Ansatz used to obtain (6.11) is

$$\rho_0(\mathbf{s}) = \bigotimes_{i=1}^{N} \bigotimes_{a=A,B} (1 + s_a^z \sigma^z + 2s_a^+ \sigma^- + 2s_a^- \sigma^+) / 2,$$

where  $\mathbb{1} = |0\rangle\langle 0| + |1\rangle\langle 1|$ . Given  $\mathbf{s}_0(t)$  such that  $\rho_0(\mathbf{s}_0(t))$  is a solution,  $\rho_0^*(\mathbf{s}_0(t)) = \rho_0(\mathbf{s}_0^*(t))$  is a solution as well, which implies that both  $\mathbf{s}_0(t)$  and  $\mathbf{s}_0^*(t)$  solve the mean-field equations (6.11).

With Eq. (6.16), we have established the emergence of  $\mathcal{PT}$  symmetry, which is spontaneously broken in the thermodynamic limit, from a physical and microscopic theory. As we show in the next section, the symmetry constrains the spin correlations and dynamics for finite-size systems away from the thermodynamic limit.

#### 6.7 Finite-size system

#### 6.7.1 Steady-state correlations

We start the analysis of finite-size systems by considering the long-time limit of master equation (6.1). For any finite number of spins, a unique time-independent steady-state density operator is obtained. This is a general property of finite-size systems and contrasts with the previous analysis in the thermodynamic limit, where a time-dependent state can be obtained. To analyze the steady state, we compute expectation values of operators

 $\langle o \rangle = \text{Tr}[\rho o]$ . Since all spins within each species are identical, we can drop the index labeling the individual spins, e.g.,  $\langle \sigma_A^z \rangle = \langle \sigma_{A,i}^z \rangle$  or  $\langle \sigma_A^+ \sigma_A^- \rangle = \langle \sigma_{A,i}^+ \sigma_{A,j}^- \rangle$  for  $i \neq j$ . The correlations within each species and between species are measurable by considering the output of the chiral waveguides; see Eq. (6.9).

The steady state respects the symmetries of the master equation, i.e., U(1) symmetry and  $\mathcal{PT}$  symmetry. As a result of the U(1) symmetry, expectation values that are affected by a global phase shift, such as  $\langle \sigma_A^+ \rangle$ , vanish, while the  $\mathcal{PT}$  symmetry defined in Eq. (6.15) enforces that the unique steady state is real valued, namely

$$\mathcal{L} = \mathcal{L}^* \Rightarrow \rho_{\rm ss} = \rho_{\rm ss}^* \,. \tag{6.17}$$

Therefore, the expectation value of certain operators, such as  $\sigma_A^+ \sigma_B^-$ , must also be real valued. We will find this to be important later on.

We compute the exact steady state of Eq. (6.1) for small numbers of spins up to N = 19 (and N = 90 for  $V_{-} = 0$  and  $V_{+} = V$ , where all spins of both species are equal). For larger N, we resort to the cumulant expansion approximation, which allows one to systematically include correlations up to a certain order [Kubo, 1962]. We used this expansion in the analysis of a single ensemble of spins; see Eq. (4.58). Here, we perform an expansion to second and to fourth order; details are provided in Appendix 6.D.

In Fig. 6.5, we show the steady-state correlations and populations as a function of the number of spins per species N. The results from the cumulant expansion agree very well with the exact solution for large and small N. For large N, the agreement is expected as the cumulant expansion is exact in the thermodynamic limit. For small N, the agreement results from the simplicity of the state that can be well captured by the approximation. In an intermediate regime,  $5 \lesssim N \lesssim 100$ , however, there are deviations. They hint at the existence of nontrivial higher-order correlations in this regime, which are not well captured by a low-order cumulant expansion. We expect the cumulant expansion to converge to the exact results when including higher-order correlations. Indeed, the fourth-order expansion agrees better with the exact solution than the second-order expansion, as highlighted in the inset of Fig. 6.5(b).

The intraspecies correlations, as measured by  $\langle \sigma_A^+ \sigma_A^- \rangle$  shown in Fig. 6.5(a), indicate synchronization within each ensemble (an analogous plot is obtained for species B). The correlations increase with the number of spins but do not change significantly beyond  $N \gtrsim 200$ . The interspecies correlations  $\langle \sigma_A^+ \sigma_B^- \rangle$  quantify the synchronization between species. In general,  $\langle \sigma_A^+ \sigma_B^- \rangle$  is a complex number whose argument determines the relative phase difference between the two species. In our case, however,  $\mathcal{PT}$  symmetry implies that these correlations are real valued. Figure 6.5(c) highlights that in the synchronized state, the phase difference is zero, while the  $\pi$ -synchronized state is indicated by negative correlations. This becomes clear from Fig. 6.6(a), which shows the correlations as a function of  $V_{\pm}$  at fixed N.

In the traveling-wave state, the correlations between the two species vanish when  $V_{+}=0$ ; see Fig. 6.5(c) and Fig. 6.6(a). However, in the thermodynamic limit, the correlations factorize:  $\langle \sigma_{A}^{+}\sigma_{B}^{-}\rangle \xrightarrow{N\to\infty} s_{A}^{+}s_{B}^{-}$ . Therefore, one could expect one of two possible nonzero complex values, each corresponding to one of two possible solutions related by  $\mathcal{PT}$  transformation, i.e., complex conjugation. The apparent discrepancy is resolved by considering that the density operator describes an ensemble of possible trajectories, which contains both states that spontaneously break  $\mathcal{PT}$  symmetry. In the two traveling-wave states, the species lock at a phase difference close to  $+\pi/2$  or  $-\pi/2$ . The average of  $s_{A}^{+}s_{B}^{-}\sim \exp(\pm i\pi/2)$  is therefore small and vanishes for  $V_{+}=0$ . We will explicitly show the spontaneous breaking of  $\mathcal{PT}$  symmetry in quantum trajectories in Section 6.8.

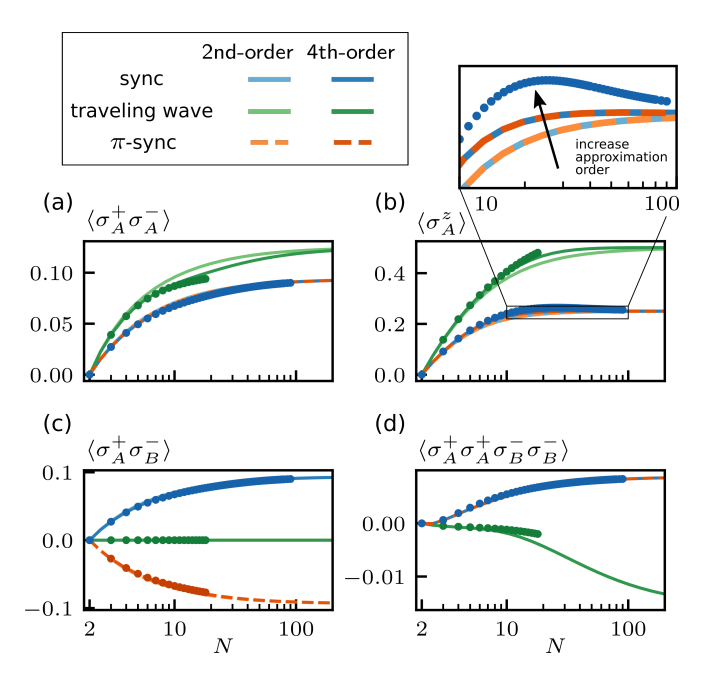


Figure 6.5: Spin correlations and population as a function of number of spins N for  $(\pi)$ -synchronized and traveling-wave state. The solid and dashed lines are computed with the cumulant expansion, and the dots (same colors) show the exact solution of the master equation. The inset shows a zoom of the nonmonotonous behavior of the populations and highlights the convergence of the approximations. Parameters:  $\delta=0$ ,  $V=2\gamma_+$ ; synchronized state:  $V_-=0$ ,  $V_+=2\gamma_+$ ; traveling-wave state:  $V_-=2\gamma_+$ ,  $V_+=0$ ;  $\pi$ -synchronized state:  $V_-=0$ ,  $V_+=0$ ,  $V_+=0$ .

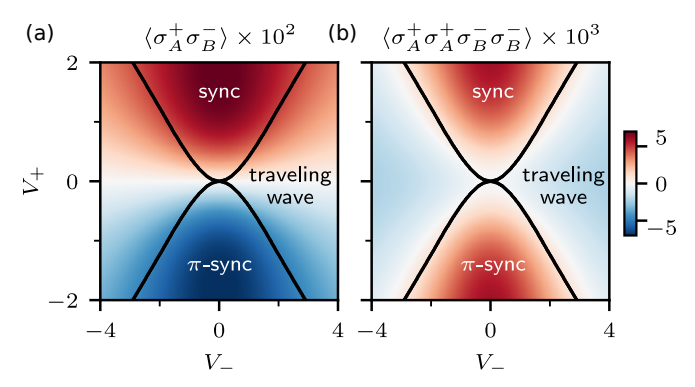


Figure 6.6: (a) Second-order correlations  $\langle \sigma_A^+ \sigma_B^- \rangle$  between the two groups. This quantity allows us to distinguish between the synchronized and  $\pi$ -synchronized phases. The correlations are suppressed in the traveling-wave phase. The black lines are the boundaries of the mean-field phase diagram in Fig. 6.2(a). (b) Fourth-order correlations  $\langle \sigma_A^+ \sigma_A^+ \sigma_B^- \sigma_B^- \rangle$ . A negative value indicates the traveling-wave state. Parameters: V=2,  $\delta=0$ , all interaction strengths in units of  $\gamma_+$ , and N=12.

Whereas features of the traveling-wave states are not revealed by second-order correlations, they become apparent in higher-order correlations. We show in Fig. 6.5(d) and Fig. 6.6(b) the fourth-order correlations  $\langle \sigma_A^+ \sigma_A^+ \sigma_B^- \sigma_B^- \rangle$  between four different spins. It is negative only in the traveling-wave regime. In the two possible traveling-wave states of the thermodynamic limit, the species maintain a phase difference close to  $\pm \pi/2$ . In both cases, the product  $s_A^+ s_A^+ s_B^- s_B^- < 0$  is negative. Therefore, averaging over the two possible traveling-wave states does not result in a suppression of these correlations. For any finite-size system, we have thus established the fourth-order correlations as a measure that signals the traveling-wave phase even from the stationary steady-state density matrix. However, this does not prove the presence of dynamics in finite-size systems yet, and this point will be addressed in the next section.

#### 6.7.2 Two-time correlations, spectra, and exceptional points

As in Section 4.2, we will analyze the dynamics of the spins through the two-time correlations and the associated spectra. The two-time correlations  $\langle \sigma_a^+(t+\tau)\sigma_b^-(t)\rangle$  quantify correlations between spins of species  $a,b\in\{A,B\}$  at two times that differ by  $\tau$ . The spectrum for each species is defined as the Fourier transform of two-time correlations

$$S_a(\omega) = \lim_{t \to \infty} \int_0^\infty d\tau \, \langle \sigma_a^+(t+\tau)\sigma_a^-(t) \rangle e^{i\omega\tau} \,. \tag{6.18}$$

In this chapter, we use a definition of the spectrum where the integral is evaluated from 0 to  $\infty$ . While this differs from the definition used in the previous chapters, the spectra give qualitatively the same results. The spectrum is experimentally accessible via standard methods like heterodyne measurements [Wiseman and Milburn, 2010] of the output of the chiral waveguides shown in Fig. 6.1(b) and defined in Eq. (6.9).

To calculate the spectrum efficiently, we employ the quantum regression theorem [Breuer and Petruccione, 2002; Meiser et al., 2009]. We factorize the third-order correlations,  $\langle \sigma_a^z(t+\tau)\sigma_b^+(t+\tau)\sigma_B^-(t)\rangle \approx s_a^z(t+\tau)\langle \sigma_b^+(t+\tau)\sigma_B^-(t)\rangle$ . Then, the two-time correlations evolve according to

$$\frac{\mathrm{d}}{\mathrm{d}\tau} \begin{pmatrix} \langle \sigma_A^+(t+\tau)\sigma_a^-(t) \rangle \\ \langle \sigma_B^+(t+\tau)\sigma_a^-(t) \rangle \end{pmatrix} = M \begin{pmatrix} \langle \sigma_A^+(t+\tau)\sigma_a^-(t) \rangle \\ \langle \sigma_B^+(t+\tau)\sigma_a^-(t) \rangle \end{pmatrix}, \tag{6.19}$$

with

$$M = \frac{1}{2} \begin{pmatrix} -\gamma_A + i\delta + V s_A^z & V_{BA} s_A^z \\ V_{AB} s_B^z & -\gamma_B - i\delta + V s_B^z \end{pmatrix}, \tag{6.20}$$

where the effective decoherence rate  $\gamma_{A,B} = \gamma_+ + V(1 + s_{A,B}^z)/N$  depends on the number of spins N. The populations  $s_a^z$  that enter M are to be evaluated at time  $t + \tau$ . To obtain the spectra, we solve Eq. (6.18) together with Eq. (6.19), setting the initial condition of the two-time correlations for  $\tau = 0$  to the steady-state correlations obtained from the cumulant expansion discussed in Section 6.7.1.

In Fig. 6.7(a), we show the spectrum  $S_A(\omega)$  of species A as a function of the non-reciprocal coupling  $V_-$  for  $\delta = 0$ . The synchronized phase exhibits a single peak at zero frequency, while the traveling-wave phase is indicated by peaks in the spectrum at nonzero frequencies. At the critical value of  $V_-$  that separates the two phases, we find an exceptional point at which the two eigenvectors of the matrix M become collinear. The exceptional point marks the crossing of a nonreciprocal phase transition [Fruchart et al., 2021]. The presence of two peaks signals the two traveling-wave states with opposite chirality.

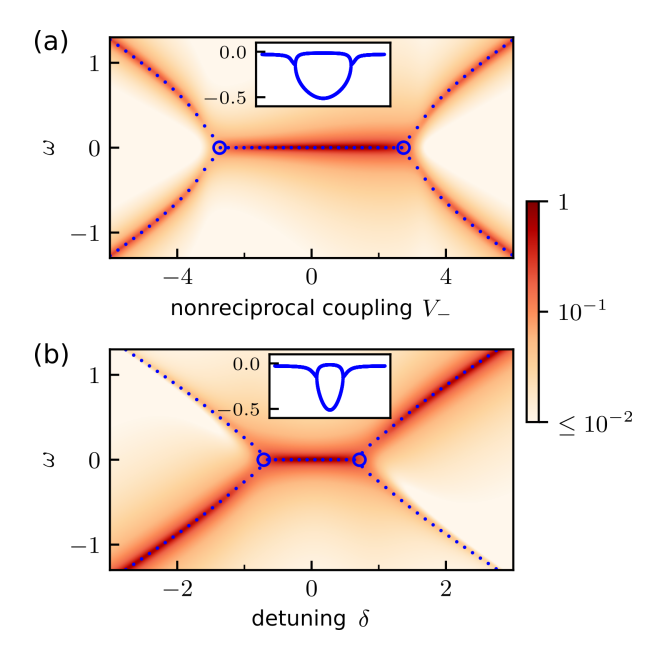


Figure 6.7: Spectrum  $|S_A(\omega)|$  for the finite-size system with N=100 as a function of  $V_-$  (a) and  $\delta$  (b). The spectrum is obtained by using Eq. (6.20) together with the cumulant expansion. It is shown on a logarithmic scale normalized to the maximum value. The blue dots mark the imaginary parts of the eigenvalues of the dynamical matrix M. Blue circles denote exceptional points. The insets show the real part of the eigenvalues of M. Parameters: N=100, V=2, (a)  $\delta=0$ , (b)  $V_-=0$ . All frequencies and interaction strengths in units of  $\gamma_+$ .

The spectrum in Fig. 6.7(a) is symmetric under  $\omega \to -\omega$ . This is a consequence of  $\mathcal{PT}$  symmetry ( $\mathcal{L} = \mathcal{L}^*$ ). To see this, we consider the following expression of the two-time correlations in the long-time limit, which depends on the steady-state density matrix  $\rho_{ss}$  [Breuer and Petruccione, 2002],

$$\lim_{t \to \infty} \langle \sigma_a^+(t+\tau)\sigma_b^-(t) \rangle = \text{Tr}\left[\sigma_a^+ e^{\mathcal{L}\tau}(\sigma_b^- \rho_{\rm ss})\right]. \tag{6.21}$$

When the Liouvillian is  $\mathcal{PT}$  symmetric, the unique steady state is real valued, as we have shown in the previous section. Therefore, the two-time correlations are also real valued and

$$\mathcal{L} = \mathcal{L}^* \Rightarrow |S_a(\omega)| = |S_a(-\omega)|. \tag{6.22}$$

Thus, the  $\mathcal{PT}$  symmetry enforces that the two traveling-wave states with opposite chirality occur with equal weight in the spectral density.

Another exceptional point occurs when explicitly breaking  $\mathcal{PT}$  symmetry by  $\delta$ ; see Fig. 6.7(b), where we set  $V_-=0$ . The synchronization behavior is qualitatively the same as the one of classical phase oscillators; see Fig. 2.5. For large detuning, the spectrum indicates an unsynchronized state in which A oscillates at  $+\delta/2$ , while B oscillates at  $-\delta/2$  (not shown). At the transition between synchronized and unsynchronized states, M exhibits an exceptional point. In this case, however, the spectrum is not symmetric under  $\omega \to -\omega$ , and the transition stems from breaking  $\mathcal{PT}$  symmetry explicitly.

Finally, the dynamics of the modulated traveling-wave state are also observable in the spectrum of a finite-size system; see Fig. 6.8(a). Between the synchronized phase and the traveling-wave phase, a comb of frequencies opens up, signaling a more intricate time-crystalline order. The higher harmonics in the spectrum are consistent with the nonlinear evolution of the phases in the thermodynamic limit; see Fig. 6.2(d). The comb

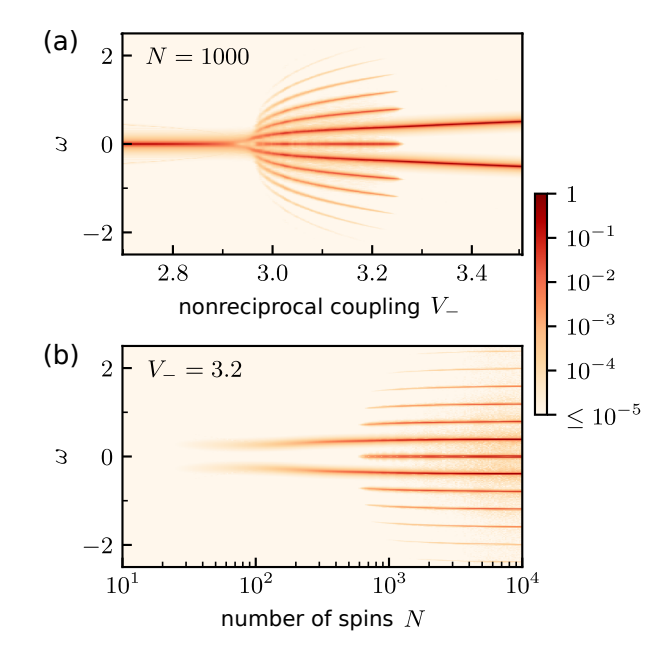


Figure 6.8: Spectrum  $|S_A(\omega)|$  for finite-size systems shown on a logarithmic scale normalized to the maximum value. The spectrum is obtained by using Eq. (6.20) together with the cumulant expansion. (a) Transition from the synchronized to the traveling-wave state via the modulated traveling-wave state for N=1000. In the modulated phase, higher harmonics appear in the spectrum. (b) Spectrum of the modulated traveling-wave state as a function of N at  $V_-=3.2$ . Parameters:  $\delta=0$ ,  $V_+=V=2$ . All frequencies and interaction strengths in units of  $\gamma_+$ .

only becomes visible for  $N \gtrsim 600$  spins as shown in Fig. 6.8(b). With increasing N, the comb structure becomes more pronounced.

## 6.8 Quantum trajectories

So far, we have analyzed quantities obtained by computing expectation values of operators using the density matrix. As discussed in Section 3.3, the density matrix can be viewed as an ensemble description of quantum trajectories. Each quantum trajectory is the evolution of the quantum system conditioned on the knowledge obtained by measurements. In this section, we will study individual quantum trajectories.

Our model allows for a continuous measurement of the spin degrees of freedom by observing the modes that mediate the interactions. For simplicity, we focus on the case  $V_{+} = V$  while varying  $V_{-}$  and consider the implementation depicted in Fig. 6.1(c). To model the measurement, we explicitly include the coupling to mode  $a_{+}$ , which mediates reciprocal interactions, in the master equation

$$\dot{\rho} = -i\left[\frac{\Omega}{2}(a_+^{\dagger}S^- + a_+S^+) + H_0 + H_{\text{inter}}, \rho\right] + \kappa \mathcal{D}[a_+]\rho + \mathcal{L}_{\text{drive}}\rho \equiv \mathcal{L}_{\text{m}}\rho.$$
 (6.23)

Here,  $S^{\pm} = S_A^{\pm} + S_B^{\pm}$  and  $\kappa$  is the decay rate of mode  $a_+$ , which can be thought of as a lossy cavity. In the limit  $\kappa \gg \Omega$ , the cavity mode can be adiabatically eliminated,  $a_+ = -i\Omega S^-/\kappa$ , and Eq. (6.23) reduces to master equation (6.1) with  $V = V_+ = Ng_+^2 = N\Omega^2/\kappa$ .

The dynamics can be observed experimentally by standard homodyne and heterodyne detection techniques: The output of the cavity  $a_+$  is mixed with a constant signal from

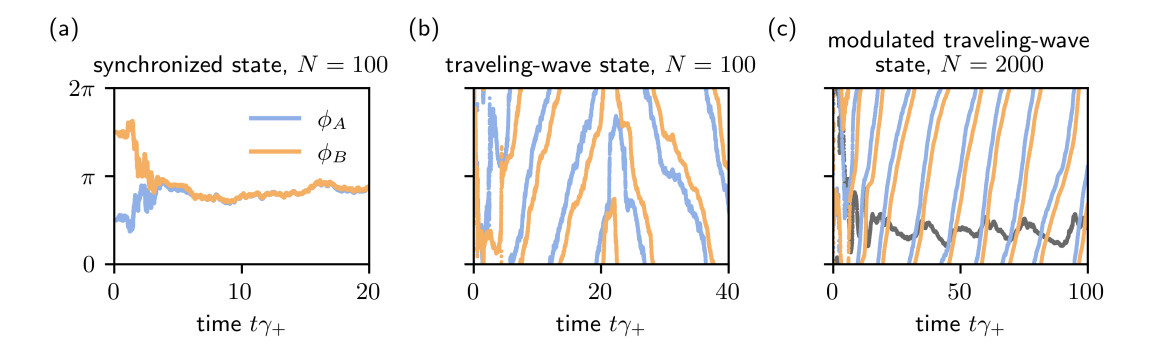


Figure 6.9: Time evolution under heterodyne detection of the phases of the spins. (a) Synchronized state for  $V_- = V_+/2$  and N = 100. The phases of spins A and B synchronize, and a state that is static up to noise is obtained. (b) Traveling-wave state for  $V_- = 2V_+$  and N = 100. The phases of the spin species continuously oscillate while the phase difference remains constant. At around  $t\gamma_+ = 22$ , the chirality of the state switches. (c) Modulated traveling-wave states for  $V_- = 1.6V_+$ , here shown for N = 2000. The gray line shows the phase difference, which is not static (compare to Fig. 6.2(d)). Parameters:  $\delta = 0$ ,  $\xi = 1$ ,  $\omega_{\rm m}/\kappa = 2\pi$ ,  $\Omega/\kappa = 1/\sqrt{5N}$ ,  $V_+ = V = 2\gamma_+$ .

a local oscillator with frequency  $\omega_{\rm m}$ . As reviewed in Section 3.3, the evolution of the quantum state is then determined by the stochastic quantum master equation [Wiseman and Milburn, 2010]

$$\dot{\rho}_{\rm m} = \mathcal{L}_{\rm m} \rho_{\rm m} + \frac{\mathrm{d}W}{\mathrm{d}t} \sqrt{\kappa \xi} \left[ e^{i\phi_{\rm m}(t)} (a_{+} - \langle a_{+} \rangle_{\rm m}) \rho_{\rm m} + \mathrm{H.c.} \right], \tag{6.24}$$

where  $\rho_{\rm m}$  is the density matrix conditioned on the measurement outcome and  $\langle a_+\rangle_{\rm m}={\rm Tr}[a_+\rho_{\rm m}]$ . The measurement backaction is described by the random Wiener increment  ${\rm d}W$ , which follows a normal distribution with variance  ${\rm d}W^2={\rm d}t$  and zero mean. The detection efficiency  $\xi$  can take values  $\xi\in[0,1]$ . For  $\xi=0$ , no information about the quantum state is obtained, and Eq. (6.24) reduces to Eq. (6.23). For simplicity, we focus on an ideal detector with  $\xi=1$ . The phase  $\phi_{\rm m}$  determines how the cavity field  $a_+$  is monitored. When the phase is set constant (in the frame rotating with the cavity field  $a_+$ ), the measurement is called homodyne detection, and it probes the quadrature  $a_+e^{i\phi_{\rm m}}+a_+^{\dagger}e^{-i\phi_{\rm m}}$ . When the phase increases with time as  $\phi_{\rm m}(t)=\omega_{\rm m}t$ , where  $\omega_{\rm m}$  is large compared to the timescale at which the dynamics occur, the measurement is called heterodyne detection. Thus, all possible quadratures are probed in quick succession, and the measurement becomes effectively isotropic.

To solve Eq. (6.24), we resort to a cumulant expansion [Zhang et al., 2022], which we have already shown in Section 6.7 to describe well the unconditional time evolution; see details in Appendix 6.E.

#### 6.8.1 Heterodyne measurement

Figure 6.9 shows quantum trajectories in the presence of heterodyne detection of synchronized, traveling-wave, and modulated traveling-wave states, respectively. These results can be compared with the time evolution in the thermodynamic limit depicted in Fig. 6.2(b-d). In the synchronized state, see Fig. 6.9(a), the phases  $\phi_a \equiv \arg[\langle \sigma_a^+ \rangle_m]$  of the two spin

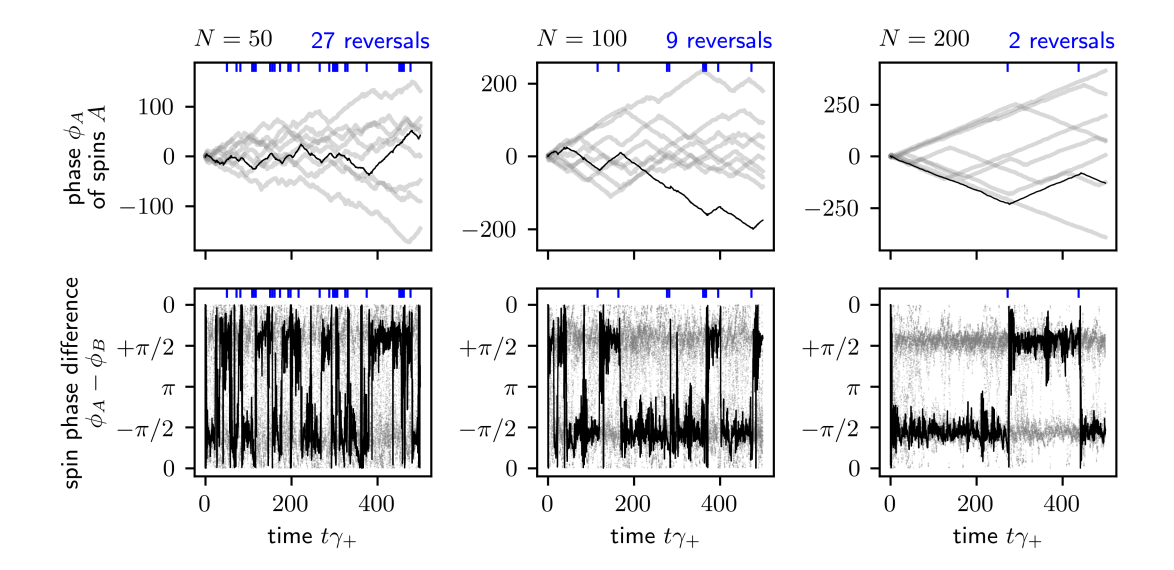


Figure 6.10: Time evolution under heterodyne detection of the phase of the spins of species A (top row) and phase difference (bottom row) for different numbers of spins (columns). Several quantum trajectories are shown in gray, and one is highlighted in black, which for each column is the same trajectory in the top and bottom panels. In the top row, the phase is unwrapped, i.e.,  $2\pi$  is added or subtracted to the value of the phases such that the absolute difference between adjacent phase values never exceeds  $\pi$ . This allows for easily distinguishing between periods of increasing and decreasing phase. Chirality reversals for  $t\gamma_+ > 50$  are marked as blue ticks on the upper horizontal axes, respectively. Parameters: same as Fig. 6.9(b) with N specified for each column.

species  $a \in \{A, B\}$  assume nearly the same constant value after some transient evolution. For any individual quantum trajectory, the U(1) symmetry of the master equation (6.1) is spontaneously broken; see also [Zhang et al., 2022]. Averaging over many trajectories recovers the density matrix description where  $\langle \sigma_a^+ \rangle = 0$  in the steady state.

In the quantum traveling-wave state shown in panel (b) of Fig. 6.9, the spins oscillate with one of two chiralities, i.e., positive or negative frequency, and the phase difference assumes values close to  $\pm \pi/2$ . The continuous time-translation invariance of Eq. (6.1) is spontaneously broken due to the measurement backaction; see also [Cabot et al., 2023]. On the other hand, the U(1) symmetry is dynamically restored, i.e., no phase is preferred in the time average of a single trajectory [Fruchart et al., 2021]. Figure 6.9(c) shows a modulated traveling-wave state. In this case, we have set N=2000 since only for larger values of N, the additional dynamics occur as we showed in Fig. 6.8(b).

The measurement backaction spontaneously breaks  $\mathcal{PT}$  symmetry: At different times, one of the two possible traveling-wave states is assumed. It further causes randomly occurring chirality reversal, i.e., switches between the two traveling-wave states. One such reversal occurs in the trajectory displayed in Fig. 6.9(b) at around  $t\gamma_{+}=22$ . This is similar to the classical nonreciprocal Kuramoto model in which noise can induce chirality reversals [Fruchart et al., 2021]. Here, the chirality reversals occur due to the measurement noise, which is unavoidable in quantum systems.

To analyze the chirality reversals further, we show the time evolution of the phase of spins of species A in Fig. 6.10 for several quantum trajectories (gray with one highlighted in black). Traveling-wave states with positive frequency are apparent as an increasing phase, while traveling-wave states with opposite chirality, i.e., negative frequency, are

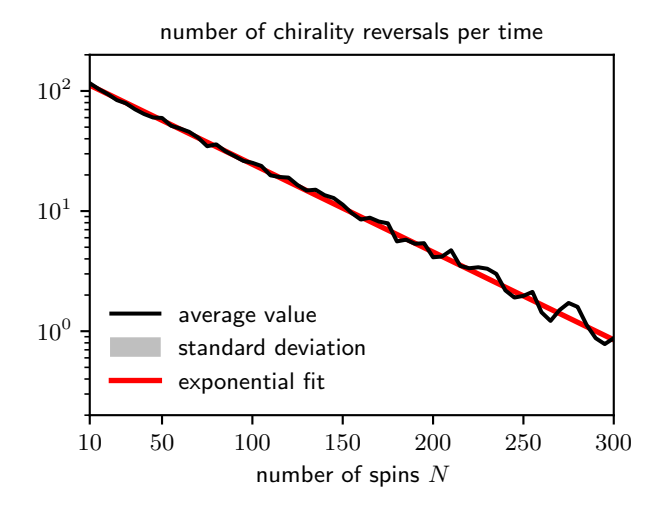


Figure 6.11: Number of chirality reversals as a function of N. The exponential fit  $\propto \exp(-N/\delta N)$  yields  $\delta N \approx 59$ . The reversals are counted for 32 trajectories, each integrated for a total time of  $10^3/\gamma_+$ , of which the first  $10^2/\gamma_+$  are discarded as a transient. To obtain the number of reversals, the phase difference was averaged over a time window of  $10/\gamma_+$ . Different values of the width of this window do not change the results qualitatively. The black line (gray area) shows the average (standard deviation) of 32 trajectories. Parameters: same as Fig. 6.9(b).

apparent as a decreasing phase. The second row of Fig. 6.10 displays the phase difference between spins of species A and B. The phase difference typically assumes values close to  $\pm \pi/2$ . As expected from the dynamics in the thermodynamic limit, see Fig. 6.2(b), the phase increases when the phase difference is close to  $+\pi/2$  and decreases when the phase difference is close to  $-\pi/2$ . Also, the chirality reversals coincide with switches between the two possible values of the phase difference. We highlight the chirality reversals by the blue ticks on the upper horizontal axes. To obtain them, the phase difference is time-averaged in a window of width  $10/\gamma_+$  (which corresponds to approximately one oscillation); a chirality reversal is then counted whenever the phase difference switches between a value closer to  $+\pi/2$  and a value closer to  $-\pi/2$ .

In Fig. 6.11, we see that the number of chirality reversals per fixed time decreases exponentially with the number of spins. This is expected from classical models [Fruchart et al., 2021], and it is compatible with fluctuations whose strength decreases in proportion to 1/N. In the thermodynamic limit, no chirality reversals occur, and the system remains in one of the two traveling-wave states.

Finally, we emphasize that these dynamics are observable in an experiment. The heterodyne signal, which is experimentally accessible is [Wiseman and Milburn, 2010]

$$I_{\text{het}} = 2\sqrt{\xi\kappa} \operatorname{Re}[e^{i\phi_{\text{m}}(t)} \langle a \rangle_{\text{m}}] + dW/dt$$
(6.25)

(extending Eq. (3.14) to an inefficient detection). Mixing this signal with  $\cos(\phi_{\rm m}(t))$  and  $\sin(\phi_{\rm m}(t))$  and time averaging allows for obtaining the cavity quadratures  ${\rm Re}[\langle a_+\rangle_{\rm m}]$  and  ${\rm Im}[\langle a_+\rangle_{\rm m}]$  and thus the cavity phase. Since the cavity is to a good approximation related to the spins by  $a_+ \approx -i\Omega S^-/\kappa$ , the two traveling-wave states can be detected by an increasing or decreasing cavity phase. While we have shown results for unit measurement efficiency  $\xi=1$ , we tested that the traveling-wave states persist for efficiencies as low as  $\xi\approx 0.1$ .

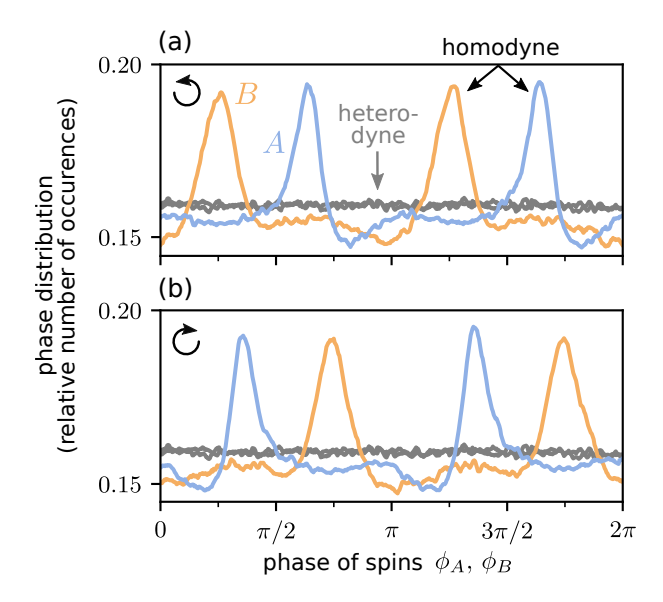


Figure 6.12: Phase distribution under heterodyne detection (gray) and homodyne detection (blue: species A, orange: species B). The distribution is obtained by counting how often each phase value occurs and averaging over multiple trajectories postselected on the traveling-wave state being left or right chiral. Parameters: same as Fig. 6.9(b) with  $\omega_{\rm m}=0$  and N=500.

#### 6.8.2 Homodyne measurement

In this section, we show that the measurement backaction can qualitatively influence the traveling-wave state. Specifically, we investigate the influence of a homodyne detection of the quadrature  $a_+ + a_+^{\dagger}$ , setting  $\phi_{\rm m} = 0$ . Quantum trajectories in the presence of homodyne detection reveal a traveling-wave state similar to that shown in Fig. 6.9 for the case of heterodyne detection. Nevertheless, as we will now show, there are qualitative differences between the traveling-wave states obtained via homodyne and heterodyne detection.

The measurement of a single cavity quadrature continuously projects the state of the cavity in states with well-defined expectation value along the  $a_+ + a_+^{\dagger}$  quadrature. Due to the coupling between spins and cavity, the measurement backaction on  $a_+$  also affects the spin degrees of freedom. Given the adiabatic relation  $a_+ \propto iS^-$ , the collective spin is effectively measured in the quadrature  $S^y = i(S^- - S^+)$ . Furthermore, the phase difference of spins of species A and B is approximately  $\pm \pi/2$  (for traveling-wave states) and  $S^- = S_A^- + S_B^-$ ; consequently, the spins A and B are effectively measured in quadratures rotated by  $\pm \pi/4$  relative to the y-quadrature. Since the sign of the phase shift depends on the chirality of the traveling-wave state, the measurement backaction on the spins depends on the chirality. Therefore, the spins tend to assume states where the quadratures along these directions are well defined, while noise is enhanced along quadratures rotated by 90°.

The expected behavior is confirmed in Fig. 6.12, which displays the phase distribution of species A and B, i.e., the likelihood for the state to assume a particular phase. We have postselected states with left and right chirality, and show the results for the two chiralities in Panels (a) and (b), respectively. For the heterodyne case, the measurement backaction is isotropic. For the homodyne case, on the other hand, the backaction on the state of the spins A and B depends on their phases  $\phi_a = \arg[\langle \sigma_a^+ \rangle_{\rm m}]$ . The backaction results in peaks of the phase distribution which occur at phases of approximately  $\pi/2 \pm \pi/4$  and

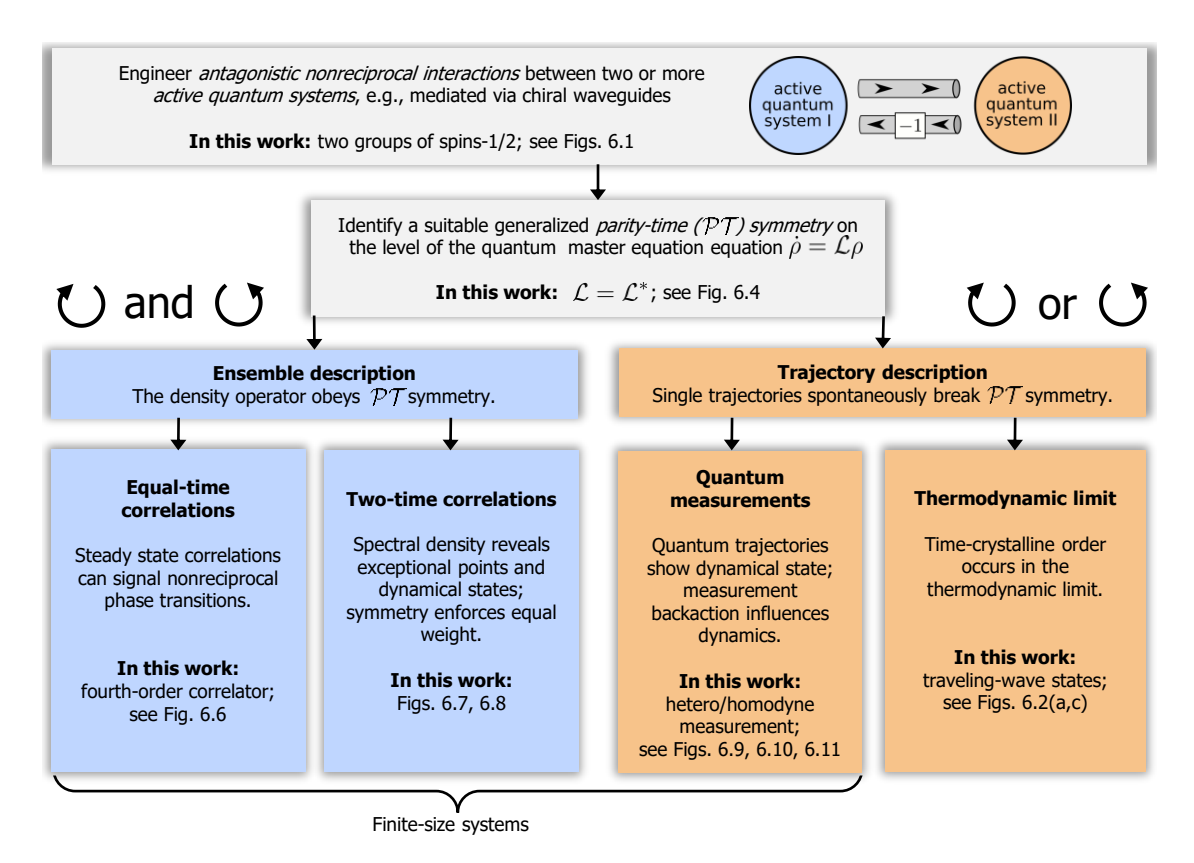


Figure 6.13: Schematic diagram for the analysis of nonreciprocal phase transitions in active quantum systems.

 $-\pi/2 \pm \pi/4$  as expected from the discussion above. The dependence of the distribution on the chirality is evident by comparing Panels (a) and (b).

It will be interesting to investigate homodyne detection for smaller ensemble sizes, where the measurement noise is stronger. However, we find that the cumulant expansion fails to approximate well the state of the system for  $N\lesssim 200$ , which hints at the presence of non-Gaussian correlations. We expect to find more qualitative differences between quantum trajectories in the presence of heterodyne and homodyne detection at these smaller values of N. Furthermore, the scaling of the number of chirality reversals may depend on the measurement.

# 6.9 Implications for nonreciprocal quantum many-body systems

In the previous sections, we have analyzed a specific model to show how to engineer nonreciprocal interactions in a quantum many-body system and how to identify their observable consequences such as dynamical traveling-wave states. While some aspects of our analysis are specific to the model considered, our results have implications for a broader class of quantum models featuring nonreciprocal interactions. In this section, we highlight what we believe are the general features of our analysis as well as discuss possible directions to extend our framework.

In Fig. 6.13, we show a flowchart illustrating the key conceptual ingredients in the analysis of a nonreciprocal quantum many-body system. The main features are listed and explained in the following.

Engineering antagonistic nonreciprocal interactions. Nonreciprocal interactions are not native to quantum systems and must be engineered instead. Chiral waveguides, in combination with phase shifts along their path, can mediate tuneable antagonistic nonreciprocal interactions between two subsystems A and B; see Fig. 6.1(b,c). While here, we focused on the case where both A and B are collections of quantum two-level systems, our framework is in principle agnostic to the nature of the subsystems. The master equation (6.7) can be employed to model antagonistic interactions among other subsystems, e.g., comprising constituents with a larger local Hilbert space. Additionally, the framework allows for studying nonreciprocal couplings in a network comprising more than two subsystems to explore the role of frustration and network topologies.

Active quantum systems. Nonreciprocal interactions among agents can be enabled by the out-of-equilibrium character of active matter [Fruchart et al., 2021; Bowick et al., 2022]. We showed that, analogous to classical active matter, a quantum system provided with a source of energy and thus driven out of equilibrium, becomes active and can therefore feature a self-organization transition in the form of synchronization as well as nonreciprocal interactions. While in our model a quantum many-body system is promoted to an active quantum system by the local incoherent drive of Eq. (6.6), other mechanisms are conceivable, such as saturated gain as in lasers or coherent light-matter interactions beyond the rotating-wave approximation [Kirton et al., 2019; Chiacchio et al., 2023].

The role of  $\mathcal{PT}$  symmetry. Nonreciprocal phase transitions are  $\mathcal{PT}$ -symmetry breaking transitions [Fruchart et al., 2021]. Since open quantum systems are described in terms of a quantum master equation [Breuer and Petruccione, 2002], or equivalently, a Liouvillian  $\mathcal{L}$ ,  $\mathcal{PT}$  symmetry should be identified at the level of the quantum master equation. In our model, the implementation based on chiral waveguides allows for identifying  $\mathcal{PT}$  symmetry as complex conjugation of the Liouvillian  $\mathcal{L} = \mathcal{L}^*$ . We expect this notion of  $\mathcal{PT}$  symmetry to be relevant beyond the model considered here. While our definition has the twofold advantage of being physically motivated and recovering the generalized  $\mathcal{PT}$  symmetry in the thermodynamic limit, parity-time symmetry is a broad concept [Bender and Hook, 2024] and several instances have been discussed in the literature [Prosen, 2012; Huber et al., 2020; Sá et al., 2023; Huybrechts et al., 2020; Nakanishi and Sasamoto, 2022; Chiacchio et al., 2023; Jachinowski and Littlewood, 2025].

Symmetry constraints in the ensemble description. For any finite-size system, the master equation typically features a unique time-independent steady state. Traveling-wave states are therefore not directly visible from the steady-state density matrix. Nevertheless, signatures of the time-crystal phase can still be identified at the ensemble level, by inspecting either equal-time or two-time correlation functions (or equivalently the spectral density). In our model, the spectral density satisfies  $|S(\omega)| = |S(-\omega)|$ , which implies that the two traveling-wave states with opposite chirality, i.e., frequency, have equal weight. Since this follows from symmetry arguments, we expect it to be a general feature of  $\mathcal{PT}$ -symmetric Liouvillians.

Spontaneous  $\mathcal{PT}$ -symmetry breaking in the thermodynamic limit. While the ensemble description obeys  $\mathcal{PT}$  symmetry, it is nonetheless possible to observe the spontaneous breaking of  $\mathcal{PT}$  symmetry in two qualitatively different ways. One way is by taking the thermodynamic limit, where  $\mathcal{PT}$  symmetry can be spontaneously broken (the system assumes one of two possible chiralities) in conjunction with the breaking of continuous time-translational symmetry. This establishes that a quantum model

can feature time-crystalline states induced by dynamical frustration [Hanai, 2024], i.e., nonreciprocal interactions.

Quantum trajectories and measurement backaction. A second way to observe spontaneous  $\mathcal{PT}$ -symmetry breaking, for any finite system size, is through measurement backaction. In quantum systems, the effects of a measurement are described by unraveling the dynamics into quantum trajectories, where each trajectory represents a possible realization of the system's evolution under continuous observation. Individual quantum trajectories reveal the oscillatory behavior characteristic of the time-crystal and the associated symmetry breaking. Additionally, the measurement backaction, i.e., the influence of the chosen measurement on the quantum state, qualitatively alters the dynamics of quantum traveling-wave states.

The role of decoherence. In classical active matter, noise or disorder is crucial for perturbing potential equilibrium states, thereby enabling the emergence of traveling-wave states [Fruchart et al., 2021]. In our model, decoherence takes up this role: By destabilizing any state with maximal coherence, it allows for persistent traveling-wave states. In any quantum system, the coupling to an environment unavoidably leads to decoherence. Therefore, it can be expected that decoherence acts to stabilize dynamical states in other quantum models featuring nonreciprocal interactions.

#### 6.10 Conclusions

Nonreciprocal interactions in active matter lead to exciting features such as a new class of critical phenomena and phase transitions. Since the laws of nature are fundamentally quantum mechanical, these features have to emerge from an underlying microscopic quantum theory. In this chapter, we have shown how this is possible by presenting a quantum many-body system that exhibits a nonreciprocal phase transition. Each constituent is an active quantum spin that is incoherently driven. The phases of one species of spins are attracted to those of the other species, which in contrast are repelled. These antagonistic interactions result in traveling-wave states. In other words, the spins spontaneously self-organize, forming a dynamical synchronized pattern. The traveling-wave states spontaneously break parity-time ( $\mathcal{PT}$ )-symmetry, which we have motivated from physical grounds and formulated as an invariance of the Liouvillian under complex conjugation.

The model can be implemented in current experimental settings and therefore offers a new platform to investigate nonreciprocal interactions in the quantum domain. Furthermore, we have shown that the traveling-wave state remains observable for finite-size systems. On the level of the density matrix, fourth-order correlations and exceptional points in the spectrum provide ways to detect traveling-wave states. Most intriguingly, standard heterodyne detection allows for observing quantum trajectories that feature traveling-wave states and spontaneously break  $\mathcal{PT}$  symmetry.

Our results are significant beyond the particular model considered here as emphasized in the previous section. Chiral waveguides and phase shifts can be used to engineer nonreciprocal interactions among arbitrary active quantum systems. We have highlighted the importance of the formulation of  $\mathcal{PT}$  symmetry on the level of the master equation. It constrains the steady state of the system and is spontaneously broken in the thermodynamic limit and in quantum trajectories. The measurement with which the quantum trajectories are obtained acts back on the quantum system and influences the dynamics. Furthermore, decoherence stabilizes a time-crystal state and thus takes the role of noise

6.10. Conclusions 101

or disorder, which stabilize the dynamical state in classical active matter. We expect these insights to be useful in future studies of nonreciprocity in quantum systems.

Antagonistic interactions of active matter in the quantum domain are a novel research direction with exciting open questions. First of all, it will be interesting to study the influence of nonreciprocity in other systems using our framework to engineer nonreciprocal interactions. Furthermore, it is intriguing to study various symmetries. While we have identified both  $\mathcal{PT}$  symmetry and U(1) symmetry, a different model showed a  $\mathcal{PT}$  symmetry together with a  $\mathbb{Z}_2$ -symmetry [Chiacchio et al., 2023]. It would also be interesting to find an instance of strong  $\mathcal{PT}$  symmetry and see if it can be spontaneously broken. Recently, a close connection between geometric and dynamical frustration has been pointed out [Hanai, 2024]. Geometric frustration is known to lead to exciting phases of quantum matter, such as quantum spin liquids, and it will be interesting to explore the consequences of nonreciprocal dynamical frustration in quantum systems.

The field of active quantum matter is just emerging [Khasseh et al., 2023; Adachi et al., 2022; Hanai et al., 2024; Yamagishi et al., 2024; Takasan et al., 2024; Yuan et al., 2024; Antonov et al., 2025; Penner et al., 2025]. Given the relevance of antagonistic interactions in classical active matter, it is important to consider similar interactions of quantum constituents. This chapter proposes a way to do so and highlights general features of nonreciprocal interactions in active quantum matter.

# Appendix for Chapter 6

# 6.A General complex coherent coupling

In this appendix, we describe how a complex-valued nonreciprocal coupling  $V_{-}$  can be implemented. The setup is shown in Fig. 6.14. Following [Karg et al., 2019], the unidirectional waveguide with mode  $a_{-}$  mediates the coherent interactions of our master equation (6.1) with

$$V_{-}/N = 2g_{-}^{2}e^{i\beta}. {(6.26)}$$

The cavity mode  $a_+$  mediates dissipative interspecies and intraspecies interactions with

$$V_{+}/N = V/N = 2g_{+}^{2}. (6.27)$$

For simplicity, we focus on the case where there are no losses in the unidirectional waveguide.

Under time reversal, the chirality of the unidirectional waveguide is reversed, and the phase shifts  $\beta$  and  $\pi - \beta$  also change sign. The setup shown in Fig. 6.14 is only invariant under the  $\mathcal{PT}$  transformation for  $\beta \in \{0, \pi\}$ , which corresponds to real-valued  $V_{-}$ . This confirms that the imaginary part of  $V_{-}$  explicitly breaks  $\mathcal{PT}$  symmetry.

In the thermodynamic limit, we obtain the mean-field equations

$$\frac{\mathrm{d}}{\mathrm{d}t}s_{A}^{+} = [(-\gamma_{+} + i\delta)s_{A}^{+} + Vs_{A}^{+}s_{A}^{z} + (V_{+} - V_{-}^{*})s_{B}^{+}s_{A}^{z}]/2,$$

$$\frac{\mathrm{d}}{\mathrm{d}t}s_{B}^{+} = [(-\gamma_{+} - i\delta)s_{B}^{+} + Vs_{B}^{+}s_{B}^{z} + (V_{+} + V_{-})s_{A}^{+}s_{B}^{z}]/2,$$

$$\frac{\mathrm{d}}{\mathrm{d}t}s_{A}^{z} = \gamma_{+}(1 - s_{A}^{z}) - 2Vs_{A}^{+}s_{A}^{-} - 2\operatorname{Re}[(V_{+} - V_{-}^{*})s_{A}^{-}s_{B}^{+}]$$

$$\frac{\mathrm{d}}{\mathrm{d}t}s_{B}^{z} = \gamma_{+}(1 - s_{B}^{z}) - 2Vs_{B}^{+}s_{B}^{-} - 2\operatorname{Re}[(V_{+} + V_{-})s_{A}^{+}s_{B}^{-}],$$
(6.28)

which reduce to Eq. (6.11) when  $V_{-}$  is real valued.

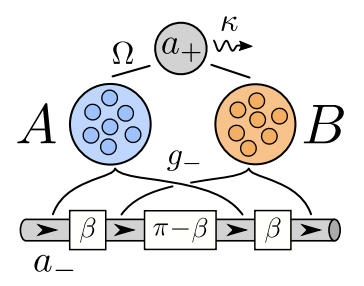


Figure 6.14: Setup to implement complex-valued nonreciprocal coupling  $V_-$ . The cavity mode  $a_+$  mediates reciprocal interactions. The phase shifters in the unidirectional chiral mode  $a_-$  transform  $a_- \to \exp(i\beta)a_-$  or  $a_- \to \exp(i(\pi - \beta))a_-$ .

# 6.B Transition between incoherent and synchronized states

Throughout the main text, we focus on the case where  $V/\gamma_+$  is large enough such that all spins of each species are synchronized. Figure 6.15(a) displays the transition from an incoherent state to either the static synchronized state or the dynamical traveling-wave state by increasing the dissipative coupling strengths. The transition is clearly indicated by the absolute value of the mean coherence  $|s_A^+|$  (or equivalently  $|s_B^+|$ , not shown), which is zero in the incoherent regime.

Damping and dephasing of the spins can also induce a transition between synchronized and incoherent states. Importantly, however, the traveling-wave state (and the other synchronized states) possesses some degree of robustness with respect to damping and dephasing. To show this, we include damping at rate  $\gamma_{-}$  and dephasing at rate  $\gamma_{z}$  by adding to the master equation (6.1) the terms

$$\sum_{a \in \{A,B\}} \sum_{i=1}^{N} \gamma_{-} \mathcal{D}[\sigma_{a,i}^{-}] \rho + \frac{\gamma_{z}}{2} \mathcal{D}[\sigma_{a,i}^{z}] \rho.$$
 (6.29)

In the thermodynamic limit, the equations Eq. (6.11) become (setting  $\delta = 0$  for simplicity),

$$\frac{\mathrm{d}}{\mathrm{d}t}s_{A}^{+} = \left[-(\gamma_{+} + \gamma_{-} + 2\gamma_{z})s_{A}^{+} + Vs_{A}^{+}s_{A}^{z} + V_{BA}s_{B}^{+}s_{A}^{z}\right]/2,$$

$$\frac{\mathrm{d}}{\mathrm{d}t}s_{B}^{+} = \left[-(\gamma_{+} + \gamma_{-} + 2\gamma_{z})s_{B}^{+} + Vs_{B}^{+}s_{B}^{z} + V_{AB}s_{A}^{+}s_{B}^{z}\right]/2,$$

$$\frac{\mathrm{d}}{\mathrm{d}t}s_{A}^{z} = \gamma_{+}(1 - s_{A}^{z}) - \gamma_{-}(1 + s_{A}^{z}) - 2Vs_{A}^{+}s_{A}^{-} - 2V_{BA}\operatorname{Re}[s_{A}^{+}s_{B}^{-}],$$

$$\frac{\mathrm{d}}{\mathrm{d}t}s_{B}^{z} = \gamma_{+}(1 - s_{B}^{z}) - \gamma_{-}(1 + s_{B}^{z}) - 2Vs_{B}^{+}s_{B}^{-} - 2V_{AB}\operatorname{Re}[s_{A}^{+}s_{B}^{-}].$$
(6.30)

We find that the incoherent steady state

$$s_{A,B}^{+} = 0, \quad s_{A,B}^{z} = z_0 \equiv \frac{\gamma_{+} - \gamma_{-}}{\gamma_{+} + \gamma_{-}}$$
 (6.31)

becomes unstable when

$$\Gamma < \begin{cases} z_0 V & \text{for } |V_-| > |V_+|, \\ z_0 \left(V + \sqrt{V_+^2 - V_-^2}\right) & \text{for } |V_-| < |V_+|, \end{cases}$$

$$(6.32)$$

where we defined the total decoherence rate  $\Gamma = \gamma_+ + \gamma_- + 2\gamma_z$ .

We show the influence of damping and dephasing on the coherence  $|s_A^+|$  of a traveling-wave state in Fig. 6.15(b). Importantly, the state also retains its dynamics throughout the region where  $|s_A^+|$  is finite (not shown). We conclude that time-crystalline traveling-wave states are robust to damping and dephasing.

# 6.C Phase diagrams: amplitude and phase difference

The data used to produce Fig. 6.2(a) is shown in Fig. 6.16. Panel (a) shows the time-averaged amplitude  $|s_A^+|$  in the long-time limit as a function of  $V_-$  and  $V_+$ . Panel (b) shows the time-averaged phase difference. In both panels, one can identify boundaries between the regions of static  $(\pi$ -)synchronized states and the regions of dynamical traveling-wave states. The modulated traveling-wave state is not apparent in Fig. 6.16, since the quantities are time averaged.

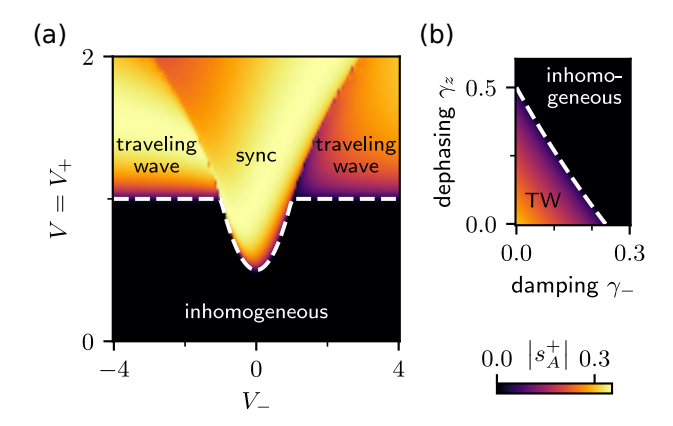


Figure 6.15: Transition from incoherent to synchronized states in the thermodynamic limit indicated by the absolute value of the coherence  $|s_A^+|$  (similar results are obtained for  $|s_B^+|$ ). (a) Transition from incoherent to synchronized states by increasing  $V=V_+$  as a function of  $V_-$ . There is both a transition to the static synchronized state and to the dynamic traveling-wave state. The white dashed line is obtained from a stability analysis of the incoherent state,  $V=V_+=\min(1,(1+V_-^2)/2)$ , a special case of Eq. (6.32) in the absence of damping and dephasing. All interaction strengths in units of  $\gamma_+$  and  $\delta=0$ . (b) Transition of the traveling-wave (TW) state to the inhomogeneous state by increasing damping and decay. The white dashed line is  $\Gamma=Vz_0$ ; see Eq. (6.32). Parameters:  $\delta=0$ ,  $V_-=2V_+=2V=4\gamma_+$ . Damping and dephasing strengths are given in units of  $\gamma_+$ .

We find numerically that the phase difference shown in Fig. 6.16(b) is precisely  $\pm \pi/2$  for  $V_{+}=0$ . As  $V_{+}$  increases and the spins approach the synchronized regime, the phase difference continuously shifts towards 0. Conversely, for negative  $V_{-}$ , as the spins approach the  $\pi$ -synchronized regime, the phase difference shifts towards  $\pi$ .

# 6.D Finite-size calculations of the steady state

To solve for the long-time limit of the full quantum master equation (6.1), we exploit the permutational symmetry, i.e., the fact that all two-level systems within each group are identical. This reduces the complexity from  $4^{2N}$  to  $(N^2)^3$ , where N is the number of spins per species. To find the steady state, we compute the eigenstate of the Liouvillian corresponding to the zero eigenvalue. Numerics are performed using PIQS [Shammah et al., 2018].

For larger N, this approach becomes unfeasible, so we resort to an approximation. We systematically include correlations by using cumulant expansions [Kubo, 1962] to second and fourth order, where third-order or fifth-order cumulants are set to zero, respectively. For instance,

$$\langle o_1 o_2 o_3 \rangle_c = \langle o_1 o_2 o_3 \rangle - \langle o_1 o_2 \rangle \langle o_3 \rangle - \langle o_1 o_3 \rangle \langle o_2 \rangle - \langle o_1 \rangle \langle o_2 o_3 \rangle + 2 \langle o_1 \rangle \langle o_2 \rangle \langle o_3 \rangle = 0.$$

$$(6.33)$$

Furthermore, we exploit the U(1) symmetry of the master equation (6.1) to set averages such as  $\langle \sigma_{a,i}^+ \rangle = 0$  or  $\langle \sigma_{a,i}^+ \sigma_{b,j}^z \rangle = 0$  to zero as they vanish in the long-time limit. Additionally, we invoke the permutational invariance to set all spins within each species equal, e.g.,  $\langle \sigma_{A,i}^+ \sigma_{A,j}^- \rangle = \langle \sigma_A^+ \sigma_A^- \rangle$  for all  $i \neq j$  or  $\langle \sigma_{A,i}^+ \sigma_{B,j}^- \rangle = \langle \sigma_A^+ \sigma_B^- \rangle$  for all i and j. In

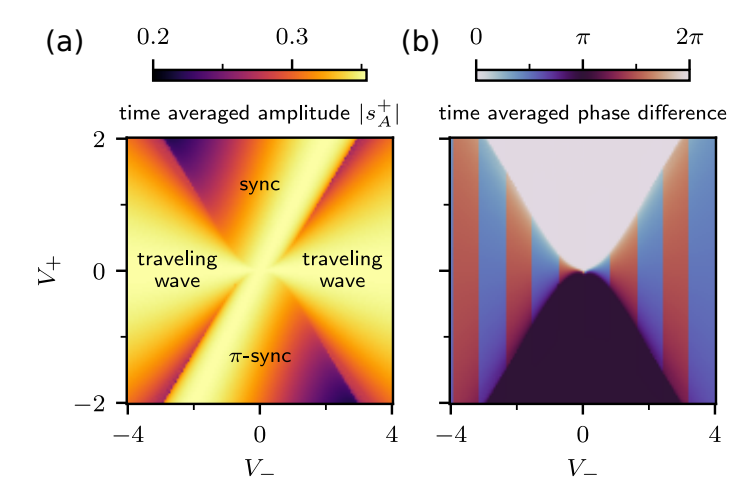


Figure 6.16: Phase diagram in the thermodynamic limit. (a) Time-averaged amplitude  $|s_A^+|$  in the long-time limit as a function of  $V_-$  and  $V_+$ . (b) Time-averaged phase difference  $\arg s_A^+/s_B^+$  in the long-time limit. The initial conditions are chosen such that either of the two traveling-wave states with phase difference  $\pm \pi/2$  is obtained in alternating vertical stripes. Parameters:  $\delta=0,\ V=2$ . All coupling strengths in units of  $\gamma_+$ .

the second-order expansion, we thus obtain a closed set of differential equations for  $\langle \sigma_a^z \rangle$ ,  $\langle \sigma_a^+ \sigma_a^- \rangle$ ,  $\langle \sigma_A^+ \sigma_B^- \rangle$ , and  $\langle \sigma_a^z \sigma_a^z \rangle$ , and  $\langle \sigma_A^z \sigma_B^z \rangle$ .

$$\begin{split} \frac{\mathrm{d}}{\mathrm{d}t}s_A^z &= -V\left(s_A^z+1\right)/N + \gamma_+\left(1-s_A^z\right) - 2V\frac{N-1}{N}\langle\sigma_A^+\sigma_A^-\rangle - 2V_{BA}\operatorname{Re}[\langle\sigma_A^+\sigma_B^-\rangle]\,,\\ \frac{\mathrm{d}}{\mathrm{d}t}s_B^z &= -V\left(s_B^z+1\right)/N + \gamma_+\left(1-s_B^z\right) - 2V\frac{N-1}{N}\langle\sigma_B^+\sigma_B^-\rangle - 2V_{AB}\operatorname{Re}[\langle\sigma_A^+\sigma_B^-\rangle]\,,\\ \frac{\mathrm{d}}{\mathrm{d}t}\langle\sigma_A^+\sigma_A^-\rangle &= -\left(\gamma_+ + \frac{V}{N}\right)\langle\sigma_A^+\sigma_A^-\rangle + \frac{V}{2N}\left(\langle\sigma_A^z\sigma_A^z\rangle + s_A^z\right)\\ &\quad + Vs_A^z(N-2)/N\langle\sigma_A^+\sigma_A^-\rangle + V_{BA}s_A^z\operatorname{Re}[\langle\sigma_A^+\sigma_B^-\rangle]\,,\\ \frac{\mathrm{d}}{\mathrm{d}t}\langle\sigma_B^+\sigma_B^-\rangle &= -\left(\gamma_+ + \frac{V}{N}\right)\langle\sigma_B^+\sigma_B^-\rangle + \frac{V}{2N}\left(\langle\sigma_B^z\sigma_B^z\rangle + s_B^z\right)\\ &\quad + Vs_B^z(N-2)/N\langle\sigma_B^+\sigma_B^-\rangle + V_{AB}s_B^z\operatorname{Re}[\langle\sigma_A^+\sigma_B^-\rangle]\,,\\ \frac{\mathrm{d}}{\mathrm{d}t}\langle\sigma_A^+\sigma_B^-\rangle &= -\left(\gamma_+ + V/N - i\delta\right)\langle\sigma_A^+\sigma_B^-\rangle + V\frac{N-1}{2N}\left(s_A^z+s_B^z\right)\langle\sigma_A^+\sigma_B^-\rangle\\ &\quad + V_{AB}(s_B^z+\langle\sigma_A^z\sigma_B^z\rangle)/4N + V_{BA}(s_A^z+\langle\sigma_A^z\sigma_B^z\rangle)/4N\\ &\quad + \frac{N-1}{2N}\left(V_{AB}s_B^z\left\langle\sigma_A^+\sigma_A^-\rangle + V_{BA}s_A^z\left\langle\sigma_B^+\sigma_B^-\rangle\right)\right)\\ \frac{\mathrm{d}}{\mathrm{d}t}\langle\sigma_A^z\sigma_A^z\rangle &= 2s_A^z(\gamma_+ - V/N) - 2\langle\sigma_A^z\sigma_A^z\rangle(\gamma_+ + V/N) - 4V_{BA}s_A^z\operatorname{Re}[\langle\sigma_A^+\sigma_B^-\rangle]\\ &\quad + V\left(4\left\langle\sigma_A^+\sigma_A^-\rangle - 4(N-2)s_A^z\left\langle\sigma_A^+\sigma_A^-\rangle\right)/N\\ \frac{\mathrm{d}}{\mathrm{d}t}\langle\sigma_B^z\sigma_B^z\rangle &= 2s_B^z(\gamma_+ - V/N) - 2\langle\sigma_B^z\sigma_B^z\rangle(\gamma_+ + V/N) - 4V_{AB}s_B^z\operatorname{Re}[\langle\sigma_A^+\sigma_B^-\rangle]\\ &\quad + V\left(4\left\langle\sigma_B^+\sigma_B^-\rangle - 4(N-2)s_B^z\left\langle\sigma_B^+\sigma_B^-\rangle\right)/N\\ \frac{\mathrm{d}}{\mathrm{d}t}\langle\sigma_A^z\sigma_B^z\rangle &= \gamma_+(s_A^z+s_B^z - 2\langle\sigma_A^z\sigma_B^z\rangle) + 2\frac{N-1}{N}V_-(s_B^z-s_A^z)\operatorname{Re}[\langle\sigma_A^+\sigma_B^-\rangle]\\ &\quad - 2\frac{N-1}{N}V_+(s_A^z+s_B^z)\operatorname{Re}[\langle\sigma_A^+\sigma_B^-\rangle] - 2\frac{N-1}{N}V(s_B^z\left\langle\sigma_A^+\sigma_A^-\rangle + s_A^z\left\langle\sigma_B^+\sigma_B^-\rangle\right)/N\,. \end{aligned}$$

In the limit  $N \to \infty$ , they are equivalent to the mean-field equations. For the fourth-order expansion, we use the julia package QuantumCumulants.jl [Plankensteiner et al., 2022].

# 6.E Trajectory calculations

We solve the stochastic master equation

$$\dot{\rho}_{\rm m} = -i\left[\frac{\Omega}{2}(a^{\dagger}S^{-} + aS^{+}) + H_0 + H_{\rm inter}, \rho_{\rm m}\right] + +\kappa \mathcal{D}[a_{+}]\rho_{\rm m} + \mathcal{L}_{\rm drive}\rho_{\rm m} + \frac{\mathrm{d}W}{\mathrm{d}t}\sqrt{\kappa\xi}\left[e^{i\phi_{\rm m}(t)}(a\rho_{\rm m} - \langle a\rangle_{\rm m}\rho_{\rm m}) + \mathrm{H.c.}\right]$$
(6.34)

by employing a cumulant expansion to second order. To this end, we compute equations of motion for expectation values of operators  $a_+, a_+^\dagger, \sigma_{A,B}^{z,\pm}$  and products of two such operators. The equation of motion for each operator o reads d $\langle o \rangle_{\rm m}/{\rm d}t = {\rm Tr}[\dot{\rho}_{\rm m}o]$ . Any expectation value of a product of three operators is factorized using Eq. (6.33). We invoke the permutational invariance to set all spins within each species equal, as was done in the finite-size calculations of the steady state; see Section 6.D. The noise explicitly breaks the U(1) symmetry; therefore, we keep terms such as  $\langle \sigma_a^+ \rangle$  or  $\langle \sigma_a^z \sigma_b^+ \rangle$ . This leads to 27 equations, e.g.,

$$\frac{\mathrm{d}}{\mathrm{d}t} \langle a \rangle = -\frac{\kappa}{2} \langle a \rangle + iN \frac{\Omega}{2} (\langle \sigma_A^+ \rangle + \langle \sigma_B^+ \rangle) + 
+ \sqrt{\kappa \xi/2} \frac{\mathrm{d}W}{\mathrm{d}t} \left[ e^{i\phi_{\mathrm{m}}(t)} (\langle aa \rangle - \langle a \rangle^2) + e^{-i\phi_{\mathrm{m}}(t)} (\langle a^{\dagger}a \rangle - |\langle a \rangle|^2) \right].$$
(6.35)

Note that the noise term vanishes in the thermodynamic limit when the mean-field factorization is exact. We do not list all equations here; they can be derived and evaluated using the QuantumCumulants.jl package [Plankensteiner et al., 2022].

# Chapter 7

# Frequency shifts in superradiant lasers

The results of this chapter have been published in

Nonreciprocal Interactions induce Frequency Shifts in Superradiant Lasers, T. Nadolny, M. Brunelli, and C. Bruder, Physical Review Letters, **134**, 193603 (2025)

In the previous chapter, we have shown how nonreciprocal interactions among quantum systems can be engineered using chiral waveguides. Other recent studies also describe ways in which such interactions can be engineered by carefully designed light-matter couplings [Chiacchio et al., 2023; Reisenbauer et al., 2024; Rudolph et al., 2024a; Hanai et al., 2024]. In this chapter, we show that nonreciprocal interactions can naturally occur between driven and undriven atoms in a superradiant laser. Building on the understanding of quantum nonreciprocal interactions gained in the previous chapter, we now explore their consequences in the context of superradiant lasers. Most strikingly, we find frequency shifts and linewidth broadening of the emitted light. These findings have practical implications for the realization of superradiant lasers, establishing the relevance of nonreciprocal phenomena for quantum technologies.

# 7.1 Introduction

We have introduced the superradiant laser in Section 4.2.3. It consists of incoherently driven atoms coupled to a cavity that rapidly loses excitations [Chen, 2009; Meiser et al., 2009]. The effective atom-atom interactions mediated by the cavity lead to phase attraction among the atomic dipoles, causing a Kuramoto-like transition to a synchronized state. As a result, superradiant lasers emit coherent light with stable frequency and narrow linewidth. Superradiant lasers offer great technological promise as their narrow linewidth is expected to improve the precision of optical atomic clocks [Ludlow et al., 2015].

In this chapter, we study a superradiant laser where a fraction of the atoms is *not* driven; see Figs. 7.1(a,b). Surprisingly, this modification results in a shift of the lasing frequency and spectral broadening, which may be detrimental to the use of a superradiant laser as a stable frequency reference with narrow linewidth. This contrasts with the expectation that the undriven atoms behave as passive spectators, causing only a reduction of the laser power.

To explain this result, we consider the superradiant laser as quantum active matter and the atomic dipoles as quantum active agents that interact in a nonreciprocal way. We find that the driven atoms tend to align their dipole with the dipoles of both driven and undriven atoms; the undriven atoms, however, have the opposite inclination: They

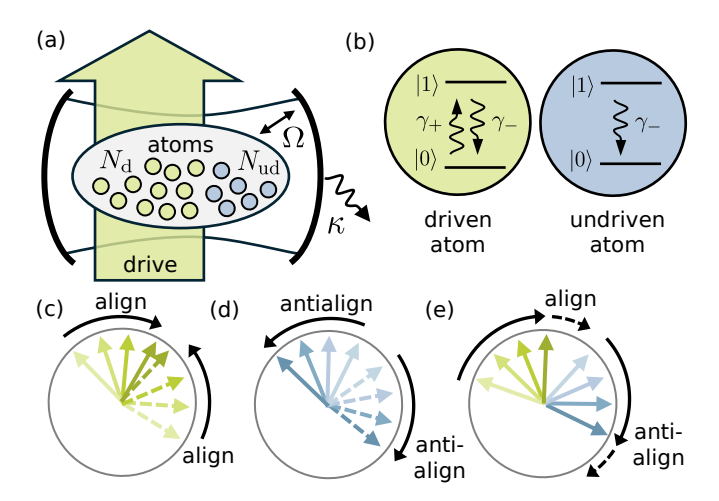


Figure 7.1: (a) Superradiant laser, where  $N_{\rm d}$  atoms are driven and  $N_{\rm ud} = N - N_{\rm d}$  are undriven. All atoms are coupled at rate  $\Omega$  to the cavity, which decays at rate  $\kappa$ . (b) Incoherent gain and loss processes within each atomic spin. (c) Alignment between two driven atomic dipoles (solid and dashed straight arrows). Lighter to darker colors indicate increasing time. (d) Antialignment between two undriven dipoles. (e) Nonreciprocal interactions between driven and undriven dipoles. The dashed circular arrows indicate the continuous motion.

tend to align their dipoles opposite to those of all other atoms; see Figs. 7.1(c-e). The nonreciprocal interactions influence the self-organization transition of the atoms that manifests as the lasing or synchronization transition; they result in a chase-and-run-away dynamics of the atomic dipoles similar to the traveling-wave states presented in Section 6.5. In the context of superradiant lasers, the traveling-wave states correspond to frequency shifts. Furthermore, the antialignment itself decreases the coherence among the atoms, causing spectral broadening and loss of power. This chapter connects fundamental concepts of active matter with quantum technologies by showing that nonreciprocal interactions have practical implications for the development of superradiant lasers.

# 7.2 Model

### Master equation

We describe a superradiant laser, which comprises N atoms, each atom modeled as a quantum spin-1/2 with states  $|0\rangle$  and  $|1\rangle$ ; see Fig. 7.1. While all spins are coupled coherently to a lossy cavity mode, only  $N_{\rm d} \leq N$  of the spins are incoherently driven; the other  $N_{\rm ud} = N - N_{\rm d}$  spins are not driven. The fraction of driven spins is  $p_{\rm d} = N_{\rm d}/N$ , and the fraction of undriven spins is  $p_{\rm ud} = 1 - p_{\rm d}$ . As before, the spins are described by Pauli matrices  $\sigma_{\mu,i}^z = |1\rangle\langle 1|_{\mu,i} - |0\rangle\langle 0|_{\mu,i}$  and ladder operators  $\sigma_{\mu,i}^+ = |1\rangle\langle 0|_{\mu,i}$ ,  $\sigma_{\mu,i}^- = |0\rangle\langle 1|_{\mu,i}$ . The index  $\mu \in \{d, ud\}$  distinguishes driven and undriven spins, and i ranges from 1 to  $N_{\mu}$ . The collective spin operators are  $S^{\pm} = \sum_{i=1}^{N_{\rm d}} \sigma_{{\rm d},i}^{\pm} + \sum_{i=1}^{N_{\rm ud}} \sigma_{{\rm ud},i}^{\pm}$ .

The Lindblad master equation for the density operator  $\rho$  is

$$\dot{\rho} = -i\Omega[a^{\dagger}S^{-} + aS^{+}, \rho] + \kappa \mathcal{D}[a]\rho + \gamma_{+} \sum_{i=1}^{N_{d}} \mathcal{D}[\sigma_{d,i}^{+}]\rho$$

$$+ \sum_{\mu = \{d, ud\}} \sum_{i=1}^{N_{\mu}} \left(\gamma_{-}\mathcal{D}[\sigma_{\mu,i}^{-}] + \gamma_{z}\mathcal{D}[\sigma_{\mu,i}^{z}]/2\right)\rho.$$

$$(7.1)$$

Both the atomic spins and the cavity are described in the frame rotating with their bare frequencies, which are set equal for simplicity. A nonzero spin-cavity detuning does not influence our results; see Appendix 7.B. All spins couple equally with strength  $\Omega$  to the cavity mode a, which decays at a rate  $\kappa$ . The last term in the first line of Eq. (7.1) describes an incoherent drive at rate  $\gamma_+$ , which can be engineered by pumping the state  $|0\rangle$  to a third state which rapidly decays to state  $|1\rangle$ . The second line describes spontaneous emission at rate  $\gamma_-$  and dephasing at rate  $\gamma_z$ . The master equation (7.1) is nearly the same as the master equation of the standard superradiant laser proposed by *Meiser* et al. [2009]; see Eq. (4.59). The only difference is that the sum only extends over  $N_{\rm d}$  spins instead of all N spins.

### Emission spectrum

As introduced before [see Eq. (2.14)], a key quantity to characterize a laser is the two-time correlation function  $\langle a^{\dagger}(t+\tau)a(t)\rangle$  or, correspondingly, the spectral density  $S(t,\omega)$  of light emitted by the cavity at time t and per frequency  $\omega$ ,

$$S(t,\omega) = \int_{-\infty}^{\infty} d\tau \left\langle a^{\dagger}(t+\tau)a(t) \right\rangle e^{i\omega\tau}. \tag{7.2}$$

The steady-state spectrum is defined as  $S(\omega) = \lim_{t\to\infty} S(t,\omega)$ . The spectrum of a high-quality laser comprises a large and narrow peak, implying high output power and small linewidth. The spectrum can be calculated by employing a cumulant expansion approximation and the quantum regression theorem [Kubo, 1962; Breuer and Petruccione, 2002; Meiser et al., 2009; Xu et al., 2014; Plankensteiner et al., 2022]. We have used the same techniques in Section 4.2.3 and Section 6.7. For this model, the relevant equations are summarized in Appendix 7.A.

Figures 7.2(a,b) show the steady-state spectrum for the model defined in Eq. (7.1) as a function of  $p_d$ . For now, we neglect spontaneous emission and dephasing, setting  $\gamma_- = \gamma_z = 0$ . If all spins are driven,  $p_d = 1$ , they collectively emit photons in a superradiant way into the cavity mode, which outputs highly coherent light as indicated by the narrow peak in the spectrum at zero frequency (relative to the bare atomic frequency). When decreasing  $p_d$ , there are two peaks in the spectrum at nonzero frequencies, indicating a positive or negative shift in the lasing frequency. Furthermore, for  $p_d$  smaller than a critical value, the peaks vanish, indicating the absence of lasing.

# 7.3 Nonreciprocal interactions

We now explain the origin of the frequency shift displayed in Figs. 7.2(a,b).

#### Mean-field equations

First, we exploit the permutational invariance: All driven spins are identical to one another, and all undriven spins are identical to one another. In the thermodynamic limit,  $N \to \infty$ , Eq. (7.1) can thus be solved exactly using a mean-field ansatz [Spohn, 1980]. The thermodynamic limit  $N \to \infty$  is well defined, when simultaneously decreasing  $\Omega \to 0$ ,

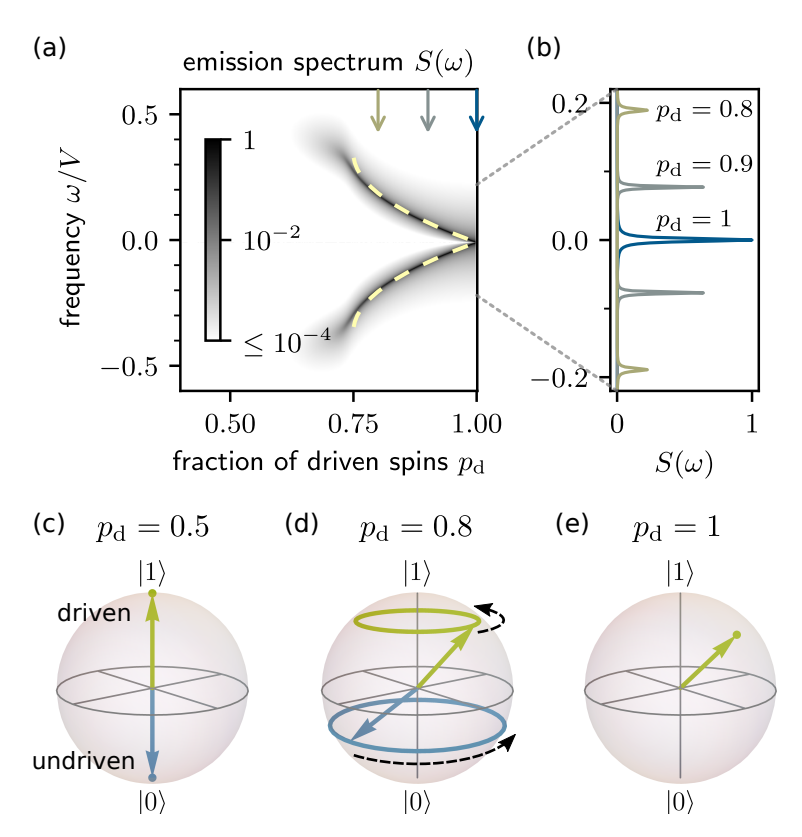


Figure 7.2: (a) Cavity emission spectrum  $S(\omega)$  (arb. units) as a function of fraction  $p_{\rm d}=N_{\rm d}/N$  of driven spins for  $N=10^3,~\kappa=10\sqrt{N}\Omega,~V=\gamma_+,$  and  $\gamma_-=\gamma_z=0$ . The frequency  $\omega$  is measured relative to the bare atomic frequency. The dashed line indicates the mean-field frequency. Below the lasing transition  $p_{\rm d}<3/4$  [see Eq. (7.11)], the emission is close to zero. (b) Line cuts through (a) as marked by the three arrows in (a) on a linear scale. (c-e) Solutions of the mean-field equations (7.5) in the long-time limit displayed on the Bloch sphere for (c)  $p_{\rm d}=0.5$ : no lasing, (d)  $p_{\rm d}=0.8$ : lasing with frequency shift, and (e)  $p_{\rm d}=1$ : standard superradiant laser. In (d), the dashed curved arrows indicate the continuous oscillations.

such that  $V \propto N\Omega^2 = \text{constant}$ . Introducing the coherences  $s_{\mu}^+ = \langle \sigma_{\mu,i}^+ \rangle$ , populations  $s_{\mu}^z = \langle \sigma_{\mu,i}^z \rangle$ , and the average coherence  $s^+ = p_{\rm d} s_{\rm d}^+ + p_{\rm ud} s_{\rm ud}^+$ , the mean-field equations are

$$\frac{d}{dt}s_{d}^{+} = -(\gamma_{+} + \gamma_{-} + 2\gamma_{z})s_{d}^{+}/2 - i\Omega\alpha^{*}s_{d}^{z},$$

$$\frac{d}{dt}s_{ud}^{+} = -(\gamma_{-} + 2\gamma_{z})s_{ud}^{+}/2 - i\Omega\alpha^{*}s_{ud}^{z},$$

$$\frac{d}{dt}s_{ud}^{z} = -\gamma_{-}(s_{d}^{z} + 1) - \gamma_{+}(s_{d}^{z} - 1) + 4\Omega\operatorname{Im}[\alpha s_{d}^{+}],$$

$$\frac{d}{dt}s_{ud}^{z} = -\gamma_{-}(s_{ud}^{z} + 1) + 4\Omega\operatorname{Im}[\alpha s_{ud}^{+}],$$

$$\frac{d}{dt}\alpha = -\kappa\alpha/2 - iN\Omega s^{-}.$$
(7.3)

Next, we derive an effective spin-only description. In the bad-cavity limit where  $\kappa/(\sqrt{N}\Omega)$  is large, the cavity field instantaneously follows the spins,  $\alpha = -2iN\Omega s^-/\kappa$ , and can be adiabatically eliminated. We obtain

$$\frac{d}{dt}s_{d}^{+} = Vs^{+}s_{d}^{z} - (\gamma_{-} + 2\gamma_{z} + \gamma_{+}) s_{d}^{+}/2,$$

$$\frac{d}{dt}s_{ud}^{+} = Vs^{+}s_{ud}^{z} - (\gamma_{-} + 2\gamma_{z})s_{ud}^{+}/2,$$

$$\frac{d}{dt}s_{d}^{z} = -4V \operatorname{Re}[s_{d}^{-}s^{+}] - \gamma_{-}(1 + s_{d}^{z}) + \gamma_{+}(1 - s_{d}^{z}),$$

$$\frac{d}{dt}s_{ud}^{z} = -4V \operatorname{Re}[s_{ud}^{-}s^{+}] - \gamma_{-}(1 + s_{ud}^{z}).$$
(7.4)

Here,  $V = 2N\Omega^2/\kappa$  is the effective dissipative coupling strength among all spins.

For now, let us analyze the case where damping and decoherence are negligible, setting  $\gamma_- = \gamma_z = 0$ . Then, the mean-field equations simplify to

$$\frac{d}{dt}s_{d}^{+} = Vs^{+}s_{d}^{z} - \gamma_{+}s_{d}^{+}/2,$$

$$\frac{d}{dt}s_{ud}^{+} = Vs^{+}s_{ud}^{z},$$

$$\frac{d}{dt}s_{d}^{z} = -4V\operatorname{Re}[s_{d}^{-}s^{+}] + \gamma_{+}(1 - s_{d}^{z}),$$

$$\frac{d}{dt}s_{ud}^{z} = -4V\operatorname{Re}[s_{ud}^{-}s^{+}],$$
(7.5)

and the purity of the undriven spins is conserved,  $(s_{\rm ud}^z)^2 + 4s_{\rm ud}^+s_{\rm ud}^- = {\rm const} \le 1$ . Equations (7.5) imply that the coherence of driven (undriven) spins tends to align in (out of) phase with respect to the average coherence. This becomes explicit in the dynamical equations for the phases  $\phi_{\mu} = {\rm arg}[s_{\mu}^+]$  derived from Eq. (7.5)

$$\dot{\phi}_{\mu} = s_{\mu}^{z} \frac{V|s^{+}|}{|s_{\mu}^{+}|} \sin(\bar{\phi} - \phi_{\mu}),$$
(7.6)

where  $\bar{\phi} = \arg[s^+]$  is the average phase. The sign of the term multiplying the sine determines whether  $\phi_{\mu}$  aligns or antialigns with  $\bar{\phi}$ . In a standard superradiant laser, all spins are driven, and their population is inverted  $s_{\rm d}^z > 0$ . Consequently, the interactions are reciprocal: All spins tend to align their phases, resulting in a synchronized state [see Fig. 7.2(e)] and the narrow linewidth of the emitted light [Meiser et al., 2009; Zhu et al.,

2015]. The population of the undriven spins, however, is not inverted and  $s_{\rm ud}^z < 0$  is obtained in the long-time limit. Therefore, the phase  $\phi_{\rm ud}$  of the undriven spins is repelled from the average phase  $\bar{\phi}$ . The phase  $\phi_{\rm d}$  of the driven spins remains to be attracted by the average phase  $\bar{\phi}$ . The competing attraction and repulsion of the phases constitute the effective nonreciprocal interactions among the atomic dipoles; they are sketched in Fig. 7.1(e).

Dynamics of the form of Eq. (7.6) have been previously described for a network of classical phase oscillators [Hong~and~Strogatz, 2011a,b]. The oscillators that tend to align with the mean field have been termed conformists. The oscillators that tend to antialign with the mean field oppose the average coherence; therefore, they have been termed contrarians. The conformist-contrarian dynamics have been connected to opinion forming, but no physical model to realize them is proposed. We have shown that the same phase interactions arise in a superradiant laser with a fraction of undriven spins, offering a physical realization of these dynamics. In the model of Hong~and~Strogatz [2011a,b], the nonreciprocity results in chase-and-run-away dynamics of the phases named traveling-wave states. They are qualitatively similar dynamical states to the traveling-wave states discussed in the previous chapter. A difference is that the contrarians aim to antialign their phases with each other, whereas in the previous chapter, the spins within each ensemble aim to align their phases. We now show that Eqs. (7.5) also result in traveling-wave states for  $p_{\rm d} < 1$ , implying emergent oscillations that explain the shift in the lasing frequency displayed in Figs. 7.1(a,b).

### Traveling-wave states

The mean-field equations Eqs. (7.5) can be solved exactly by an ansatz with constant populations  $s_{\rm d,ud}^z$  as well as oscillating  $s_{\rm d}^+ = \left| s_{\rm d}^+ \right| e^{i\omega t + i(\phi_{\rm d} - \phi_{\rm ud})}$  and  $s_{\rm ud}^+ = \left| s_{\rm ud}^+ \right| e^{i\omega t}$ . We introduced the shared oscillation frequency  $\omega$ , and the constant phase difference  $(\phi_{\rm d} - \phi_{\rm ud})$  between driven and undriven spins. In the Bloch-sphere picture, the ansatz describes oscillations on circles with radii  $\left| s_{\mu}^+ \right|$  at constant  $s_{\mu}^z$ ; see Fig. 7.2(d). Inserting this ansatz in Eqs. (7.5) and solving the resulting algebraic equations, the frequency of the traveling-wave states is obtained as

$$\omega = \pm \sqrt{\frac{\gamma_{+}}{4} \left( v - 2V p_{\rm ud} - \sqrt{v(v - 4V p_{\rm ud})} \right)}, \tag{7.7}$$

where  $v = 2V - \gamma_+$ . The frequency is shown by the dashed line in Fig. 7.2(a). It matches well with the spectrum, which confirms that our ansatz of traveling-wave states, where the spins oscillate with positive or negative frequency, explains the frequency shifts. Since the cavity output closely follows the collective spin state  $a = -i(2\Omega/\kappa)S^-$ , the emergent dynamics of the spins imply a (positive or negative) frequency shift of the laser, detrimental to a stable frequency reference.

We numerically integrate Eqs. (7.5) for different initial conditions and find that the spins always settle to either one of the two traveling-wave states in the long-time limit. This behavior corresponds to spontaneous symmetry breaking discussed in Section 6.6. As discussed in the previous chapter, noise can induce random switching between the two traveling-wave states; the switching rate, however, is in general exponentially suppressed in the number of spins. Consequently, it is extremely small for large numbers of spins that are typical in superradiant lasers.

### Lasing transition

Using Eqs. (7.4), we perform a stability analysis around the incoherent state. The fixed point, which characterizes the incoherent state, is  $s_{\rm d,ud}^+ = 0$ ,  $s_{\rm d}^z = (\gamma_+ - \gamma_-)/(\gamma_+ + \gamma_-)$ , and  $s_{\rm ud}^z = -1$ ; see Fig. 7.2(c). The stability analysis around this fixed point reveals that lasing occurs above a critical fraction of driven spins

$$p_{\rm d} > \frac{1}{2} + \frac{\gamma_+}{4V} \,.$$
 (7.8)

Here, we still consider the limit of vanishing damping and decoherence. At least half of the ensemble needs to be driven for lasing to occur. This is intuitive as there need to be more spins that behave as conformists rather than contrarians for phase alignment to occur. For the parameters of Fig. 7.2(a), the expression evaluates to  $p_{\rm d} > 3/4$ , which agrees well with the emission spectrum and the mean-field frequency shown in this figure.

### Comparison to standard laser

The traveling-wave states are unique to the superradiant regime of lasers. In a standard laser, the presence of undriven spins results in a smaller effective size of the gain medium but does not cause a frequency shift, as we now show.

In a standard laser, the cavity is a 'good' cavity with a decay rate  $\kappa$  that is small compared to the incoherent gain and damping of the atoms. In this case, one can adiabatically eliminate the spin degrees of freedom in Eq. (7.3) by setting  $\dot{s}^z_{\mu} = \dot{s}^+_{\mu} = 0$  to obtain

$$\frac{\mathrm{d}}{\mathrm{d}t}\alpha = \alpha \left( -\frac{\kappa}{2} + 2Np_{\mathrm{d}} \frac{\gamma_{+} - \gamma_{-}}{\tilde{\Gamma}_{\mathrm{d}}^{2}/\Omega^{2} + 8|\alpha|^{2}} - 2Np_{\mathrm{ud}} \frac{\gamma_{-}}{\tilde{\Gamma}_{\mathrm{ud}}^{2}/\Omega^{2} + 8|\alpha|^{2}} \right), \tag{7.9}$$

where we have defined  $\tilde{\Gamma}_{d}^{2} = (\gamma_{-} + \gamma_{+})(\gamma_{-} + \gamma_{+} + 2\gamma_{z})$  and  $\tilde{\Gamma}_{ud}^{2} = \gamma_{-}(\gamma_{-} + 2\gamma_{z})$ . Since the term in brackets on the right-hand side is real-valued, there are no oscillations and no traveling-wave states. The lasing transition (obtained by expanding around  $\alpha = 0$ ) is

$$p_{\rm d} \frac{\gamma_+ - \gamma_-}{\tilde{\Gamma}_{\rm d}^2} - p_{\rm ud} \frac{\gamma_-}{\tilde{\Gamma}_{\rm ud}^2} > \frac{\kappa}{4N\Omega^2} \,. \tag{7.10}$$

For any nonzero  $p_{\rm d}$ , the drive rate  $\gamma_+$  can be increased sufficiently to cross the lasing threshold. This contrasts with the behavior of the superradiant laser, where no lasing can be obtained for  $p_{\rm d} < 1/2$  as we saw in Eq. (7.8).

# 7.4 Spontaneous emission and dephasing

We now investigate the effects of spontaneous emission at rate  $\gamma_{-}$  and dephasing at rate  $\gamma_{z}$  of each spin. As a first consequence, the lasing transition condition from Eq. (7.8) changes; the full expression including  $\gamma_{-}$  and  $\gamma_{z}$  reads

$$p_{\rm d} > \frac{1}{2} \left( 1 + \frac{\gamma_-}{\gamma_+} \right) \left( 1 + \frac{2\gamma_- + 4\gamma_z + \gamma_+}{2V} \right) .$$
 (7.11)

Most importantly, the incoherent drive needs to overcome the spontaneous emission to allow for population inversion. We see this from the first bracket on the right side: The inequality can only be fulfilled when  $\gamma_+ > \gamma_-$ , since otherwise the right-hand side evaluates to a value larger than one. Figure 7.3(a) shows the steady-state laser power computed within the cumulant approximation for  $N=10^5$  as a function of  $\gamma_+/V$  and  $p_{\rm d}$ . The transition from small to large power is compatible with the mean-field prediction

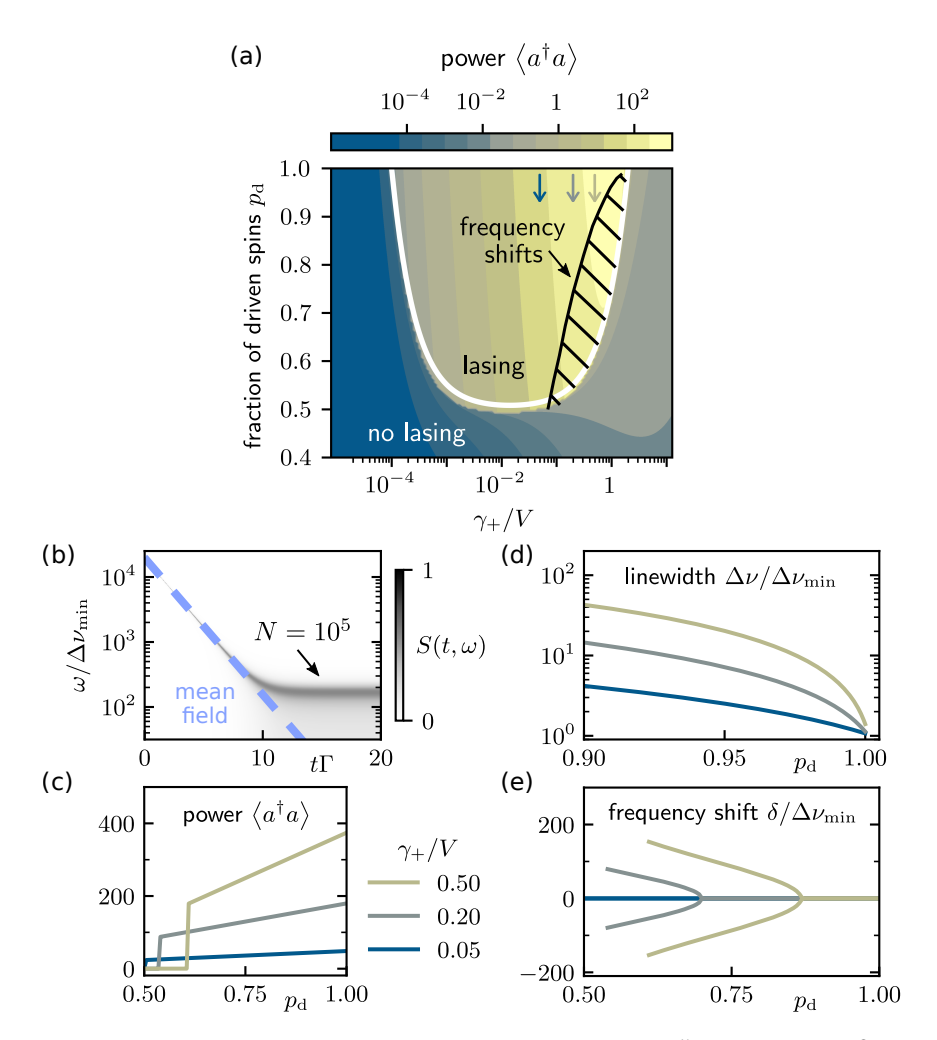


Figure 7.3: Steady-state lasing properties for  $N=10^5, \, \gamma_z/V=10^{-3}, \, \gamma_-/V=10^{-4},$  and  $\kappa=10\sqrt{N}\Omega$ , so that the cooperativity is C=0.2. (a) Laser power as a function of drive rate and fraction of driven spins. The white line shows the mean-field lasing transition. The hatched region indicates the regime in which frequency shifts occur in the steady state. (b) Frequency shift as a function of time for  $p_{\rm d}=0.8$  and  $\gamma_+=V$ . The initial state at t=0 is the stationary state when  $\gamma_-=\gamma_z=0$ . The dashed line is the mean-field solution, which follows an exponential decay at rate  $\Gamma/2=(\gamma_-+2\gamma_z)/2$ . The spectrum for  $N=10^5$  is shown in grayscale (arb. units). (c) Line cuts through (a) as marked by the three arrows in (a) on a linear scale. (d,e) Steady-state linewidth and frequency shifts in units of the minimum linewidth  $\Delta\nu_{\rm min}=V/N$  (same legend as (c)).

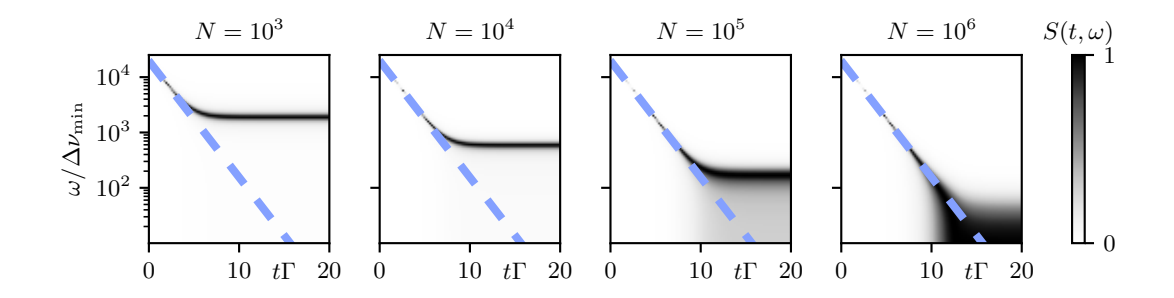


Figure 7.4: Time dependence of the frequency shift in the spectrum for different values of N. The spectrum is normalized to a maximum value of 1 for each time t. The dashed line is the mean-field prediction of the frequency. The initial state at t=0 is the stationary state when  $\gamma_- = \gamma_z = 0$ . Parameters as in Fig. 7.3(b) with N specified for each panel.

of Eq. (7.11) (white line). Experimentally,  $\gamma_+$  can be varied through the pump laser intensity, while the collective coupling  $V = NC\gamma_-/2$  is set by the number of spins N and the cooperativity  $C = 4\Omega^2/(\kappa\gamma_-)$ .

The second consequence of spontaneous emission and dephasing is that the purity of the undriven spins is no longer conserved; their coherence decays at rate  $\Gamma/2 \equiv (\gamma_- + 2\gamma_z)/2$ . As the undriven spins decohere, they become less important as antagonists to the driven spins. The frequency shift, which arises due to the competition of alignment and antialignment, consequently decreases. Figure 7.3(b) shows the time evolution of the frequency  $\omega$ . In the mean-field limit, it exponentially decays to zero at rate  $\Gamma$  (dashed line). For finite N, after an initial exponential decay, a nonzero frequency shift remains in the spectrum in the long-time limit even in the presence of spontaneous emission and dephasing. The initial frequency is large compared to  $\Gamma$  for typical experimental parameters [Meiser et al., 2009] and therefore remains observable as a transient in experiments.

Figure 7.4 shows the time evolution of the frequency shift for different values of N. For increasing N, the spectrum approaches the mean-field prediction (dashed line). For  $N \to \infty$ , the frequency shift vanishes in the long-time limit, consistent with the mean-field analysis.

To characterize the steady-state lasing, we analyze the dependence of three key properties of the laser on the fraction of driven spins  $p_{\rm d}$ : the laser power, the linewidth, and the frequency. The spectral properties are obtained by fitting a double-peaked Lorentzian

$$\frac{A}{\pi} \left( \frac{\Delta \nu}{\Delta \nu^2 + (\omega - \delta)^2} + \frac{\Delta \nu}{\Delta \nu^2 + (\omega + \delta)^2} \right) , \tag{7.12}$$

with amplitude A and linewidth  $\Delta \nu$ , displaced by  $\pm \delta$ , to the spectrum.

The linewidth shown in Fig. 7.3(d) significantly increases as the fraction of driven spins decreases, revealing a strong spectral broadening caused by the antialignment of undriven dipoles. Taking for example  $\gamma_+ = V/2$ , the linewidth increases by one order of magnitude for only 3% of undriven spins. While for smaller drive rates, there is less spectral broadening, the laser power is smaller; see Fig. 7.3(c). Finally, as shown in Fig. 7.3(e), a frequency shift can occur below a critical value of  $p_{\rm d}$ . This regime of nonzero frequency shifts is highlighted as the hatched region in Fig. 7.3(a). It largely coincides with the regime of large powers where  $\gamma_+ \approx V$ .

# 7.5 Conclusion

In this chapter, we discussed a simple modification to the model of a superradiant laser that has significant consequences. Introducing a fraction of undriven atomic spins limits the optimal operation of the laser in three ways: an increased spectral linewidth, a shift of the lasing frequency, and a reduced power. We explained these effects by identifying nonreciprocal interactions between driven and undriven atoms. The atoms self-organize into a collective state, and the nonreciprocal interactions between driven and undriven atoms result in a dynamical pattern, namely the traveling-wave states.

There are various directions to explore in further studies. First, we have only focused on a continuous incoherent drive to achieve continuous superradiant lasing. While this is simple to model theoretically, it presents experimental challenges due to heating and atom loss; see for example Norcia and Thompson [2016]. Other proposals to achieve continuous superradiant lasing employ a beam of initially excited atoms that pass through the cavity [Kazakov and Schumm, 2014; Liu et al., 2020; Tang et al., 2022;  $Fam\grave{a}$  et al., 2024]. If a fraction of those atoms is not excited, similar dynamics as described here may occur. Furthermore, atoms that have already de-excited might remain in the cavity for some time, effectively acting as undriven atoms. Second, one can explore distributions of incoherent drive rates other than the bimodal distribution considered here. For example, a Gaussian distribution that could result from the intensity profile of a repump laser. Third, it would be interesting to study the phenomena described in this chapter in the context of superradiant masers operating at microwave frequencies [Arroo et al., 2021; Wu et al., 2022]. These are described by the same master equation that we analyzed in this chapter and should therefore also show the effects described here.

Here, we have shown that the laser's performance degrades when introducing spins with the goal to hinder the formation of a coherent state. It is therefore intriguing to ask whether the interactions and properties of individual quantum constituents can be engineered in such a way that the resulting collective state corresponds to *improved* lasing properties. In other words, can the environment of the atoms be designed so that they tend to autonomously form a more robust and precise source of coherent light? To explore this possibility, it may be useful to view the superradiant laser as a self-organizing system comprising individual constituents, and to build on insights from classical and quantum synchronization.

# Appendix for Chapter 7

# 7.A Cumulant expansion and spectrum

To calculate the output power and the spectrum for large but finite N, we use a cumulant expansion [Kubo, 1962], neglecting third and higher-order correlations. Additionally, we exploit the permutational invariance of driven and undriven spins respectively, and the global U(1)-symmetry to set terms like  $\langle a \rangle$  or  $\langle a^{\dagger} \sigma_{\mu}^{+} \rangle$  equal to zero. This leads to a closed set of eight equations,

$$\begin{split} \frac{\mathrm{d}}{\mathrm{d}t} s_{\mathrm{d}}^{z} &= -\gamma_{-}(s_{\mathrm{d}}^{z}+1) - \gamma_{+}(s_{\mathrm{d}}^{z}-1) - 4\Omega \operatorname{Im}[\langle a^{\dagger}\sigma_{\mathrm{d}}^{-} \rangle] \,, \\ \frac{\mathrm{d}}{\mathrm{d}t} s_{\mathrm{ud}}^{z} &= -\gamma_{-}(s_{\mathrm{ud}}^{z}+1) - 4\Omega \operatorname{Im}[\langle a^{\dagger}\sigma_{\mathrm{ud}}^{-} \rangle] \,, \\ \frac{\mathrm{d}}{\mathrm{d}t} \left\langle a^{\dagger}a \right\rangle &= -\kappa \left\langle a^{\dagger}a \right\rangle + 2\Omega \left( N_{\mathrm{d}} \operatorname{Im}[\left\langle a^{\dagger}\sigma_{\mathrm{ud}}^{-} \right\rangle] + N_{\mathrm{ud}} \operatorname{Im}[\left\langle a^{\dagger}\sigma_{\mathrm{ud}}^{-} \right\rangle] \right) \,, \\ \frac{\mathrm{d}}{\mathrm{d}t} \left\langle a^{\dagger}\sigma_{\mathrm{d}}^{-} \right\rangle &= -(\gamma_{+} + \Gamma + \kappa) \langle a^{\dagger}\sigma_{\mathrm{d}}^{-} \rangle / 2 + \\ &\qquad \qquad + i\Omega \left( (N_{\mathrm{d}}-1) \left\langle \sigma_{\mathrm{d}}^{+}\sigma_{\mathrm{d}}^{-} \right\rangle + \frac{1 + s_{\mathrm{d}}^{z}}{2} + N_{\mathrm{ud}} \left\langle \sigma_{\mathrm{d}}^{+}\sigma_{\mathrm{d}}^{-} \right\rangle + \left\langle a^{\dagger}a \right\rangle s_{\mathrm{d}}^{z} \right) \,, \\ \frac{\mathrm{d}}{\mathrm{d}t} \left\langle a^{\dagger}\sigma_{\mathrm{ud}}^{-} \right\rangle &= -(\Gamma + \kappa) \langle a^{\dagger}\sigma_{\mathrm{ud}}^{-} \rangle / 2 + \\ &\qquad \qquad + i\Omega \left( (N_{\mathrm{ud}}-1) \left\langle \sigma_{\mathrm{ud}}^{+}\sigma_{\mathrm{ud}}^{-} \right\rangle + \frac{1 + s_{\mathrm{ud}}^{z}}{2} + N_{\mathrm{d}} \left\langle \sigma_{\mathrm{d}}^{+}\sigma_{\mathrm{ud}}^{-} \right\rangle + \left\langle a^{\dagger}a \right\rangle s_{\mathrm{ud}}^{z} \right) \,, \\ \frac{\mathrm{d}}{\mathrm{d}t} \left\langle \sigma_{\mathrm{d}}^{+}\sigma_{\mathrm{d}}^{-} \right\rangle &= -(\gamma_{+} + \Gamma) \left\langle \sigma_{\mathrm{d}}^{+}\sigma_{\mathrm{d}}^{-} \right\rangle + 2\Omega s_{\mathrm{d}}^{z} \operatorname{Im}[\langle a^{\dagger}\sigma_{\mathrm{d}}^{-} \rangle] \,, \\ \frac{\mathrm{d}}{\mathrm{d}t} \left\langle \sigma_{\mathrm{ud}}^{+}\sigma_{\mathrm{ud}}^{-} \right\rangle &= -\Gamma \left\langle \sigma_{\mathrm{ud}}^{+}\sigma_{\mathrm{ud}}^{-} \right\rangle + 2\Omega s_{\mathrm{ud}}^{z} \operatorname{Im}[\langle a^{\dagger}\sigma_{\mathrm{ud}}^{-} \rangle] \,, \\ \frac{\mathrm{d}}{\mathrm{d}t} \left\langle \sigma_{\mathrm{d}}^{+}\sigma_{\mathrm{ud}}^{-} \right\rangle &= -(\gamma_{+} / 2 + \Gamma) \left\langle \sigma_{\mathrm{d}}^{+}\sigma_{\mathrm{ud}}^{-} \right\rangle + i\Omega \left( s_{\mathrm{ud}}^{z} \left\langle a^{\dagger}\sigma_{\mathrm{d}}^{-} \right\rangle^{*} - s_{\mathrm{d}}^{z} \left\langle a^{\dagger}\sigma_{\mathrm{ud}}^{-} \right\rangle \right) \,, \end{cases}$$

where  $\Gamma = \gamma_- + 2\gamma_z$ . We use the Julia package QuantumCumulants.jl [Plankensteiner et al., 2022] to integrate these equations numerically.

The spectrum is computed within the cumulant-expansion approximation using the quantum regression theorem [Breuer and Petruccione, 2002]. By factorizing

$$\langle \sigma_{\mu}^{z}(t+\tau)a^{\dagger}(t+\tau)a(t)\rangle \approx s_{\mu}^{z}(t+\tau)\langle a^{\dagger}(t+\tau)a(t)\rangle$$
, (7.13)

the two-time correlations evolve according to

$$\frac{\mathrm{d}}{\mathrm{d}\tau}\mathbf{c}(t,\tau) = M(t+\tau)\mathbf{c}(t,\tau), \quad \mathbf{c}(t,\tau) = \begin{pmatrix} \langle a^{\dagger}(t+\tau)a(t) \rangle \\ \langle \sigma_{\mathrm{d}}^{\dagger}(t+\tau)a(t) \rangle \\ \langle \sigma_{\mathrm{ud}}^{\dagger}(t+\tau)a(t) \rangle \end{pmatrix}, 
M(t+\tau) = \begin{pmatrix} -\kappa/2 & iN_{\mathrm{d}}\Omega & iN_{\mathrm{ud}}\Omega \\ -i\Omega s_{\mathrm{d}}^{z}(t+\tau) & -(\Gamma+\gamma_{+})/2 & 0 \\ -i\Omega s_{\mathrm{ud}}^{z}(t+\tau) & 0 & -\Gamma/2 \end{pmatrix}.$$
(7.14)

In the steady state  $t \to \infty$ , where  $s^z_{\mu}$  obtains a constant value, the matrix M is time independent, and the steady-state spectrum can be calculated using the Laplace transform,

$$S(\omega) = \lim_{t \to \infty} \int_{-\infty}^{\infty} d\tau \left\langle a^{\dagger}(t+\tau)a(t) \right\rangle e^{i\omega\tau} = 2 \operatorname{Re} \left\{ \left[ (i\omega - M)^{-1} \mathbf{c}_{ss} \right]_{1} \right\}.$$
 (7.15)

Here, the subscript 1 refers to the first component of the vector, and  $\mathbf{c}_{ss} = \lim_{t\to\infty} \mathbf{c}(t,0)$ . The spectrum in Fig. 7.3(b) can be calculated by a discrete Fourier transform of solutions of Eq. (7.14) in consecutive time intervals. By using that  $s^z_{\mu}$  changes at rate  $\Gamma$  during the transient, which is small compared to the typical frequency  $\omega$ , we set  $s^z_{\mu}(t+\tau) = s^z_{\mu}(t)$  constant for each time interval and use the Laplace transform at each time t to approximately calculate the spectrum,

$$S(t,\omega) = \int_{-\infty}^{\infty} d\tau \left\langle a^{\dagger}(t+\tau)a(t) \right\rangle e^{i\omega\tau} \approx 2 \operatorname{Re}\left\{ \left[ (i\omega - M(t)^{-1}\mathbf{c}(t,0)) \right]_{1} \right\}.$$
 (7.16)

# 7.B Influence of cavity-spin detuning

This appendix discusses the effect of a nonzero detuning between cavity frequency  $\omega_c$  and spin frequency  $\omega_s$ . The master equation in the laboratory frame is (setting  $\gamma_- = \gamma_z = 0$  for simplicity)

$$\dot{\rho} = -i[H, \rho] + \kappa \mathcal{D}[a]\rho + \gamma_{+} \sum_{i=1}^{N_{d}} \mathcal{D}[\sigma_{d,i}^{+}]\rho, \quad H = \frac{\omega_{s}}{2} S^{z} + \omega_{c} a^{\dagger} a + \Omega(a^{\dagger} S^{-} + a S^{+}).$$
 (7.17)

The collective spin operators are as before  $S^{\pm,z} = \sum_{i=1}^{N_{\rm d}} \sigma_{{\rm d},i}^{\pm,z} + \sum_{i=1}^{N_{\rm ud}} \sigma_{{\rm ud},i}^{\pm,z}$ . In the frame where both spins and cavity rotate with the spin frequency  $\omega_s$ , the Hamiltonian becomes

$$H = (\omega_c - \omega_s)a^{\dagger}a + \Omega(a^{\dagger}S^- + aS^+). \tag{7.18}$$

The cavity-spin detuning  $\omega_c - \omega_s$  results in a frequency shift of the laser. In the badcavity limit, the frequency shift is smaller than the detuning by a factor of approximately  $\Gamma/\kappa \sim 10^{-3} - 10^{-5}$  and therefore does not limit the stability of a superradiant laser [Bohnet et al., 2012; Norcia and Thompson, 2016]. Note the qualitative difference between the frequency shift due to nonzero detuning and the frequency shifts due to nonreciprocal interactions. A nonzero detuning induces a unique and deterministic frequency shift. The nonreciprocal interactions, however, result in one of two possible frequency shifts through spontaneous symmetry breaking.

The influence of the detuning  $\omega_c - \omega_s$  between cavity and spins on the traveling-wave states, and correspondingly the frequency shifts, is shown in Fig. 7.5. The detuning explicitly breaks the symmetry between the two frequencies of the traveling-wave states; see also Section 6.5.3. Therefore, one of the two traveling-wave states is more likely to occur, which is indicated by the asymmetry in the peaks, see Fig. 7.5(b). However, for experimentally relevant values of the detuning,  $\omega_c - \omega_s \ll \kappa$ , the influence of the detuning on the frequency shifts induced by nonreciprocal interactions is negligible. When the detuning is comparable to the cavity dissipation rate, the coherent spin-spin interactions mediated by the cavity result in rich physics beyond the scope of the present work [Norcia et al., 2018; Muniz et al., 2020; Young et al., 2024].

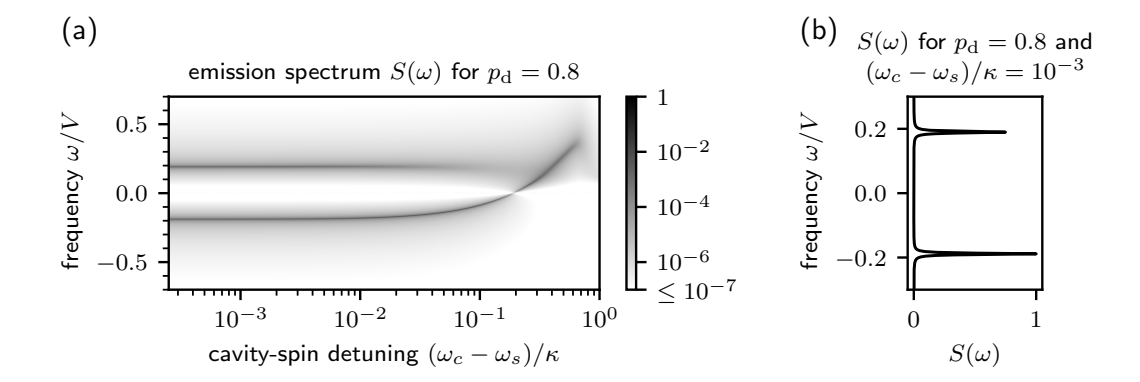


Figure 7.5: Influence of detuning  $\omega_c - \omega_s$  between cavity and spins on the frequency shift. Parameters are the same as in Fig. 7.2 with  $p_{\rm d}=0.8$ . (a) Cavity emission spectrum  $S(\omega)$  (arb. units) as a function of cavity-spin detuning  $\omega_c - \omega_s$ . The frequency  $\omega$  is measured relative to the bare spin frequency. For negative detuning,  $\omega_c - \omega_s < 0$ , the same result is obtained but mirrored at  $\omega=0$ . (b) Line cut through (a) at  $\omega_c - \omega_s = 10^{-3} \kappa$  on a linear scale, highlighting the asymmetry in the two peaks.

# Chapter 8

# Conclusions and outlook

### 8.1 Conclusions

We presented models of quantum systems that exhibit synchronization and nonreciprocal phase transitions. Both of these are self-organization transitions where pairwise interactions give rise to a collectively ordered state without any external control. Synchronization results in a phase-coherent state; nonreciprocal phase transitions result in dynamical traveling-wave states. Let us conclude by summarizing the key results and overarching themes of this thesis.

### Nonreciprocal interactions

The concept of nonreciprocal interactions is central to classical active matter but has remained largely unexplored in quantum physics. We presented a general framework for engineering antagonistic nonreciprocal interactions in quantum systems using chiral waveguides. Within this framework, we showed that nonreciprocal phase transitions can occur in a quantum-optical model of interacting spins. We formulated a suitable parity-time symmetry at the level of the quantum master equation and established its correspondence with the symmetry that is spontaneously broken in the thermodynamic limit. Our results are of fundamental interest as they establish how nonreciprocal interactions can arise in quantum physics and what their consequences are. These insights are also practically relevant as they allowed us to explain how the presence of undriven spins results in nonreciprocal interactions that cause frequency shifts in superradiant lasers. This finding has implications for the design of superradiant lasers. For example, in the case of atomic beam lasers, it may be crucial to avoid slow atoms that remain in the cavity for extended times, taking the role of the undriven spins.

#### Measurement

We placed a special emphasis on the role of measurement, which generally imparts a backaction on the system and causes fluctuations. In the context of quantum limit cycles, we showed that the time evolution under heterodyne detection yields quantum trajectories that make the similarity between classical and quantum limit cycles apparent. Furthermore, the current of the photodetector allows one to approximate the degree of quantum synchronization, connecting previously established theoretical measures of quantum synchronization with experimentally accessible quantities.

Moreover, the measurement induces symmetry breaking. For quantum limit cycles, the master equation is invariant under a phase shift; however, the trajectory obtained through heterodyne detection selects a phase at every point in time. Similarly, quantum trajectories of traveling-wave states select a chirality, thereby spontaneously breaking parity-time symmetry. Simultaneously, the continuous time-translation symmetry is broken, resulting in the time-crystalline state. In both cases, the fluctuations due to the

measurement restore the symmetry over long timescales in finite-size systems. Phase diffusion randomly changes the selected phase of the limit cycle, and chirality reversals restore parity-time symmetry. In the thermodynamic limit, these fluctuations become effectively suppressed, so that the symmetry remains broken indefinitely.

### Classical versus quantum dynamics

In several contexts, we highlighted the analogy between the dynamics of quantum and classical systems. For example, synchronization of quantum van-der-Pol oscillators or spins-1/2 resembles synchronization of classical oscillators subject to noise. Furthermore, the phase transition induced by nonreciprocal interactions among quantum spins-1/2 is qualitatively the same as that of the nonreciprocal Kuramoto model for classical phase oscillators. It is an important result to show how these phenomena can occur in models that obey the laws of quantum mechanics. The formulation within the framework of open quantum systems enables future studies to explore similar models in which the quantum character is more pronounced; see also the following outlook section.

The quantum models of this thesis also exhibit differences from classical models. For instance, we discussed qualitatively unique features in the synchronization of quantum three-level limit-cycle oscillators. Their quantum nature is significant in a Kuramoto-like model of synchronization of many coupled oscillators and shapes the dynamics of the macroscopic ensemble. Furthermore, we emphasized the role of the measurement backaction. While the measurement backaction in classical systems is usually negligible, measurement backaction in quantum systems is generally inevitable and influences the dynamics significantly. In the context of nonreciprocal interactions, we showed that two types of continuous measurements – homodyne and heterodyne detection – induce qualitatively different dynamics in traveling-wave states.

#### Microscopic origins of self-organization

A central theme of this work was to develop an intuitive understanding of the quantum many-body dynamics. To achieve this, we traced the collective dynamics back to the pairwise interactions between any two individual constituents. By identifying the "goals" of individual constituents, we intuitively explained the self-organization into collective states, like phase-coherent synchronized states or dynamical traveling-wave states. Specifically, for the spin-1 oscillators, the quantum nature that governs the synchronization of one or two oscillators also shapes the macroscopic patterns. For the spins (or atomic dipoles) of the models with nonreciprocal interactions, we identified the competition of alignment and antialignment that results in traveling-wave states. While our quantitative results are obtained from numerical simulations and analytical calculations, this physical bottom-up perspective provides an understanding of why the systems exhibit the rich phenomenology.

### 8.2 Outlook

Finally, we list connections to other fields as well as possibilities for future work and open questions.

#### Finite-range interactions

A natural extension of our work is the study of finite-range interactions instead of global interactions. Throughout this thesis, we have focused on situations where all constituents are identically coupled to all others (within one species). Such interactions can be mediated by a cavity or a freely propagating light mode. Finite-range interactions occur,

8.2. Outlook 125

for example, among trapped ions mediated by phonons [Zhu et al., 2006] or the Coulomb force [Brown et al., 2011; Harlander et al., 2011], as well as among Rydberg atoms in the form of dipole-dipole interactions [de Léséleuc et al., 2017]. When the coupling is sufficiently long-range, given a specific dimension, it is to be expected that the phenomena discussed in this thesis will still occur; for short-range interactions, however, the self-organization transitions may be absent, and for intermediate-range couplings, further interesting effects may occur [Defenu et al., 2023]. The numerical analysis of models with finite-range couplings will be more complex as they do not possess the permutational invariance of the constituents.

### Extensions of nonreciprocal interactions

Another direction to explore are the effects of antagonistic interactions on different quantum systems. We outlined a general framework for engineering antagonistic interactions between quantum systems via opposing chiral waveguides that include a phase shift. In this context, we studied spin models where each spin is incoherently driven. Kehrer and Bruder [2025] applied the framework to two coupled quantum van-der-Pol oscillators. In both cases, the quantum systems are driven out of equilibrium, and in this sense made active, by incoherent processes. These incoherent processes also result in large rates of decoherence. It will be interesting to apply the framework to quantum systems with smaller rates of decoherence. For example, a fully collective model of a superradiant laser that does not rely on incoherent repumping has been recently suggested by Reilly et al. [2025]. Similarly, the nonreciprocal Dicke model [Chiacchio and Nunnenkamp, 2019; Buča and Jaksch, 2019; Chiacchio et al., 2023; Jachinowski and Littlewood, 2025] is fully coherent when considering the effective spin model. In these models with less local dissipation, it will be interesting to address questions regarding the effect of antagonistic nonreciprocal interactions on quantum correlations. One may also explore nonreciprocity in multilevel systems, where there are dark and subradiant states that can be used for entanglement generation; see for example [Piñeiro Orioli et al., 2022; Finger et al., 2024]

Furthermore, the framework to engineer antagonistic interactions readily extends to networks of more than two species. These networks feature a rich phase diagram and novel dynamics in classical systems [Kehrer and Bruder, 2025; Weis and Hanai, 2025]. There can be dynamical frustration due to antagonistic interactions between two subsystems and geometric frustration among three or more subsystems. This enables the exploration of similarities and the interplay between dynamical and geometric frustration in quantum systems [Hanai, 2024].

#### **Applications**

While we have demonstrated practical consequences of nonreciprocity for superradiant lasers, there are other applications of synchronization and nonreciprocal interactions that remain to be explored. For one, limit cycles and synchronization could find relevance in quantum sensing. Steps in this direction have been taken for single limit-cycle oscillators [Fernández-Lorenzo and Porras, 2017; Dutta and Cooper, 2019; Vaidya et al., 2025]. In coupled limit-cycle oscillators, the self-organization transition to a phase-coherent state potentially offers advantages in sensing due to the robustness of the phase stabilized by the interactions. Additionally, the synchronization transition and the exceptional points at the nonreciprocal phase transition could be exploited for sensing, building on the enhancement of sensing close to phase transitions [Wiersig, 2020] and exceptional points [Sarkar et al., 2025].

More speculatively, it is intriguing to consider self-organization as an advantageous way for the formation of complex structures in quantum many-body systems. Since

self-organization is often robust and scalable, it has advantages compared with structure formation by external control, which is prone to errors and difficult to apply to an increasing number of constituents. Given the high control of driven-dissipative quantum many-body systems in current experimental settings, one could aim to engineer the environment and the interactions such that each constituent has the "goal" of forming the desired structure. As a result, the ensemble of constituents may then self-organize into the desired collective state. A natural case, where this concept of engineered selforganization may apply, is the generation of squeezed states of spin ensembles, which can be used for sensing beyond the standard shot-noise limit [Pezzè et al., 2018]. An example of this is presented in Krešić et al. [2023]. Potentially, self-organization akin to synchronization offers a robust and scalable path for the formation of squeezing. More broadly, engineered self-organization could be relevant in the spontaneous occurrence of algorithms in quantum machine learning [Biamonte et al., 2017] or emergent phenomena in quantum materials [Tokura et al., 2017]. An intuitive understanding of how the collective states occur based on analyzing the microscopic interactions, as developed in this thesis in the contexts of synchronization and nonreciprocal phase transitions, may help design quantum systems where self-organization results in useful many-body states.

# Acknowledgements

First, I would like to thank Christoph Bruder for accepting me as a PhD student in his group and for the support and guidance during the last four years. I am particularly grateful for the trust and the academic freedom that you grant young researchers including me, while always being there and offering advice when needed. I also appreciate that you create a stimulating and respectful atmosphere in your research group allowing for an inspiring time at the office.

I am grateful to Philipp Treutlein for the feedback and the helpful scientific discussions during the annual meetings.

I would like to thank Ana Maria Rey for serving as the external expert of this thesis.

Furthermore, I want to thank Stefan Antusch for chairing the doctoral defense.

I am grateful to Matteo Brunelli for the very pleasant and fruitful collaborations during my PhD. Thank you for making me aware of the topic of nonreciprocal interactions and sparking my interest in it. I very much appreciate your time, your advice, and the inspiring discussions over the last years.

I am thankful to all the members of the research group in Basel. I highly appreciate the collaborative, respectful, and helpful atmosphere, the mutual support, and many interesting journal clubs and discussions. Thank you all for contributing to this environment: Tobias Kehrer, Julian Arnold, Niels Lörch, Petr Zapletal, Parvinder Solanki, Markus Hoffmann, Ryan Tan, Gaomin Tang, Frank Schäfer, and Martin Koppenhöfer. I would like to additionally thank Tobias Kehrer for the enjoyable collaboration on two interesting projects that are not part of this thesis. Also, thanks to Livia Benedict and Nils Lerch for investing their time in student projects that I was glad to supervise.

Regarding this thesis, I am grateful for discussions with Martin Koppenhöfer, Niels Lörch and Ryan Tan on limit cycles in quantum systems, Julian Arnold on stochastic differential equations and phase transitions, Petr Zapletal on lasers and linewidths, Parvinder Solanki on time crystals, Matteo Simoni on trapped-ion physics, Albert Cabot and Simon Jäger on superradiant lasers, Michel Fruchart on nonreciprocal phase transitions, Philipp Treutlein on remote Hamiltonian interactions, and Tobias Kehrer on quantum synchronization. Furthermore, I would like to thank Niels Lörch, Matteo Brunelli, and Julian Arnold for proofreading parts of this thesis.

One of the most important aspects of research for me is having discussions and exchanging ideas with others. During my PhD, this has allowed me to learn a great deal. Therefore, I am immensely grateful to all the scientists, colleagues and friends with whom I have been able to discuss physics. You sharing your expert knowledge of experiments and theory is inspiring, interesting and highly appreciated. Thank you, David Baur, Tanja Behrle, Frederik van der Brugge, Alessandro Bruno, Federico Carollo, Aaron Daniel, Romain Daviet, Sebastian Diehl, Tobias Donner, Alexander Grimm, Simon Hertlein, Marcelo Janovitch, Martin Koppenhöfer, Álvaro de Melo, Marc Nairn, Gabriele Natale, Andreas Nunnenkamp, Preeti Pandey, Patrick Potts, Kacper Prech, Florentin Reiter, Nicola Reiter, Ivan Rojkov, Felix Russo, Johannes Schading, Marco Schirò, Gian-Luca Schmid, Pavel

Sekatski, Justyna Stefaniak, Benjamin Stickler, Christopher Wächtler, Ian Yang Yen Wei, Stephan Welte, Elias Zapusek, and Carl Philipp Zelle.

I would like to thank all the organizers of the conferences I attended for creating meetings of inspiring discussions and talks. This extends to all the participants on conferences that I met, who took the time to share their insights or ask about my research. Thanks also to all the visitors who traveled to Basel, and to everyone who invited me to visit.

Also, I would like to acknowledge all the anonymous referees who were involved in reviewing our publications. Thank you for the valuable questions and comments, as well as the constructive feedback.

I acknowledge the use of the SciCore cluster and several software packages. I am thankful to everyone who developed code and numerical tools that are useful for research in physics and made them publicly available. This includes basic software packages like numpy, matplotlib, or julia's Differential Equations.jl, and extends to more specialized packages like qutip and Quantum Cumulants.jl.

Next, I would like to thank Thilo Glatzel for coordinating our PhD school, for organizing interesting soft-skill courses, for the summer barbecues, and for the recognition through the excellence award. And I thank, Tatsiana Dolmat and Dominique Zbinden, for the fast and reliable administrative support.

I acknowledge the financial support of the Swiss national science foundation (grant no. 200020 200481).

Finally, I am deeply grateful to my family – Andrea, Bruno and Johanna – who supported and trusted me in all my endeavors, and to all my friends and especially Nicola for their constant support and for the joy they brought along the way.

# **Bibliography**

- Acebrón, J. A., L. L. Bonilla, C. J. Pérez Vicente, F. Ritort, and R. Spigler (2005): The Kuramoto Model: A Simple Paradigm for Synchronization Phenomena. Reviews of Modern Physics 77, 137–185.
- Adachi, K., K. Takasan, and K. Kawaguchi (2022): Activity-induced phase transition in a quantum many-body system. Physical Review Research 4, 013194.
- Adler, R. (1946): A Study of Locking Phenomena in Oscillators. Proceedings of the IRE 34, 351–357.
- Albert, V. V. and L. Jiang (2014): Symmetries and conserved quantities in Lindblad master equations. Physical Review A 89, 022118.
- Ameri, V., M. Eghbali-Arani, A. Mari, A. Farace, F. Kheirandish, V. Giovannetti, and R. Fazio (2015): *Mutual information as an order parameter for quantum synchronization*. Physical Review A **91**, 012301.
- Amitai, E., M. Koppenhöfer, N. Lörch, and C. Bruder (2018): Quantum Effects in Amplitude Death of Coupled Anharmonic Self-Oscillators. Physical Review E 97, 052203.
- Antonov, A. P., Y. Zheng, B. Liebchen, and H. Löwen (2025): Engineering active motion in quantum matter. Physical Review Research 7, 033008.
- Arroo, D. M., N. M. Alford, and J. D. Breeze (2021): Perspective on room-temperature solid-state masers. Applied Physics Letters 119, 140502.
- Avni, Y., M. Fruchart, D. Martin, D. Seara, and V. Vitelli (2025): *Nonreciprocal Ising Model*. Physical Review Letters **134**, 117103.
- Baconnier, P., D. Shohat, C. H. López, C. Coulais, V. Démery, G. Düring, and O. Dauchot (2022): Selective and collective actuation in active solids. Nature Physics 18, 1234–1239.
- Bandyopadhyay, B. and T. Banerjee (2022): Kerr nonlinearity hinders symmetry-breaking states of coupled quantum oscillators. Physical Review E 106, 024216.
- Bandyopadhyay, B. and T. Banerjee (2023): Aging transition in coupled quantum oscillators. Physical Review E 107, 024204.
- Barzanjeh, S., A. Xuereb, A. Alù, S. A. Mann, N. Nefedkin, V. Peano, and P. Rabl (2025): *Nonreciprocity in Quantum Technology*. arXiv: 2508.03945.
- Bechinger, C., R. Di Leonardo, H. Löwen, C. Reichhardt, G. Volpe, and G. Volpe (2016): Active particles in complex and crowded environments. Reviews of Modern Physics 88, 045006.
- Begg, S. E. and R. Hanai (2024): Quantum Criticality in Open Quantum Spin Chains with Nonreciprocity. Physical Review Letters 132, 120401.

Behrle, T., T. L. Nguyen, F. Reiter, D. Baur, B. de Neeve, M. Stadler, M. Marinelli, F. Lancellotti, S. F. Yelin, and J. P. Home (2023): *Phonon Laser in the Quantum Regime*. Physical Review Letters **131**, 043605.

- Belyansky, R., C. Weis, R. Hanai, P. B. Littlewood, and A. A. Clerk (2025): *Phase Transitions in Nonreciprocal Driven-Dissipative Condensates*. arXiv: 2502.05267.
- Ben Arosh, L., M. C. Cross, and R. Lifshitz (2021): Quantum limit cycles and the Rayleigh and van der Pol oscillators. Physical Review Research 3, 013130.
- Bender, C. M. and D. W. Hook (2024):  $\mathcal{PT}$ -symmetric quantum mechanics. Reviews of Modern Physics **96**, 045002.
- Bennett, M., M. F. Schatz, H. Rockwood, and K. Wiesenfeld (2002): *Huygens's clocks*. Proceedings of the Royal Society A **458**, 563–579.
- Biamonte, J., P. Wittek, N. Pancotti, P. Rebentrost, N. Wiebe, and S. Lloyd (2017): *Quantum machine learning*. Nature **549**, 195–202.
- Blais, A., R.-S. Huang, A. Wallraff, S. M. Girvin, and R. J. Schoelkopf (2004): Cavity quantum electrodynamics for superconducting electrical circuits: An architecture for quantum computation. Physical Review A 69, 062320.
- Bohnet, J. G., Z. Chen, J. M. Weiner, D. Meiser, M. J. Holland, and J. K. Thompson (2012): A steady-state superradiant laser with less than one intracavity photon. Nature 484, 78–81.
- Bowick, M. J., N. Fakhri, M. C. Marchetti, and S. Ramaswamy (2022): Symmetry, Thermodynamics, and Topology in Active Matter. Physical Review X 12, 010501.
- Brandenbourger, M., X. Locsin, E. Lerner, and C. Coulais (2019): *Non-reciprocal robotic metamaterials*. Nature Communications **10**, 4608.
- Brauns, F. and M. C. Marchetti (2024): Nonreciprocal Pattern Formation of Conserved Fields. Physical Review X 14, 021014.
- Breuer, H.-P. and F. Petruccione (2002): *The Theory of Open Quantum Systems* (Oxford University Press, New York, United States).
- Brighi, P. and A. Nunnenkamp (2024): Nonreciprocal dynamics and the non-Hermitian skin effect of repulsively bound pairs. Physical Review A 110, L020201.
- Browaeys, A. and T. Lahaye (2020): Many-body physics with individually controlled Rydberg atoms. Nature Physics 16, 132–142.
- Brown, E., J. Moehlis, and P. Holmes (2004): On the Phase Reduction and Response Dynamics of Neural Oscillator Populations. Neural Computation 16, 673–715.
- Brown, K. R., C. Ospelkaus, Y. Colombe, A. C. Wilson, D. Leibfried, and D. J. Wineland (2011): Coupled quantized mechanical oscillators. Nature 471, 196–199.
- Brunelli, M., C. C. Wanjura, and A. Nunnenkamp (2023): Restoration of the non-Hermitian bulk-boundary correspondence via topological amplification. SciPost Physics 15, 173.
- Buča, B., C. Booker, and D. Jaksch (2022): Algebraic theory of quantum synchronization and limit cycles under dissipation. Scipost Physics 12, 097.

Buča, B. and D. Jaksch (2019): Dissipation Induced Nonstationarity in a Quantum Gas. Physical Review Letters 123, 260401.

- Buča, B. and T. Prosen (2012): A note on symmetry reductions of the Lindblad equation: transport in constrained open spin chains. New Journal of Physics 14, 073007.
- Buck, J. B. (1938): Synchronous Rhythmic Flashing of Fireflies. The Quarterly Review of Biology 13, 301–314.
- Cabot, A., L. S. Muhle, F. Carollo, and I. Lesanovsky (2023): Quantum trajectories of dissipative time crystals. Physical Review A 108, L041303.
- Callen, H. B. and T. A. Welton (1951): *Irreversibility and Generalized Noise*. Physical Review 83, 34–40.
- Caloz, C., A. Alù, S. Tretyakov, D. Sounas, K. Achouri, and Z.-L. Deck-Léger (2018): *Electromagnetic Nonreciprocity*. Physical Review Applied **10**, 047001.
- Campagne-Ibarcq, P., P. Six, L. Bretheau, A. Sarlette, M. Mirrahimi, P. Rouchon, and B. Huard (2016): Observing Quantum State Diffusion by Heterodyne Detection of Fluorescence. Physical Review X 6, 011002.
- Carmichael, H. J. (1993): Quantum trajectory theory for cascaded open systems. Physical Review Letters 70, 2273–2276.
- Carmichael, H. J. (1999): Statistical Methods in Quantum Optics 1 (Springer, Berlin, Germany).
- Carusotto, I. and C. Ciuti (2013): Quantum fluids of light. Reviews of Modern Physics 85, 299–366.
- Castellano, C., S. Fortunato, and V. Loreto (2009): Statistical physics of social dynamics. Reviews of Modern Physics 81, 591–646.
- Chen, J. (2009): Active optical clock. Chinese Science Bulletin 54, 348–352.
- Chia, A., L.-C. Kwek, and C. Noh (2020): Relaxation oscillations and frequency entrainment in quantum mechanics. Physical Review E 102, 042213.
- Chia, A., W.-K. Mok, L.-C. Kwek, and C. Noh (2025): Quantization of nonlinear non-Hamiltonian systems. arXiv: 2503.06939.
- Chiacchio, E. I. R. and A. Nunnenkamp (2019): Dissipation-Induced Instabilities of a Spinor Bose-Einstein Condensate Inside an Optical Cavity. Physical Review Letters 122, 193605.
- Chiacchio, E. I. R., A. Nunnenkamp, and M. Brunelli (2023): *Nonreciprocal Dicke Model*. Physical Review Letters **131**, 113602.
- Clerk, A. A., M. H. Devoret, S. M. Girvin, F. Marquardt, and R. J. Schoelkopf (2010): Introduction to quantum noise, measurement, and amplification. Reviews of Modern Physics 82, 1155–1208.
- Cox, K. C., J. M. Weiner, and J. K. Thompson (2014): Phase diagram for injection locking a superradiant laser. Physical Review A 90, 053845.
- Cross, M. and H. Greenside (2009): Pattern Formation and Dynamics in Nonequilibrium Systems (Cambridge University Press, New York, United States).

Davis-Tilley, C., C. K. Teoh, and A. D. Armour (2018): *Dynamics of many-body quantum synchronisation*. New Journal of Physics **20**, 113002.

- de Léséleuc, S., D. Barredo, V. Lienhard, A. Browaeys, and T. Lahaye (2017): Optical Control of the Resonant Dipole-Dipole Interaction between Rydberg Atoms. Physical Review Letters 119, 053202.
- Defenu, N., T. Donner, T. Macrì, G. Pagano, S. Ruffo, and A. Trombettoni (2023): Long-range interacting quantum systems. Reviews of Modern Physics 95, 035002.
- Defenu, N., A. Lerose, and S. Pappalardi (2024): Out-of-equilibrium dynamics of quantum many-body systems with long-range interactions. Physics Reports 1074, 1–92.
- Delmonte, A., A. Romito, G. E. Santoro, and R. Fazio (2023): Quantum effects on the synchronization dynamics of the Kuramoto model. Physical Review A 108, 032219.
- Delteil, A., Z. Sun, S. Fält, and A. Imamoğlu (2017): Realization of a Cascaded Quantum System: Heralded Absorption of a Single Photon Qubit by a Single-Electron Charged Quantum Dot. Physical Review Letters 118, 177401.
- Deák, L. and T. Fülöp (2012): Reciprocity in quantum, electromagnetic and other wave scattering. Annals of Physics **327**, 1050–1077.
- Dicke, R. H. (1954): Coherence in Spontaneous Radiation Processes. Phys. Rev. 93, 99–110.
- Dutta, S. and N. R. Cooper (2019): Critical Response of a Quantum van der Pol Oscillator. Physical Review Letters 123, 250401.
- Dutta, S., S. Zhang, and M. Haque (2025): Quantum Origin of Limit Cycles, Fixed Points, and Critical Slowing Down. Physical Review Letters 134, 050407.
- Eisert, J., M. Friesdorf, and C. Gogolin (2015): Quantum many-body systems out of equilibrium. Nature Physics 11, 124–130.
- Es'haqi-Sani, N., G. Manzano, R. Zambrini, and R. Fazio (2020): Synchronization along quantum trajectories. Physical Review Research 2, 023101.
- Famà, F., S. Zhou, B. Heizenreder, M. Tang, S. Bennetts, S. B. Jäger, S. A. Schäffer, and F. Schreck (2024): Continuous cavity QED with an atomic beam. Physical Review A 110, 063721.
- Fang, X., K. Kruse, T. Lu, and J. Wang (2019): Nonequilibrium physics in biology. Reviews of Modern Physics 91, 045004.
- Farmer, J. D. and D. Foley (2009): The economy needs agent-based modelling. Nature 460, 685–686.
- Fernández-Lorenzo, S. and D. Porras (2017): Quantum sensing close to a dissipative phase transition: Symmetry breaking and criticality as metrological resources. Physical Review A 96, 013817.
- Finger, F., R. Rosa-Medina, N. Reiter, P. Christodoulou, T. Donner, and T. Esslinger (2024): Spin- and Momentum-Correlated Atom Pairs Mediated by Photon Exchange and Seeded by Vacuum Fluctuations. Physical Review Letters 132, 093402.

Foss-Feig, M., G. Pagano, A. C. Potter, and N. Y. Yao (2025): *Progress in Trapped-Ion Quantum Simulation*. Annual Review of Condensed Matter Physics pages 145–172.

- Fruchart, M., R. Hanai, P. B. Littlewood, and V. Vitelli (2021): *Non-reciprocal phase transitions*. Nature **592**, 363–369.
- Gardiner, C. W. (1993): Driving a quantum system with the output field from another driven quantum system. Physical Review Letters **70**, 2269–2272.
- Gardiner, C. W. (1997): Stochastic Methods (Springer, Berlin, Germany).
- Gardiner, C. W. and P. Zoller (2000): Quantum Noise (Springer, Berlin, Germany).
- Giorgi, G. L., F. Galve, G. Manzano, P. Colet, and R. Zambrini (2012): Quantum correlations and mutual synchronization. Physical Review A 85, 052101.
- Goldsztein, G. H., A. N. Nadeau, and S. H. Strogatz (2021): Synchronization of clocks and metronomes: A perturbation analysis based on multiple timescales. Chaos: An Interdisciplinary Journal of Nonlinear Science 31, 023109.
- Gross, M. and S. Haroche (1982): Superradiance: An essay on the theory of collective spontaneous emission. Physics Reports 93, 301–396.
- Haken, H. (1983): Synergetics (Springer, Berlin, Germany).
- Hanai, R. (2024): Nonreciprocal Frustration: Time Crystalline Order-by-Disorder Phenomenon and a Spin-Glass-like State. Physical Review X 14, 011029.
- Hanai, R., A. Edelman, Y. Ohashi, and P. B. Littlewood (2019): Non-Hermitian Phase Transition from a Polariton Bose-Einstein Condensate to a Photon Laser. Physical Review Letters 122, 185301.
- Hanai, R. and P. B. Littlewood (2020): Critical fluctuations at a many-body exceptional point. Physical Review Research 2, 033018.
- Hanai, R., D. Ootsuki, and R. Tazai (2024): Photoinduced non-reciprocal magnetism. arXiv: 2406.05957.
- Harlander, M., R. Lechner, M. Brownnutt, R. Blatt, and W. Hänsel (2011): Trapped-ion antennae for the transmission of quantum information. Nature 471, 200–203.
- Harrington, P. M., E. J. Mueller, and K. W. Murch (2022): Engineered dissipation for quantum information science. Nature Reviews Physics 4, 660–671.
- Hatano, N. and D. R. Nelson (1996): Localization Transitions in non-Hermitian Quantum Mechanics. Physical Review Letters 77, 570–573.
- Hatano, N. and D. R. Nelson (1997): Vortex pinning and non-Hermitian quantum mechanics. Physical Review B 56, 8651–8673.
- Helbing, D. (2012): Social Self-Organization (Springer, Berlin, Germany).
- Hong, H. and S. H. Strogatz (2011a): Conformists and contrarians in a Kuramoto model with identical natural frequencies. Physical Review E 84, 046202.
- Hong, H. and S. H. Strogatz (2011b): Kuramoto Model of Coupled Oscillators with Positive and Negative Coupling Parameters: An Example of Conformist and Contrarian Oscillators. Physical Review Letters 106, 054102.

Huber, J., P. Kirton, S. Rotter, and P. Rabl (2020): Emergence of PT-symmetry breaking in open quantum systems. SciPost Physics 9, 052.

- Hush, M. R., W. Li, S. Genway, I. Lesanovsky, and A. D. Armour (2015): Spin correlations as a probe of quantum synchronization in trapped-ion phonon lasers. Physical Review A 91, 061401.
- Hübener, H., U. De Giovannini, C. Schäfer, J. Andberger, M. Ruggenthaler, J. Faist, and A. Rubio (2021): Engineering quantum materials with chiral optical cavities. Nature Materials 20, 438–442.
- Huybrechts, D., F. Minganti, F. Nori, M. Wouters, and N. Shammah (2020): Validity of mean-field theory in a dissipative critical system: Liouvillian gap, PT-symmetric antigap, and permutational symmetry in the XYZ model. Physical Review B 101, 214302.
- Iemini, F., A. Russomanno, J. Keeling, M. Schirò, M. Dalmonte, and R. Fazio (2018): *Boundary Time Crystals*. Physical Review Letters **121**, 035301.
- Ishibashi, K. and R. Kanamoto (2017): Oscillation Collapse in Coupled Quantum van der Pol Oscillators. Physical Review E **96**, 052210.
- Ivlev, A. V., J. Bartnick, M. Heinen, C.-R. Du, V. Nosenko, and H. Löwen (2015): Statistical Mechanics where Newton's Third Law is Broken. Physical Review X 5, 011035.
- Jachinowski, J. and P. B. Littlewood (2025): Spin-only dynamics of the multi-species nonreciprocal Dicke model. arXiv: 2507.07960.
- Jaseem, N., M. Hajdušek, P. Solanki, L.-C. Kwek, R. Fazio, and S. Vinjanampathy (2020a): Generalized measure of quantum synchronization. Physical Review Research 2, 043287.
- Jaseem, N., M. Hajdušek, V. Vedral, R. Fazio, L.-C. Kwek, and S. Vinjanampathy (2020b): Quantum Synchronisation in Nanoscale Heat Engines. Physical Review E 101, 020201.
- Johansson, J. R., P. D. Nation, and F. Nori (2012): QuTiP: An open-source Python framework for the dynamics of open quantum systems. Computer Physics Communications 183, 1760–1772.
- Joshi, C., F. Yang, and M. Mirhosseini (2023): Resonance fluorescence of a chiral artificial atom. Physical Review X 13, 021039.
- Kannan, B., M. J. Ruckriegel, D. L. Campbell, A. Frisk Kockum, J. Braumüller, D. K. Kim, M. Kjaergaard, P. Krantz, A. Melville, B. M. Niedzielski, A. Vepsäläinen, R. Winik, J. L. Yoder, F. Nori, T. P. Orlando, et al. (2020): Waveguide quantum electrodynamics with superconducting artificial giant atoms. Nature 583, 775–779.
- Karg, T. M., B. Gouraud, C. T. Ngai, G.-L. Schmid, K. Hammerer, and P. Treutlein (2020): Light-mediated strong coupling between a mechanical oscillator and atomic spins 1 meter apart. Science **369**, 174–179.
- Karg, T. M., B. Gouraud, P. Treutlein, and K. Hammerer (2019): Remote Hamiltonian interactions mediated by light. Physical Review A 99, 063829.
- Kato, Y. and H. Nakao (2021): Enhancement of quantum synchronization via continuous measurement and feedback control. New Journal of Physics 23, 013007.

Kaufman, A. M. and K.-K. Ni (2021): Quantum science with optical tweezer arrays of ultracold atoms and molecules. Nature Physics 17, 1324–1333.

- Kazakov, G. A. and T. Schumm (2014): Active optical frequency standards using cold atoms: Perspectives and challenges. In: 2014 European Frequency and Time Forum (EFTF). pages 411–414.
- Kehrer, T. and C. Bruder (2025): Quantum synchronization blockade induced by nonreciprocal coupling. Physical Review A 112, 012223.
- Kehrer, T., T. Nadolny, and C. Bruder (2024): Quantum synchronization through the interference blockade. Physical Review A 110, 042203.
- Khasseh, R., S. Wald, R. Moessner, C. A. Weber, and M. Heyl (2023): *Active quantum flocks*. arXiv: 2308.01603.
- Kirton, P., M. M. Roses, J. Keeling, and E. G. Dalla Torre (2019): *Introduction to the Dicke Model: From Equilibrium to Nonequilibrium, and Vice Versa*. Advanced Quantum Technologies 2, 1800043.
- Kockum, A. F., G. Johansson, and F. Nori (2018): Decoherence-Free Interaction between Giant Atoms in Waveguide Quantum Electrodynamics. Physical Review Letters 120, 140404.
- Kongkhambut, P., J. Skulte, L. Mathey, J. G. Cosme, A. Hemmerich, and H. Keßler (2022): Observation of a continuous time crystal. Science **377**, 670–673.
- Koppenhöfer, M., C. Bruder, and A. Roulet (2020): Quantum Synchronization on the IBM Q system. Physical Review Research 2, 023026.
- Koppenhöfer, M. and A. Roulet (2019): Optimal Synchronization Deep in the Quantum Regime: Resource and Fundamental Limit. Physical Review A 99, 043804.
- Krešić, I., G. R. M. Robb, G.-L. Oppo, and T. Ackemann (2023): Generating Multiparticle Entangled States by Self-Organization of Driven Ultracold Atoms. Physical Review Letters 131, 163602.
- Kristensen, S. L., E. Bohr, J. Robinson-Tait, T. Zelevinsky, J. W. Thomsen, and J. H. Müller (2023): Subnatural Linewidth Superradiant Lasing with Cold <sup>88</sup>Sr Atoms. Physical Review Letters 130, 223402.
- Krithika, V. R., P. Solanki, S. Vinjanampathy, and T. S. Mahesh (2022): Observation of quantum phase synchronization in a nuclear-spin system. Physical Review A 105, 062206.
- Kubo, R. (1962): Generalized Cumulant Expansion Method. Journal of the Physical Society of Japan 17, 1100.
- Kubo, R. (1966): The fluctuation-dissipation theorem. Reports on Progress in Physics, 29, 255.
- Kuramoto, Y. (1975): Self-entrainment of a population of coupled non-linear oscillators. In: Araki, H. (editor), International Symposium on Mathematical Problems in Theoretical Physics (Springer, Berlin, Germany), page 420.
- Kuramoto, Y. (1984): Chemical Oscillations, Waves, and Turbulence (Springer, Berlin, Germany).

Kuznetsov, Y. A. (2023): Elements of Applied Bifurcation Theory (Springer, Cham, Switzerland).

- Landi, G. T., D. Poletti, and G. Schaller (2022): Nonequilibrium boundary-driven quantum systems: Models, methods, and properties. Reviews of Modern Physics 94, 045006.
- Laskar, A. W., P. Adhikary, S. Mondal, P. Katiyar, S. Vinjanampathy, and S. Ghosh (2020): Observation of Quantum Phase Synchronization in Spin-1 Atoms. Physical Review Letters 125, 013601.
- Laske, T., H. Winter, and A. Hemmerich (2019): Pulse Delay Time Statistics in a Superradiant Laser with Calcium Atoms. Physical Review Letters 123, 103601.
- Lau, H.-K. and A. A. Clerk (2018): Fundamental limits and non-reciprocal approaches in non-Hermitian quantum sensing. Nature Communications 9, 4320.
- Lecocq, F., L. Ranzani, G. A. Peterson, K. Cicak, R. W. Simmonds, J. D. Teufel, and J. Aumentado (2017): Nonreciprocal Microwave Signal Processing with a Field-Programmable Josephson Amplifier. Physical Review Applied 7, 024028.
- Lee, T. E., C.-K. Chan, and S. Wang (2014): Entanglement Tongue and Quantum Synchronization of Disordered Oscillators. Physical Review E 89, 022913.
- Lee, T. E. and H. R. Sadeghpour (2013): Quantum Synchronization of Quantum van der Pol Oscillators with Trapped Ions. Physical Review Letters 111, 234101.
- Leibfried, D., R. Blatt, C. Monroe, and D. Wineland (2003): Quantum dynamics of single trapped ions. Reviews of Modern Physics 75, 281–324.
- Li, W., W. Zhang, C. Li, and H. Song (2017): Properties and relative measure for quantifying quantum synchronization. Physical Review E 96, 012211.
- Li, Y., Z. Xie, X. Yang, Y. Li, X. Zhao, X. Cheng, X. Peng, J. Li, E. Lutz, Y. Lin, and J. Du (2025): Experimental realization and synchronization of a quantum van der Pol oscillator. arXiv: 2504.00751.
- Librandi, G., E. Tubaldi, and K. Bertoldi (2021): Programming nonreciprocity and reversibility in multistable mechanical metamaterials. Nature Communications 12, 3454.
- Liedl, C., S. Pucher, F. Tebbenjohanns, P. Schneeweiss, and A. Rauschenbeutel (2023): Collective Radiation of a Cascaded Quantum System: From Timed Dicke States to Inverted Ensembles. Physical Review Letters 130, 163602.
- Liedl, C., F. Tebbenjohanns, C. Bach, S. Pucher, A. Rauschenbeutel, and P. Schneeweiss (2024): Observation of Superradiant Bursts in a Cascaded Quantum System. Physical Review X 14, 011020.
- Liu, H., S. B. Jäger, X. Yu, S. Touzard, A. Shankar, M. J. Holland, and T. L. Nicholson (2020): Rugged mHz-Linewidth Superradiant Laser Driven by a Hot Atomic Beam. Physical Review Letters 125, 253602.
- Liu, T., V. Raskatla, J. Li, K. F. MacDonald, and N. I. Zheludev (2024): Breaking of Time Translation Symmetry and Ergodicity, and Entropy decrease in a Continuous Time Crystal Driven by Nonreciprocal Optical Forces. arXiv: 2404.10525.

Loos, S. A. M., S. H. L. Klapp, and T. Martynec (2023): Long-Range Order and Directional Defect Propagation in the Nonreciprocal XY Model with Vision Cone Interactions. Physical Review Letters 130, 198301.

- Lörch, N., E. Amitai, A. Nunnenkamp, and C. Bruder (2016): Genuine Quantum Signatures in Synchronization of Anharmonic Self-Oscillators. Physical Review Letters 117, 073601.
- Lörch, N., S. E. Nigg, A. Nunnenkamp, R. P. Tiwari, and C. Bruder (2017): Quantum Synchronization Blockade: Energy Quantization Hinders Synchronization of Identical Oscillators. Physical Review Letters 118, 243602.
- Lörch, N., J. Qian, A. Clerk, F. Marquardt, and K. Hammerer (2014): Laser Theory for Optomechanics: Limit Cycles in the Quantum Regime. Physical Review X 4, 011015.
- Lorenzo, S., B. Militello, A. Napoli, R. Zambrini, and G. M. Palma (2022): Quantum synchronisation and clustering in chiral networks. New Journal of Physics 24, 023030.
- Lotka, A. J. (1925): *Elements of Physical Biology* (Williams & Wilkins, Baltimore, United States). (accessed via archive.org).
- Ludlow, A. D., M. M. Boyd, J. Ye, E. Peik, and P. O. Schmidt (2015): *Optical atomic clocks*. Reviews of Modern Physics 87, 637–701.
- Ludwig, M. and F. Marquardt (2013): Quantum Many-Body Dynamics in Optomechanical Arrays. Physical Review Letters 111, 073603.
- Majer, J., J. M. Chow, J. M. Gambetta, J. Koch, B. R. Johnson, J. A. Schreier, L. Frunzio, D. I. Schuster, A. A. Houck, A. Wallraff, A. Blais, M. H. Devoret, S. M. Girvin, and R. J. Schoelkopf (2007): Coupling superconducting qubits via a cavity bus. Nature 449, 443–447.
- Manzano, D. (2020): A short introduction to the Lindblad master equation. AIP Advances 10, 025106.
- Marchetti, M. C., J. F. Joanny, S. Ramaswamy, T. B. Liverpool, J. Prost, M. Rao, and R. A. Simha (2013): *Hydrodynamics of soft active matter*. Reviews of Modern Physics 85, 1143–1189.
- Mari, A., A. Farace, N. Didier, V. Giovannetti, and R. Fazio (2013): Measures of Quantum Synchronization in Continuous Variable Systems. Physical Review Letters 111, 103605.
- Matthews, P. C., R. E. Mirollo, and S. H. Strogatz (1991): Dynamics of a large system of coupled nonlinear oscillators. Physica D 52, 293–331.
- McCrea, M., B. Ermentrout, and J. E. Rubin (2022): A model for the collective synchronization of flashing in Photinus carolinus. Journal of the Royal Society Interface 19, 20220439.
- McDonald, A., R. Hanai, and A. A. Clerk (2022): Nonequilibrium stationary states of quantum non-Hermitian lattice models. Physical Review B 105, 064302.
- Meiser, D., J. Ye, D. R. Carlson, and M. J. Holland (2009): Prospects for a Millihertz-Linewidth Laser. Physical Review Letters 102, 163601.

Meredith, C. H., P. G. Moerman, J. Groenewold, Y.-J. Chiu, W. K. Kegel, A. van Blaaderen, and L. D. Zarzar (2020): *Predator-prey interactions between droplets driven by non-reciprocal oil exchange*. Nature Chemistry 12, 1136–1142.

- Metelmann, A. and A. A. Clerk (2015): Nonreciprocal Photon Transmission and Amplification via Reservoir Engineering. Physical Review X 5, 021025.
- Mitsch, R., C. Sayrin, B. Albrecht, P. Schneeweiss, and A. Rauschenbeutel (2014): Quantum state-controlled directional spontaneous emission of photons into a nanophotonic waveguide. Nature Communications 5, 1–5.
- Mivehvar, F., F. Piazza, T. Donner, and H. Ritsch (2021): Cavity QED with quantum gases: new paradigms in many-body physics. Advances in Physics 70, 1–153.
- Mok, W.-K., L.-C. Kwek, and H. Heimonen (2020): Synchronization boost with single-photon dissipation in the deep quantum regime. Physical Review Research 2, 033422.
- Montbrió, E., J. Kurths, and B. Blasius (2004): Synchronization of two interacting populations of oscillators. Physical Review E 70, 056125.
- Muniz, J. A., D. Barberena, R. J. Lewis-Swan, D. J. Young, J. R. K. Cline, A. M. Rey, and J. K. Thompson (2020): *Exploring dynamical phase transitions with cold atoms in an optical cavity*. Nature **580**, 602–607.
- Nadolny, T. and C. Bruder (2023): Macroscopic Quantum Synchronization Effects. Physical Review Letters 131, 190402.
- Nadolny, T., C. Bruder, and M. Brunelli (2025a): Nonreciprocal Synchronization of Active Quantum Spins. Physical Review X 15, 011010.
- Nadolny, T., M. Brunelli, and C. Bruder (2025b): Nonreciprocal Interactions Induce Frequency Shifts in Superradiant Lasers. Physical Review Letters 134, 193603.
- Nakanishi, Y. and T. Sasamoto (2022): *PT phase transition in open quantum systems with Lindblad dynamics*. Physical Review A **105**, 022219.
- Natale, G., A. Baumgärtner, J. Stefaniak, D. Baur, S. Hertlein, D. Rivero, T. Esslinger, and T. Donner (2025): Synchronization of Quasi-Particle Excitations in a Quantum Gas with Cavity-Mediated Interactions. arXiv: 2504.17731.
- Newton, I. (1687): *Philosophiae Naturalis Principia Mathematica*. (Royal Society, London, England). (accessed via e-rara).
- Nielsen, M. A. and I. L. Chuang (2010): Quantum Computation and Quantum Information: 10th Anniversary Edition (Cambridge University Press, New York, United States).
- Nigg, S. E. (2018): Observing quantum synchronization blockade in circuit quantum electrodynamics. Physical Review A 97, 013811.
- Norcia, M. A., R. J. Lewis-Swan, J. R. K. Cline, B. Zhu, A. M. Rey, and J. K. Thompson (2018): Cavity-mediated collective spin-exchange interactions in a strontium superradiant laser. Science 361, 259–262.
- Norcia, M. A. and J. K. Thompson (2016): Cold-Strontium Laser in the Superradiant Crossover Regime. Physical Review X 6, 011025.

Okuda, K. and Y. Kuramoto (1991): Mutual Entrainment between Populations of Coupled Oscillators. Progress of Theoretical Physics 86, 1159–1176.

- Okuma, N. and M. Sato (2023): Non-Hermitian Topological Phenomena: A Review. Annual Review of Condensed Matter Physics 14, 83–107.
- Onodera, T., E. Ng, and P. L. McMahon (2020): A quantum annealer with fully programmable all-to-all coupling via Floquet engineering. npj Quantum Information 6, 48.
- Oppenheim, A., R. Schafer, and J. Buck (2013): Discrete-time Signal Processing (Pearson International, London, England).
- Ott, E. and T. M. Antonsen (2008): Low dimensional behavior of large systems of globally coupled oscillators. Chaos 18, 037113.
- Ott, E. and T. M. Antonsen (2009): Long time evolution of phase oscillator systems. Chaos 19, 023117.
- Parra-López, Á. and J. Bergli (2020): Synchronization in Two-Level Quantum Systems. Physical Review A 101, 062104.
- Patra, A., B. L. Altshuler, and E. A. Yuzbashyan (2019a): Chaotic synchronization between atomic clocks. Physical Review A 100, 023418.
- Patra, A., B. L. Altshuler, and E. A. Yuzbashyan (2019b): Driven-dissipative dynamics of atomic ensembles in a resonant cavity: Nonequilibrium phase diagram and periodically modulated superradiance. Physical Review A 99, 033802.
- Patra, A., B. L. Altshuler, and E. A. Yuzbashyan (2020): Driven-dissipative dynamics of atomic ensembles in a resonant cavity: Quasiperiodic route to chaos and chaotic synchronization. Annals of Physics 417, 168106.
- Penner, A.-G., L. Viotti, R. Fazio, L. Arrachea, and F. von Oppen (2025): *Heat-to-motion conversion for quantum active matter*. arXiv: 2503.07751.
- Petersen, J., J. Volz, and A. Rauschenbeutel (2014): Chiral nanophotonic waveguide interface based on spin-orbit interaction of light. Science **346**, 67–71.
- Pezzè, L., A. Smerzi, M. K. Oberthaler, R. Schmied, and P. Treutlein (2018): Quantum metrology with nonclassical states of atomic ensembles. Reviews of Modern Physics 90, 035005.
- Pichler, H., T. Ramos, A. J. Daley, and P. Zoller (2015): Quantum optics of chiral spin networks. Physical Review A 91, 042116.
- Pikovsky, A. and M. Rosenblum (2011): Dynamics of heterogeneous oscillator ensembles in terms of collective variables. Physica D 240, 872–881.
- Pikovsky, A. and M. Rosenblum (2015): Dynamics of globally coupled oscillators: Progress and perspectives. Chaos 25, 097616.
- Pikovsky, A., M. Rosenblum, and J. Kurths (2001): Synchronization: A Universal Concept in Nonlinear Sciences. Cambridge Nonlinear Science Series (Cambridge University Press, New York, United States).

Piñeiro Orioli, A., J. K. Thompson, and A. M. Rey (2022): Emergent Dark States from Superradiant Dynamics in Multilevel Atoms in a Cavity. Physical Review X 12, 011054.

- Plankensteiner, D., C. Hotter, and H. Ritsch (2022): QuantumCumulants.jl: A Julia framework for generalized mean-field equations in open quantum systems. Quantum 6, 617.
- Polkovnikov, A., K. Sengupta, A. Silva, and M. Vengalattore (2011): *Colloquium: Nonequilibrium dynamics of closed interacting quantum systems*. Reviews of Modern Physics 83, 863–883.
- Porras, D. and S. Fernández-Lorenzo (2019): Topological Amplification in Photonic Lattices. Physical Review Letters 122, 143901.
- Prigogine, I. (1978): Time, Structure, and Fluctuations. Science 201, 777–785.
- Prosen, T. (2012): *PT-Symmetric Quantum Liouvillean Dynamics*. Physical Review Letters **109**, 090404.
- Ranzani, L. and J. Aumentado (2015): Graph-based analysis of nonreciprocity in coupled-mode systems. New Journal of Physics 17, 023024.
- Reilly, J. T., S. B. Jäger, J. Cooper, and M. J. Holland (2025): Fully Collective Superradiant Lasing with Vanishing Sensitivity to Cavity Length Vibrations. arXiv: 2506.12267.
- Reisenbauer, M., H. Rudolph, L. Egyed, K. Hornberger, A. V. Zasedatelev, M. Abuzarli, B. A. Stickler, and U. Delić (2024): *Non-Hermitian dynamics and non-reciprocity of optically coupled nanoparticles*. Nature Physics **20**, 1629–1635.
- Risken, H. (1989): The Fokker-Planck Equation (Springer, Berlin, Germany).
- Ritsch, H., P. Domokos, F. Brennecke, and T. Esslinger (2013): Cold atoms in cavity-generated dynamical optical potentials. Reviews of Modern Physics 85, 553–601.
- Roth, A. and K. Hammerer (2016): Synchronization of active atomic clocks via quantum and classical channels. Physical Review A 94, 043841.
- Roulet, A. and C. Bruder (2018a): Quantum Synchronization and Entanglement Generation. Physical Review Letters 121, 063601.
- Roulet, A. and C. Bruder (2018b): Synchronizing the Smallest Possible System. Physical Review Letters 121, 053601.
- Rudolph, H., U. Delić, K. Hornberger, and B. A. Stickler (2024a): *Quantum Optical Binding of Nanoscale Particles*. Physical Review Letters **133**, 233603.
- Rudolph, H., U. Delić, K. Hornberger, and B. A. Stickler (2024b): Quantum theory of non-Hermitian optical binding between nanoparticles. Physical Review A 110, 063507.
- Sá, L., P. Ribeiro, and T. Prosen (2023): Symmetry Classification of Many-Body Lindbladians: Tenfold Way and Beyond. Physical Review X 13, 031019.
- Sacha, K. and J. Zakrzewski (2017): *Time crystals: a review*. Reports on Progress in Physics 81, 016401.
- Sarkar, S., A. Bayat, S. Bose, and R. Ghosh (2025): Exponentially-enhanced quantum sensing with many-body phase transitions. Nature Communications 16, 1–11.

Schaller, G. (2014): Open Quantum Systems Far from Equilibrium (Springer, Heidelberg, Germany).

- Schweitzer, F. (2003): Brownian Agents and Active Particles: Collective Dynamics in the Natural and Social Sciences (Springer, Berlin, Germany).
- Scully, M. O. and M. S. Zubairy (1997): *Quantum Optics* (Cambridge University Press, Cambridge, England).
- Setoyama, W. and Y. Hasegawa (2024): *Lie Algebraic Quantum Phase Reduction*. Physical Review Letters **132**, 093602.
- Setoyama, W. and Y. Hasegawa (2025): Lie-algebraic quantum phase reduction based on heterodyne detection. Physical Review A 111, 012202.
- Shammah, N., S. Ahmed, N. Lambert, S. De Liberato, and F. Nori (2018): Open quantum systems with local and collective incoherent processes: Efficient numerical simulations using permutational invariance. Physical Review A 98, 063815.
- Shankar, S., A. Souslov, M. J. Bowick, M. C. Marchetti, and V. Vitelli (2022): *Topological active matter*. Nature Reviews Physics 4, 380–398.
- Shen, Y., W.-K. Mok, C. Noh, A. Q. Liu, L.-C. Kwek, W. Fan, and A. Chia (2023a): Quantum synchronization effects induced by strong nonlinearities. Physical Review A 107, 053713.
- Shen, Y., H. Y. Soh, W. Fan, and L.-C. Kwek (2023b): Enhancing quantum synchronization through homodyne measurement, noise, and squeezing. Physical Review E 108, 024204.
- Sieberer, L. M., M. Buchhold, J. Marino, and S. Diehl (2025): Universality in driven open quantum matter. Reviews of Modern Physics 97, 025004.
- Siegman, A. (1986): Lasers (University Science Books, Mill Valley, United States).
- Solanki, P., F. M. Mehdi, M. Hajdušek, and S. Vinjanampathy (2023): Symmetries and synchronization blockade. Physical Review A 108, 022216.
- Sonnenschein, B., T. K. D. M. Peron, F. A. Rodrigues, J. Kurths, and L. Schimansky-Geier (2015): Collective dynamics in two populations of noisy oscillators with asymmetric interactions. Physical Review E 91, 062910.
- Söllner, I., S. Mahmoodian, S. L. Hansen, L. Midolo, A. Javadi, G. Kiršanskė, T. Pregnolato, H. El-Ella, E. H. Lee, J. D. Song, S. Stobbe, and P. Lodahl (2015): Deterministic photon-emitter coupling in chiral photonic circuits. Nature Nanotechnology 10, 775–778.
- Spohn, H. (1980): Kinetic equations from Hamiltonian dynamics: Markovian limits. Reviews of Modern Physics **52**, 569–615.
- Stannigel, K., P. Rabl, and P. Zoller (2012): Driven-dissipative preparation of entangled states in cascaded quantum-optical networks. New Journal of Physics 14, 063014.
- Strogatz, S. H. (2003): Sync: The Emerging Science of Spontaneous Order (Hyperion, New York, United States).
- Strogatz, S. H. (2019): Nonlinear Dynamics and Chaos: With Applications to Physics, Biology, Chemistry, and Engineering (Taylor & Francis, Andover, England).

Strogatz, S. H., D. Abrams, F. McRobie, B. Eckhardt, and E. Ott (2005): Crowd synchrony on the Millennium Bridge. Nature 438, 43–4.

- Strogatz, S. H. and R. E. Mirollo (1991): Stability of incoherence in a population of coupled oscillators. Journal of Statistical Physics 63, 613–635.
- Suárez-Forero, D. G., M. Jalali Mehrabad, C. Vega, A. González-Tudela, and M. Hafezi (2025): Chiral Quantum Optics: Recent Developments and Future Directions. PRX Quantum 6, 020101.
- Takasan, K., K. Adachi, and K. Kawaguchi (2024): Activity-induced ferromagnetism in one-dimensional quantum many-body systems. Physical Review Research 6, 023096.
- Tang, M., S. A. Schäffer, and J. H. Müller (2022): Prospects of a superradiant laser based on a thermal or guided beam of <sup>88</sup>Sr. Physical Review A 106, 063704.
- te Vrugt, M., B. Liebchen, and M. E. Cates (2025): What exactly is 'active matter'? arXiv 2507.21621.
- te Vrugt, M. and R. Wittkowski (2025): *Metareview: a survey of active matter reviews*. The European Physical Journal E **48**, 1–38.
- Tokura, Y., M. Kawasaki, and N. Nagaosa (2017): Emergent functions of quantum materials. Nature Physics 13, 1056–1068.
- Tyulkina, I. V., D. S. Goldobin, L. S. Klimenko, and A. Pikovsky (2018): Dynamics of Noisy Oscillator Populations beyond the Ott-Antonsen Ansatz. Physical Review Letters 120, 264101.
- Uhlhaas, P., G. Pipa, B. Lima, L. Melloni, S. Neuenschwander, D. Nikolić, and W. Singer (2009): Neural synchrony in cortical networks: history, concept and current status. Frontiers in Integrative Neuroscience 3, 543.
- Vaidya, G. M., S. B. Jäger, and A. Shankar (2025): Quantum synchronization and dissipative quantum sensing. Physical Review A 111, 012410.
- Verhagen, E. and A. Alù (2017): Optomechanical nonreciprocity. Nature Physics 13, 922–924.
- Volterra, V. (1926): Variazioni e fluttuazioni del numero d'individui in specie animali conviventi. Memoria della Reale Accademia Nazionale dei Lincei 2, 31–113.
- Wächtler, C. W. and J. E. Moore (2024): Topological Quantum Synchronization of Fractionalized Spins. Physical Review Letters 132, 196601.
- Walter, S., A. Nunnenkamp, and C. Bruder (2014): Quantum Synchronization of a Driven Self-Sustained Oscillator. Physical Review Letters 112, 094102.
- Walter, S., A. Nunnenkamp, and C. Bruder (2015): Quantum synchronization of two Van der Pol oscillators. Annalen der Physik 527, 131–138.
- Wang, Y.-X., C. Wang, and A. A. Clerk (2023): Quantum Nonreciprocal Interactions via Dissipative Gauge Symmetry. PRX Quantum 4, 010306.
- Wang, Z.-Q., Y.-P. Wang, J. Yao, R.-C. Shen, W.-J. Wu, J. Qian, J. Li, S.-Y. Zhu, and J. Q. You (2022): Giant spin ensembles in waveguide magnonics. Nature Communications 13, 1–7.

Wanjura, C. C., M. Brunelli, and A. Nunnenkamp (2020): Topological framework for directional amplification in driven-dissipative cavity arrays. Nature Communications 11, 3149.

- Wanjura, C. C., J. J. Slim, J. del Pino, M. Brunelli, E. Verhagen, and A. Nunnenkamp (2023): Quadrature nonreciprocity in bosonic networks without breaking time-reversal symmetry. Nature Physics 19, 1429–1436.
- Weiner, J. M., K. C. Cox, J. G. Bohnet, and J. K. Thompson (2017): Phase synchronization inside a superradiant laser. Physical Review A 95, 033808.
- Weis, C. and R. Hanai (2025): Generalized non-reciprocal phase transitions in multipopulation systems. arXiv 2507.16763.
- Weiss, T., A. Kronwald, and F. Marquardt (2016): Noise-induced transitions in optome-chanical synchronization. New Journal of Physics 18, 013043.
- Weiss, T., S. Walter, and F. Marquardt (2017): Quantum-coherent phase oscillations in synchronization. Physical Review A 95, 041802.
- Wiersig, J. (2020): Review of exceptional point-based sensors. Photonics Research 8, 1457–1467.
- Wiseman, H. M. (1996): Quantum trajectories and quantum measurement theory. Quantum and Semiclassical Optics 8, 205.
- Wiseman, H. M. and G. J. Milburn (2010): Quantum Measurement and Control (Cambridge University Press, New York, United States).
- Witthaut, D., F. Hellmann, J. Kurths, S. Kettemann, H. Meyer-Ortmanns, and M. Timme (2022): Collective nonlinear dynamics and self-organization in decentralized power grids. Reviews of Modern Physics **94**, 015005.
- Witthaut, D., S. Wimberger, R. Burioni, and M. Timme (2017): Classical synchronization indicates persistent entanglement in isolated quantum systems. Nature Communications 8, 14829.
- Wu, Q., Y. Zhang, X. Yang, S.-L. Su, C. Shan, and K. Mølmer (2022): A superradiant maser with nitrogen-vacancy center spins. Science China Physics, Mechanics & Astronomy 65, 1–10.
- Xu, M. and M. J. Holland (2015): Conditional Ramsey Spectroscopy with Synchronized Atoms. Physical Review Letters 114, 103601.
- Xu, M., D. A. Tieri, E. C. Fine, J. K. Thompson, and M. J. Holland (2014): Synchronization of Two Ensembles of Atoms. Physical Review Letters 113, 154101.
- Yamagishi, M., N. Hatano, and H. Obuse (2024): Proposal of a quantum version of active particles via a nonunitary quantum walk. Scientific Reports 14, 1–14.
- You, Z., A. Baskaran, and M. C. Marchetti (2020): Nonreciprocity as a generic route to traveling states. Proceedings of the National Academy of Sciences 117, 19767–19772.
- Young, D. J., A. Chu, E. Y. Song, D. Barberena, D. Wellnitz, Z. Niu, V. M. Schäfer, R. J. Lewis-Swan, A. M. Rey, and J. K. Thompson (2024): Observing dynamical phases of BCS superconductors in a cavity QED simulator. Nature 625, 679–684.

Yuan, H., L. X. Cui, L. T. Chen, and C. P. Sun (2024): Quantum Vicsek Model for Active Matter. arXiv: 2407.09860.

- Zelle, C. P., R. Daviet, A. Rosch, and S. Diehl (2024): Universal Phenomenology at Critical Exceptional Points of Nonequilibrium O(N) Models. Physical Review X 14, 021052.
- Zhang, L., Z. Wang, Y. Wang, J. Zhang, Z. Wu, J. Jie, and Y. Lu (2023): Quantum synchronization of a single trapped-ion qubit. Physical Review Research 5, 033209.
- Zhang, Y., C. Shan, and K. Mølmer (2022): Active Frequency Measurement on Superradiant Strontium Clock Transitions. Physical Review Letters 128, 013604.
- Zhirov, O. V. and D. L. Shepelyansky (2006): *Quantum synchronization*. The European Physical Journal D **38**, 375–379.
- Zhirov, O. V. and D. L. Shepelyansky (2008): Synchronization and Bistability of a Qubit Coupled to a Driven Dissipative Oscillator. Physical Review Letters 100, 014101.
- Zhirov, O. V. and D. L. Shepelyansky (2009): Quantum synchronization and entanglement of two qubits coupled to a driven dissipative resonator. Physical Review B 80, 014519.
- Zhu, B., J. Schachenmayer, M. Xu, F. Herrera, J. G. Restrepo, M. J. Holland, and A. M. Rey (2015): *Synchronization of Interacting Quantum Dipoles*. New Journal of Physics 17, 083063.
- Zhu, G.-L., C.-S. Hu, H. Wang, W. Qin, X.-Y. Lü, and F. Nori (2024): Nonreciprocal Superradiant Phase Transitions and Multicriticality in a Cavity QED System. Physical Review Letters 132, 193602.
- Zhu, S.-L., C. Monroe, and L.-M. Duan (2006): Trapped Ion Quantum Computation with Transverse Phonon Modes. Physical Review Letters 97, 050505.
- Zwanzig, R. (2001): Nonequilibrium statistical mechanics (Oxford University Press, New York, United States).